NACA RM L58C07

[redacted]

Copy
RM L58C07

C 2

RESEARCH MEMORANDUM

ANALYSIS OF PRESSURE DISTRIBUTIONS FOR A SERIES OF TIP AND TRAILING-EDGE CONTROLS ON A 60° DELTA WING AT MACH NUMBERS OF 1.61 AND 2.01

By Douglas R. Lord and K. R. Czarnecki

Langley Aeronautical Laboratory
Langley Field, Va.

LIBRARY COPY

MAY 16 1958

LANGLEY AERONAUTICAL LABORATORY
LIBRARY, NACA
LANGLEY FIELD, VIRGINIA

NASA CCD HAS 2-16-66

kmC
2-9-66

CLASSIFIED DOCUMENT

This material contains information affecting the National Defense of the United States within the meaning of the espionage laws, Title 18, U.S.C., Secs. 793 and 794, the transmission or revelation of which in any manner to an unauthorized person is prohibited by law.

NATIONAL ADVISORY COMMITTEE FOR AERONAUTICS

WASHINGTON

May 16, 1958

[redacted]

NASA Technical Library
3 1176 01437 7916

CATION CHANGED
UNCLASSIFIED

CONTENTS

NASA CCN #50 2-16-66
By authority of
RMC 3-9-66

	Page	Figure
SUMMARY	1	
INTRODUCTION	2	
SYMBOLS	2	
APPARATUS	3	
Wind Tunnel	3	
Model and Model Mounting	3	1 to 4
TESTS	4	3
PRECISION OF DATA	5	
RESULTS	5	
DISCUSSION	6	
Basic Pressure Distributions	6	5 to 16
Wing	6	
Trailing-edge controls	7	
Tip controls	7	
Comparison of Experimental and Theoretical Results	8	17 to 21
Application and limitations of theory	8	
Trailing-edge controls - surface pressure coefficients due to δ	9	
Trailing-edge controls - surface pressure coefficients due to α	10	
Trailing-edge controls - resultant pressure coefficients	11	
Tip controls - surface pressure coefficients due to δ	11	
Tip controls - surface pressure coefficients due to α	12	
Tip controls - resultant pressure coefficients	12	
Experimental Comparisons	13	
Effect of Mach number	13	22
Effect of Reynolds number	13	23
Effect of hinge-line location	13	24 and 25
Effect of offsetting tip control	14	26
Effect of control plan form	14	27

[redacted]

	Page	Figure
Effect of fixed tab on a boom	14	28
Effect of fences	14	29 to 33
Effect of control span and location	15	34 and 35
Effect of trailing-edge thickness	15	36
Effect of paddle balances	16	37
CONCLUSIONS	16	
Basic Pressure Distributions	16	
Comparison of Experimental and Theoretical Results	16	
Experimental Comparisons	17	
REFERENCES	19	
TABLES	20	
FIGURES	28	

NATIONAL ADVISORY COMMITTEE FOR AERONAUTICS

RESEARCH MEMORANDUM

ANALYSIS OF PRESSURE DISTRIBUTIONS FOR A SERIES OF TIP AND TRAILING-EDGE CONTROLS ON A 60° DELTA WING AT MACH NUMBERS OF 1.61 AND 2.01

By Douglas R. Lord and K. R. Czarnecki

SUMMARY

An investigation has been made at Mach numbers of 1.61 and 2.01 and at Reynolds numbers from 1.7×10^6 to 7.6×10^6 to determine the pressure distributions for a series of 20 controls on a 60° delta wing. Thirteen of the controls were of the balanced tip type and seven of the controls were of the more conventional trailing-edge type. Tests were made at wing angles of attack from 0° to 15° for control deflections from -30° to 30°.

Deflecting the controls causes the pressure distributions on the low-pressure surface to approach a rectangular loading with a negative pressure coefficient of about 80-percent vacuum and on the high-pressure surface to develop a pressure peak followed by an expansion toward the trailing edge. There is a load carryover ahead of the trailing-edge controls, but very little carryover across the wing-control parting lines for any of the controls.

Linear-theory predictions of the pressure distributions due to control deflection were only fair because of viscous and shock-detachment effects not considered by linear theory. The linear-theory predictions of the pressure distributions due to angle of attack were good at the low control deflections but tended to be considerably worse as the control deflections increased.

At small angular conditions, the pressure changes due to increasing the Mach number from 1.61 to 2.01 were in agreement with theory. Increasing the Reynolds number from 1.7×10^6 to 7.6×10^6 caused negligible changes in the pressure distributions. Hinge-line movement or parting-line fences on the tip-type controls resulted in sizeable changes in the pressure distributions near the parting lines because of the strong crossflows in these regions.

INTRODUCTION

As part of a general program of research on controls, an investigation is under way in the Langley 4- by 4-foot supersonic pressure tunnel to determine the important parameters in the design of controls for use on a 60° delta wing at supersonic speeds. The results have been obtained from two series of tests by means of pressure distributions and direct measurements of the hinge moments. The first series was conducted at a Mach number of 1.61 and included primarily tip controls, some fence configurations, and a trailing-edge control with and without a spoiler mounted on the wing just ahead of the control. The second series included tests of several trailing-edge controls, two additional tip controls, and several tab and fence configurations, each at a Mach number of 1.61, and four of the tip controls at a Mach number of 2.01. All of the control hinge-moment results and some of the effectiveness, span-loading, and pressure-distribution results for the two series of tests have been presented in references 1 to 9.

Although preliminary pressure-distribution analysis for some of the configurations has been presented in references 3 and 5, the purpose of the present report is to complete the pressure-distribution analysis for all of the configurations tested. Comparison of the experimental results with theoretical predictions and analysis of the effects of configuration changes are also included. Tests were made for a wing angle-of-attack range from 0° to 15° and for a control-deflection range from -30° to 30° at Mach numbers of 1.61 and 2.01. All configurations were tested at a Reynolds number of 4.2×10^6, based on the wing mean aerodynamic chord of 12.10 inches. One configuration was also tested at Reynolds numbers of 1.7×10^6 and 7.6×10^6 at a Mach number of 1.61.

SYMBOLS

$b/2$	wing semispan, 10.48 in.
$\bar{c}$	wing mean aerodynamic chord, 12.10 in.
c_R	wing root chord, 18.14 in.
C_p	pressure coefficient, $\frac{p_l - p}{q}$
$C_{p,R}$	resultant pressure coefficient (Lower-surface pressure coefficient minus upper-surface pressure coefficient)

M	stream Mach number
p	stream static pressure
p_l	local wing surface static pressure
q	stream dynamic pressure
R	Reynolds number (based on wing mean aerodynamic chord)
x	distance from wing apex in chordwise direction
y	distance from wing apex in spanwise direction
α	wing angle of attack
δ	control deflection relative to wing (positive when control trailing edge is deflected down)
Δ	prefix indicating change due to α or δ

APPARATUS

Wind Tunnel

This investigation was conducted in the Langley 4- by 4-foot supersonic pressure tunnel, which is a rectangular, closed-throat, single-return wind tunnel with provisions for the control of the pressure, temperature, and humidity of the enclosed air. Flexible-nozzle walls were adjusted to give the desired test-section Mach numbers of 1.61 and 2.01. During the tests, the dewpoint was kept below -20° F so that the effects of water condensation in the supersonic nozzle were negligible.

Model and Model Mounting

The model used in this investigation consisted of a semispan delta wing having 11 interchangeable controls and various associated control adapters (or replacement sections) that were required to fit the controls to the basic wing component. The control configurations are presented in figure 1 grouped according to whether they were tip controls (fig. 1(a)), trailing-edge controls (fig. 1(b)), or tip controls with modifications such as fences or tabs (fig. 1(c)). The 11 basic configurations are identified as configurations A through G, I, J, J1, and J2. Modifications were made to these basic configurations to obtain the

remaining 9 configurations. Configuration H was obtained by installing the control of configuration F in the hinge-line hole for configuration E. Configurations J3 and J4 were made from configuration J by adding paddle balances and a spoiler, respectively. Configuration E1 was obtained by adding a tab on a boom mounted on the inboard edge of the control of configuration E. Configurations E2, E3, and F1, F2, and F3 were made by mounting various fences on the wing at the wing-control juncture of configurations E and F, respectively. The location of the pressure orifices can be determined from tables 1 and 2 and the sketches in figure 2.

The basic wing had a 60° sweptback leading edge, a root chord of 18.14 inches, and a semispan of 10.48 inches. The wing had a rounded NACA 63-series section extending 30 percent of the root chord back from the leading edge, a constant-thickness center section with a thickness-chord ratio of 3 percent based on the root chord, and a sharp trailing edge. The trailing-edge bevel began at 86.7 percent of the root chord. Near the wing tip, the nose section joined directly to the tapered trailing edge without a flat midsection. Configurations J1 and J2 had thickened trailing edges as shown in the sketches of figure 1(b).

The basic wing and controls were constructed of steel. (For the details of construction, see ref. 1.) The paddle balances and tab were also constructed of steel. The spoiler and the fences were constructed of $\frac{1}{16}$-inch stock brass.

The semispan wing was mounted horizontally in the tunnel from a turntable in a steel boundary-layer bypass plate which was located vertically in the test section about 10 inches from the sidewall, as shown in figures 3 and 4.

TESTS

The model angle of attack was changed by rotating the turntable in the bypass plate on which the wing was mounted. (See fig. 3.) The angle of attack was measured by a vernier on the outside of the tunnel, inasmuch as the angular deflection of the wing under load was negligible. Control deflection was changed by a gear mechanism mounted on the pressure box which rotated the strain-gage balance, the torque tube, and the control as a unit. The control deflections were set approximately with the aid of an electrical control-position indicator mounted on the torque tube close to the wing root and measured under load during testing with a cathetometer mounted outside the tunnel. The pressure distributions were determined from photographs of the multiple-tube manometer boards to which the pressure leads from the model orifices were connected.

Tests were made over an angle-of-attack range from 0° to 15° at increments of either 3° or 6°. The control-deflection range was from -30° to 30° at increments of 5° or 10°. Most of the tests were made at a tunnel stagnation pressure of 15 lb/sq in. abs at $M = 1.61$, and 17.5 lb/sq in. abs at $M = 2.01$, corresponding to a Reynolds number, based on the wing mean aerodynamic chord of 12.10 inches, of 4.2×10^{6}. Configuration E was also tested at $R = 1.7 \times 10^{6}$ and 7.6×10^{6} at $M = 1.61$. Although no attempt was made to fix transition on the model, the surface roughness was probably great enough to cause a turbulent boundary layer.

PRECISION OF DATA

The mean Mach numbers in the region occupied by the model are estimated from calibrations to be 1.61 and 2.01 with local variations being smaller than ± 0.02. There is no evidence of any significant flow angularities. The estimated accuracies in setting the wing angle of attack and control deflection are $\pm 0.05^{\circ}$ and $\pm 0.1^{\circ}$, respectively. The measured pressure coefficients are believed accurate to ± 0.01.

RESULTS

The pressure-distribution results of this investigation are presented in three sections. The first section includes samples of the basic pressure distributions for configurations A to J at $M = 1.61$ and for configurations A and F at $M = 2.01$. These results are presented in figures 5 to 16. It will be noted that in general the plots are presented for positive control deflections at positive and negative angles of attack or for negative control deflection at positive and negative angles of attack. Some of the plots are presented for positive and negative control deflections at positive angles of attack only. These differences are unimportant since the model is symmetrical. Plots of the basic pressure distributions are not presented herein for the complete range of configurations and test conditions; however, the tabular data are available in reference 8.

In the second section, comparisons are made between some of the experimental results and the linear-theory predictions by plotting the incremental surface pressure coefficients and the incremental resultant pressure coefficients due to control deflection or angle of attack, normalized by the respective angles. These plots are presented for configurations A, C, F, and J at $M = 1.61$ and configuration F at $M = 2.01$

in figures 17 to 21. These configurations are considered to be representative of the basic configurations included in the present investigation.

In the third section, experimental comparisons are presented to demonstrate the effect of Mach number, Reynolds number, and configuration changes on the surface pressure distributions. These comparisons, which are presented in figures 22 to 37, show the upper-surface pressure distributions at the most significant stations for a limited number of angular conditions. Both positive and negative angles of attack and control deflections are shown, so that the changes on both high and low pressure surfaces of the model can be seen.

No results are presented in the present report for configuration J4 (the spoiler—trailing-edge-flap configuration), for which sufficient analysis has already been presented in reference 5. Neither are results presented herein for configuration J1 (the half-thickened trailing-edge configuration) because the pressure changes due to the thickening of the trailing edge are the same as, but smaller than, those shown for configuration J2.

DISCUSSION

Basic Pressure Distributions

Wing.- Consider first the pressure distributions over the various configurations with 0° control deflection. Although there are some local differences due to model inaccuracies, lack of sufficient orifices, parting-line gaps, and errors in fairing, in general the pressure distributions for all of the configurations at a given Mach number are nearly the same.

At $\alpha = 0^{\circ}$ (parts (a) of figs. 5 to 16), the pressure distributions show that the airfoil section (which has a rounded leading edge, flat midsection, and wedge trailing edge) causes a rapid acceleration of the air from the leading-edge stagnation point to a relatively constant pressure equal to the free-stream value $\left(C_p = 0\right)$. At the wing surface discontinuity where the trailing-edge wedge begins $\left(x/c_R = 0.867\right.$ for stations 1 to 5$\left.\right)$, a sudden expansion occurs as would be expected.

As the angle of attack is increased from 0° to 12°, there is a general increase in loading over the entire chord at the inboard stations. This increase in loading is fairly uniform except near the leading edge, where localized upper-surface flow separation, characteristic of a subsonic leading edge, occurs. (See ref. 3.) Outboard along

the span the upper-surface leading-edge flow separation increases in chordwise extent until it covers the entire chord. When the Mach number is increased from 1.61 to 2.01, at which point the leading edge becomes sonic, the area of separation is reduced considerably.

Trailing-edge controls.- The basic trailing-edge controls investigated herein are configurations A (also considered to be a basic tip control), I, and J. The chordwise pressure distributions for these configurations at $M = 1.61$ are shown in figures 5, 13, and 14 and for configuration A at $M = 2.01$ are shown in figure 15. Consider first the pressure distributions for the orifice stations located between the root and tip of the partial-span controls (stations 5 and 6 on configuration A and stations 1 to 4 on configuration I). Comparison of these pressure distributions with those for the full-span control (configuration J) in figure 14 shows the same effects due to control deflection. As the controls are deflected, the pressures on the control upper surface (for positive control deflection) decrease and approach asymptotically a negative pressure coefficient of about 80 percent of the perfect vacuum value $\left(C_p \text{ at vacuum is } -0.55 \text{ at } M = 1.61 \text{ and } -0.35 \text{ at } M = 2.01\right)$. The tendency on the upper surface is for the loading to remain or approach the rectangular type of loading. On the lower surface of the controls, as the controls are deflected, the increase in pressure coefficient is fairly regular up to the 30° limit of these tests; however, the loading tends to change from rectangular in nature to one which has a definite pressure peak, followed by a marked expansion toward the trailing edge. In reference 10, it was shown that at essentially two-dimensional stations the pressure peak tended to reach a maximum at each angle of attack and the trailing-edge pressure to be approximately sonic $\left(C_p = 0.64 \text{ at } M = 1.61\right)$. In the present report these trends are approached at station 1 only (figs. 13(b), 13(d), 14(b), and 14(d)), because of the strong spanwise flow on the delta wing. In addition to these changes on the control, large pressure rises occur on the wing ahead of the control high-pressure surface as a result of separation of the turbulent boundary layer or shock detachment. This pressure rise does not appear until the control deflections approach 20°, but then it moves rapidly forward with further increase in control deflection. A more detailed investigation and analysis of the pressure distributions ahead of and on trailing-edge controls having unswept hinge lines are presented in reference 10.

Tip controls.- The tip controls included in the present investigation fall into two general categories: the half-delta tip controls and the tip controls modified to reduce the control area ahead of or behind the control hinge line. The chordwise pressure distributions for the half-delta tip controls (configurations E, F, G, and H) at $M = 1.61$ are presented in figures 9 to 12 and for configuration F at $M = 2.01$ in figure 16. The chordwise pressure distributions for the modified

tip controls (configurations B, C, and D) at $M = 1.61$ are presented in figures 6 to 8.

The general effects of control deflection on the pressure distributions for all of the tip controls are similar. On the control low-pressure surface, the pressure coefficients again approach asymptotically a value of about 80 percent of the perfect vacuum value (C_p at vacuum is -0.55 at $M = 1.61$ and -0.35 at $M = 2.01$). At 0° angle of attack, the flow tends to separate from the control leading edge with the extent of the separation increasing from the control apex outboard (e.g., fig. 10(a)). At angles of attack this leading-edge separation, as described previously, originates at the wing apex and therefore covers most of the control. These large regions of separation result in a general tendency toward a rectangular loading over the control upper surface as α and δ are increased (e.g., fig. 10(d)).

On the high-pressure surface of the tip controls (lower surface at positive control deflections), the pressure coefficients increase regularly with control deflection and the chordwise loading tends to become triangular. At stations near the wing-control parting line, large variations in the pressures occur, both on the wing and on the control, because of the large spanwise gradients present. These, in turn, induce strong cross flows in these regions. Note in particular the rapid expansion on the control upper surface at station 5 for positive angle of attack and negative control deflections (e.g., fig. 9(d)). This indicates that the low pressure on the adjacent wing upper surface causes a strong relieving effect on the control pressures. As a result of the loss in loading over the rear portion of the control, the tip controls exhibit sizeable reductions in hinge moments for these conditions as shown in references 1 and 9.

Comparison of Experimental and Theoretical Results

Application and limitations of theory.- In making a comparison of the experimental results with theoretical predictions, it would be logical to begin with the wing-thickness effects. For this investigation, however, this comparison is impossible because of two factors. First, the leading edge is blunt and hence involves shock detachment, which cannot be treated reliably by linear theory. Secondly, the line generators of the forward section of the wing are sonic at $M = 2.0$ and subsonic at $M = 1.6$. Any representation of this portion of the wing by line sources and sinks such as was used for the wing of reference 10, thus leads to infinite pressures at these lines and inadequate accuracy in determining the summation of the pressures. The absence of theoretical values for comparison is, nevertheless, of little consequence since the wing is so thin that experimental results (figs. 5 to 16) indicate

negligible increments in pressure coefficient due to thickness except at the wing leading edge and on the trailing-edge wedge.

In order to make theoretical predictions of the surface pressure coefficients due to control deflection and/or angle of attack, the three-dimensional linear theory (e.g., ref. 11) was employed. This theoretical method makes several simplifying assumptions which should be considered before a detailed comparison of the experimental and theoretical results is made. First, the theory assumes that the angular deflections are small and that the effects due to control deflection and angle of attack can be superimposed. Within the range of the present tests, this means that at some conditions, linear theory predicts pressures lower than absolute vacuum. It also means that as the controls are deflected, sizeable openings will appear at the wing-control parting lines contrary to the theoretical assumption. A second simplification of the linear theory is that viscous effects will be nonexistent. As shown in the previous section, the flow over the model exhibits extensive regions of flow separation which can be expected to cause regions of disagreement between linear theory and experiment. Despite these shortcomings of the linear theory, it can be used to indicate trends, and in conditions where the linear-theory assumptions are approached, it can show the magnitudes of the pressure coefficients.

Trailing-edge controls - surface pressure coefficients due to δ.- A comparison of the experimental increments in surface pressure coefficients due to control deflection with the linear-theory predictions is presented for two of the trailing-edge controls (configurations A and J) in parts (a) to (f) of figures 17 and 20. At $\alpha = 0^{\circ}$ the experimental pressures on the low-pressure surface of the controls (figs. 17(a) and 20(a)) are considerably less than those for theory because of the asymptotic change in pressures and because of flow separation ahead of the trailing-edge shock.

On the high-pressure surface of the controls (figs. 17(b) and 20(b)), the experimental results are in fair agreement with the theoretical predictions. Ahead of the full-span control, however, considerable differences can be observed due to the aforementioned separation or shock detachment ahead of the hinge line for $\delta = 30^{\circ}$. The orifices on the wing just ahead of the hinge line indicate that some separation has started at $\delta = 20^{\circ}$.

At $\alpha = 12^{\circ}$ the experimental pressures on the low-pressure surface of the controls (figs. 17(c) and 20(c)) are approximately zero since the pressures in the undeflected case were already at the experimental minimum as discussed in the section on the basic pressure distributions. This refutes the validity in the linear-theory assumption that the angle-of-attack and control-deflection effects can be treated independently of one another. Note also that on the inboard stations of the full-span control

(fig. 20(c)) some pressure increments are obtained since the leading-edge separation which is limiting the pressures farther outboard does not affect these stations. On the high-pressure surface of the controls at $\alpha = 12^{\circ}$ (figs. 17(d) and 20(d)), the agreement between linear theory and experiment is again fairly good, however the separation or shock detachment ahead of the hinge line is greater than at $\delta = 0^{\circ}$.

At $\alpha = -12^{\circ}$ (figs. 17(e) and 20(e)) the experimental pressures on the control upper surface are generally less than those predicted by theory, and tend to decrease with increasing angle of attack because of the nonlinear combination of α and δ effects. On the full-span control lower surface at $\alpha = -12^{\circ}$ (fig. 20(f)), the experimental pressures at the inboard wing stations approach the theoretical predictions, but at the outboard stations the experimental pressures decrease because of the leading-edge flow separation. The disagreement at the outboard stations is similar for the partial-span control (fig. 17(f)).

The prediction of the carryover pressures adjacent to the parting line of the partial-span control (figs. 17(a) to 17(f)) is generally much greater than the experimental carryovers. The largest experimental carryovers are obtained on the wing surface adjacent to the control surfaces which are experiencing the largest loadings (figs. 17(d) and 17(e)).

Except for the stronger spanwise effects at angles of attack, the flow characteristics just described are identical to those described for trailing-edge controls in reference 10. The strong spanwise effects, however, prevent the use of advanced nonlinear techniques for more accurate predictions of surface pressures at moderate combined angles of attack and control deflections such as was done in reference 10.

Trailing-edge controls - surface pressure coefficients due to α.- A comparison of the experimental increments in surface pressure coefficients due to angle of attack with those predicted by linear theory is presented in parts (g) to (l) of figures 17 and 20 for the trailing-edge controls (configurations A and J). It is important to note that in determining the normalized pressure coefficients due to angle of attack both positive and negative pressure increments are represented in each figure, although the reduced coefficients are generally negative on the upper surface and positive on the lower surface. With the controls undeflected (figs. 17(g), 17(h), 20(g), and 20(h)) the linear-theory predictions of the pressure coefficients due to angle of attack are good except near the trailing edge and near the wing tip. The discrepancies in these regions can probably be attributed to separation over the trailing-edge wedge, separation near the leading edge (which increases in chordwise extent toward the tip), and changes in upwash associated with this separation.

As the controls are deflected to 10° and then to 30° (parts (i) to (l) of figs. 17 and 20) the differences between theory and experiment, just noted, gradually increase. In addition to these differences at the trailing edge and at the wing tip, considerable disagreement also appears ahead of the control at $\delta = 30^{\circ}$ because of the hinge-line separation or shock detachment.

Trailing-edge controls - resultant pressure coefficients.- The experimental and theoretical resultant pressure coefficients due to control deflection are shown in parts (m) to (o) of figures 17 and 20 for the trailing-edge controls (configurations A and J). The addition of the experimental pressures for the two surfaces, which have already been discussed individually in detail, results in total pressure loadings on the controls of about one-half to three-fourths of the theoretical values. The best agreement is obtained at small values of α and δ and at the inboard wing stations. Ahead of the control the unpredicted loading at $\delta = 30^{\circ}$ is most evident on the full-span control (figs. 20(m) and 20(n)). The experimental load carryover to the wing from the inboard edge of the partial-span control (figs. 17(m) to 17(o)) is considerably less than theory. In general, except for the greater spanwise variation, the resultant pressure coefficients due to control deflection are very similar to those on the trailing-edge controls reported in reference 10.

The resultant pressure coefficients due to angle of attack are shown in parts (p) to (r) of figures 17 and 20. In general the theory and experiment are in good agreement except near the wing tip, and ahead of or on the controls at large combined angles of attack and control deflections.

Tip controls - surface pressure coefficients due to δ.- A comparison of the experimental increments in surface pressure coefficients due to control deflection with the linear-theory predictions is presented for two of the tip controls (configurations C and F) in parts (a) to (f) of figures 18, 19, and 21. The major geometrical differences between the tip controls and the trailing-edge controls are that more of the leading edge of the control coincides with the wing leading edge, and the parting line is considerably larger with respect to the control span. As shown in figures 19 and 21 for the half-delta tip control, both of these differences have strong effects.

At $\alpha = 0^{\circ}$ the experimental pressures due to control deflection are in good agreement with the linear theory on the low-pressure surface of the control (figs. 19(a) and 21(a)) except near the wing tip where separation from the control leading edge causes sizeable differences. On the control high-pressure surface (figs. 19(b) and 21(b)) there is considerable scatter in the experimental pressures due to nonlinear changes with control deflection. In general the experimental values tend to be greater than the linear-theory predictions except at the wing tip.

At $\alpha = 12^{\circ}$, the control upper surface (figs. 19(c) and 21(c)) shows practically no change in pressure due to control deflection as a result of the asymptotic approach to a negative pressure-coefficient limit as was observed on the trailing-edge controls. Meanwhile, on the control lower surface (figs. 19(d) and 21(d)) the pressures again tend to be considerably greater than theory.

At $\alpha = -12^{\circ}$, the control upper surface (figs. 19(e) and 21(e)) exhibits trends similar to those shown at $\alpha = 0^{\circ}$, except for regions of higher than theoretical pressures on station 5 due to the stronger crossflows at the parting line. On the control lower surface at $\alpha = -12^{\circ}$ (figs. 19(f) and 21(f)) the pressure increments are generally lower than those predicted by theory because of the leading-edge separation existing at $\alpha = -12^{\circ}$, $\delta = 0^{\circ}$, but on the forward part of station 5, strong crossflows again cause pressure increments greater than those predicted by theory.

Now consider the pressure carryovers due to control deflection for the half-delta tip control (parts (a) to (f) of figs. 19 and 21). At station 4, next to the parting line, a shock can be observed on the upper surface near $x/c_R = 0.7$ and a region of expansion occurs on the lower surface near the trailing edge. These unpredicted effects are a result of the unporting at the parting line which is neglected by the linear theory. At stations farther inboard on the wing, the linear-theory predictions are considerably better.

The increments in surface pressure coefficients for configuration C (fig. 18) will not be discussed in detail. In general the characteristics are similar to those discussed for configuration F except that the shock on the upper surface of the wing in the carryover region is moved outboard to station 6 due to the modification of the control plan form. (See fig. 2.) In general, as was the case with the trailing-edge controls, it appears that it will be very difficult to develop any simple procedure for a more accurate prediction of the surface pressures on tip controls.

Tip controls - surface pressure coefficients due to α.- The surface pressure coefficients due to angle of attack for the tip controls (configurations C and F) are compared with the linear theory in parts (g) to (l) of figures 18, 19, and 21. The agreement between linear theory and experiment in these figures is very similar to that previously shown for the trailing-edge controls, except that the largest discrepancies occur on the control and on the wing stations near the parting line as the control deflections increase.

Tip controls - resultant pressure coefficients.- The resultant pressure coefficients due to control deflection are shown in parts (m) to (o) of figures 18, 19, and 21 for the tip controls (configurations C and F).

Because of compensating effects of the pressures on the two surfaces, the resultant coefficients are in fairly good agreement. The carryover loading on the wing is predicted fairly well at stations 2 and 3 but is much smaller than that predicted by theory at station 4.

The resultant pressure coefficients due to angle of attack for the tip controls are presented in parts (p) to (r) of figures 18, 19, and 21. A detailed discussion of these figures is again unnecessary as the features of the pressure increments on the individual surfaces have already been discussed. The largest differences again appear on the control and on the wing stations near the parting line as the control deflections increase.

Experimental Comparisons

Effect of Mach number.- Although four of the model configurations were tested at the two test Mach numbers (configurations A, E, F, and G), the Mach number change is quite small and the pressure coefficient changes are similar for the four configurations. Therefore, some of the surface pressure distributions for only configuration E at selected angles of attack are presented in figure 22 for $M = 1.61$ and 2.01. At small angles of attack and control deflections, the change with Mach number amounts to a reduction in magnitude of the pressure coefficients similar to the theoretical prediction of a reduction inversely proportional to $\sqrt{M^2 - 1}$. At larger angles, the greatest differences are in the regions of separated flow on the wing or control low-pressure surface, where, as previously described, increasing the Mach number considerably decreases the regions of separation.

Effect of Reynolds number.- The available results of tests at the maximum Reynolds number of 7.6×10^6 are very limited, but what is available is shown in figure 23 for configuration E as compared with similar data at the minimum test Reynolds number of 1.7×10^6. Figure 23 indicates that some differences do exist in the pressure distributions for this Reynolds number range; however the data for $R = 7.6 \times 10^6$ are almost identical to the data previously shown for $R = 4.2 \times 10^6$. It appears therefore that the differences shown in figure 23 are probably due to the inaccuracies in measuring the pressure coefficients at the low tunnel pressures.

Effect of hinge-line location.- Configurations E, F, and G were the same except for the location of the hinge lines. The effect on the pressure distributions of moving the hinge line $1\frac{1}{2}$ inches is shown in

figure 24 at $M = 1.61$ and in figure 25 at $M = 2.01$. The overall changes are relatively small, which demonstrates why in reference 6 little change was found in the effectiveness values. The most notable changes shown in figure 24 occur at the stations near the parting line where local shifts in the shocks and expansions associated with the intricate crossflows in this region cause local changes in the pressure distributions (e.g., station 5 in fig. 25(b) and station 4 in fig. 24(c)).

Effect of offsetting tip control.- The effect on the pressure distributions of offsetting the control on configuration F to make configuration H is shown in figure 26. Here again, the general effect is small, as might be anticipated from the small effect shown in the hinge-moment results of reference 9. The slight increase in hinge-moment coefficient due to angle of attack, found in reference 9, is apparently caused by the increased pressures on the control upper surface at the apex and the increased pressures generally experienced over the control lower surface for $\delta = 0^{\circ}$.

Effect of control plan form.- The effect of removing a portion of a tip control rearward of the hinge line is shown in figure 27, where the pressure distributions for configuration D are compared with those for configuration E. It must be remembered that station 6 on configuration D is located some distance inboard from station 6 on configuration E. In general the pressure distributions are similar and there seems to have been little effect from removal of the control tip even though the trailing edge of the control on configuration D was very blunt.

Effect of fixed tab on a boom.- In figure 28, the pressure distributions for configuration E1, which had a fixed triangular tab mounted on a boom ahead of the control, are compared with those for configuration E. The tab seemed to cause only negligible changes on the pressures measured over the wing inboard of the control. On the control, however, the tab caused considerable changes at all control deflections and angles of attack. In general, the tab tended to increase the pressures on the control low-pressure surface, and decrease the pressures on the control high-pressure surface.

Effect of fences.- The effect of fences at the parting lines of two of the tip controls is shown in figures 29 to 33. Configurations E2 and F1 are similar, the fences extending from 0.3 inch ahead of the leading edge to 0.3 inch downstream of the trailing edge. Configurations E3 and F3 are also similar, the fences of each extending from 0.3 inch ahead of the leading edge to the hinge line. Configuration F2 had a fence extending from the hinge line to 0.3 inch downstream of the trailing edge.

The effect of the full-chord fences and the forward fences is very similar. Inboard of the control, the fence leading edge causes a shock which strikes the wing near the leading edge at station 4 and intersects station 3 somewhere ahead of $x/c_R = 0.65$. (See fig. 29(c).) Deflecting the control produces negligible changes in the pressure distributions at these stations on the full-chord fence configurations, but does produce some changes over the rear portions of the wing for the forward fence configurations (figs. 30 and 33). On the control surfaces, the full-chord and forward fences cause the greatest changes in pressure distribution at angles of attack for the negative control deflections, where the pressures tend to be more negative ahead of the hinge line and more positive behind the hinge line. These changes are in the direction that would be expected from the previous discussion of the parting-line cross-flows, and are responsible for the positive increments in hinge moments discussed in reference 9 for these conditions.

The rearward fence configuration F2 (fig. 32) does not seem to produce any noticeable shock over the wing inboard of the control but it does cause some changes in the pressure distributions at station 4, particularly near the trailing edge at $\alpha = -12^{\circ}$. On the control, the data for this configuration appear questionable for $\alpha = 12^{\circ}$ at the negative control deflections and for $\alpha = -12^{\circ}$ at the positive control deflections. Indications are that for these conditions the control deflections may have been erroneous by an increment of 5°. Analysis of the pressures on the control for all of the conditions known to be correct (including many not presented herein) shows that the rearward fence generally decreases the load over both surfaces of the control.

Effect of control span and location.- A comparison of the pressure distributions for the partial-span trailing-edge controls with those for the full-span trailing-edge control is shown in figures 34 and 35. The outboard control generally exhibits less viscous flow-separation or shock-detachment effect ahead of the control hinge line at station 6 than does the full-span control. The pressure distributions over the inboard control at station 2, however, are nearly identical to those on the full-span configuration, particularly at angles of attack. The outboard edge of the inboard control causes a relieving effect at station 4.

Effect of trailing-edge thickness.- The effect of increasing the trailing-edge thickness from 0 to a value equal to that at the hinge line is shown in figure 36. The general effect is to increase the pressures over the control and to increase the amount of flow separation or shock detachment ahead of the control. These changes are in agreement with the changes found owing to increasing the trailing-edge thickness on the unswept wing of reference 10. In the present tests, increasing the trailing-edge thickness causes the greatest pressure changes on the control at control deflections of 20° or less.

Effect of paddle balances.- Paddle balances, mounted to the full-span trailing-edge control, were shown to reduce the hinge-moment curve slopes with control deflection in reference 9. The pressure distributions on the paddles could not be obtained in the present tests; however, the effect of the paddle balances on the pressure distributions over configuration J is presented in figure 37. In general, the paddles tended to reduce the loading over either surface of the control as the control was deflected. In some instances the severe gradients created by the flow field from the paddles are vividly illustrated, even with the limited number of orifices available (for example; station 6 at $\alpha = -12^{\circ}$, $\delta = -20^{\circ}$).

CONCLUSIONS

The results have been reported herein of an experimental and theoretical investigation of 20 controls on a 60° delta wing at Mach numbers of 1.61 and 2.01. From the investigation, which covered a range of angles of attack from 0° to 15° and control deflections from -30° to 30°, the following primary conclusions may be reached:

Basic Pressure Distributions

1. On the low-pressure surface of all the controls, increasing control deflection causes the pressure distribution to approach a rectangular loading with a negative pressure coefficient of about 80 percent of the perfect vacuum value.

2. On the high-pressure surface of the trailing-edge controls, increasing control deflection causes a pressure peak followed by an expansion toward the trailing edge. Ahead of the controls, flow separation or shock detachment occurs.

3. On the high-pressure surface of the tip controls, increasing control deflection causes the pressure coefficients to increase regularly with control deflection and the loading to become triangular.

Comparison of Experimental and Theoretical Results

1. For trailing-edge controls the experimental increments in surface pressure coefficient due to control deflection are generally in only fair or poor agreement with theory because of flow separations and possibly shock detachment. There is a pressure rise ahead of the control hinge line not predicted by theory and the carryover at the parting line is smaller than predicted theoretically.

2. The experimental increments in surface pressure coefficient due to angle of attack were generally in very good agreement with those predicted by theory for the trailing-edge controls at small control deflection but the agreement tends to deteriorate over the wing trailing-edge wedge and near the wing tip as the control deflection increases.

3. The experimental resultant pressure coefficients due to control deflection or angle of attack generally followed the theoretical trends for the trailing-edge controls but the values usually fell below the theoretical predictions.

4. In the case of the tip controls the experimental increments in surface pressure coefficients due to control deflection generally are even in poorer agreement with theoretical predictions owing to additional complications resulting from control leading-edge separation and the stronger parting-line crossflow effects. Again, the parting-line carry-over is much smaller than the theoretical prediction.

5. For tip controls the experimental-theoretical relationships of the increments in pressure due to angle of attack are very similar to those of the trailing-edge controls with the additional factor that the experimental pressures on both wing and control in the neighborhood of the parting line become more erratic and in poorer agreement with theory as the control angle increases.

6. For tip controls the experimental values of resultant pressure coefficient due to control deflection or angle of attack were generally in fairly good agreement with theory in both magnitude and trends because of compensating effects on the two surfaces.

Experimental Comparisons

1. The pressure changes due to increasing the Mach number M from 1.61 to 2.01 were in fair agreement with the changes predicted by the relationship $1/\sqrt{M^2 - 1}$ at small angles of attack and control deflections. At larger angles, there was little change with increasing Mach number except for a reduction in the leading-edge separation.

2. The effect of increasing the Reynolds number from 1.7×10^6 to 7.6×10^6 appeared to be negligible.

3. Movement of the tip-control hinge line caused little change in the overall pressure distributions, but did cause local shifts in the shocks and expansions associated with the parting-line crossflows.

REFERENCES

1. Czarnecki, K. R., and Lord, Douglas R.: Hinge-Moment Characteristics for Several Tip Controls on a 60° Sweptback Delta Wing at Mach Number 1.61. NACA RM L52K28, 1953.

2. Czarnecki, K. R., and Lord, Douglas R.: Preliminary Investigation of the Effect of Fences and Balancing Tabs on the Hinge-Moment Characteristics of a Tip Control on a 60° Delta Wing at Mach Number 1.61. NACA RM L53D14, 1953.

3. Czarnecki, K. R., and Lord, Douglas R.: Load Distributions Associated With Controls at Supersonic Speeds. NACA RM L53D15a, 1953.

4. Lord, Douglas R., and Czarnecki, K. R.: Recent Information on Flap and Tip Controls. NACA RM L53I17a, 1953.

5. Lord, Douglas R., and Czarnecki, K. R.: Aerodynamic Characteristics of a Full-Span Trailing-Edge Control on a 60° Delta Wing With and Without a Spoiler at a Mach Number of 1.61. NACA RM L53L17, 1954.

6. Lord, Douglas R., and Czarnecki, K. R.: Aerodynamic Characteristics of Several Tip Controls on a 60° Delta Wing at a Mach Number of 1.61. NACA RM L54E25, 1954.

7. Czarnecki, K. R., and Lord, Douglas R.: Simplified Procedures for Estimating Flap-Control Loads at Supersonic Speeds. NACA RM L55E12, 1955.

8. Lord, Douglas R., and Czarnecki, K. R.: Tabulated Pressure Data for a Series of Controls on a 60° Delta Wing at Mach Numbers of 1.61 and 2.01. NACA RM L55L05, 1956.

9. Lord, Douglas R., and Czarnecki, K. R.: Hinge-Moment Characteristics for a Series of Controls and Balancing Devices on a 60° Delta Wing at Mach Numbers of 1.61 and 2.01. NACA RM L57B01, 1957.

10. Lord, Douglas R., and Czarnecki, K. R.: Pressure Distributions and Aerodynamic Loadings for Several Flap-Type Trailing-Edge Controls on a Trapezoidal Wing at Mach Numbers of 1.61 and 2.01. NACA RM L55J03, 1956.

11. Lagerstrom, P. A., and Graham, Martha E.: Linearized Theory of Supersonic Control Surfaces. Jour. Aero. Sci., vol. 16, no. 1, Jan. 1949, pp. 31-34.

[redacted]

TABLE 1

SPANWISE LOCATION OF ORIFICE STATIONS

[Chordwise extent of stations shown in fig. 2 and table 2]

Configuration	Values of 2y/b at station -								
	1	2	3	4	5	6	7	8	9
A	0.048	0.210	0.372	0.537	0.592	0.745	0.860	See fig. 2	----------
B	.048	.210	.372	.537	See fig. 2	.602	See fig. 2	0.734	See fig. 2
C	.048	.210	.372	.537	.601	.640	.683	.758	See fig. 2
D	.055	.242	.430	.619	.688	.776	.876	.958	----------
E, E1, E2, E3, F F1, F2, F3, G, H	.048	.210	.372	.537	.597	.733	.869	.967	----------
I	.048	.210	.372	.537	.592	.745	See fig. 2	----------	----------
J, J1, J2, J3, J4	.048	.210	.372	.537	.592	.745	See fig. 2	----------	----------

[redacted]

TABLE 2

CHORDWISE LOCATION OF ORIFICES

[Spanwise location of orifice stations shown in fig. 2 and table 1]

(a) Configuration A

Orifice	Values of x/c_R at station -								
	1	2	3	4	5	6	7	8	9
1	0.048	0.210	0.372	0.535	0.592	0.745	0.872	0.852	
2	.075	.238	.400	.562	.619	.772	.919	.872	
3	.219	.381	.538	.700	.713	.816	.952	.919	
4	.334	.502	.659	.860	.779	.860	.982	.952	
5	.445	.612	.747	.897	.860	.852		.982	
6	.588	.756	.860	.936	.852	.872			
7	.742	.860	.897	.985	.872	.919			
8	.860	.897	.936		.919	.952			
9	.897	.936	.985		.952	.982			
10	.936	.985			.982				
11	.985								
12									
13									

TABLE 2.- Continued

CHORDWISE LOCATION OF ORIFICES

[Spanwise location of orifice stations shown in fig. 2 and table 1]

(b) Configuration B

Orifice	Values of x/c_R at station -								
	1	2	3	4	5	6	7	8	9
1	0.048	0.210	0.372	0.535	0.708	0.875	0.754	0.769	0.819
2	.075	.238	.400	.562	.761	.906	.799	.824	.871
3	.219	.381	.538	.700	.810	.945	.835	.879	.926
4	.334	.502	.659	.846		.986		.934	.988
5	.445	.612	.747	.901				.992	
6	.588	.756	.846	.950					
7	.742	.846	.901	.986					
8	.846	.901	.950						
9	.901	.950	.986						
10	.950	.986							
11	.986								
12									
13									

TABLE 2.- Continued

CHORDWISE LOCATION OF ORIFICES

[Spanwise location of orifice stations shown in fig. 2 and table 1]

(c) Configuration C

Orifice	Values of x/c_R at station -								
	1	2	3	4	5	6	7	8	9
1	0.048	0.210	0.372	0.535	0.876	0.674	0.683	0.758	0.871
2	.075	.238	.400	.562	.909	.769	.711	.785	.928
3	.219	.381	.538	.700	.947	.857	.780	.879	.986
4	.334	.502	.659	.846	.991		.876	.929	
5	.445	.612	.747	.901				.992	
6	.588	.756	.846	.950					
7	.742	.846	.901	.986					
8	.846	.901	.950						
9	.901	.950	.986						
10	.950	.986							
11	.986								
12									
13									

TABLE 2.- Continued

CHORDWISE LOCATION OF ORIFICES

[Spanwise location of orifice stations shown in fig. 2 and table 1]

(d) Configuration D

Orifice	Values of x/c_R at station -								
	1	2	3	4	5	6	7	8	9
1	0.048	0.210	0.372	0.535	0.595	0.672	0.758	0.862	
2	.075	.238	.400	.562	.623	.699	.785		
3	.219	.381	.538	.700	.675	.752	.813		
4	.334	.502	.659	.846	.744	.826	.851		
5	.445	.612	.747	.901	.821	.876	.901		
6	.588	.756	.846	.950	.899	.937			
7	.742	.846	.901	.984	.970				
8	.846	.901	.950						
9	.901	.950	.984						
10	.950	.984							
11	.984								
12									
13									

TABLE 2.- Continued

CHORDWISE LOCATION OF ORIFICES

[Spanwise location of orifice stations shown in fig. 2 and table 1]

(e) Configurations E, E1, E2, E3, F, F1, F2, F3, G, H

Orifice	Values of x/c_R at station -								
	1	2	3	4	5	6	7	8	9
1	0.048	0.210	0.372	0.535	0.597	0.730	0.864	0.987	
2	.075	.238	.400	.562	.625	.758	.892		
3	.219	.381	.538	.700	.674	.808	.941		
4	.334	.502	.659	.846	.746	.879	.986		
5	.445	.612	.747	.901	.840	.973			
6	.588	.756	.846	.950	.939				
7	.742	.846	.901	.984	.988				
8	.846	.901	.950						
9	.901	.950	.984						
10	.950	.984							
11	.984								
12									
13									

TABLE 2.- Continued

CHORDWISE LOCATION OF ORIFICES

[Spanwise location of orifice stations shown in fig. 2 and table 1]

(f) Configuration I

Orifice	Values of x/c_R at station -								
	1	2	3	4	5	6	7	8	9
1	0.048	0.210	0.372	0.535	0.597	0.753	0.890		
2	.075	.238	.400	.562	.624	.778	.985		
3	.219	.381	.538	.700	.719	.853			
4	.334	.502	.659	.860	.839	.945			
5	.445	.612	.747	.852	.919	.995			
6	.588	.756	.860	.896	.972				
7	.742	.860	.852	.935					
8	.860	.852	.896	.984					
9	.852	.896	.935						
10	.896	.935	.984						
11	.935	.984							
12	.984								
13									

TABLE 2.- Concluded

CHORDWISE LOCATION OF ORIFICES

[Spanwise location of orifice stations shown in fig. 2 and table 1]

(g) Configurations J, J1, J2, J3, J4

Orifice	Values of x/c_R at station -								
	1	2	3	4	5	6	7	8	9
1	0.048	0.210	0.372	0.535	0.592	0.745	0.852		
2	.075	.238	.400	.562	.619	.772	.872		
3	.219	.381	.538	.700	.713	.816	.910		
4	.334	.502	.659	.860	.779	.860	.948		
5	.445	.612	.747	.852	.860	.872	.986		
6	.588	.756	.860	.872		.905			
7	.742	.860		.905		.949			
8	.860	.852		.949		.982			
9	.872	.872		.982					
10	.905	.905		1.000					
11	.949	.949							
12	.982	.982							
13		1.000							

[redacted]

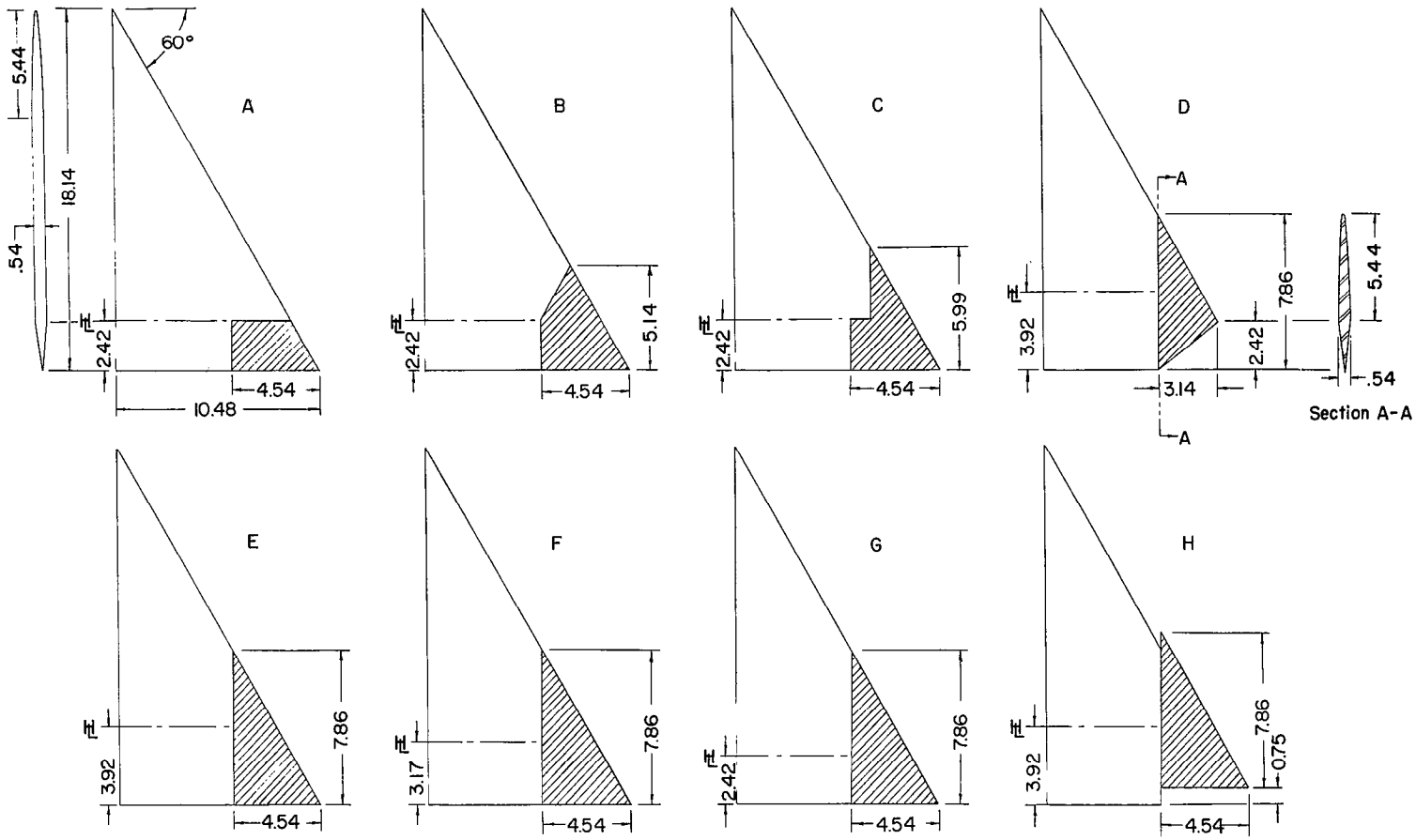

(a) Tip controls.

Figure 1.- Sketches of model configurations. All dimensions are in inches.

[redacted]

[redacted]

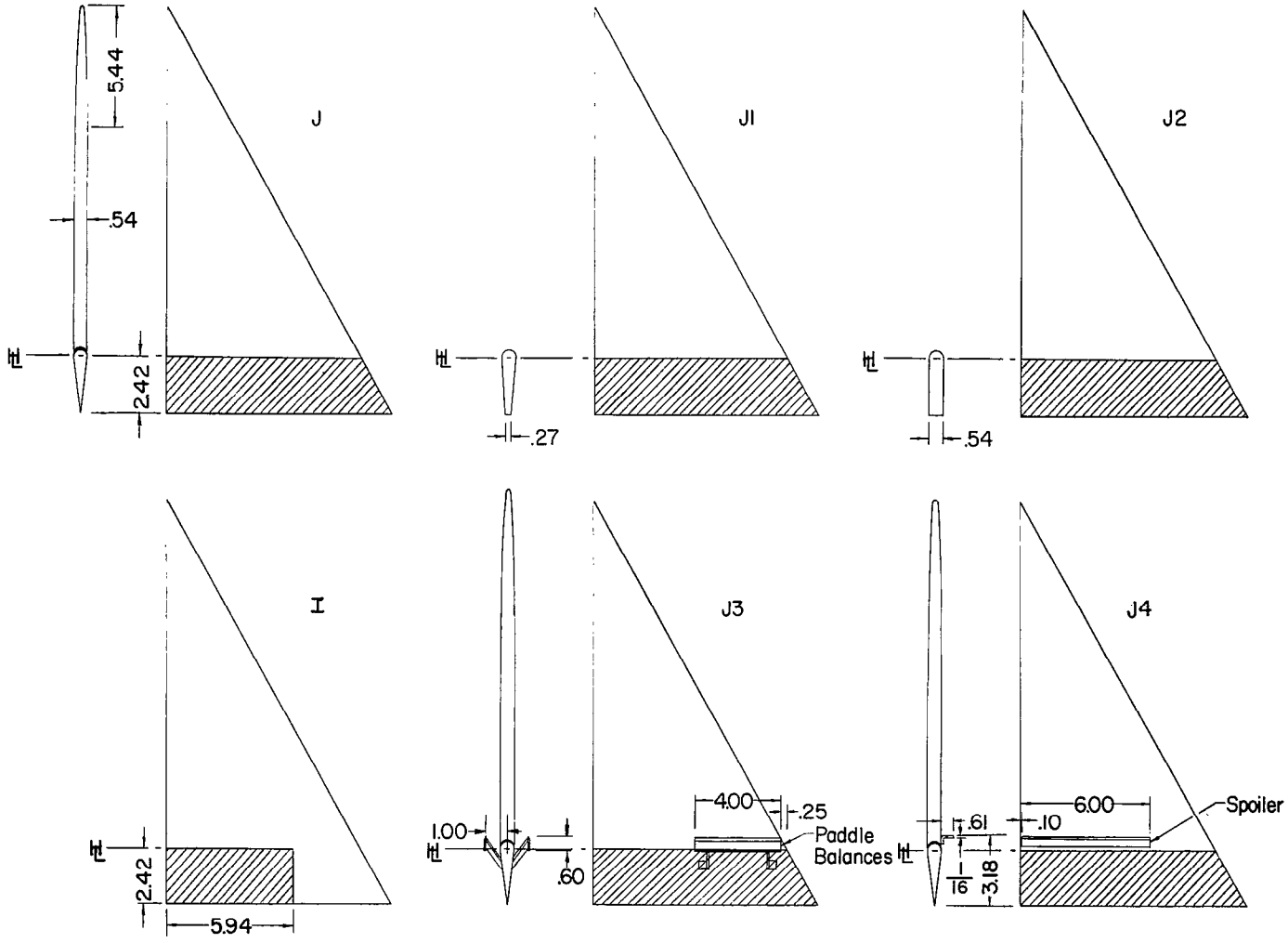

(b) Trailing-edge controls. (Configuration A could be included here also.)

Figure 1.- Continued.

[redacted]

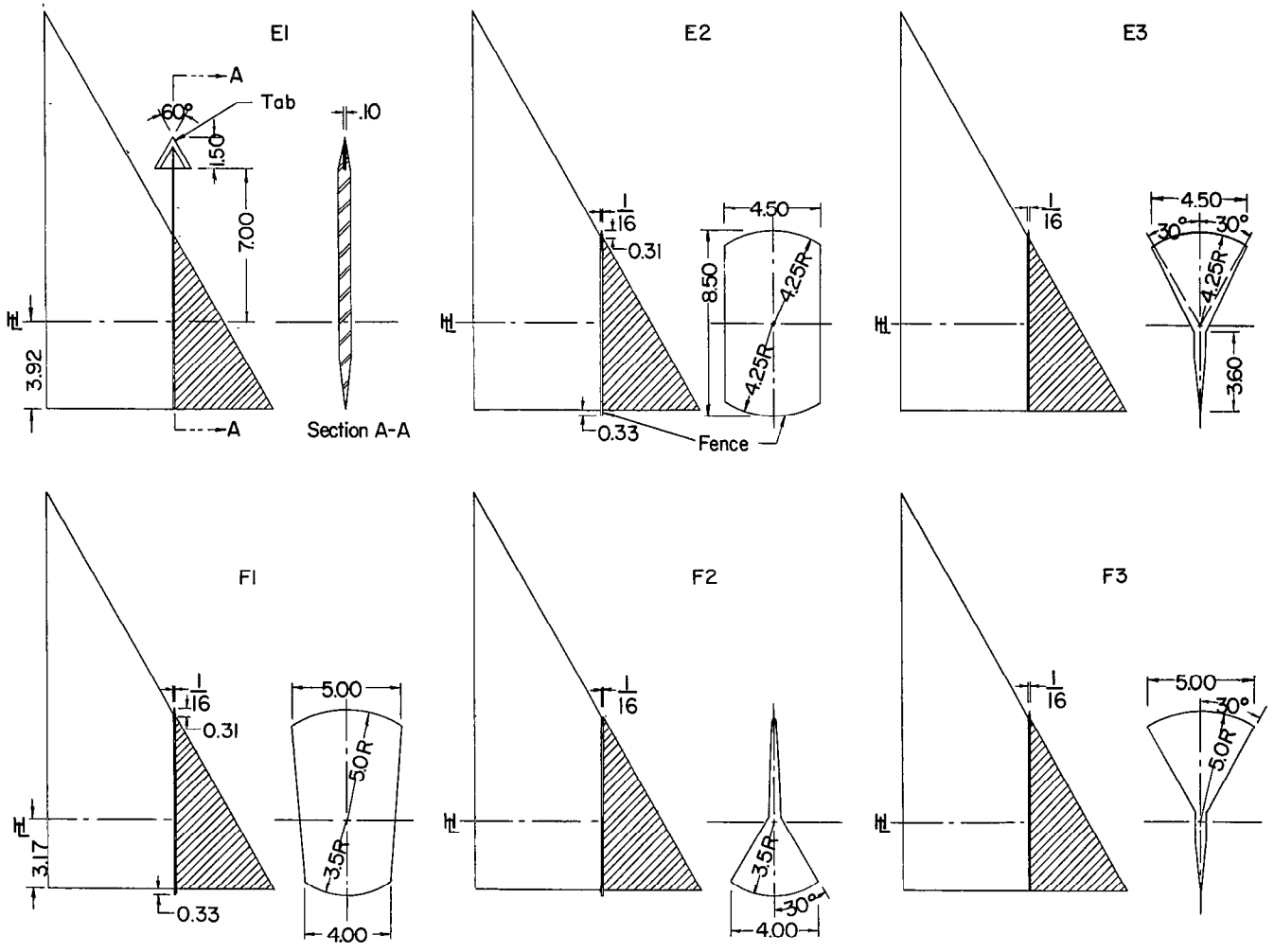

(c) Tip controls with tabs and fences.

Figure 1.- Concluded.

[redacted]

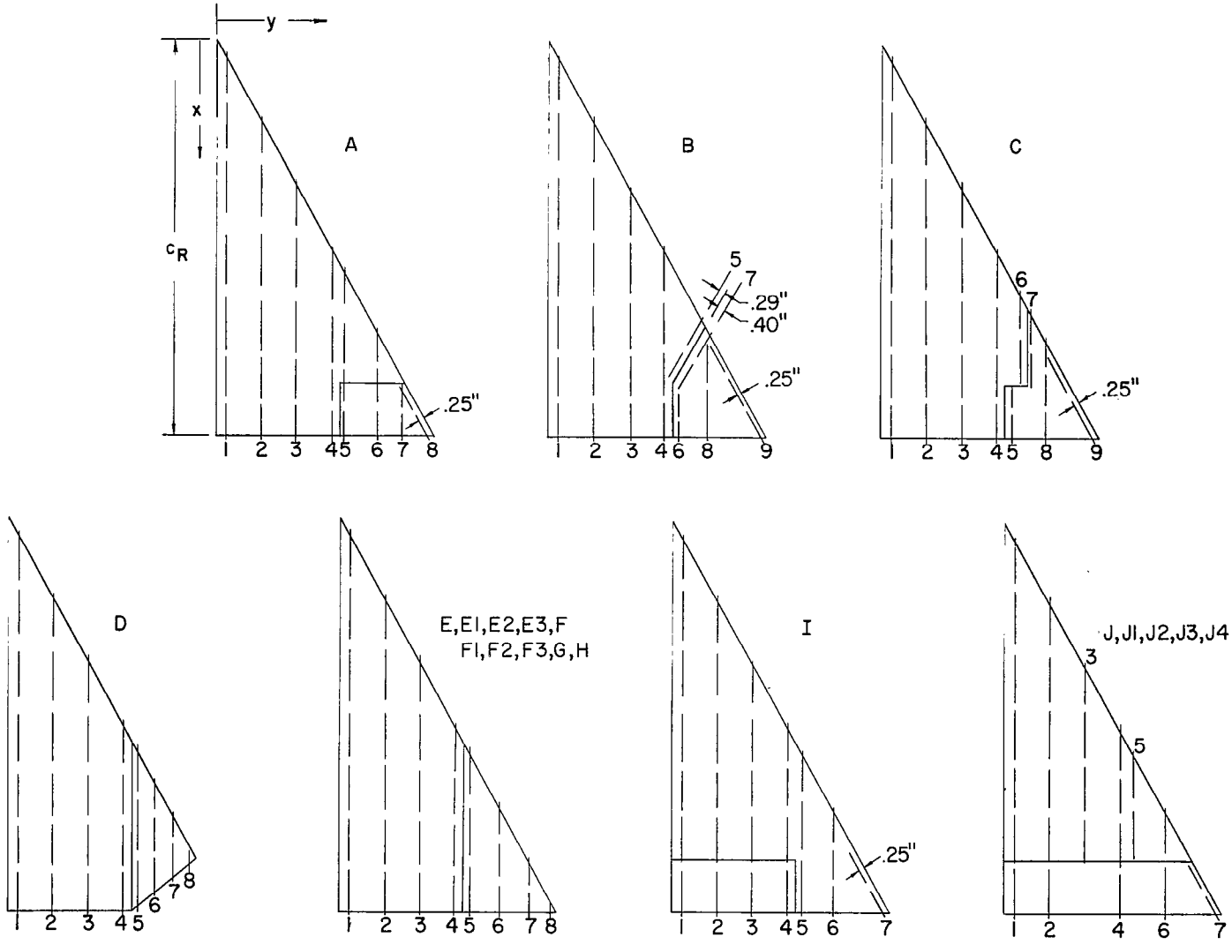

Figure 2.- Sketches showing approximate extent and location of orifice stations. Spanwise locations of stations are given in table 1 and chordwise locations of orifices in table 2.

[redacted]

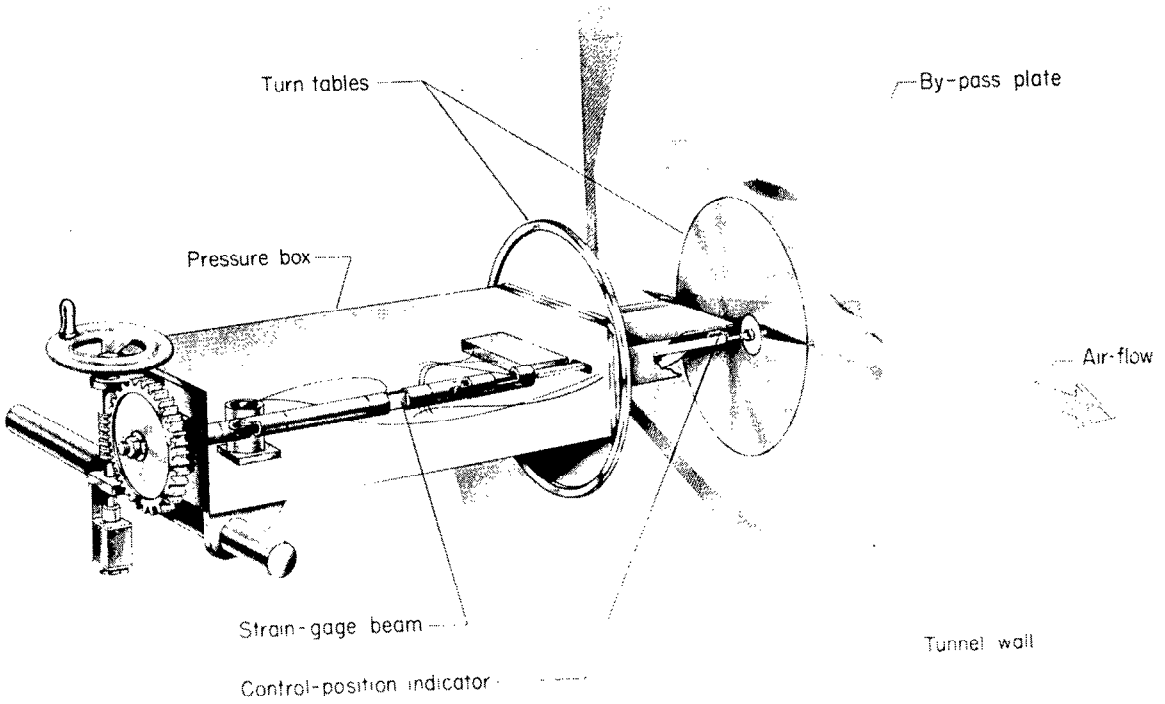

L-77038

Figure 3.- Sketch of test setup showing one of the tip-control installations.

L-752941.1

Figure 4.- Photograph of configuration J mounted on the boundary-layer bypass plate.

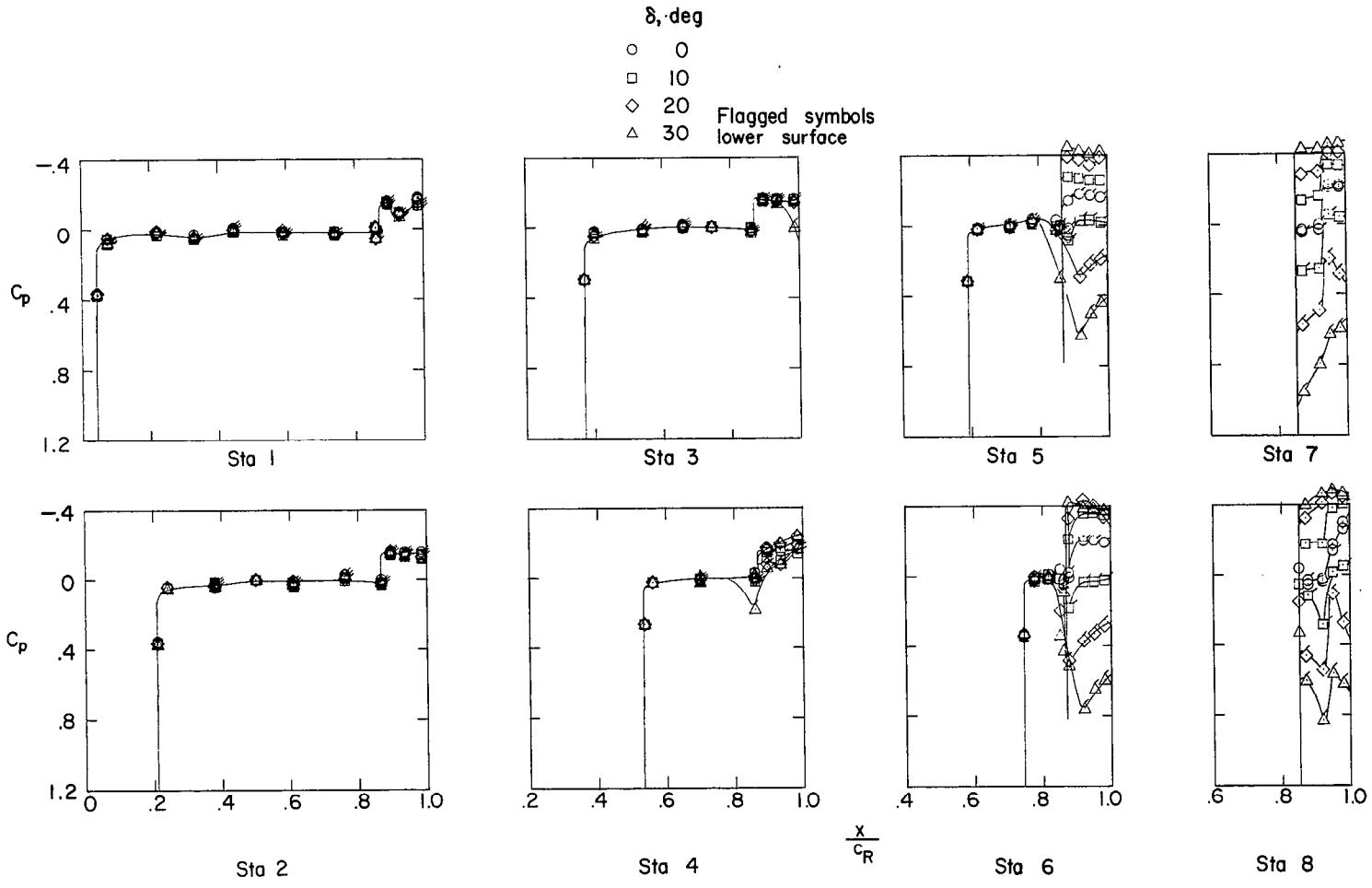

(a) $\alpha = 0^{\circ}$.

Figure 5.- Chordwise pressure distributions for configuration A. $M = 1.61$; $R = 4.2 \times 10^6$.

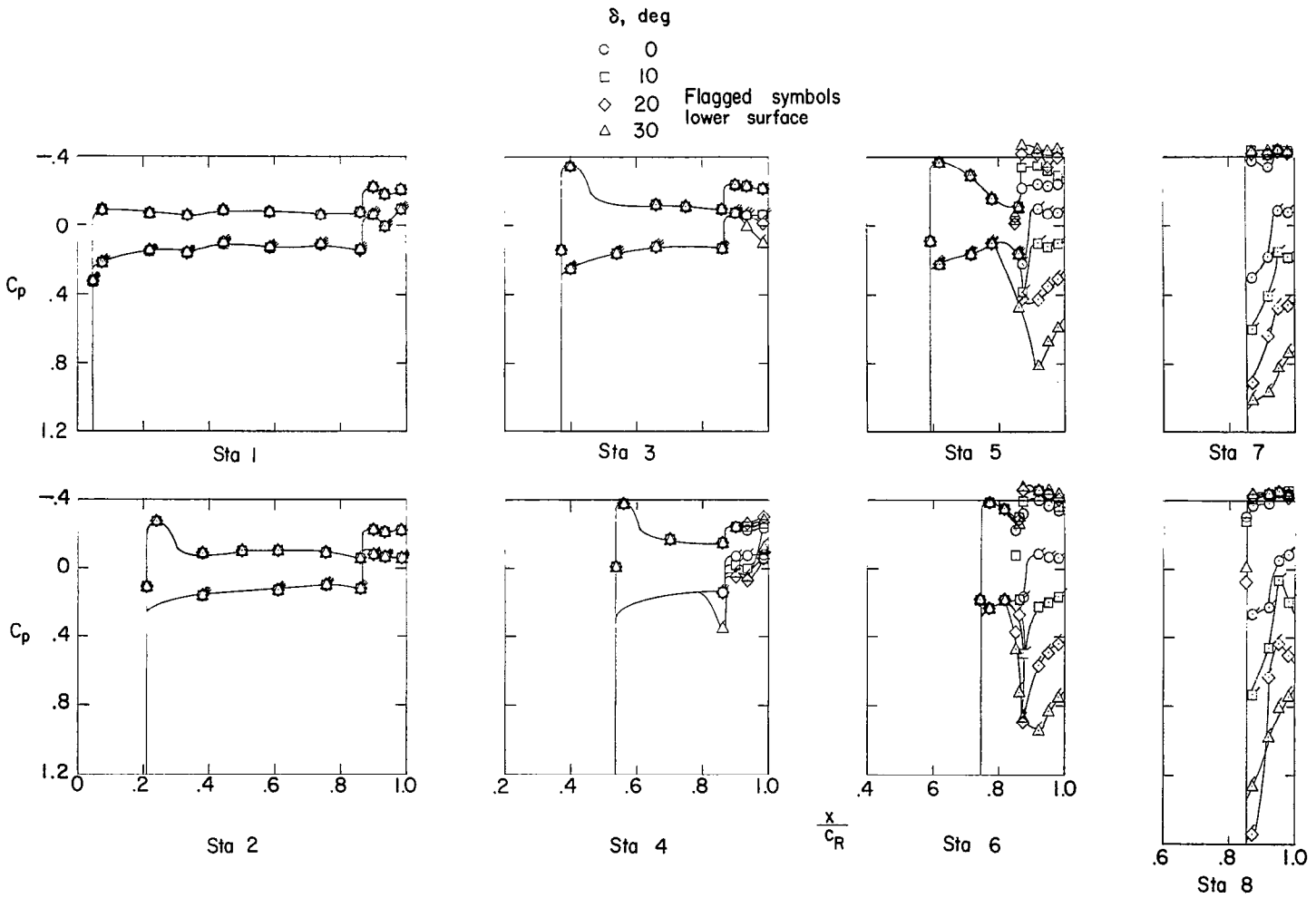

(b) $\alpha = 6^{\circ}$.

Figure 5.- Continued.

[redacted]

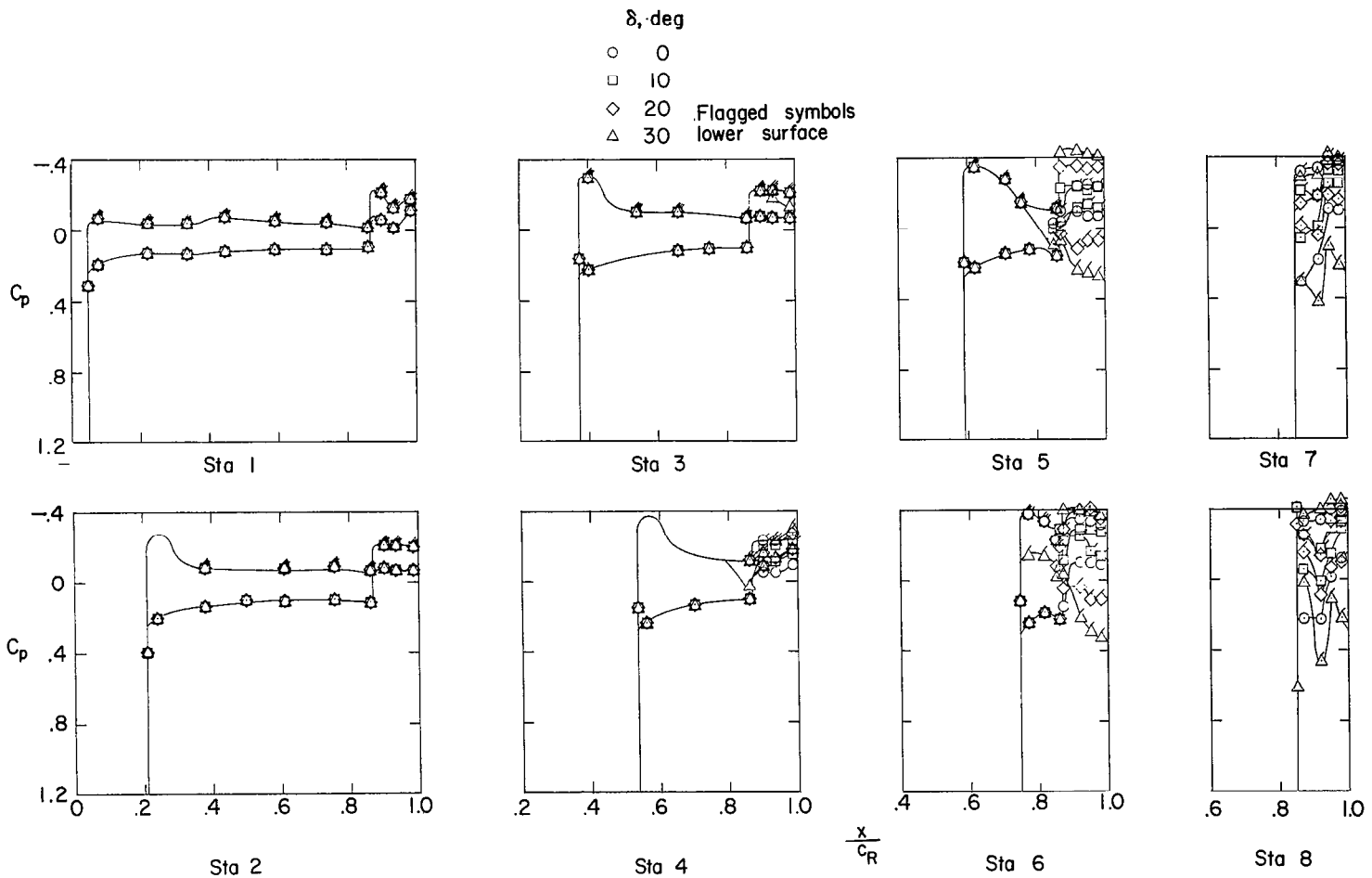

(c) $\alpha = -6^{\circ}$.

Figure 5.- Continued.

[redacted]

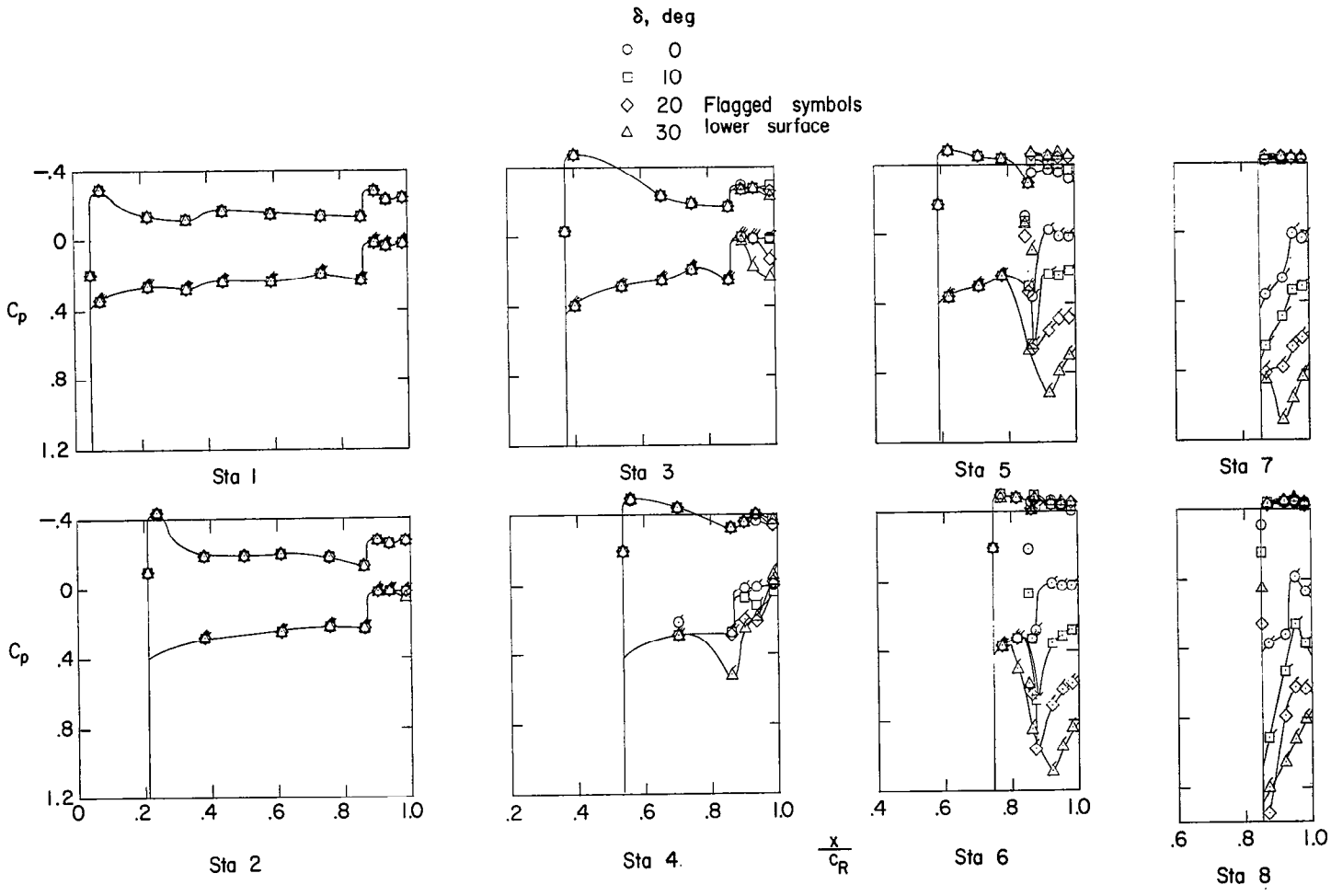

(d) $\alpha = 12^{\circ}$.

Figure 5.- Continued.

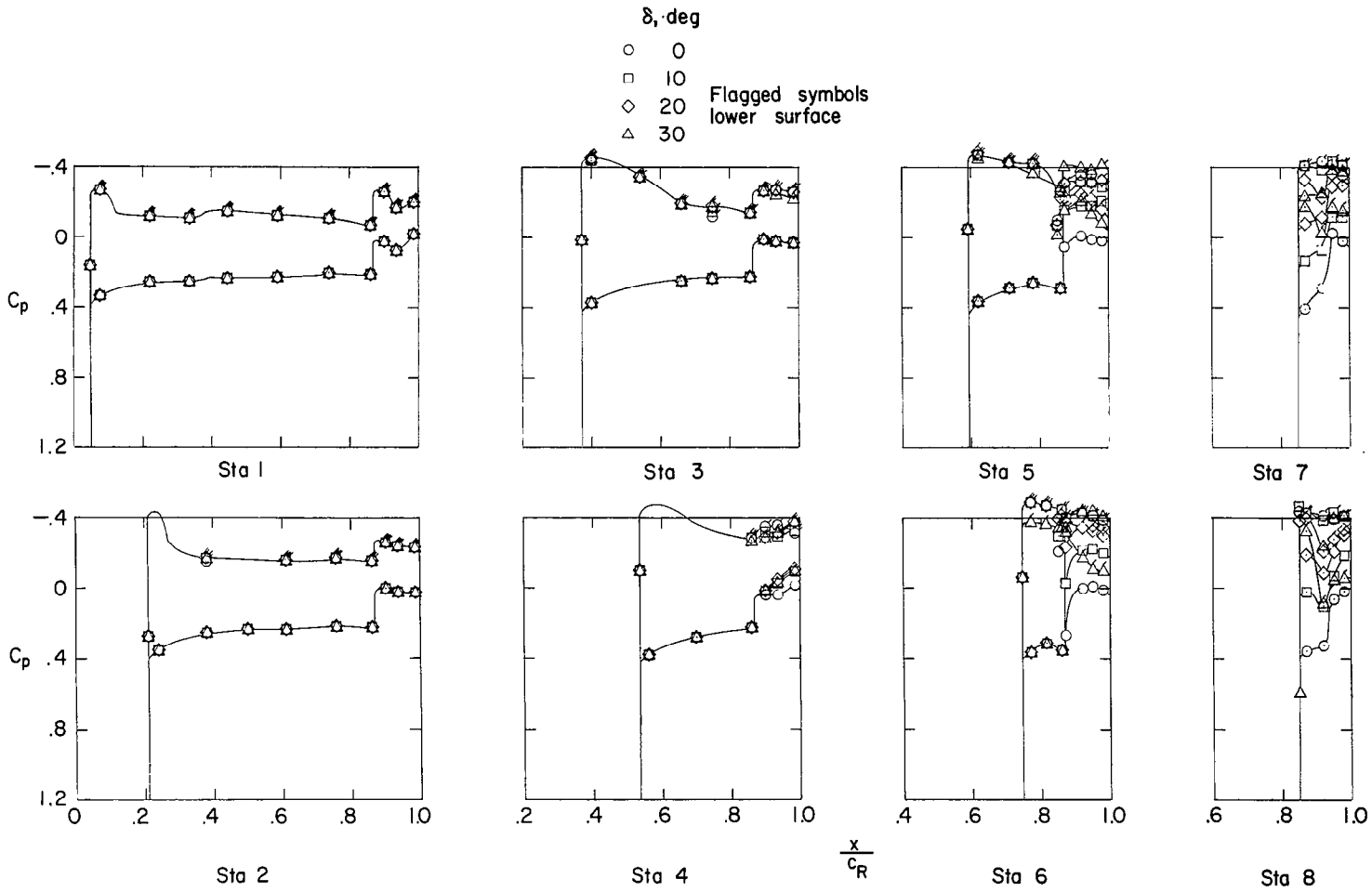

(e) $\alpha = -12^{\circ}$.

Figure 5.- Concluded.

[redacted]

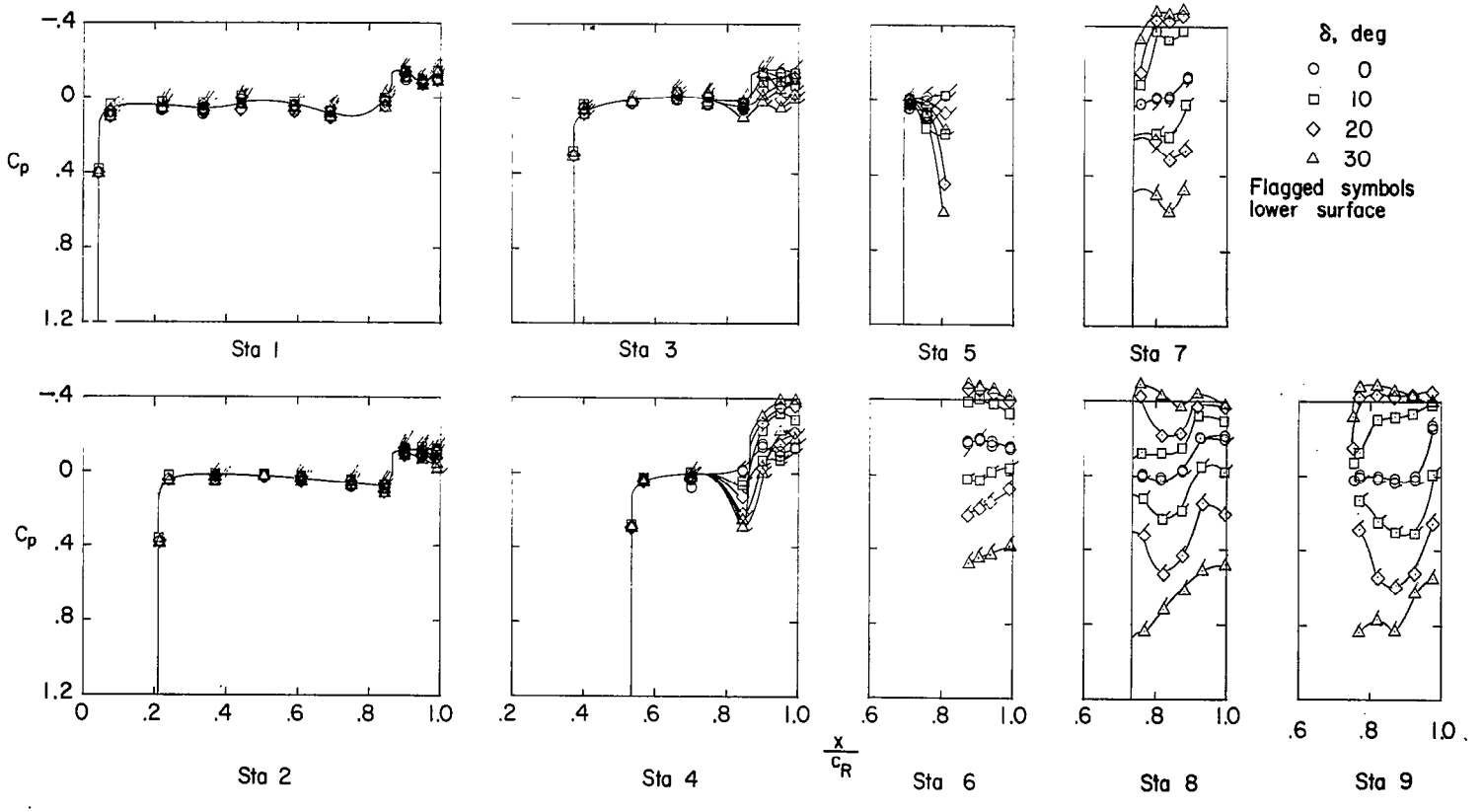

(a) $\alpha = 0^{\circ}$.

Figure 6.- Chordwise pressure distributions for configuration B. $M = 1.61$; $R = 4.2 \times 10^6$.

[redacted]

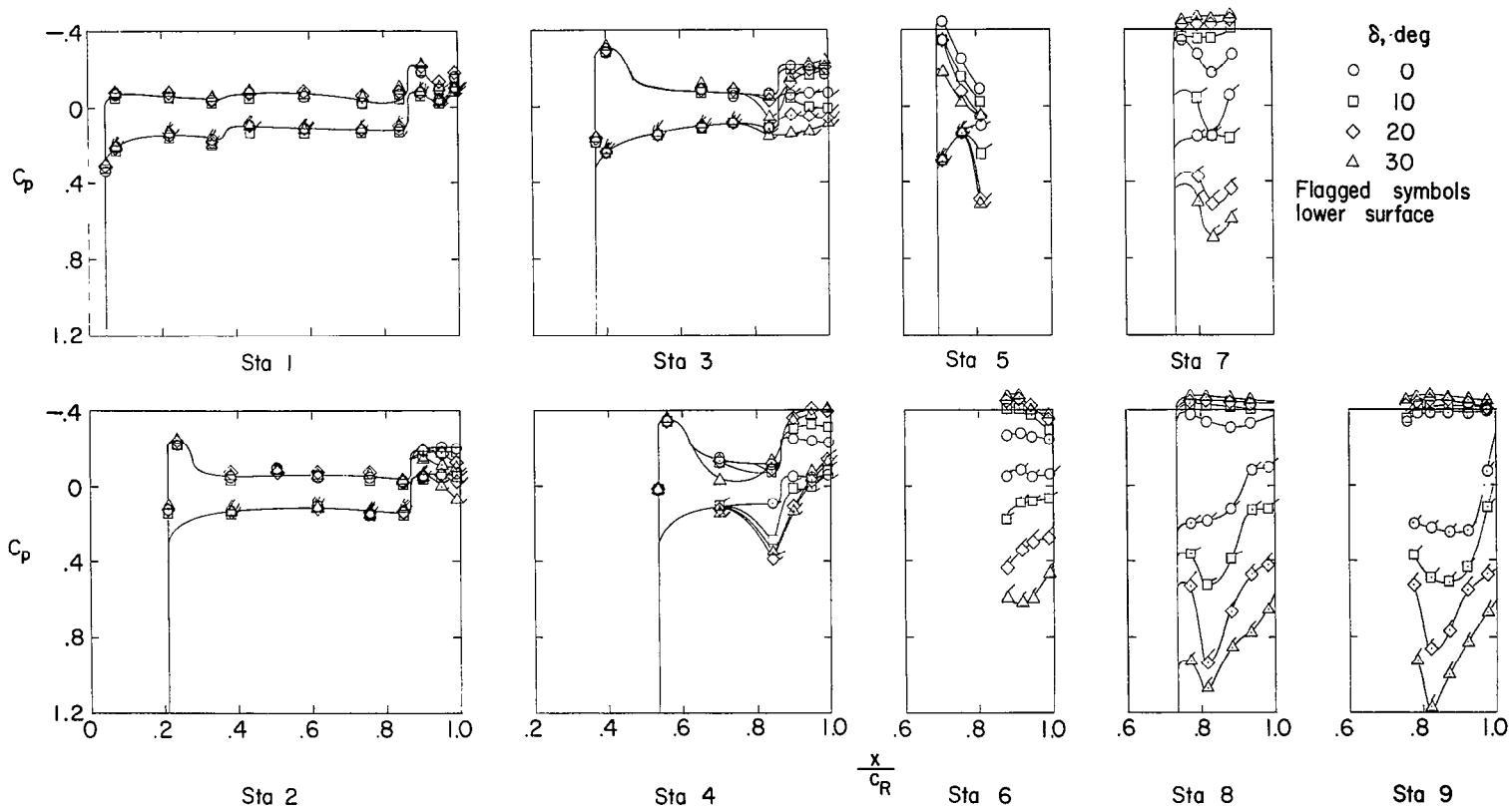

(b) $\alpha = 6^{\circ}$.

Figure 6.- Continued.

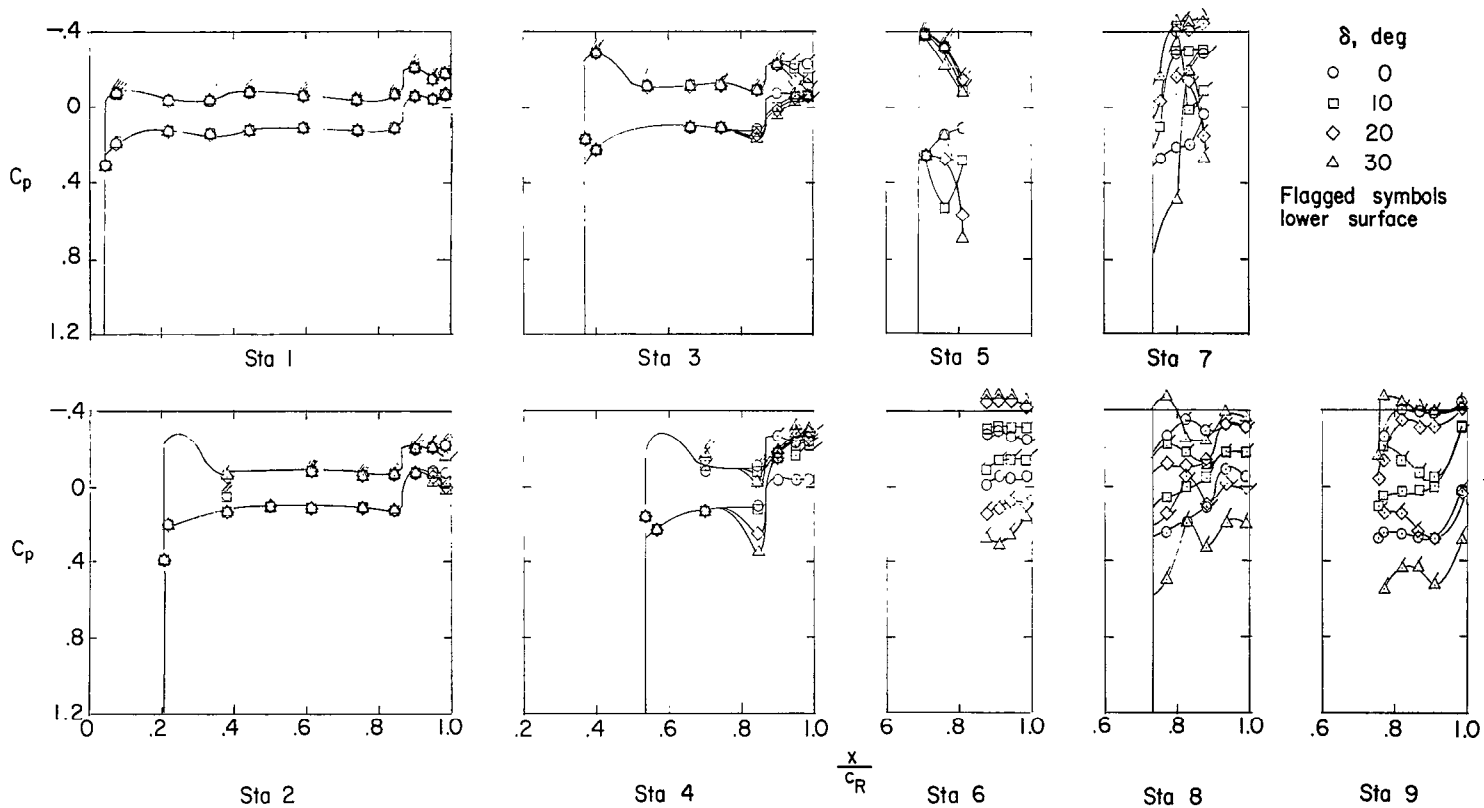

(c) $\alpha = -6^{\circ}$.

Figure 6.- Continued.

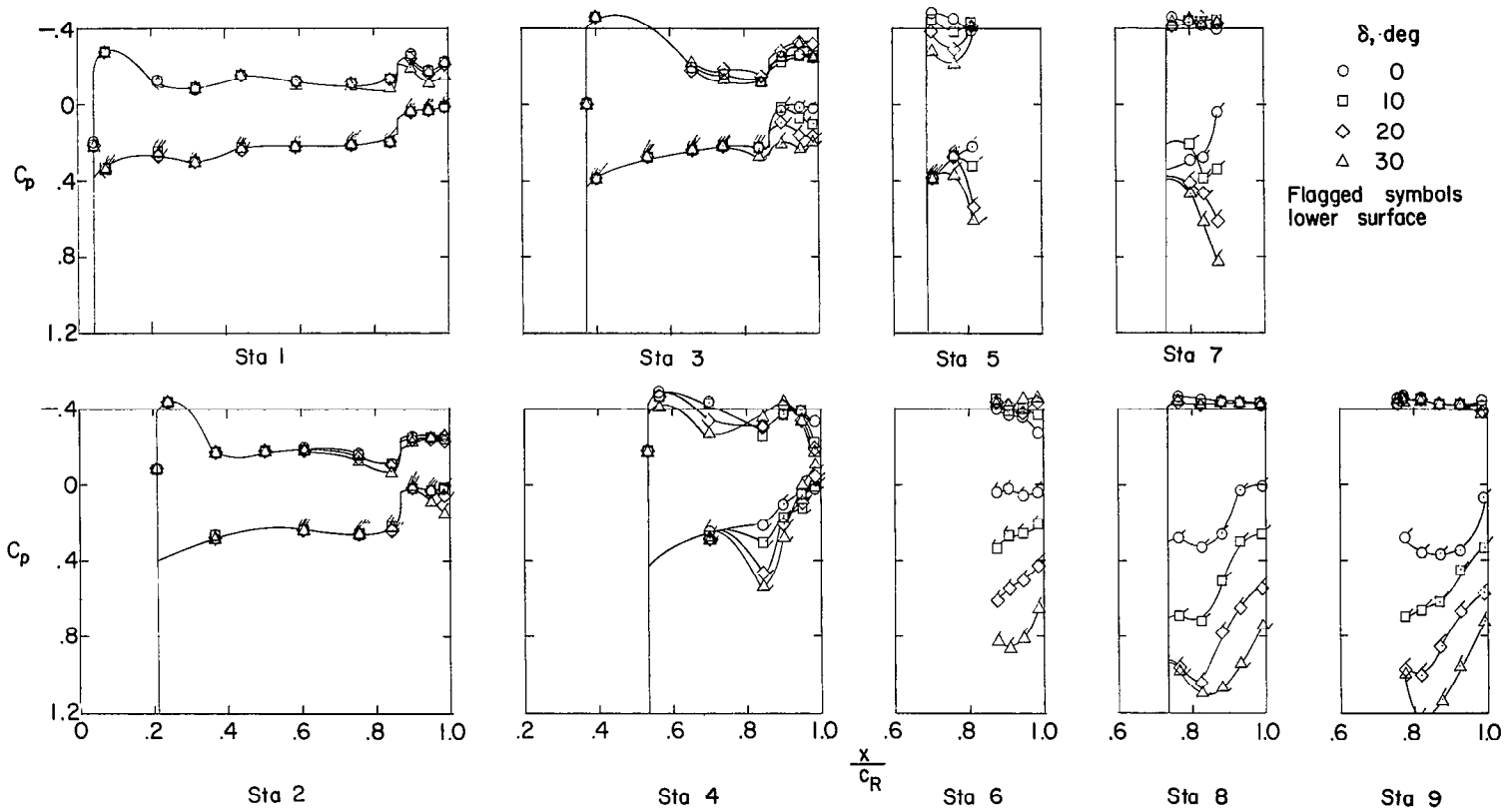

(d) $\alpha = 12^{\circ}$.

Figure 6.- Continued.

[redacted]

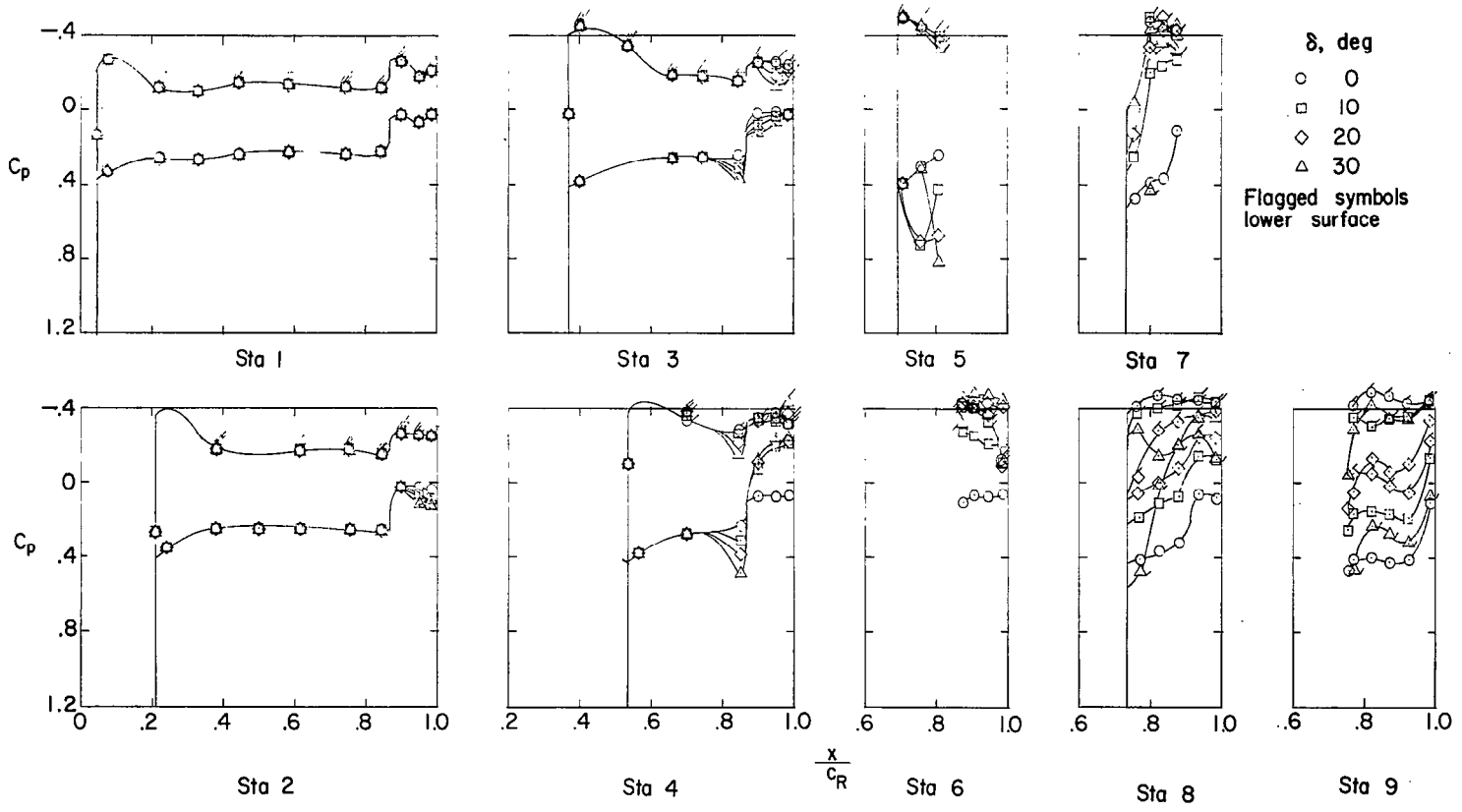

(e) $\alpha = -12^{\circ}$.

Figure 6.- Concluded.

[redacted]

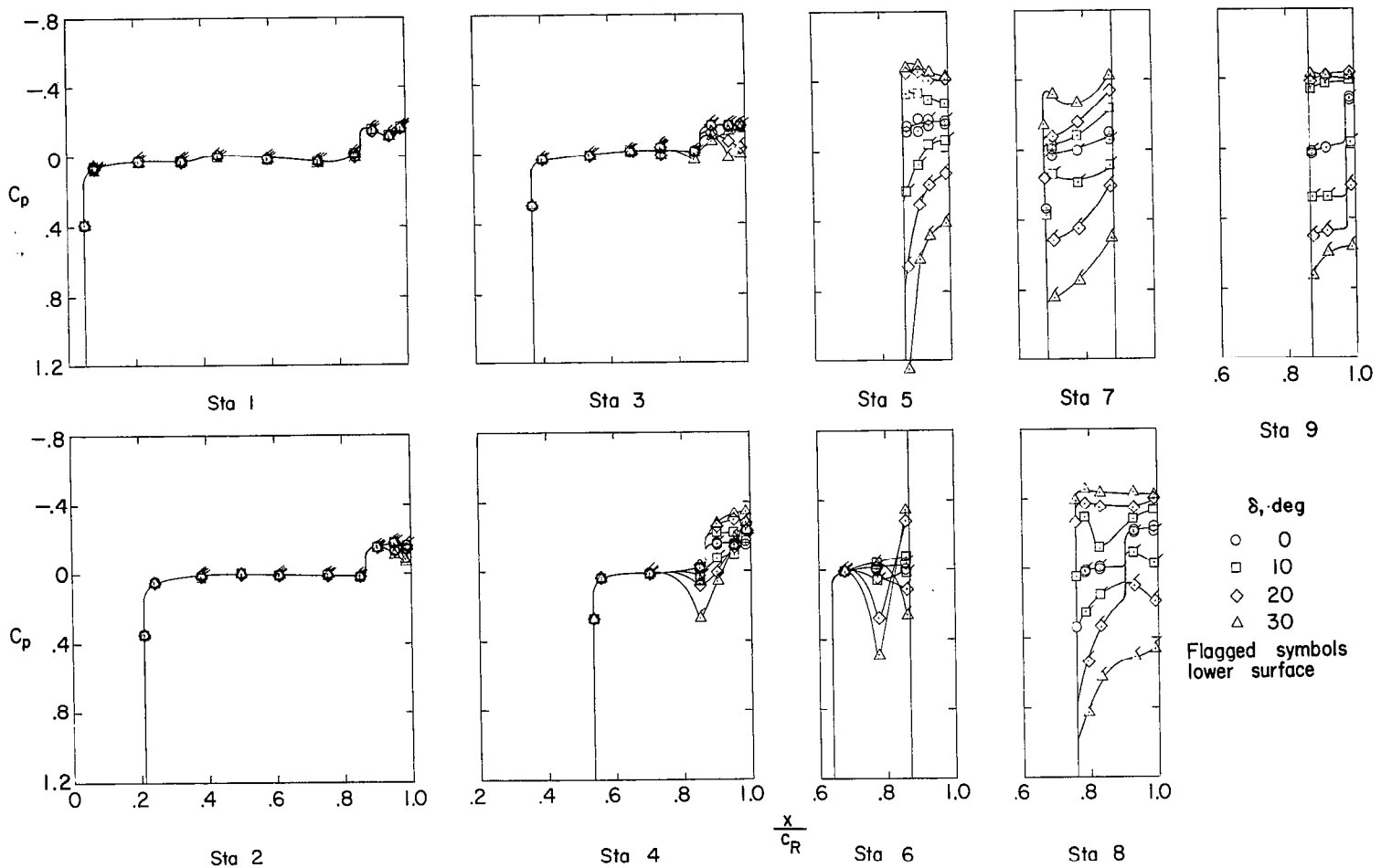

(a) $\alpha = 0^{\circ}$.

Figure 7.- Chordwise pressure distributions for configuration C. $M = 1.61$; $R = 4.2 \times 10^6$.

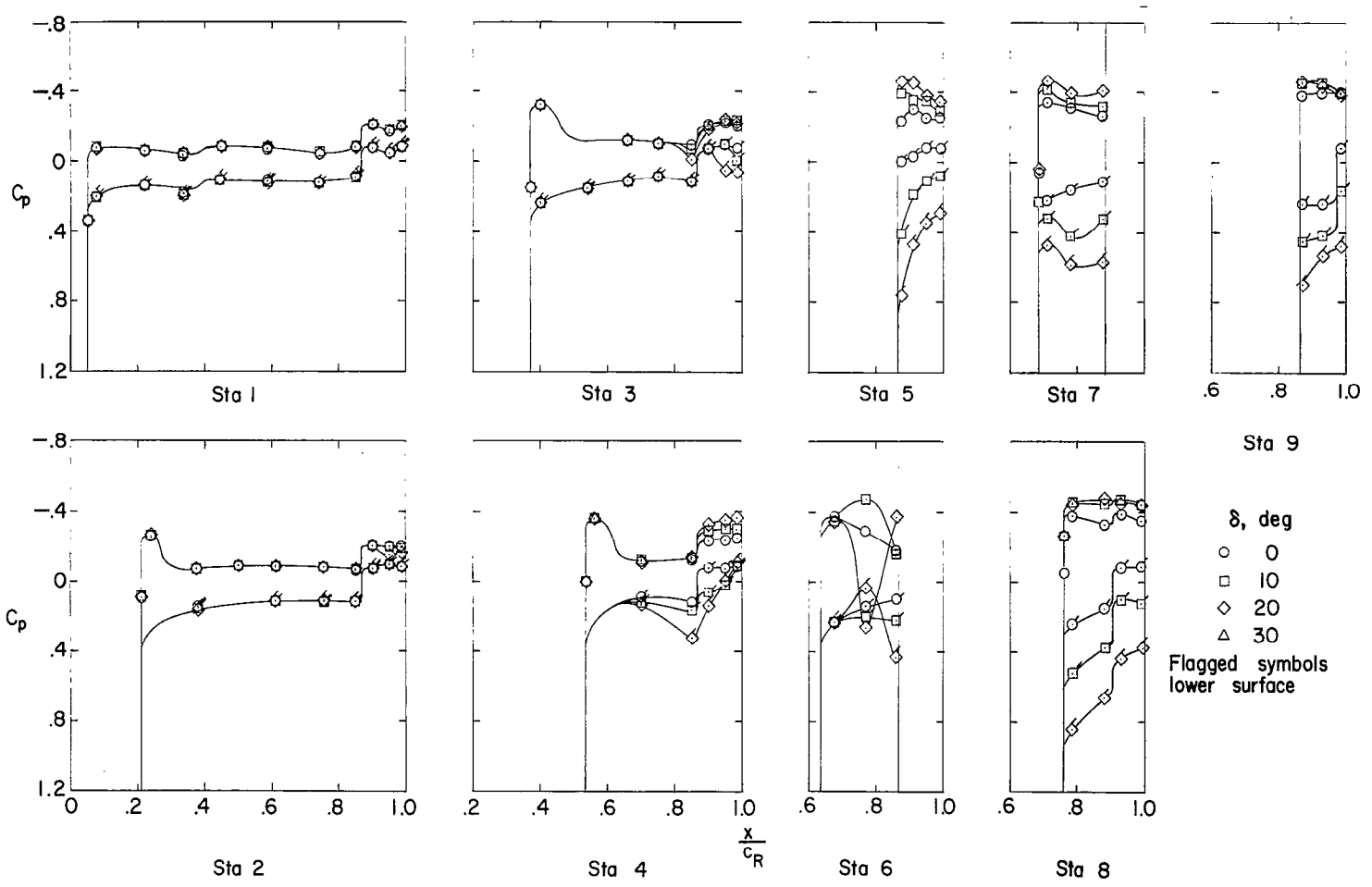

(b) $\alpha = 6^{\circ}$.

Figure 7.- Continued.

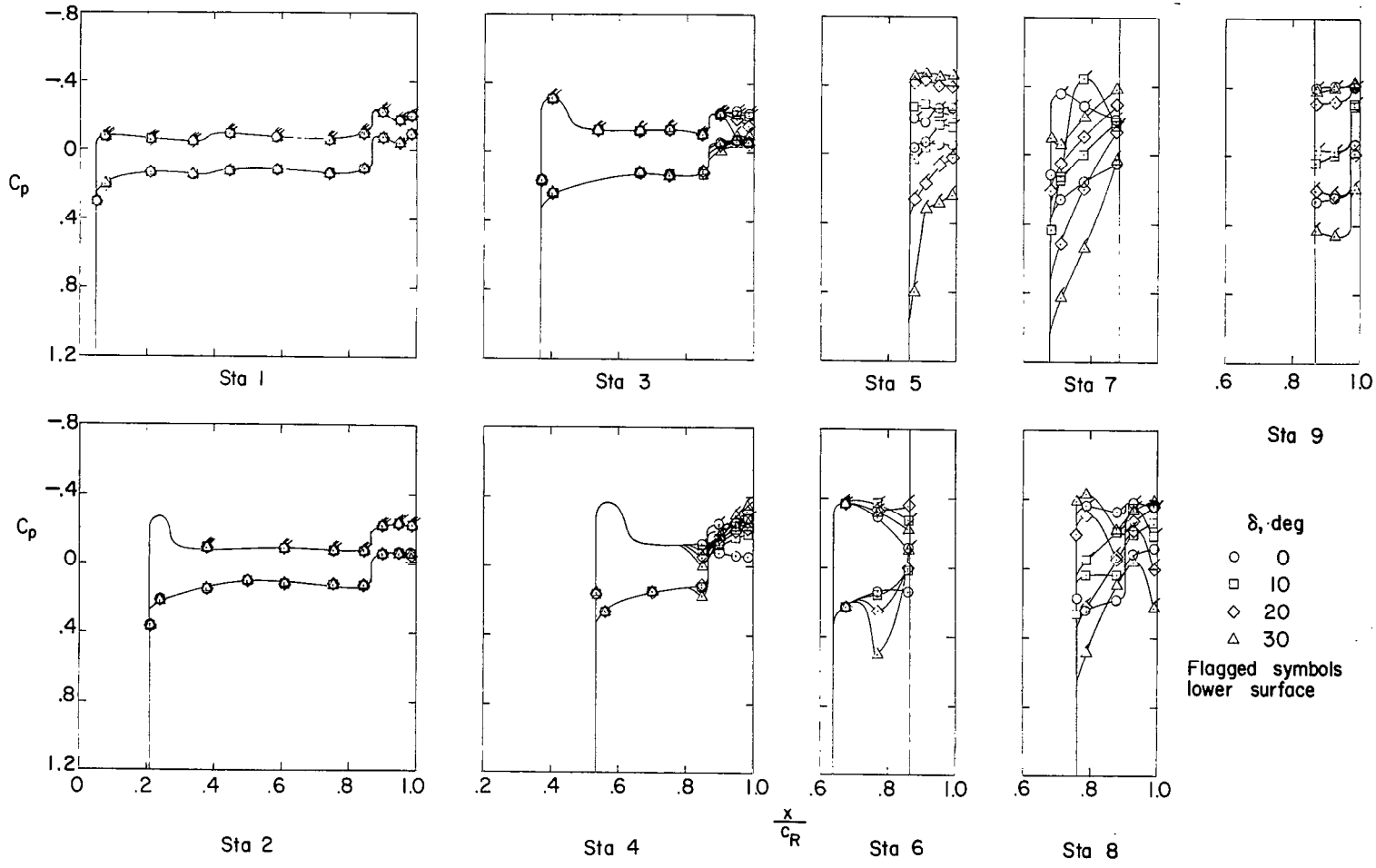

(c) $\alpha = -6^{\circ}$.

Figure 7.- Continued.

[redacted]

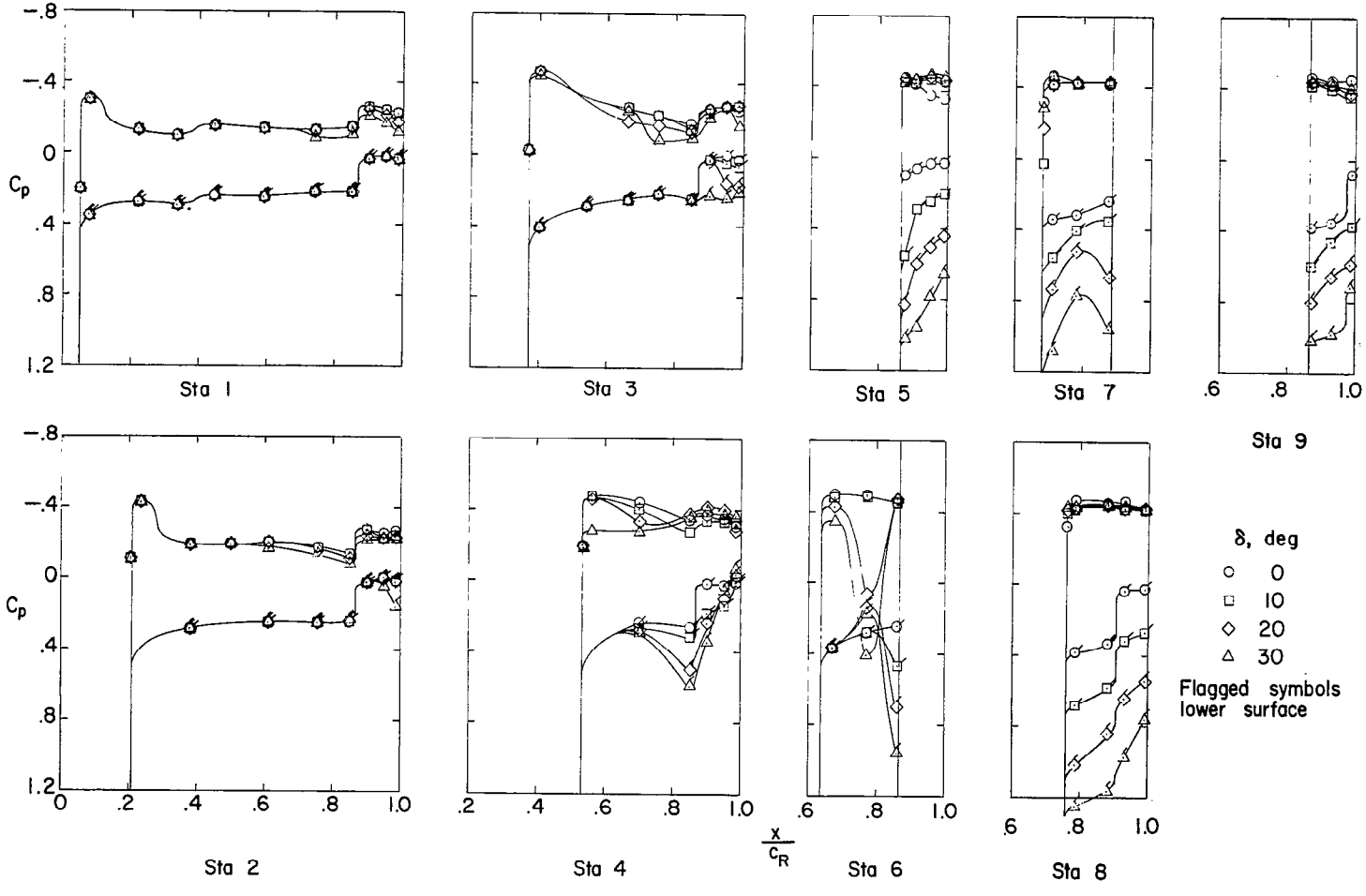

(d) $\alpha = 12^{\circ}$.

Figure 7.- Continued.

[redacted]

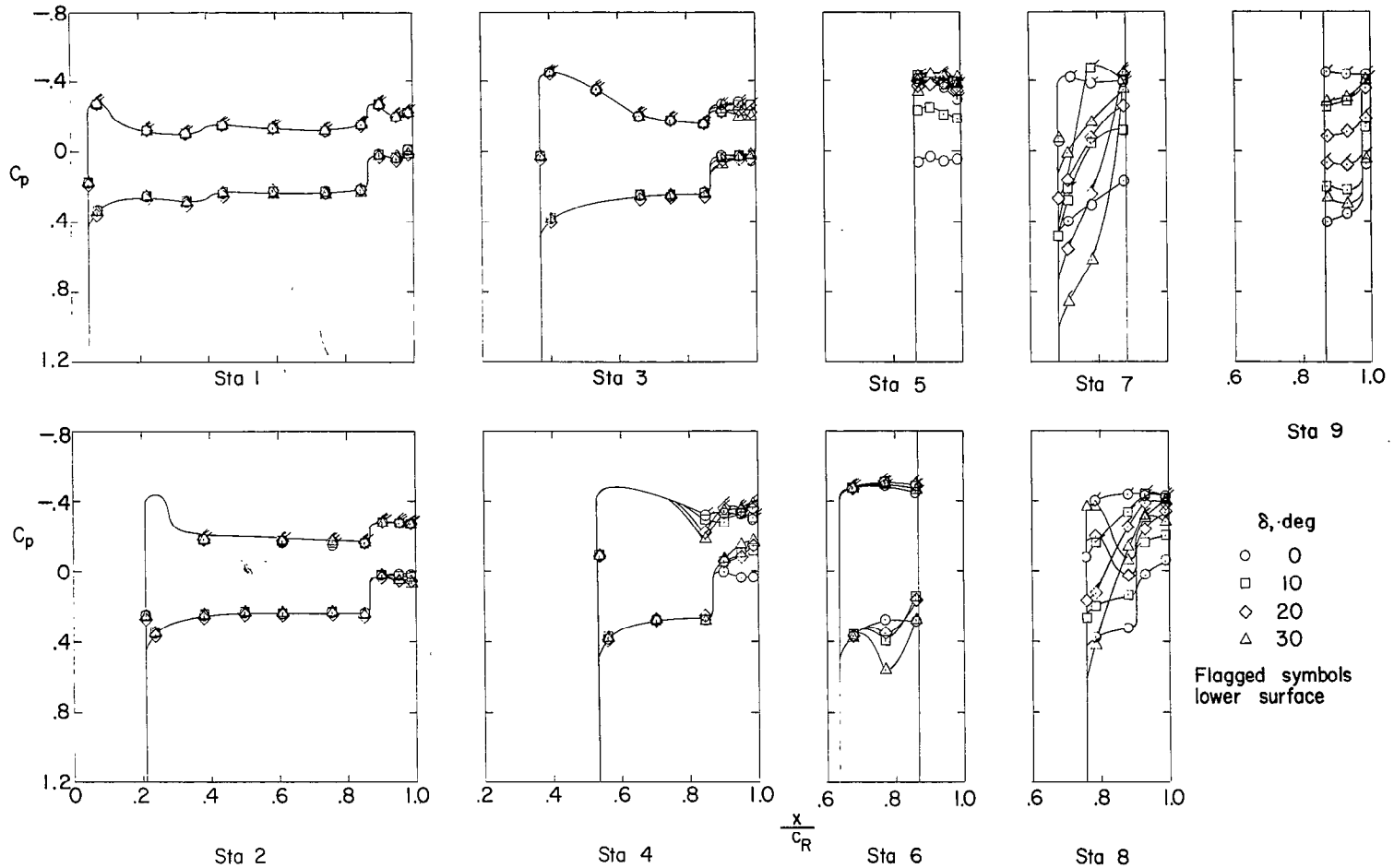

(e) $\alpha = -12^{\circ}$.

Figure 7.- Concluded.

[redacted]

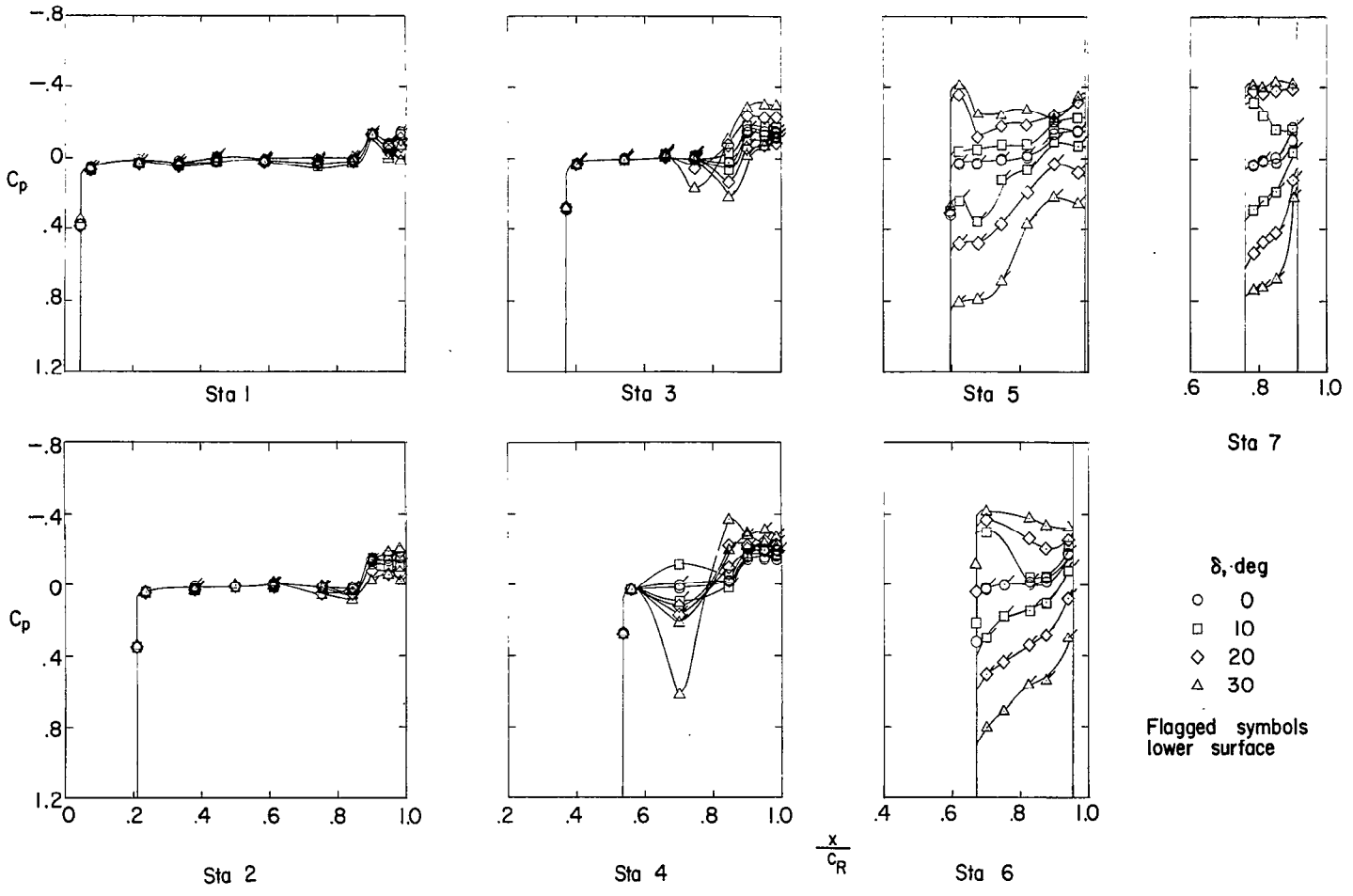

(a) $\alpha = 0^{\circ}$.

Figure 8.- Chordwise pressure distributions for configuration D. $M = 1.61$; $R = 4.2 \times 10^6$.

[redacted]

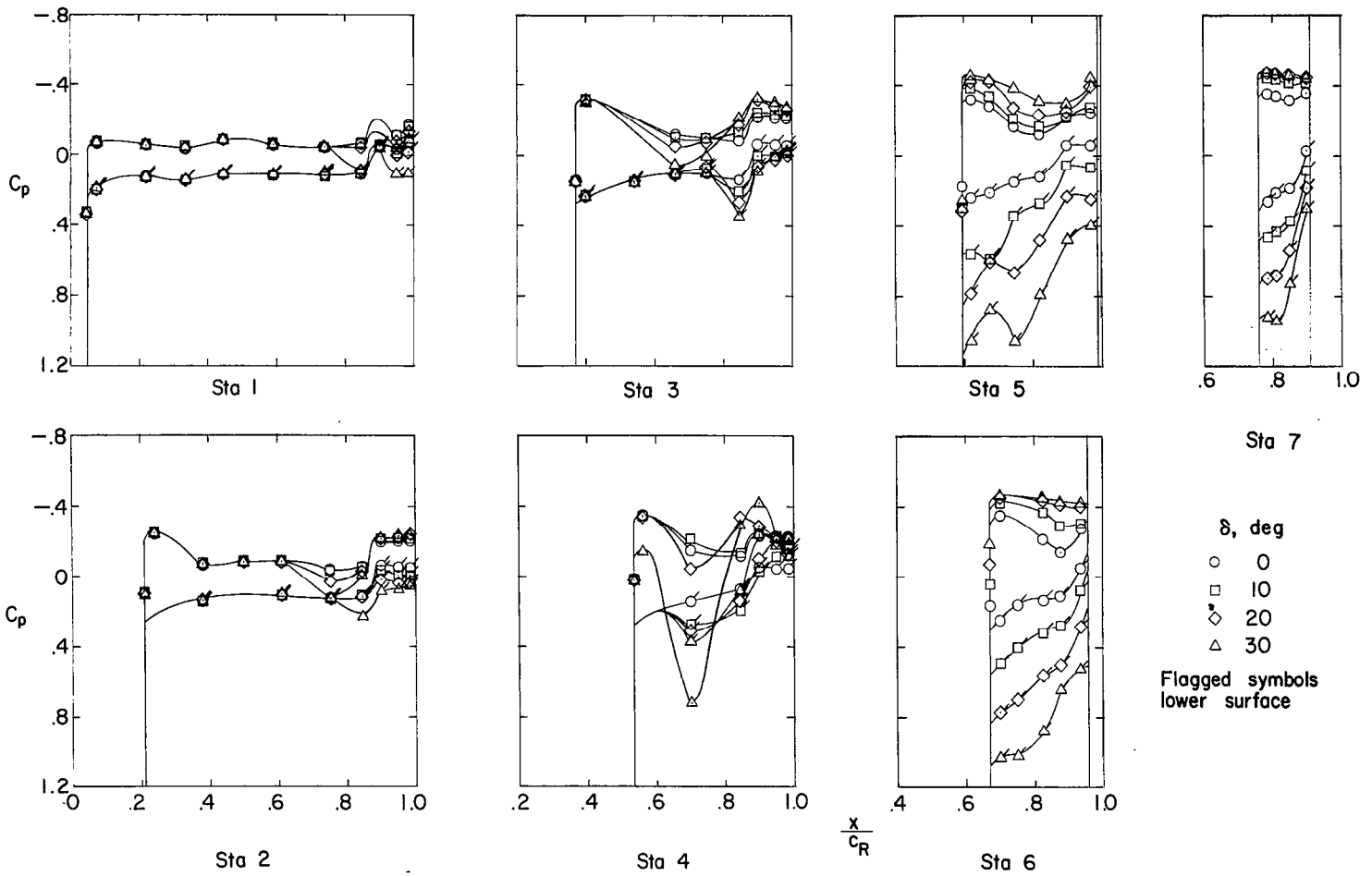

(b) $\alpha = 6^{\circ}$.

Figure 8.- Continued.

CONFIDENTIAL

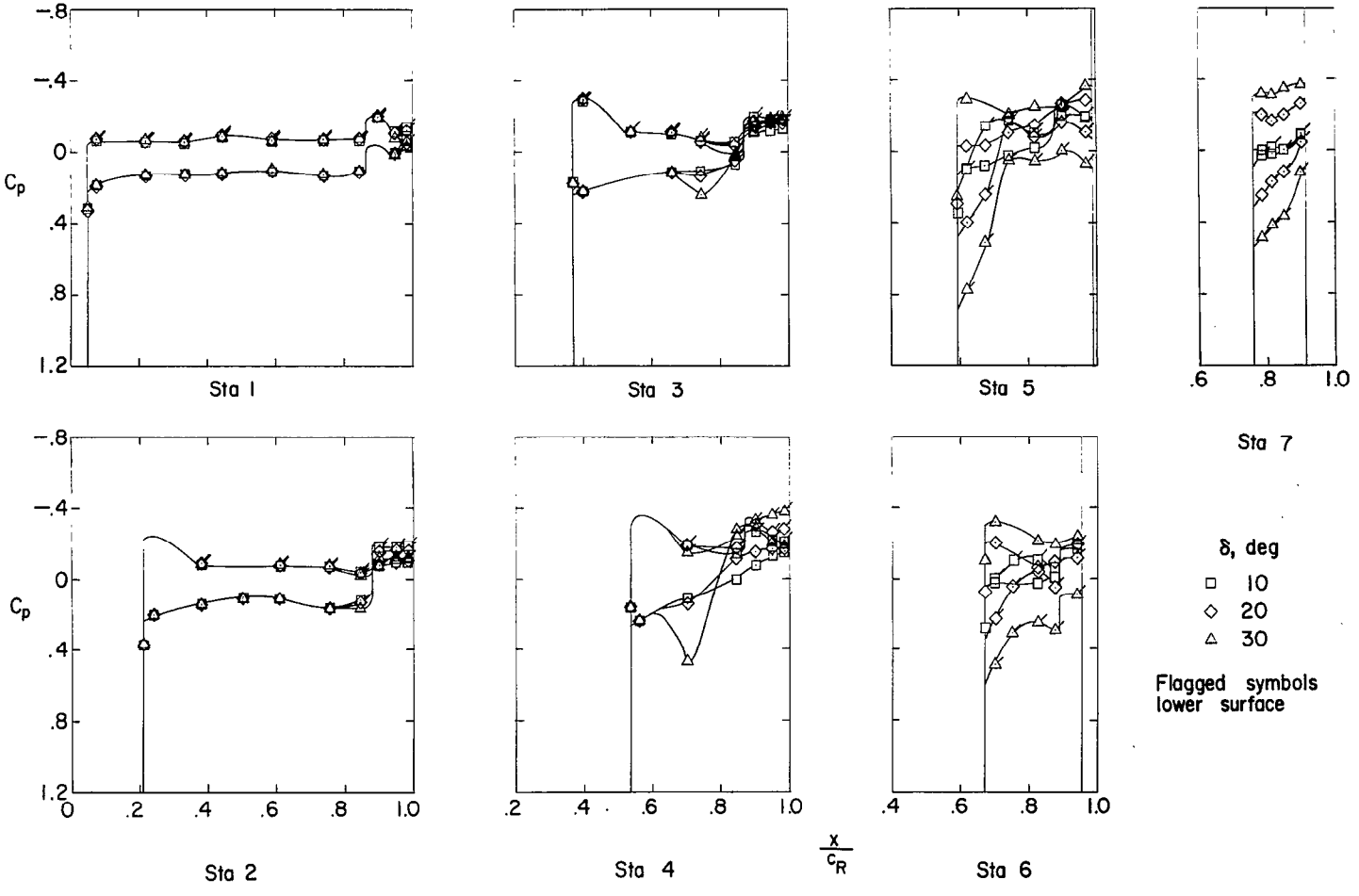

(c) $\alpha = -6^{\circ}$.

Figure 8.- Continued.

CONFIDENTIAL

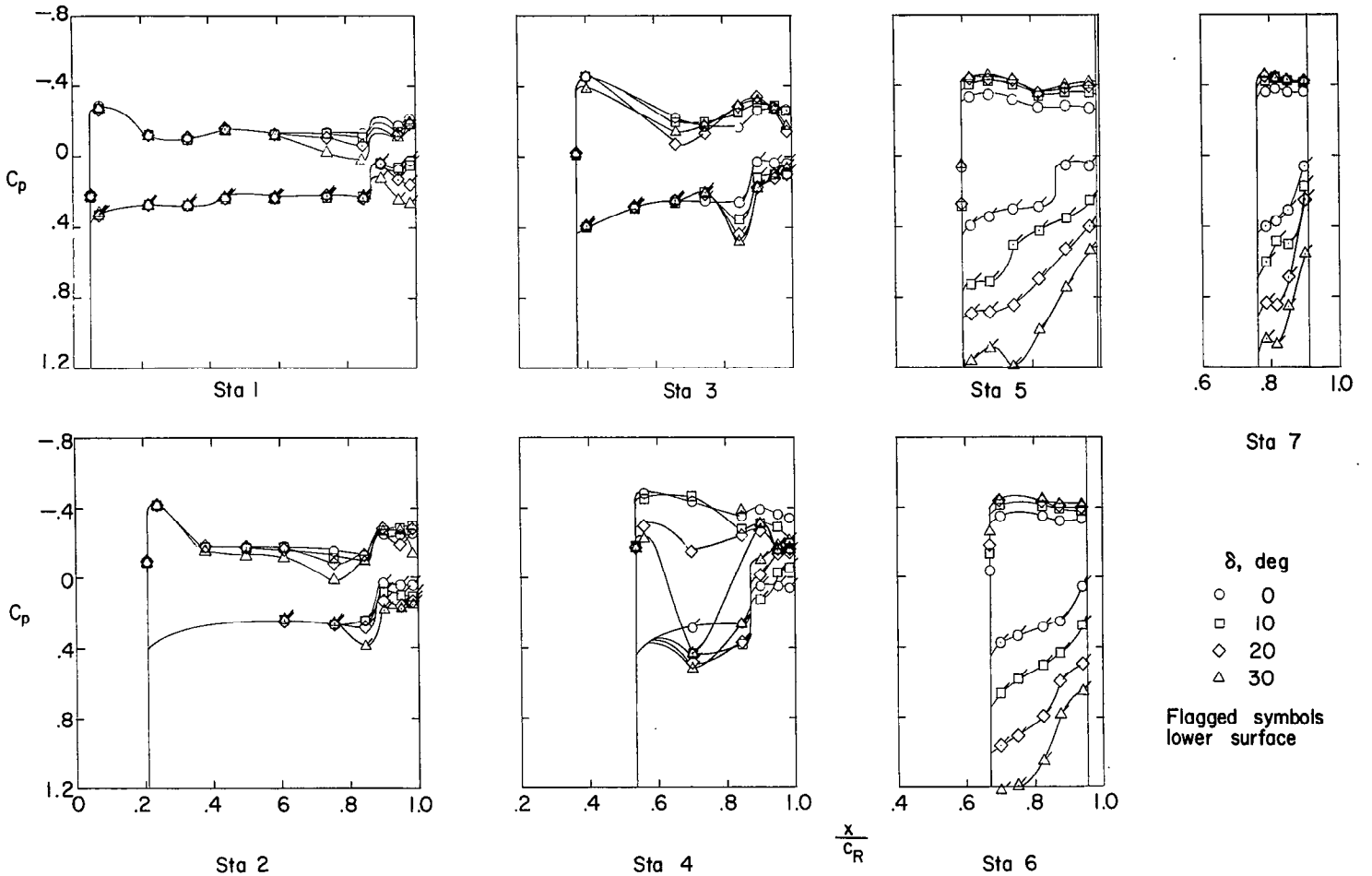

(d) $\alpha = 12^{\circ}$.

Figure 8.- Continued.

[redacted]

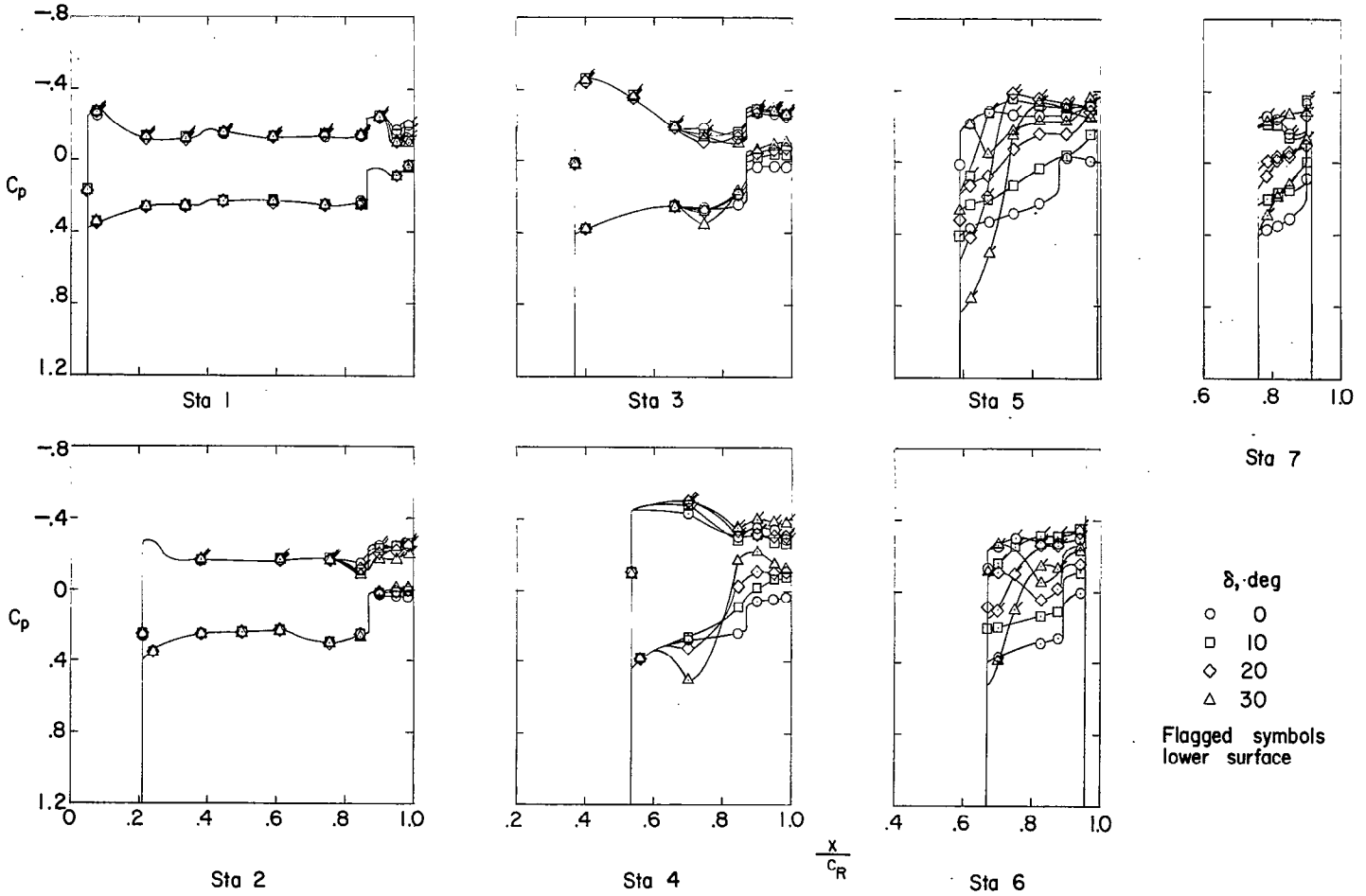

(e) $\alpha = -12^{\circ}$.

Figure 8.- Concluded.

[redacted]

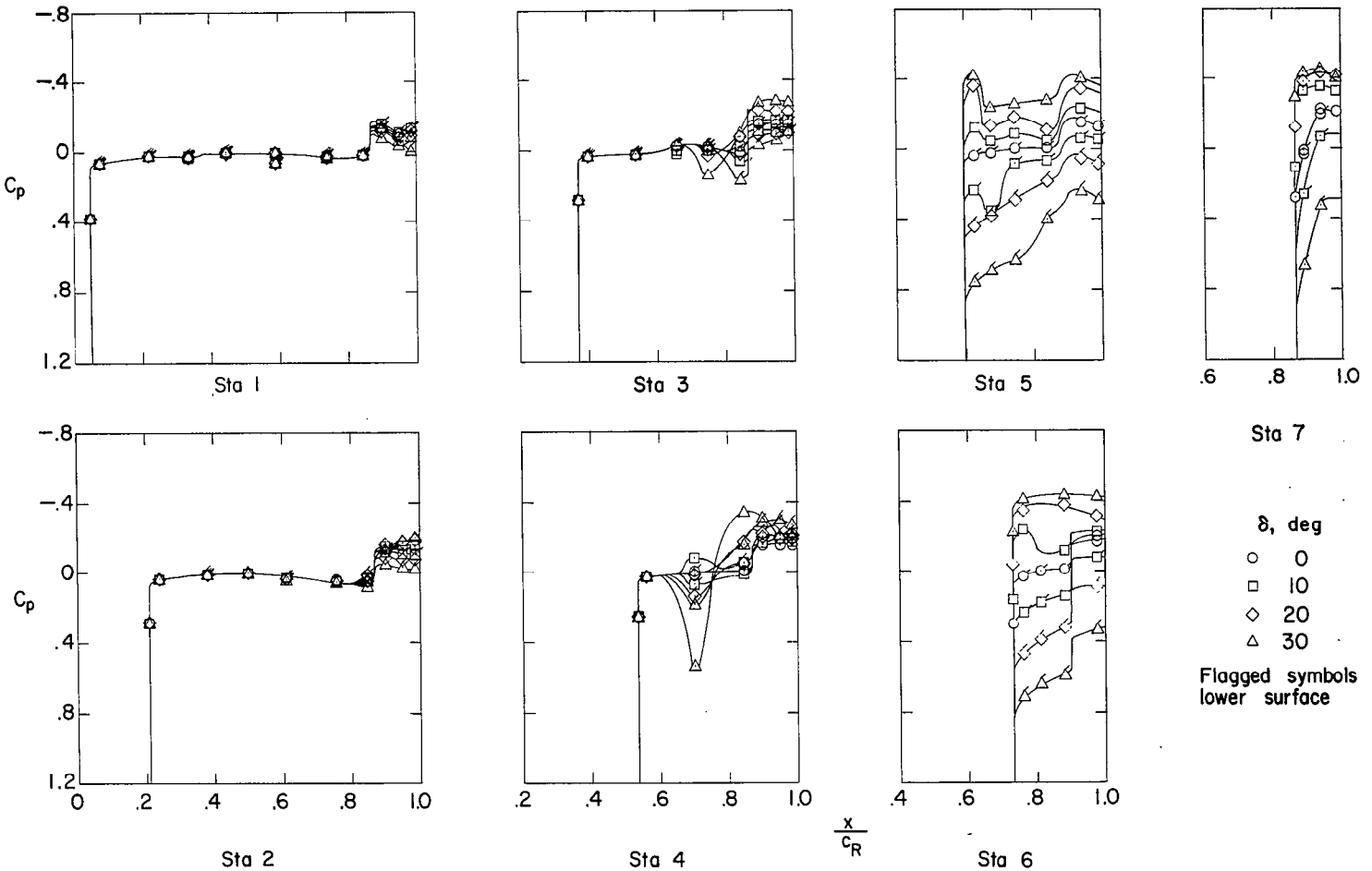

(a) $\alpha = 0^{\circ}$.

Figure 9.- Chordwise pressure distributions for configuration E. $M = 1.61$; $R = 4.2 \times 10^6$.

[redacted]

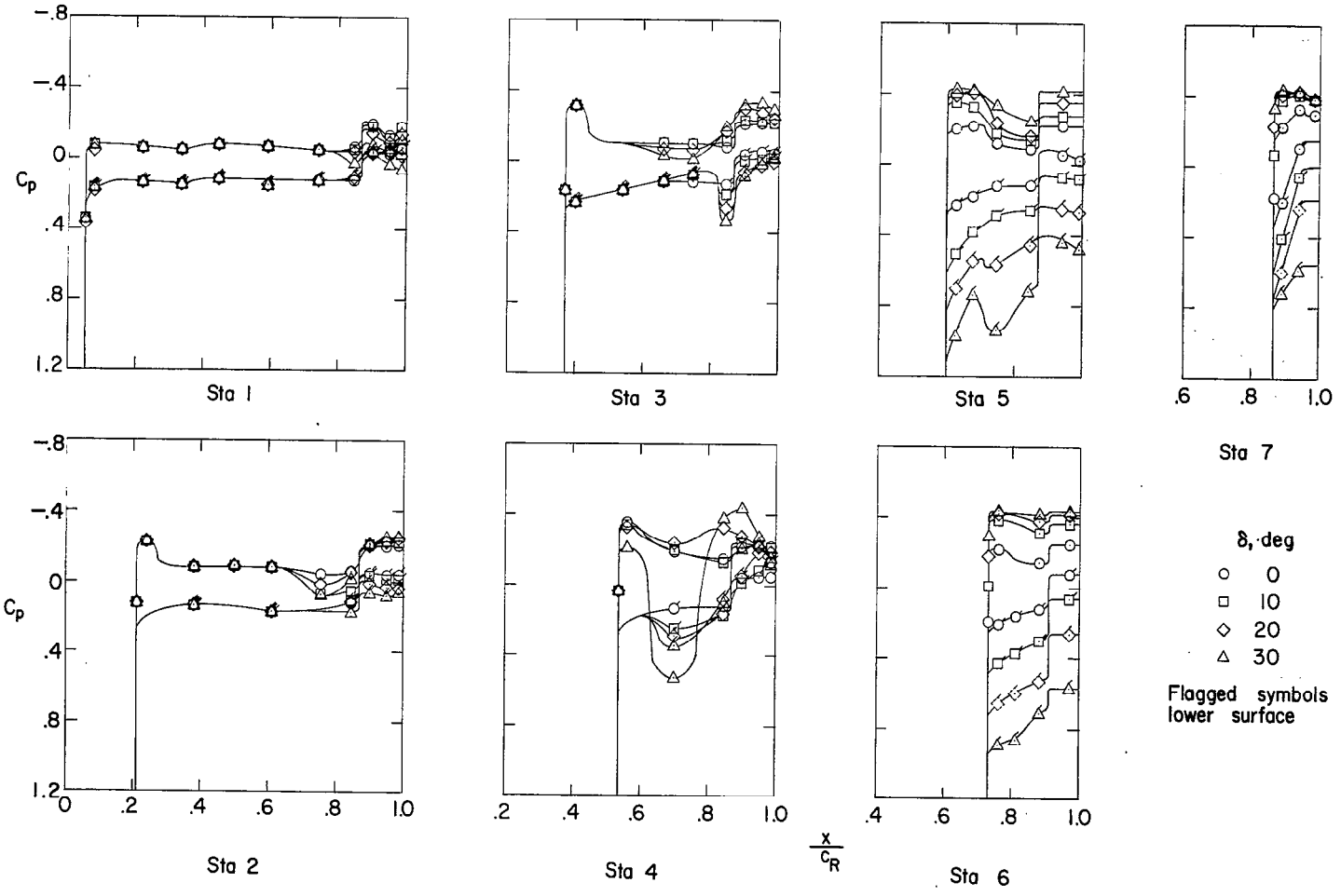

(b) $\alpha = 6^{\circ}$.

Figure 9.- Continued.

[redacted]

[redacted]

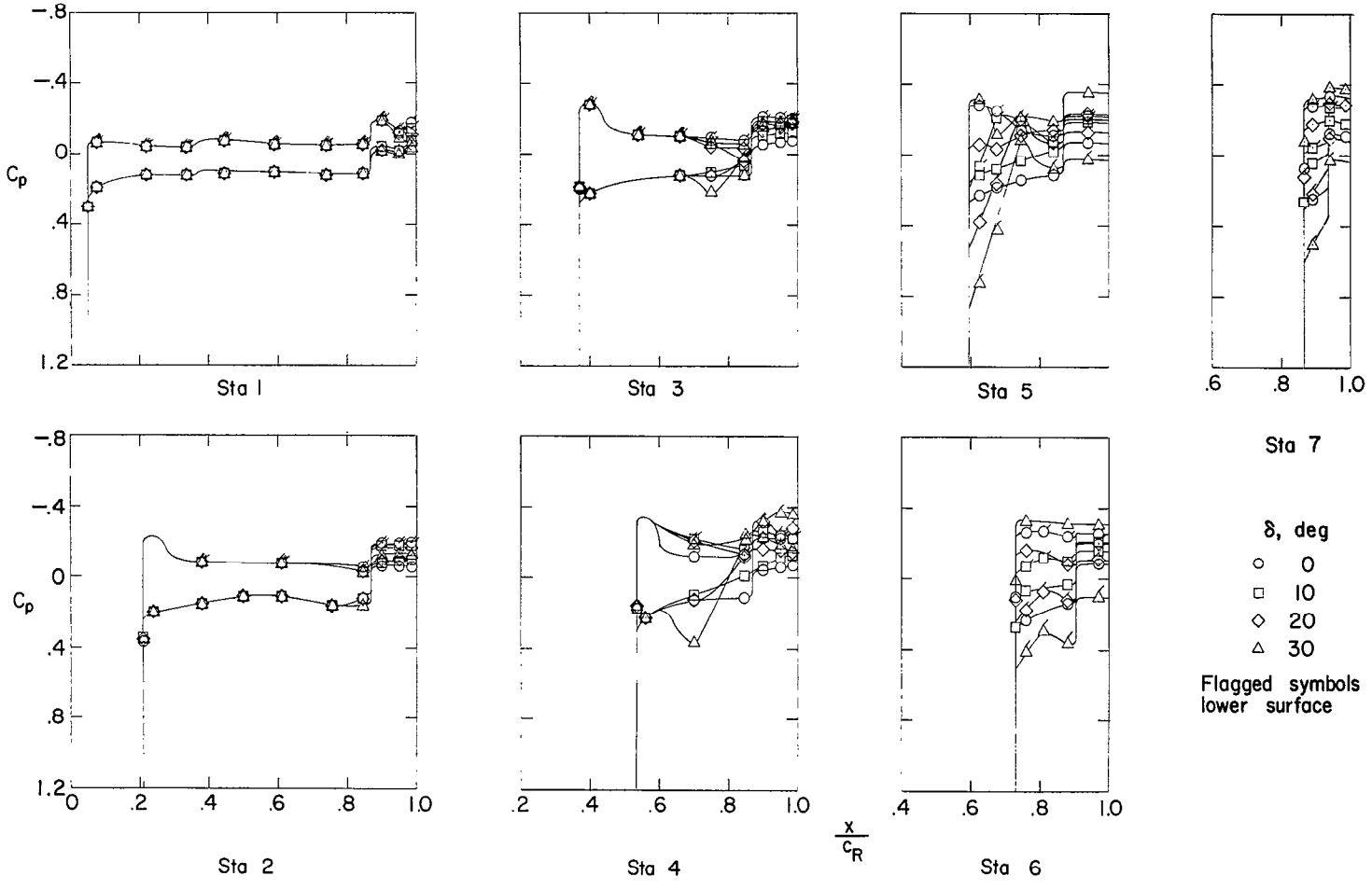

(c) $\alpha = -6^{\circ}$.

Figure 9.- Continued.

[redacted]

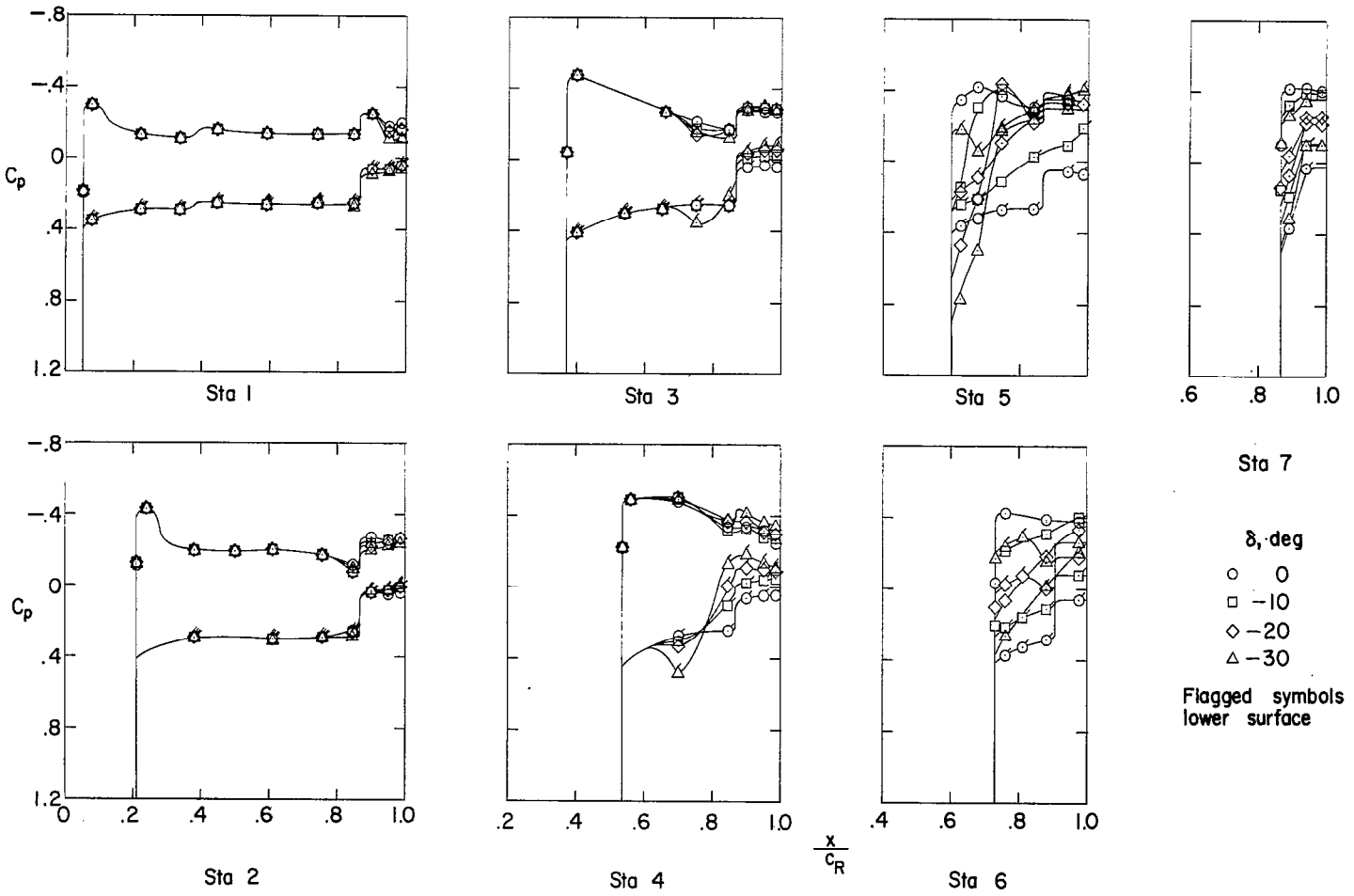

(d) $\alpha = 12^{\circ}$.

Figure 9.- Continued.

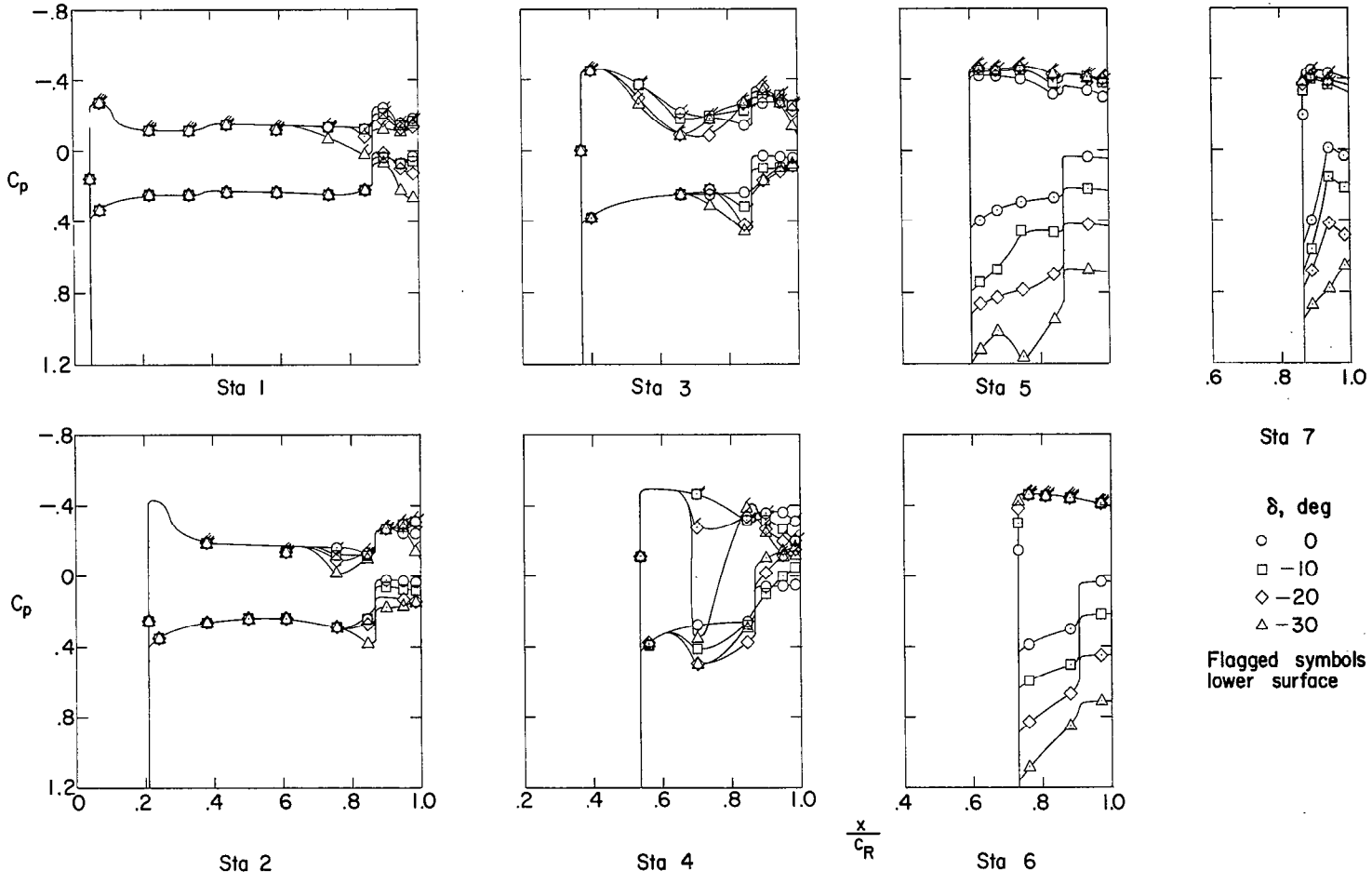

(e) $\alpha = -12^{\circ}$.

Figure 9.- Concluded.

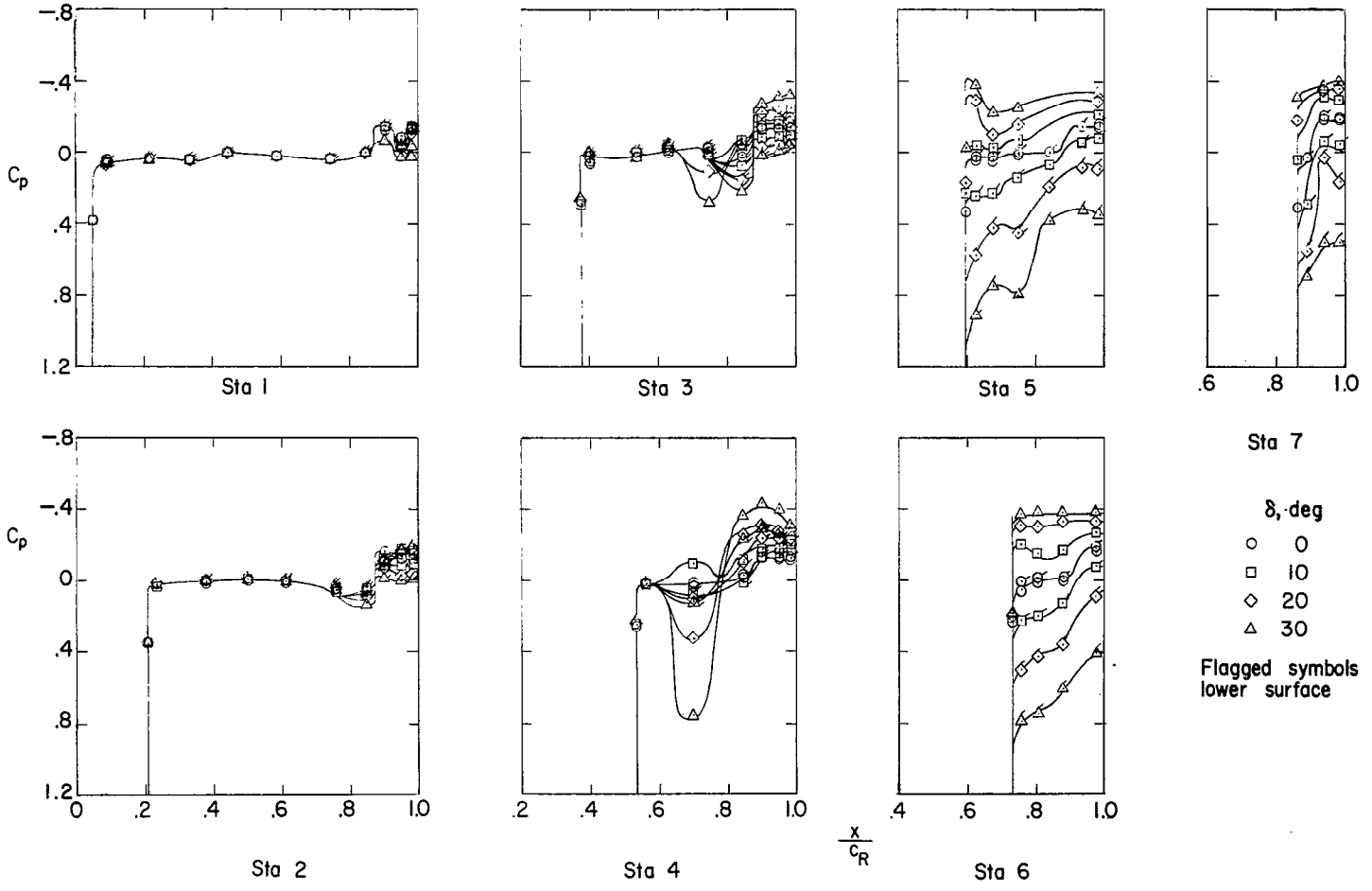

(a) $\alpha = 0^{\circ}$.

Figure 10.- Chordwise pressure distributions for configuration F. $M = 1.61$; $R = 4.2 \times 10^6$.

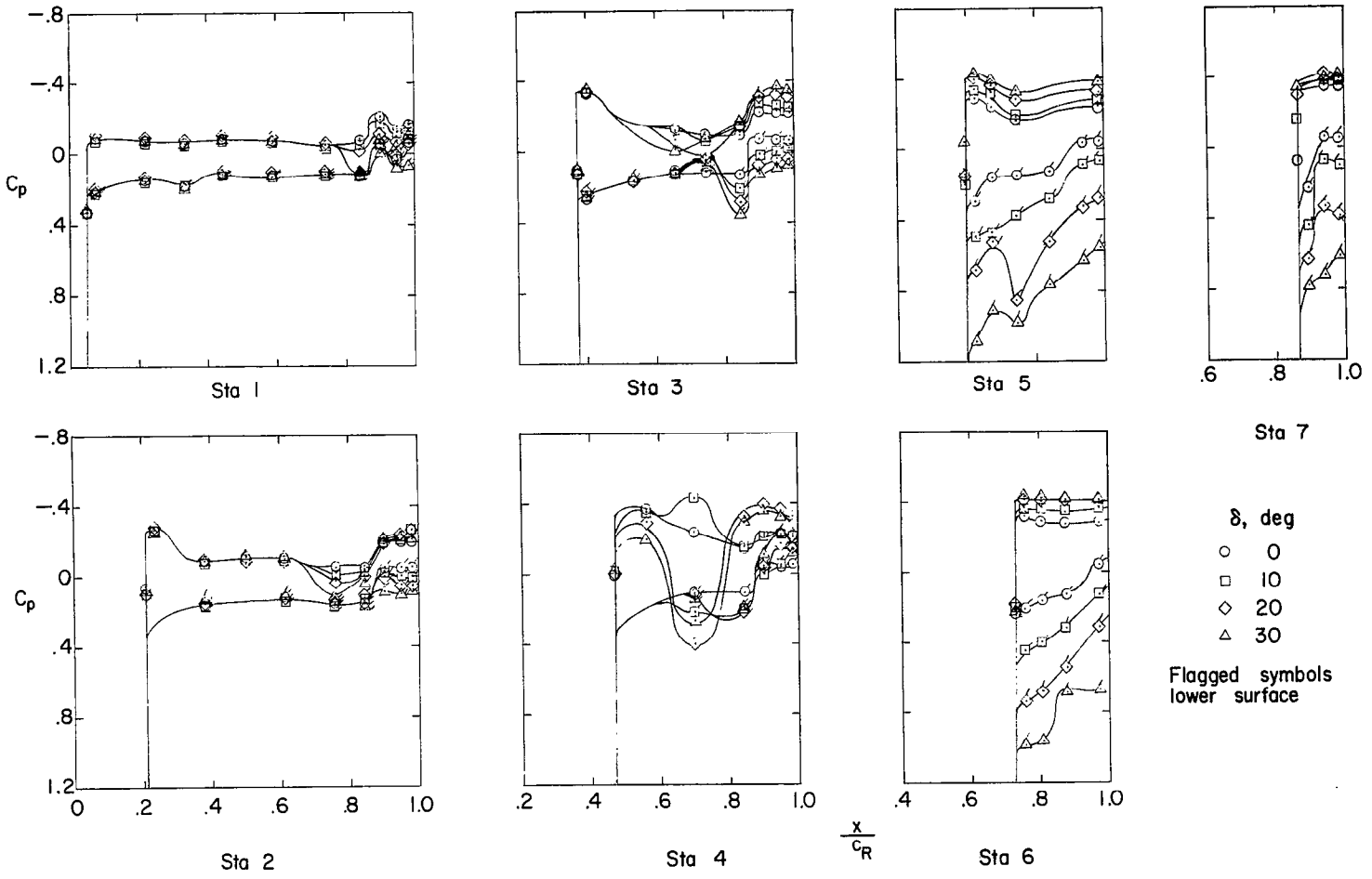

(b) $\alpha = 6^{\circ}$.

Figure 10.- Continued.

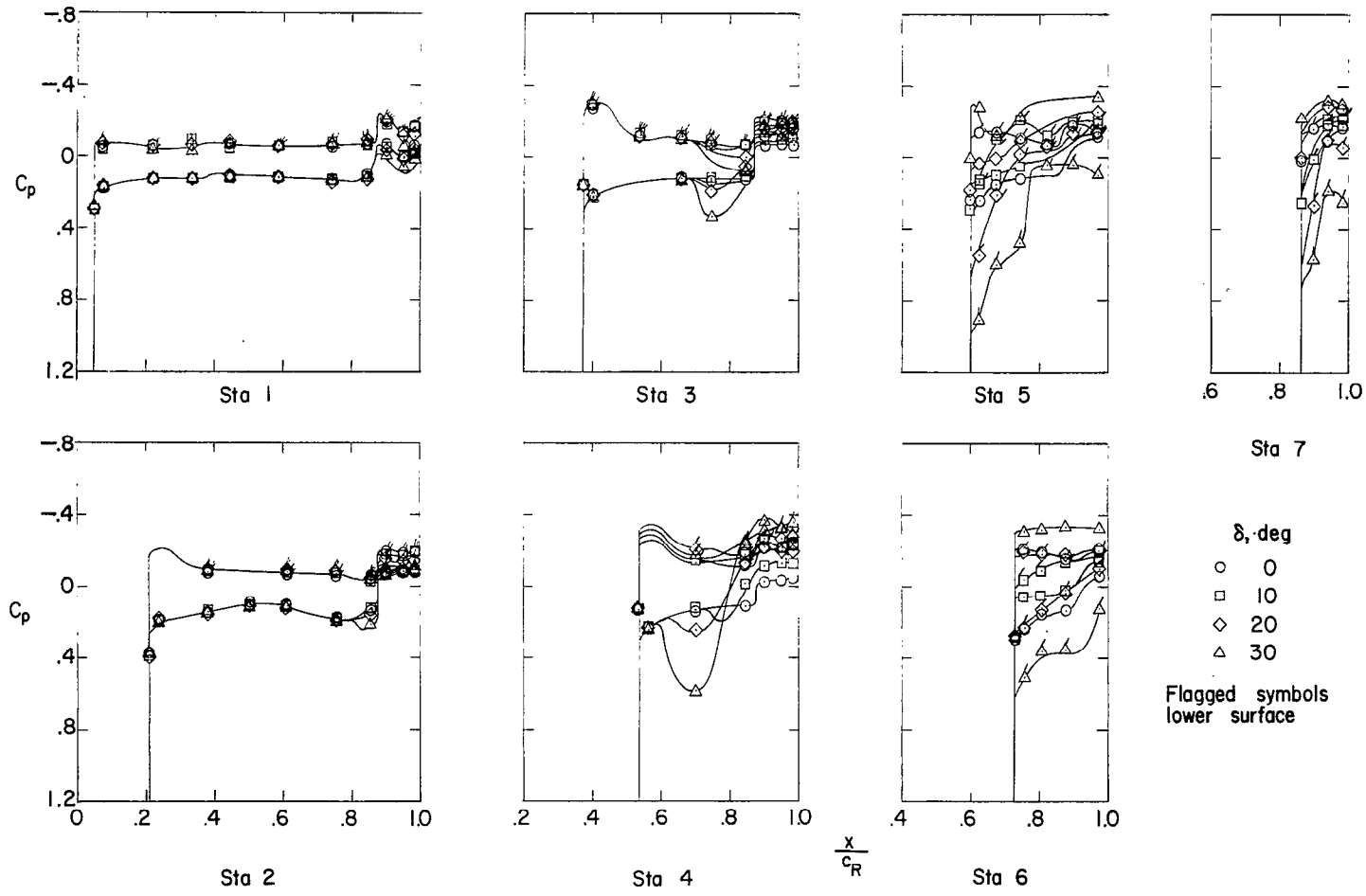

(c) $\alpha = -6^{\circ}$.

Figure 10.- Continued.

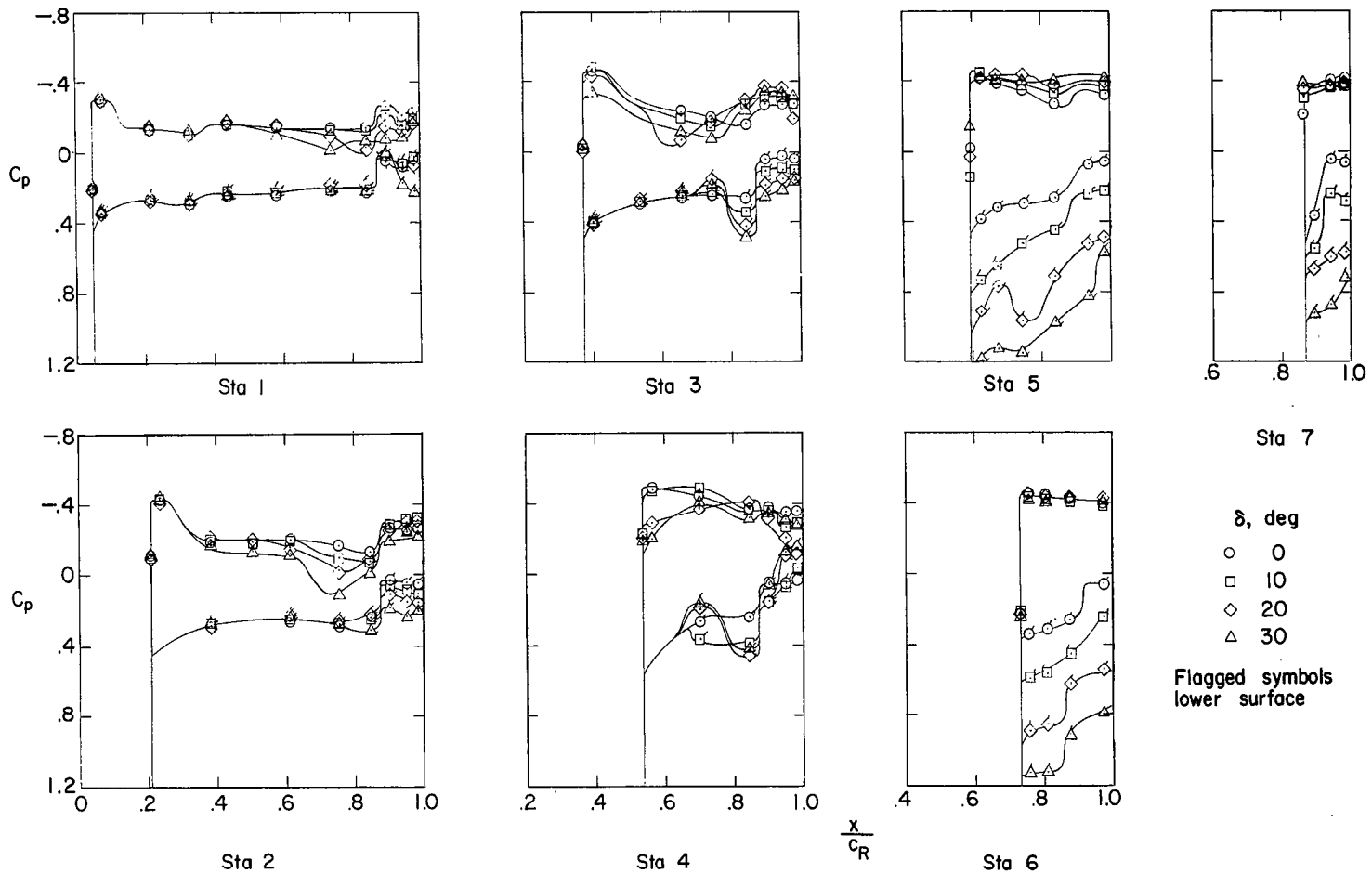

(d) $\alpha = 12^{\circ}$.

Figure 10.- Continued.

[redacted]

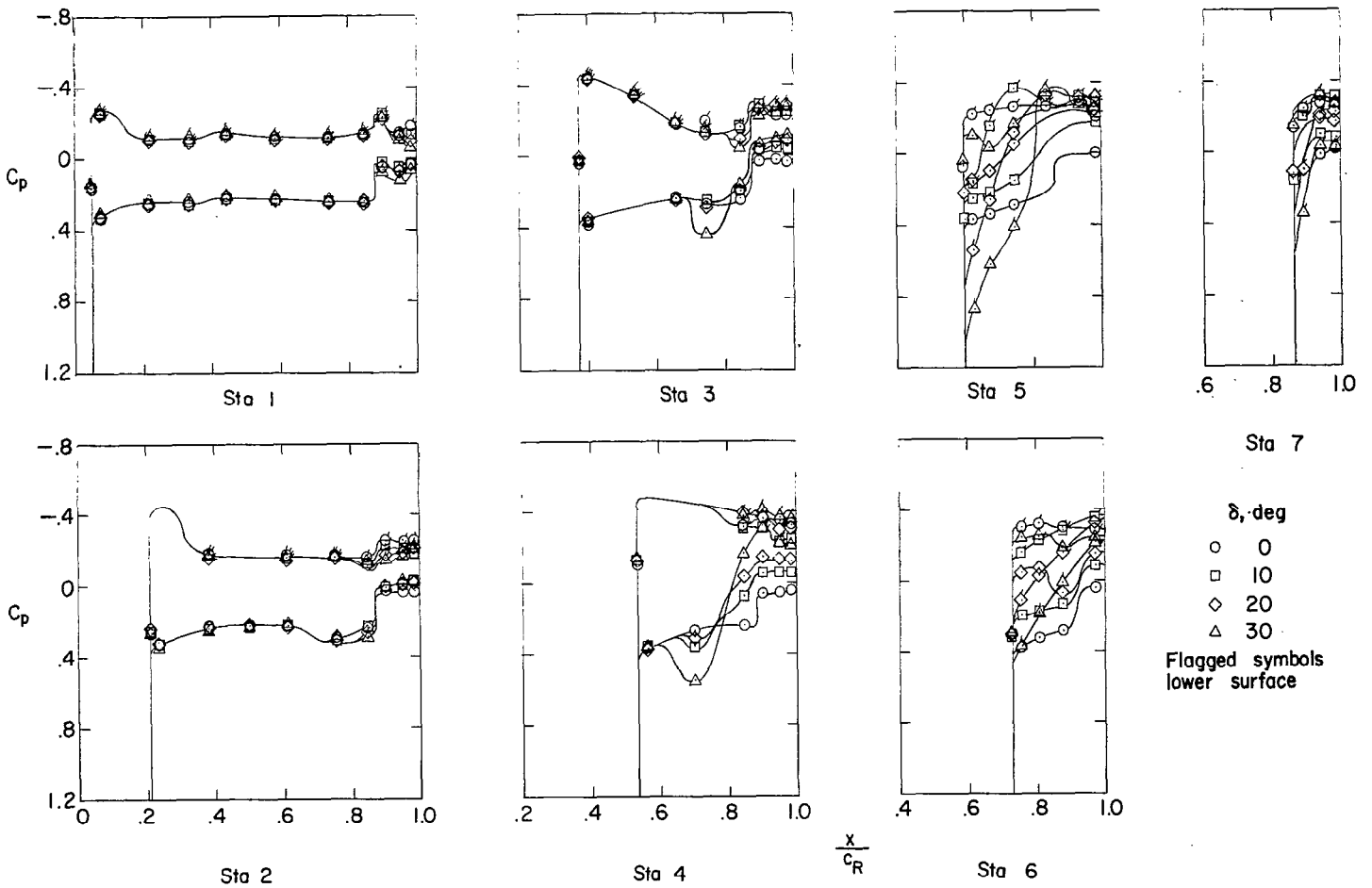

(e) $\alpha = -12^{\circ}$.

Figure 10.- Concluded.

[redacted]

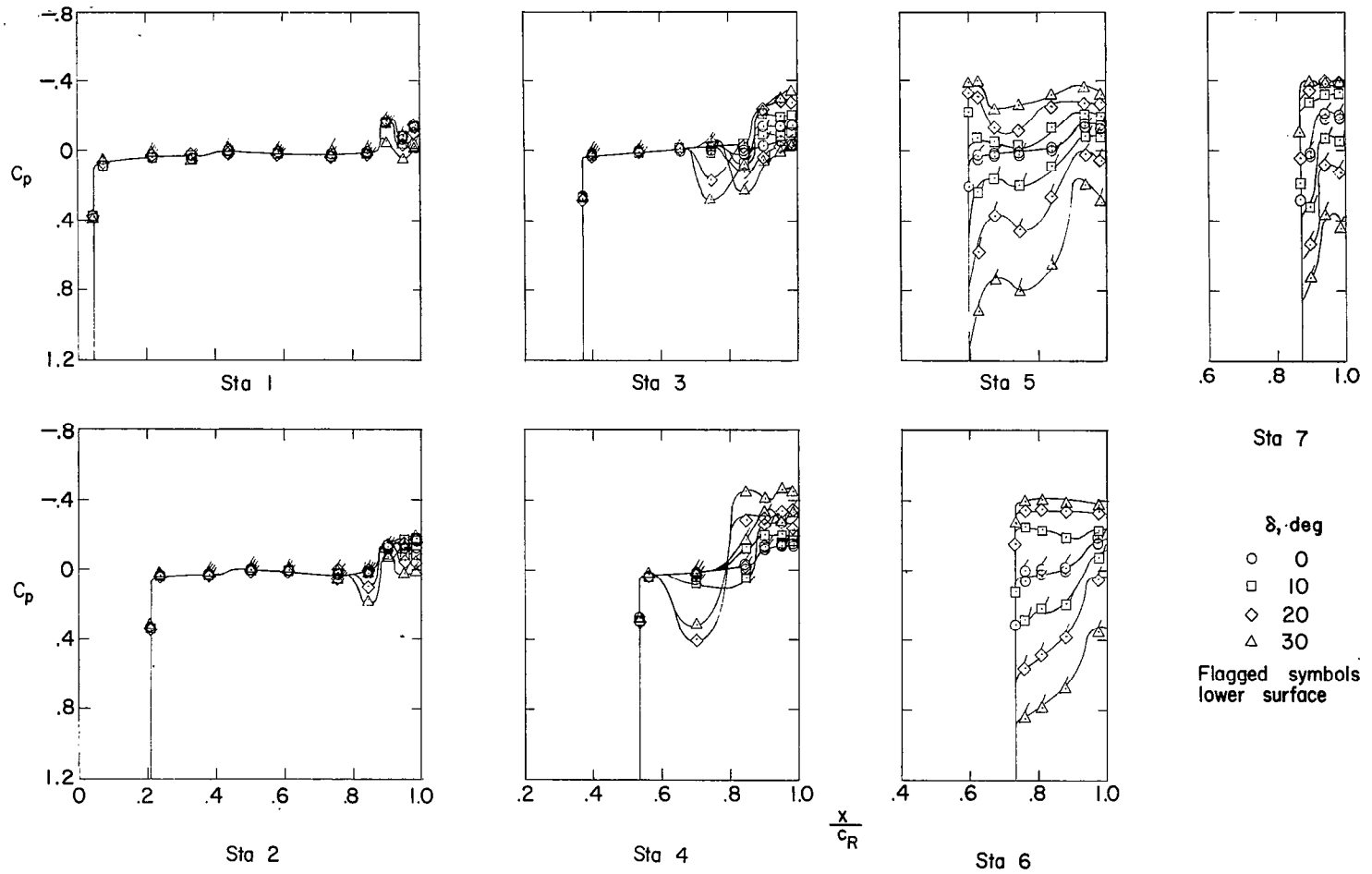

(a) $\alpha = 0^{\circ}$.

Figure 11.- Chordwise pressure distributions for configuration G. $M = 1.61$; $R = 4.2 \times 10^6$.

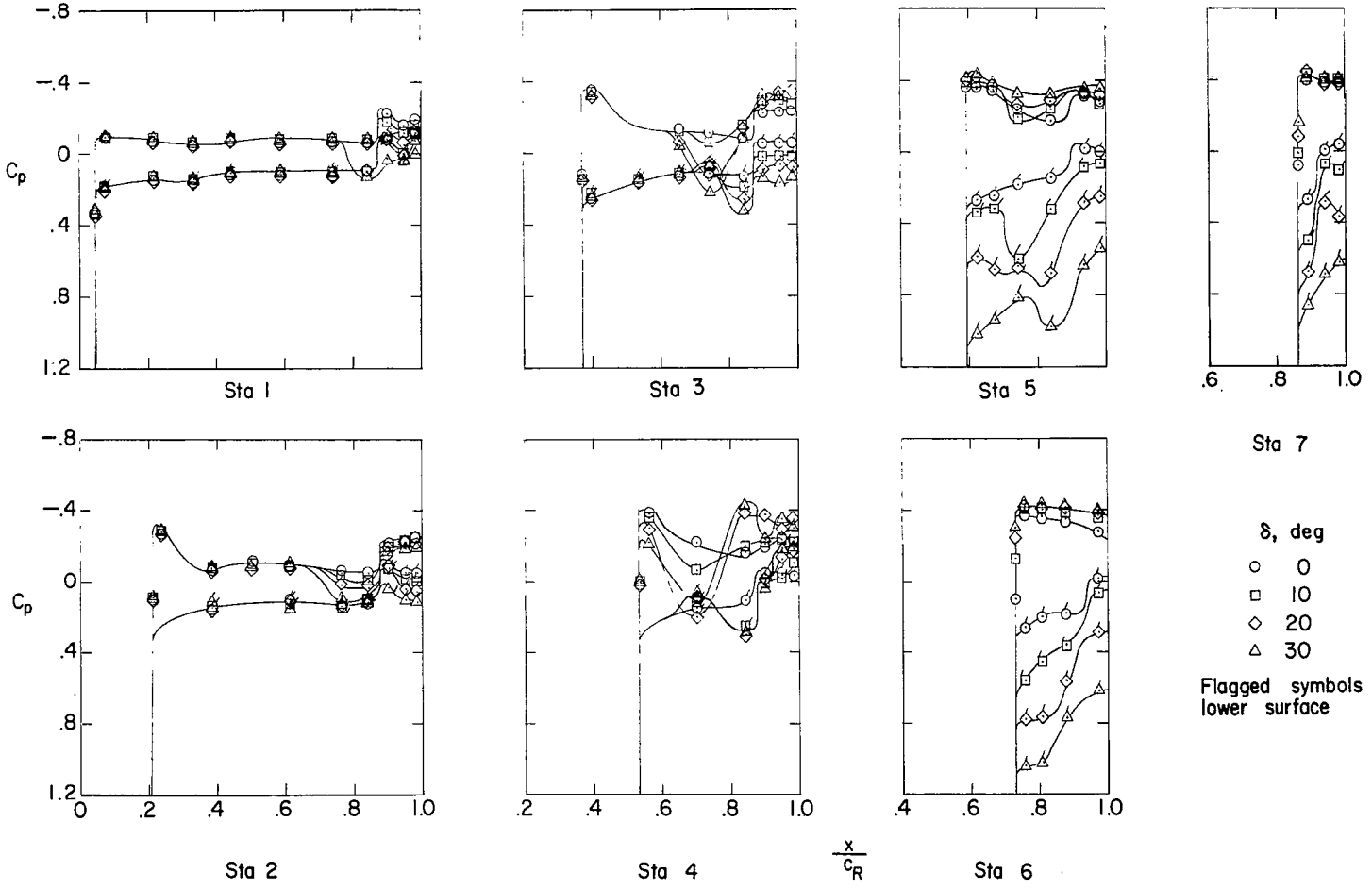

(b) $\alpha = 6^{\circ}$.

Figure 11.- Continued.

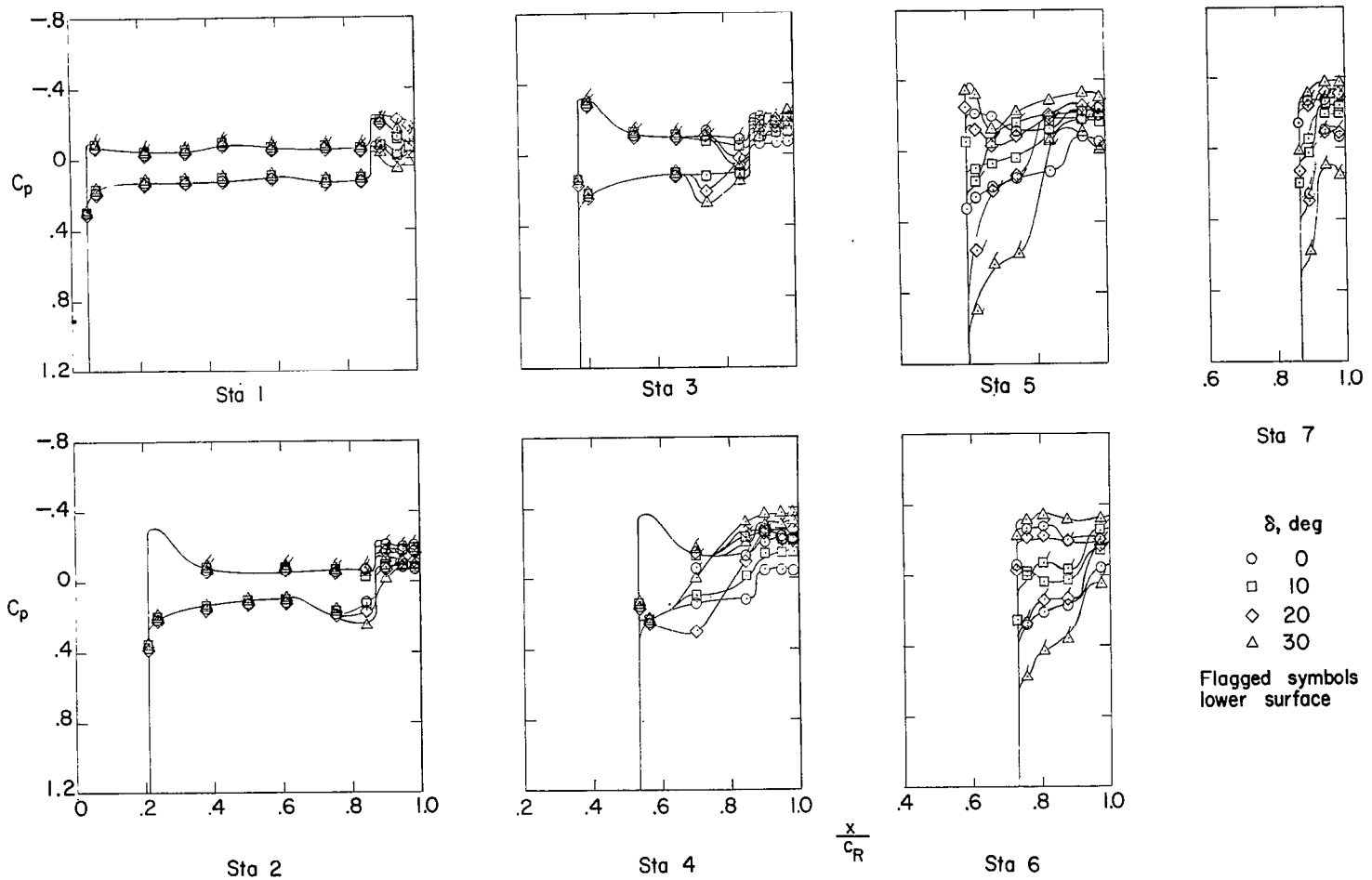

(c) $\alpha = -6^{\circ}$.

Figure 11.- Continued.

[redacted]

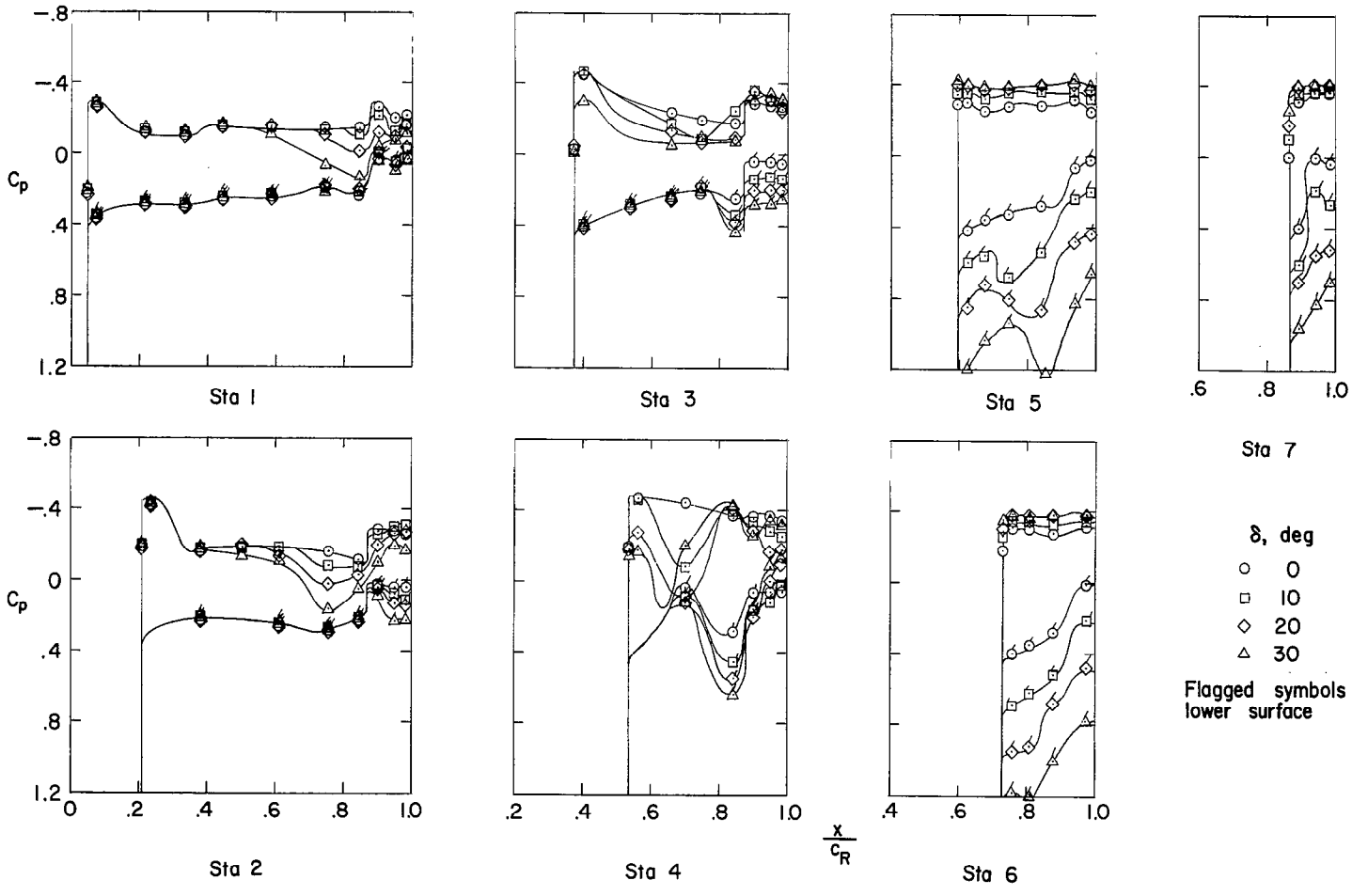

(d) $\alpha = 12^{\circ}$.

Figure 11.- Continued.

[redacted]

[redacted]

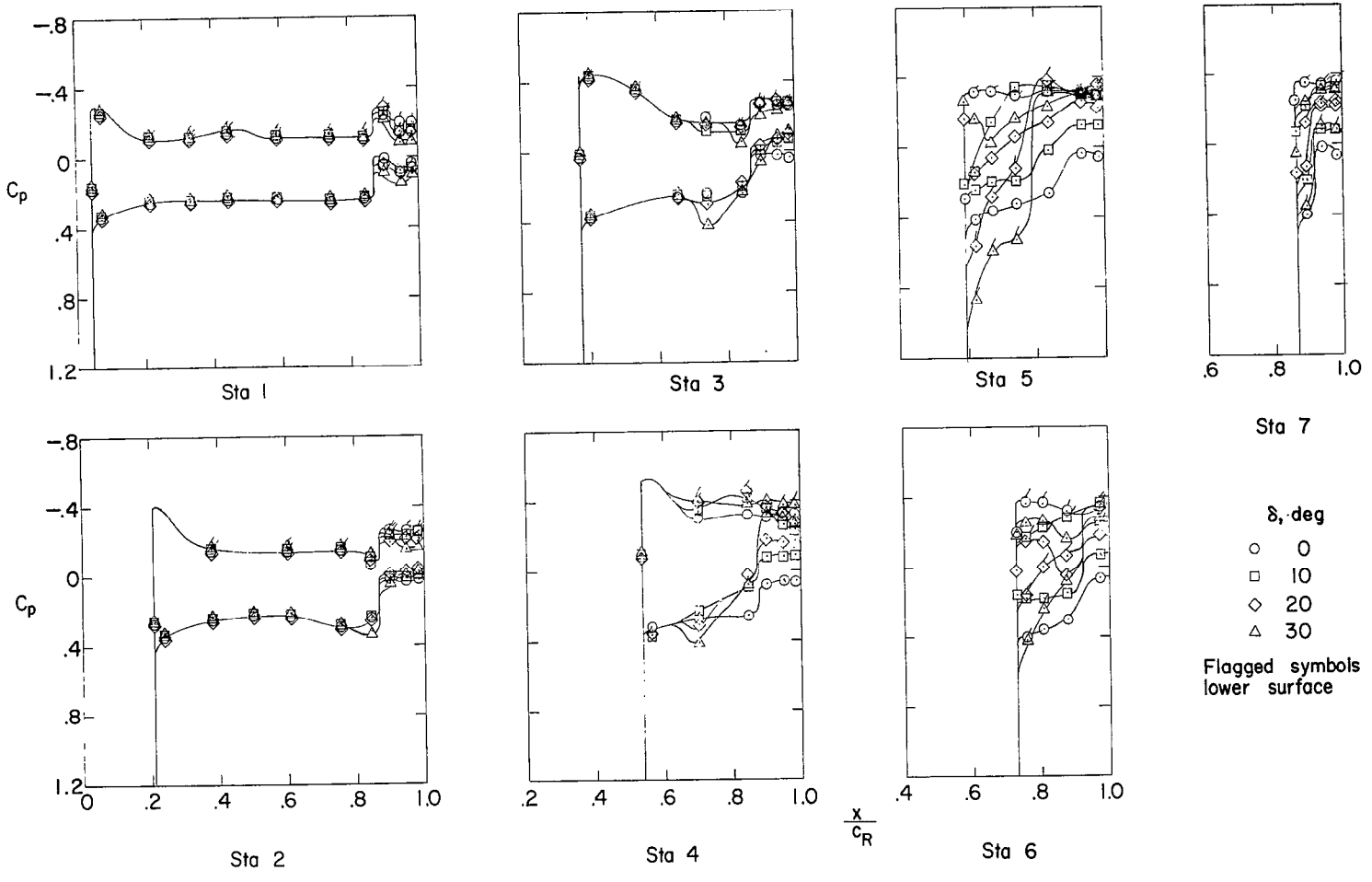

(e) $\alpha = -12^{\circ}$.

Figure 11.- Concluded.

[redacted]

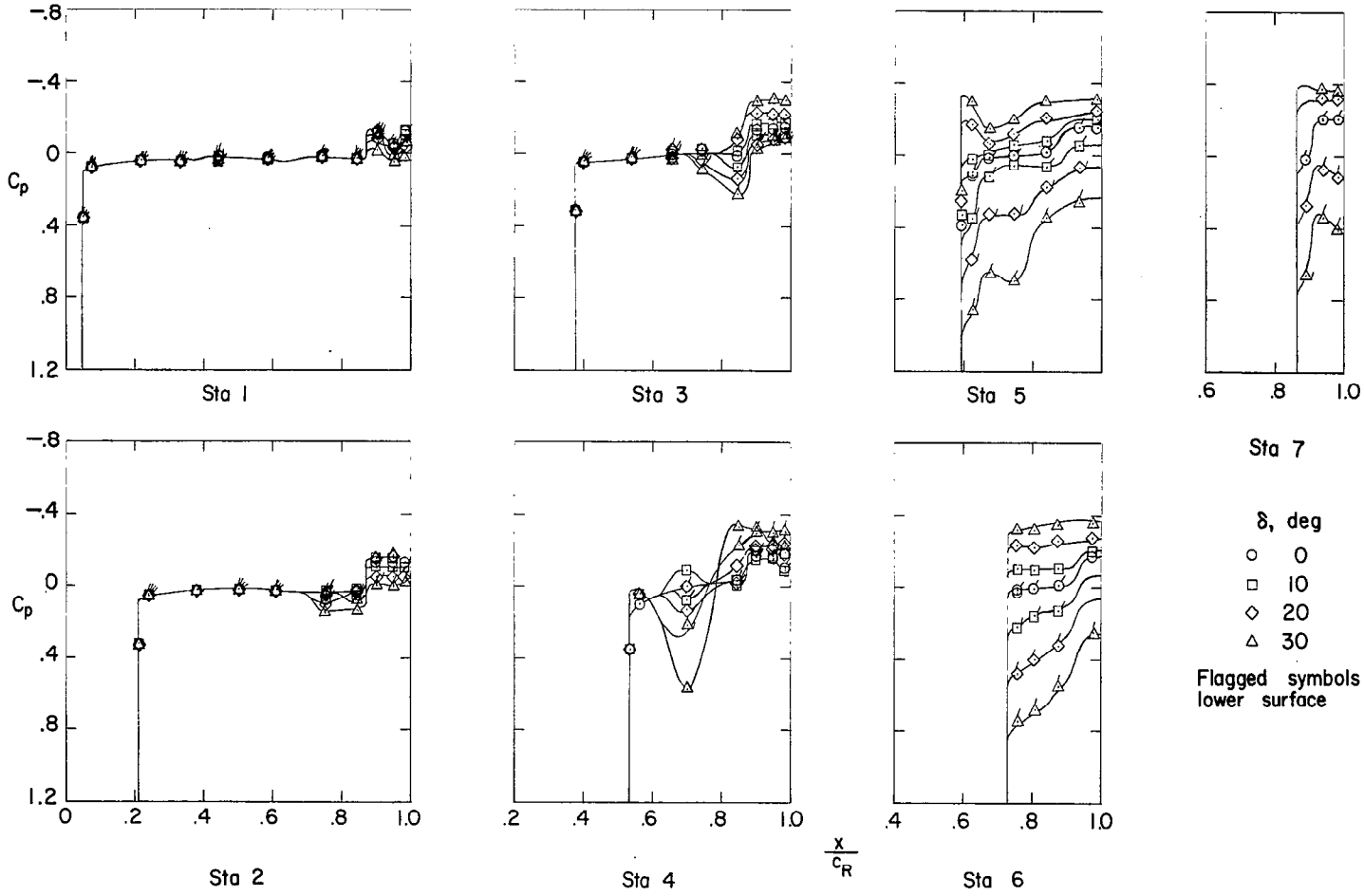

(a) $\alpha = 0^{\circ}$.

Figure 12.- Chordwise pressure distributions for configuration H. $M = 1.61$; $R = 4.2 \times 10^{6}$.

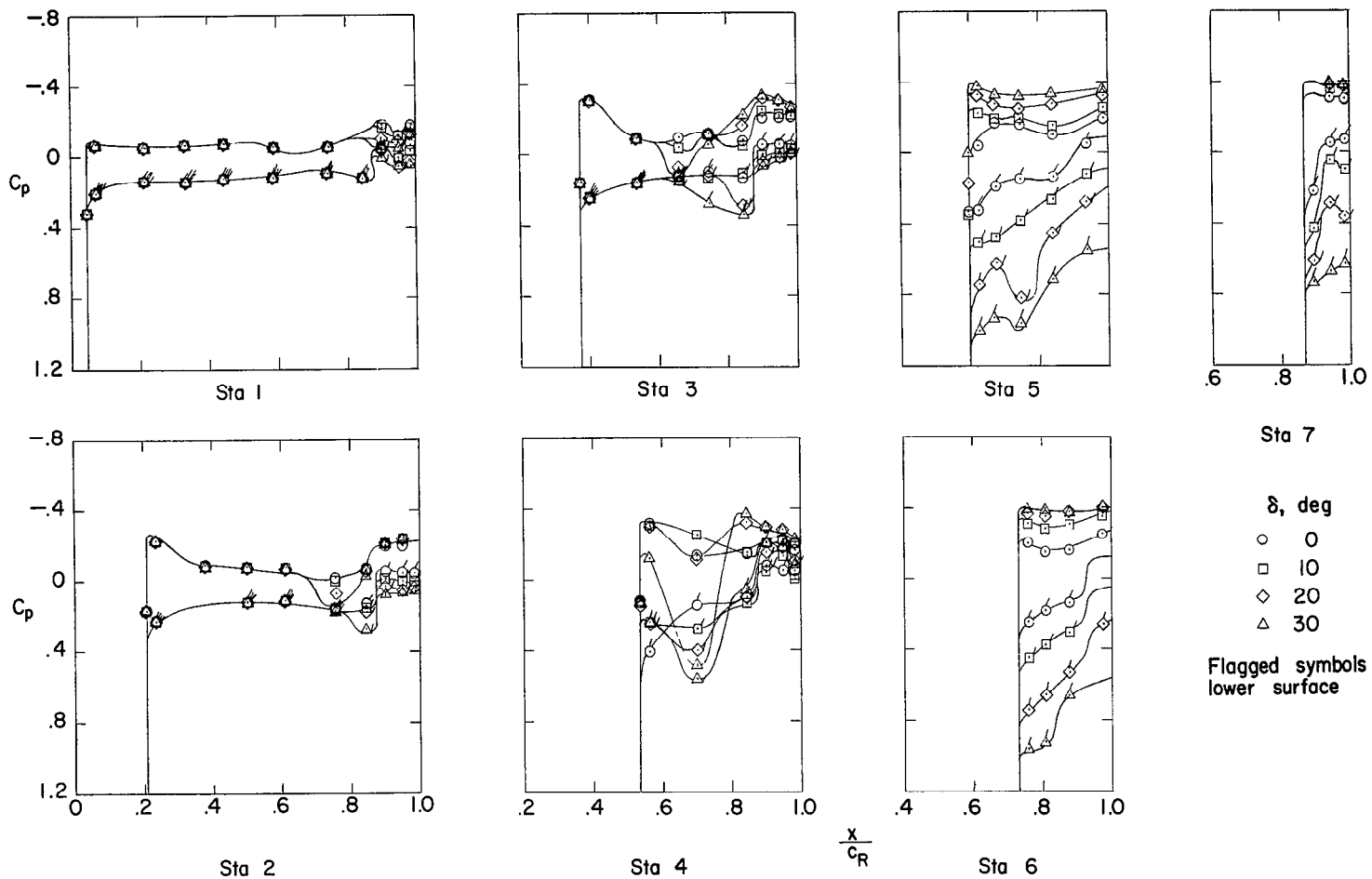

(b) $\alpha = 6^{\circ}$.

Figure 12.- Continued.

CO[redacted]

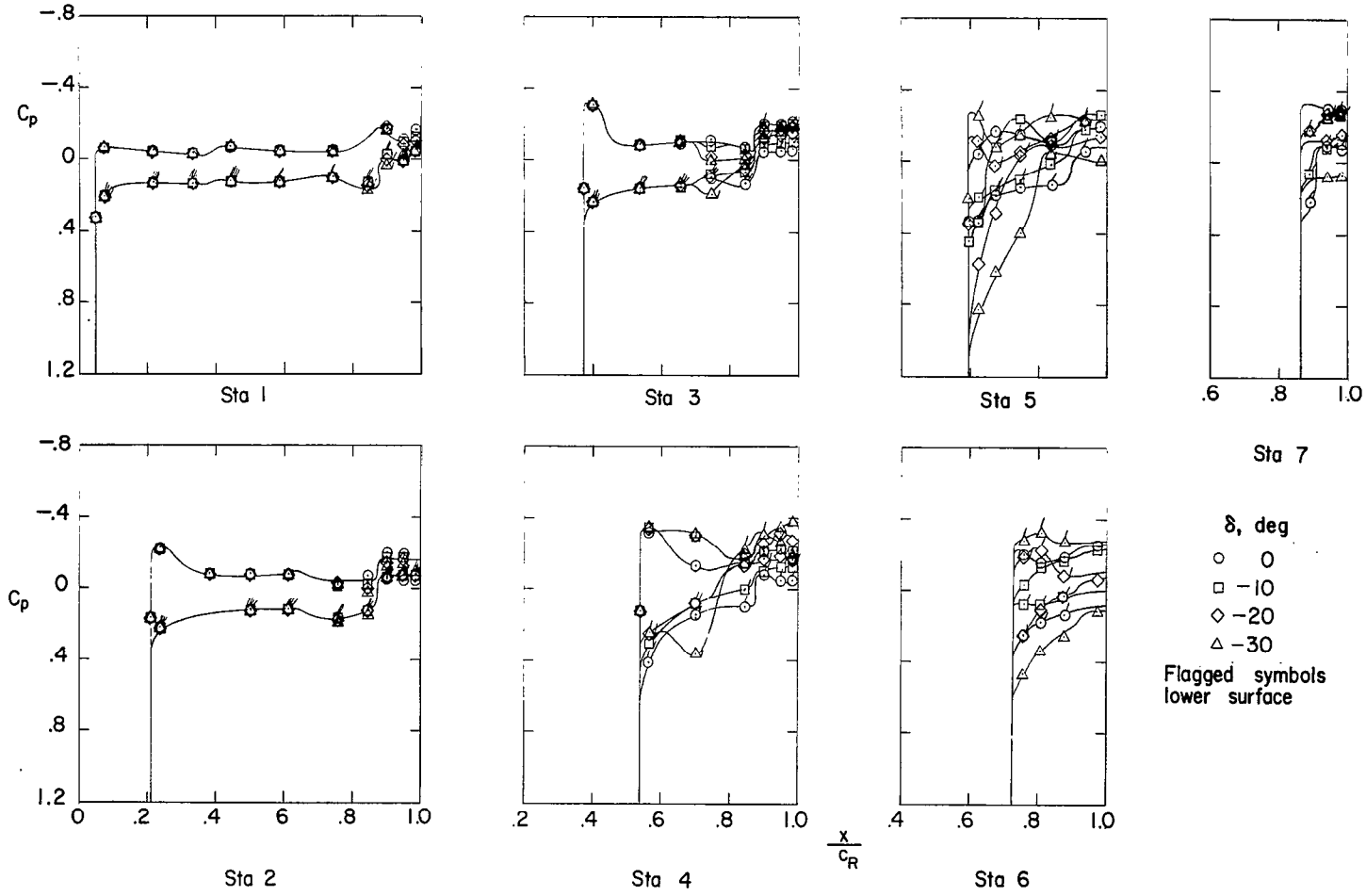

(c) $\alpha = 6^{\circ}$.

Figure 12.- Continued.

[redacted]

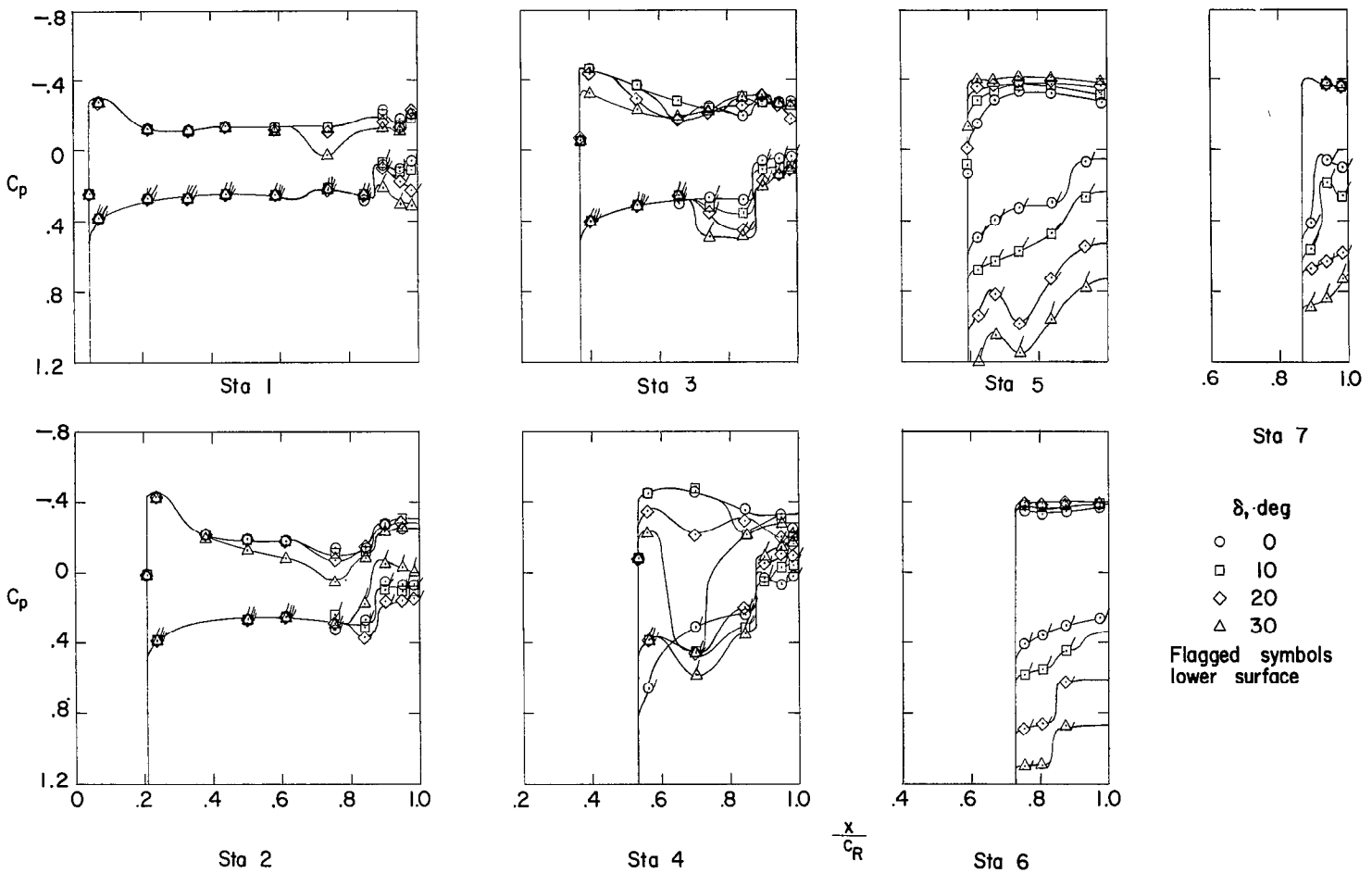

(d) $\alpha = 12^{\circ}$.

Figure 12.- Continued.

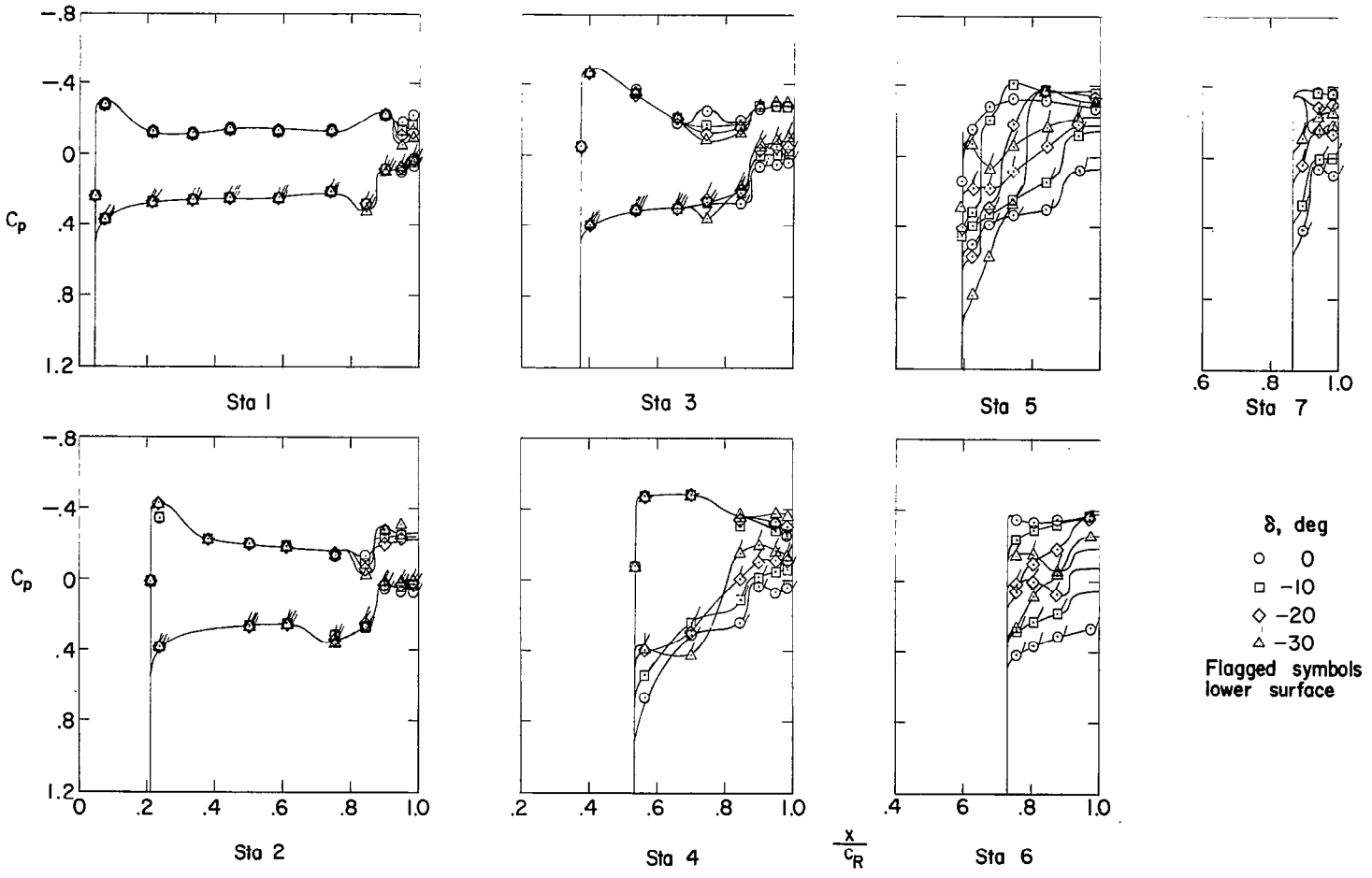

(e) $\alpha = 12^{\circ}$.

Figure 12.- Concluded.

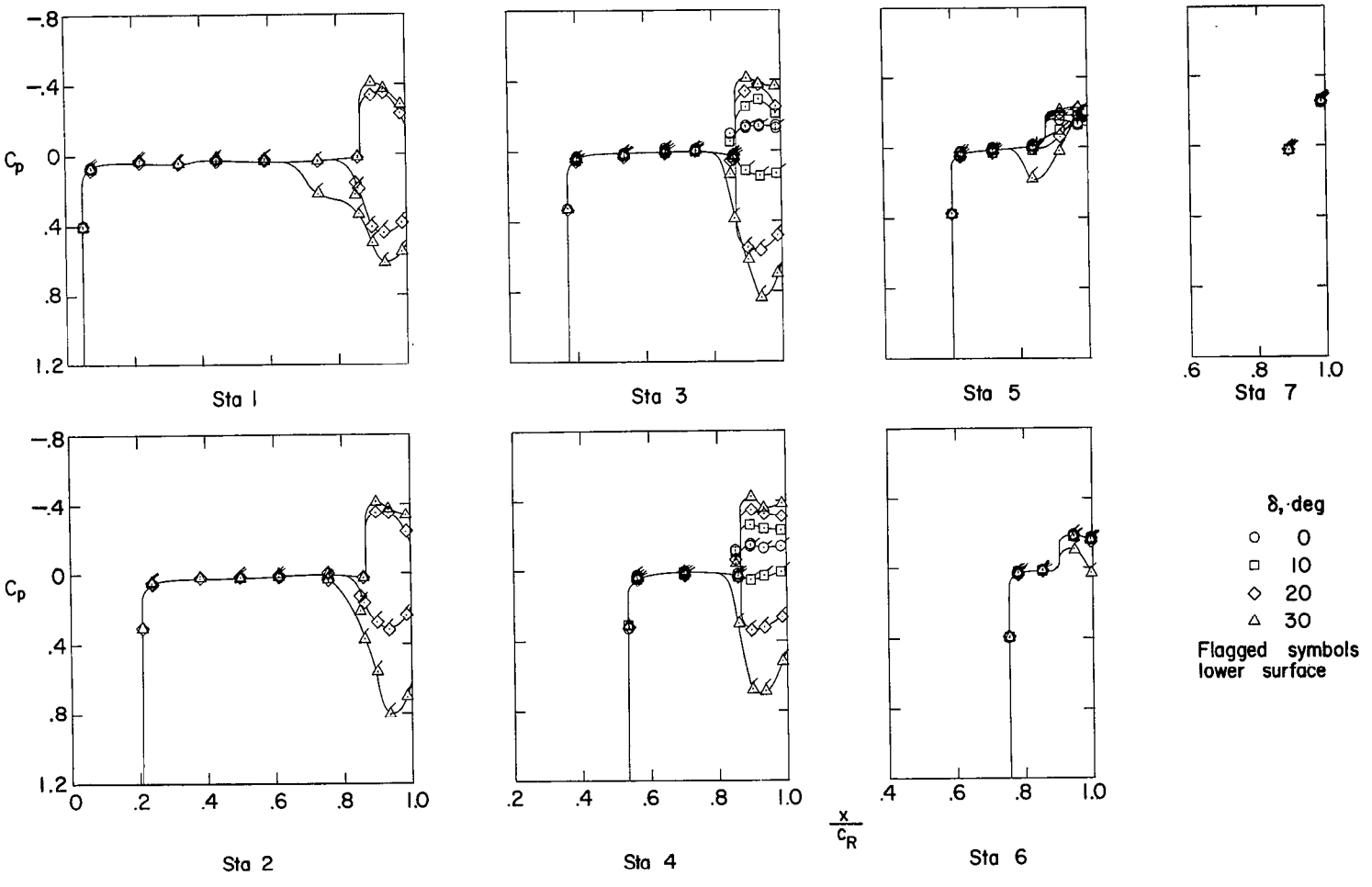

(a) $\alpha = 0^{\circ}$.

Figure 13.- Chordwise pressure distributions for configuration I. $M = 1.61$; $R = 4.2 \times 10^6$.

[redacted]

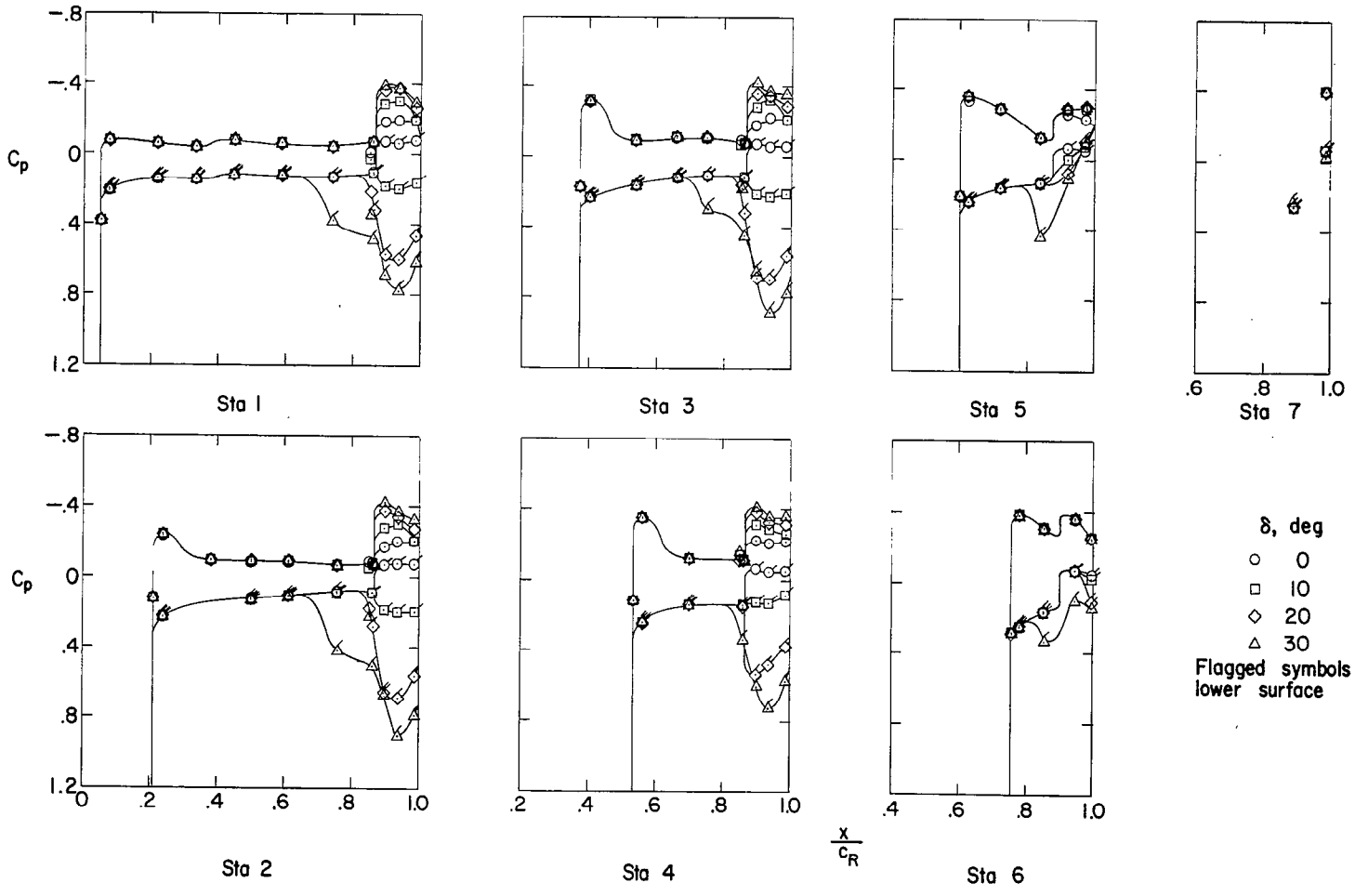

(b) $\alpha = 6^{\circ}$.

Figure 13.- Continued.

[redacted]

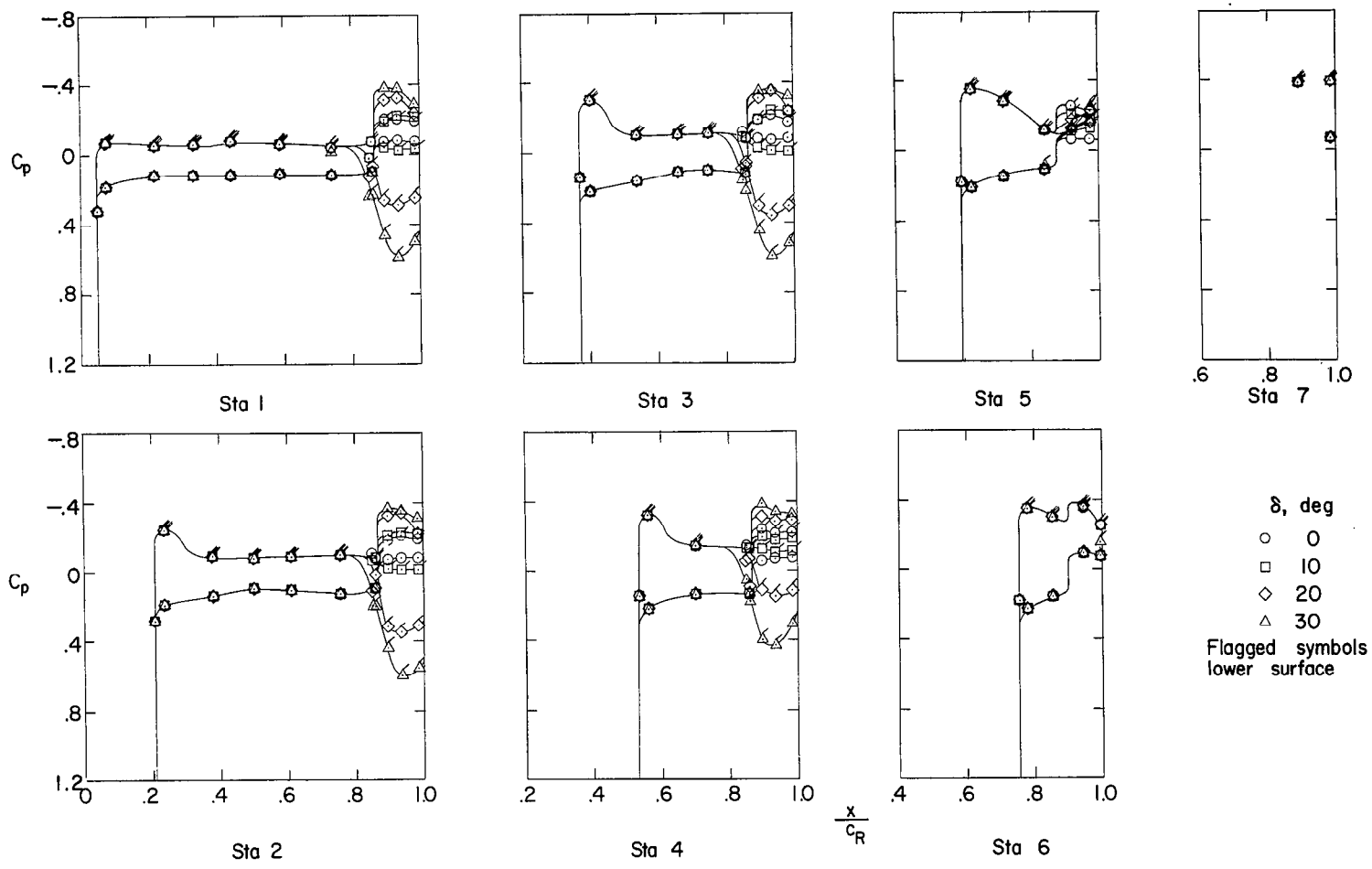

(c) $\alpha = -6^{\circ}$.

Figure 13.- Continued.

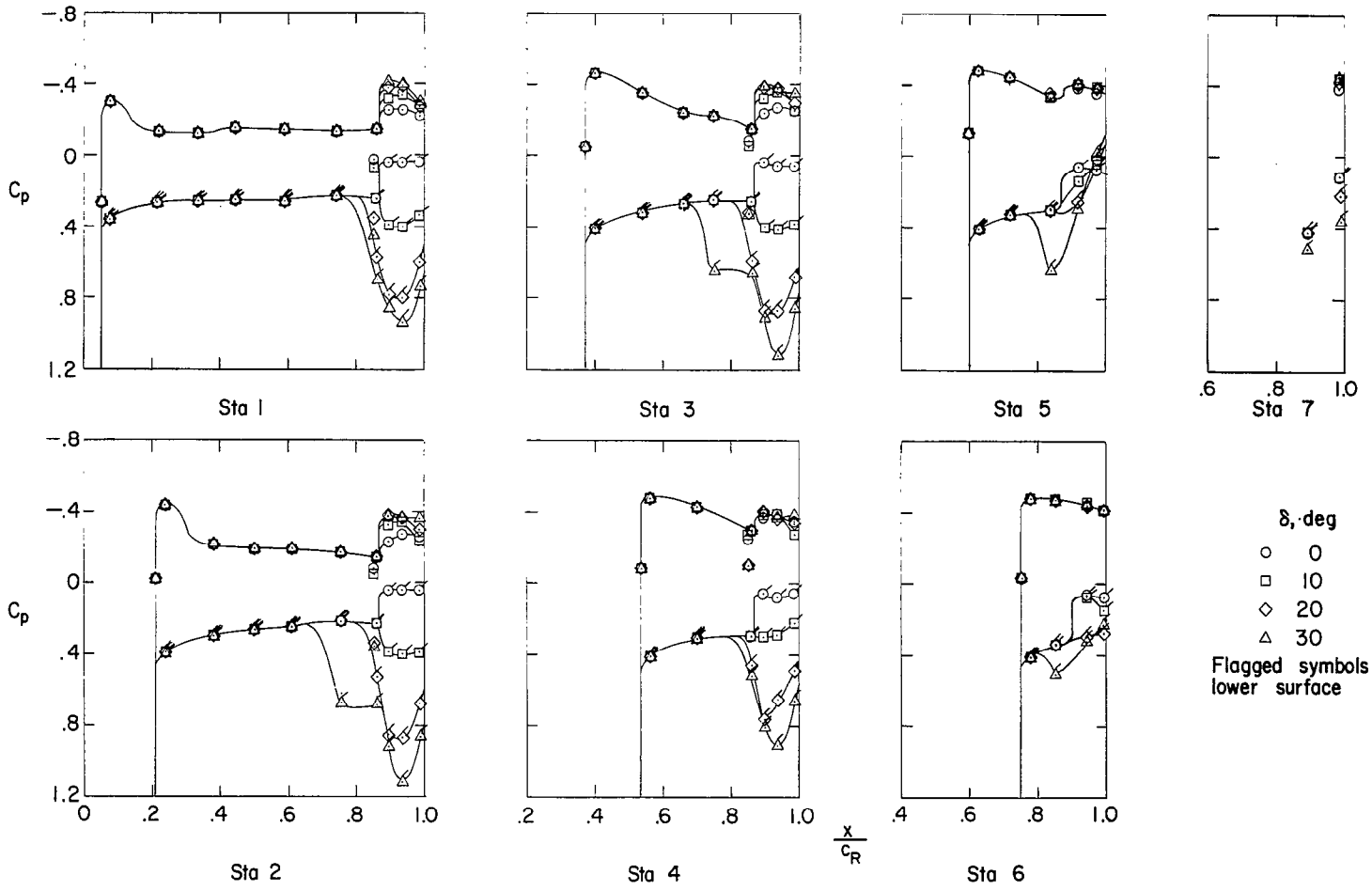

(d) $\alpha = 12^{\circ}$.

Figure 13.- Continued.

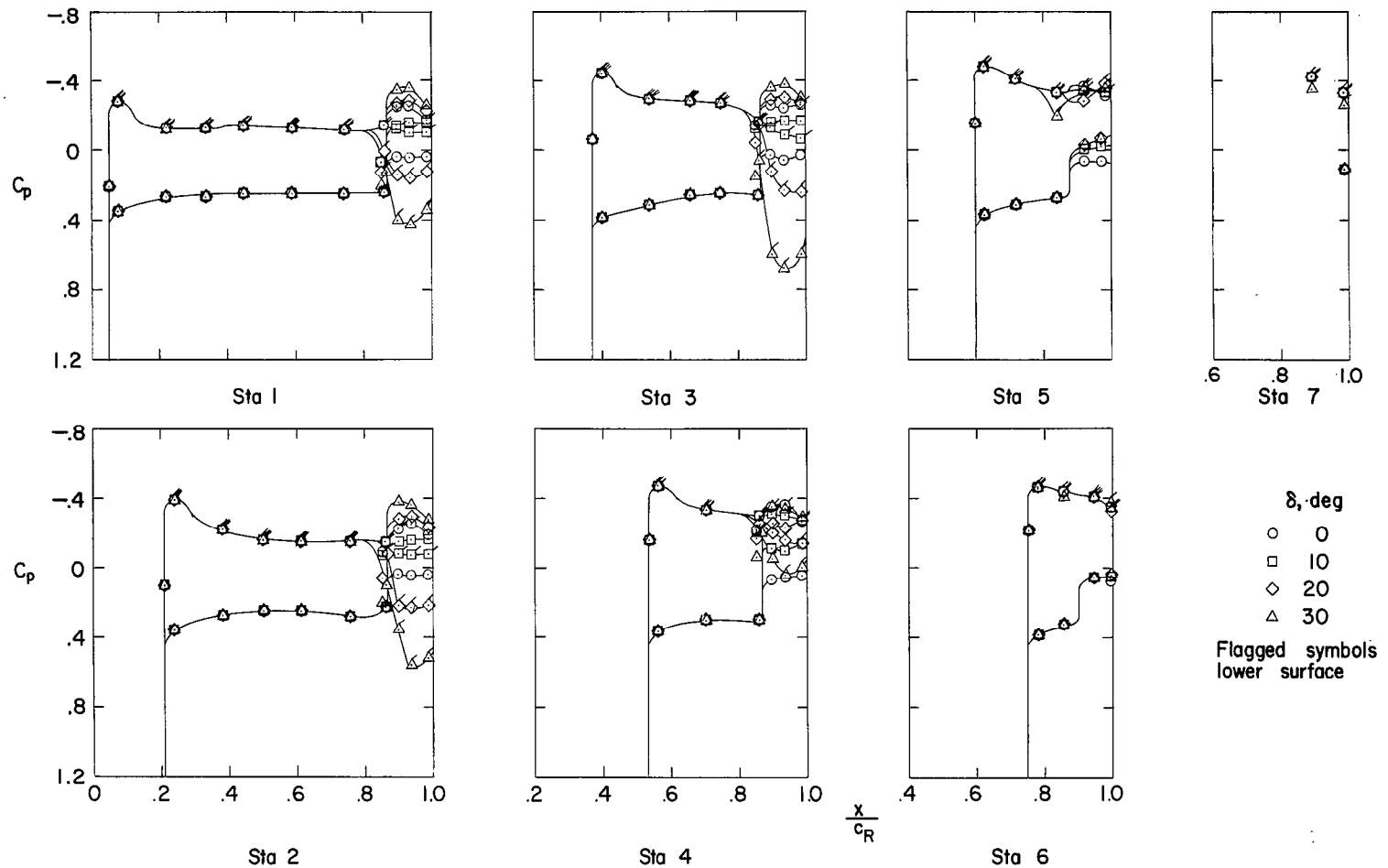

(e) $\alpha = -12^{\circ}$.

Figure 13.- Concluded.

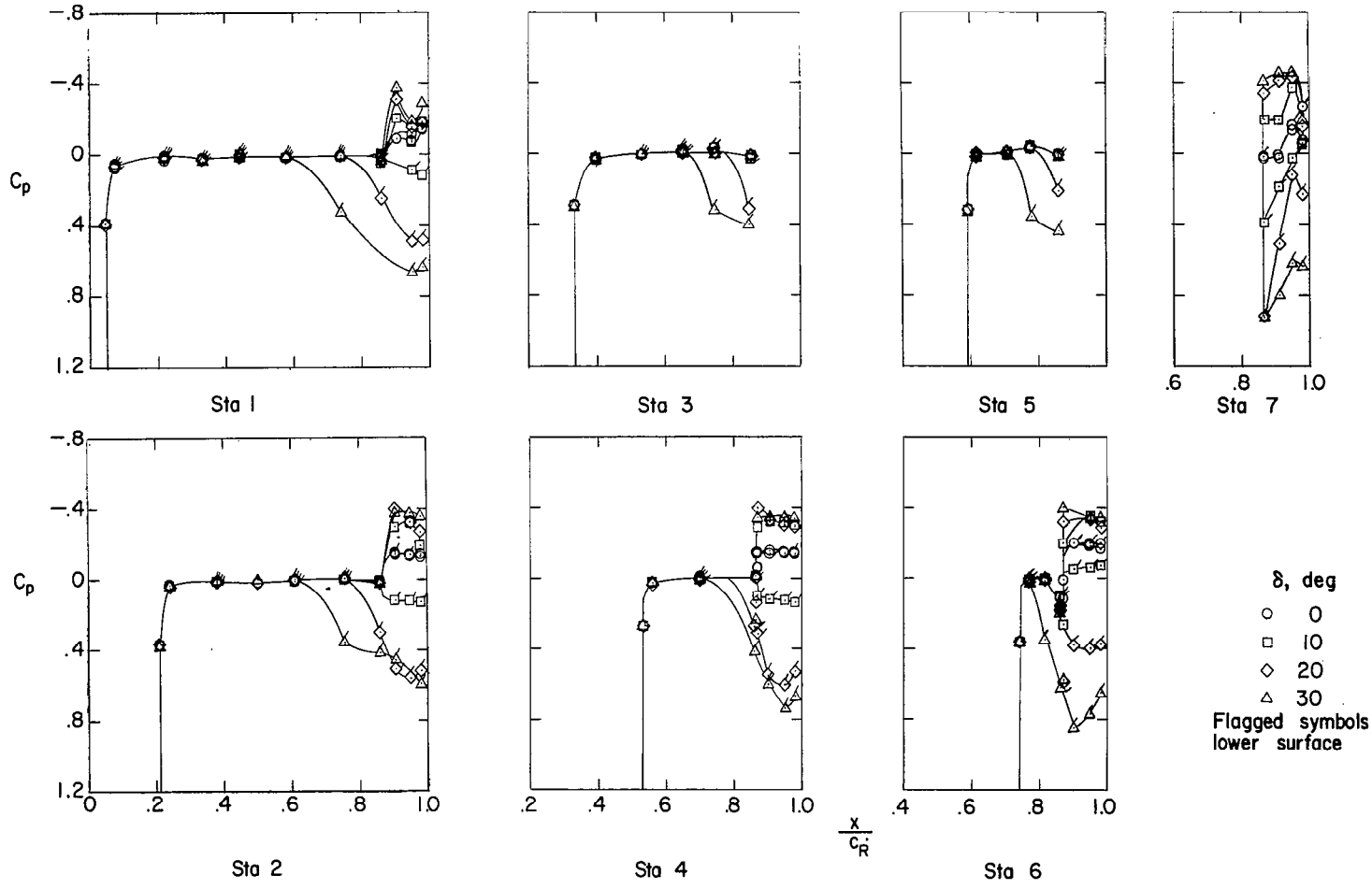

(a) $\alpha = 0^{\circ}$.

Figure 14.- Chordwise pressure distributions for configuration J. $M = 1.61$; $R = 4.2 \times 10^6$.

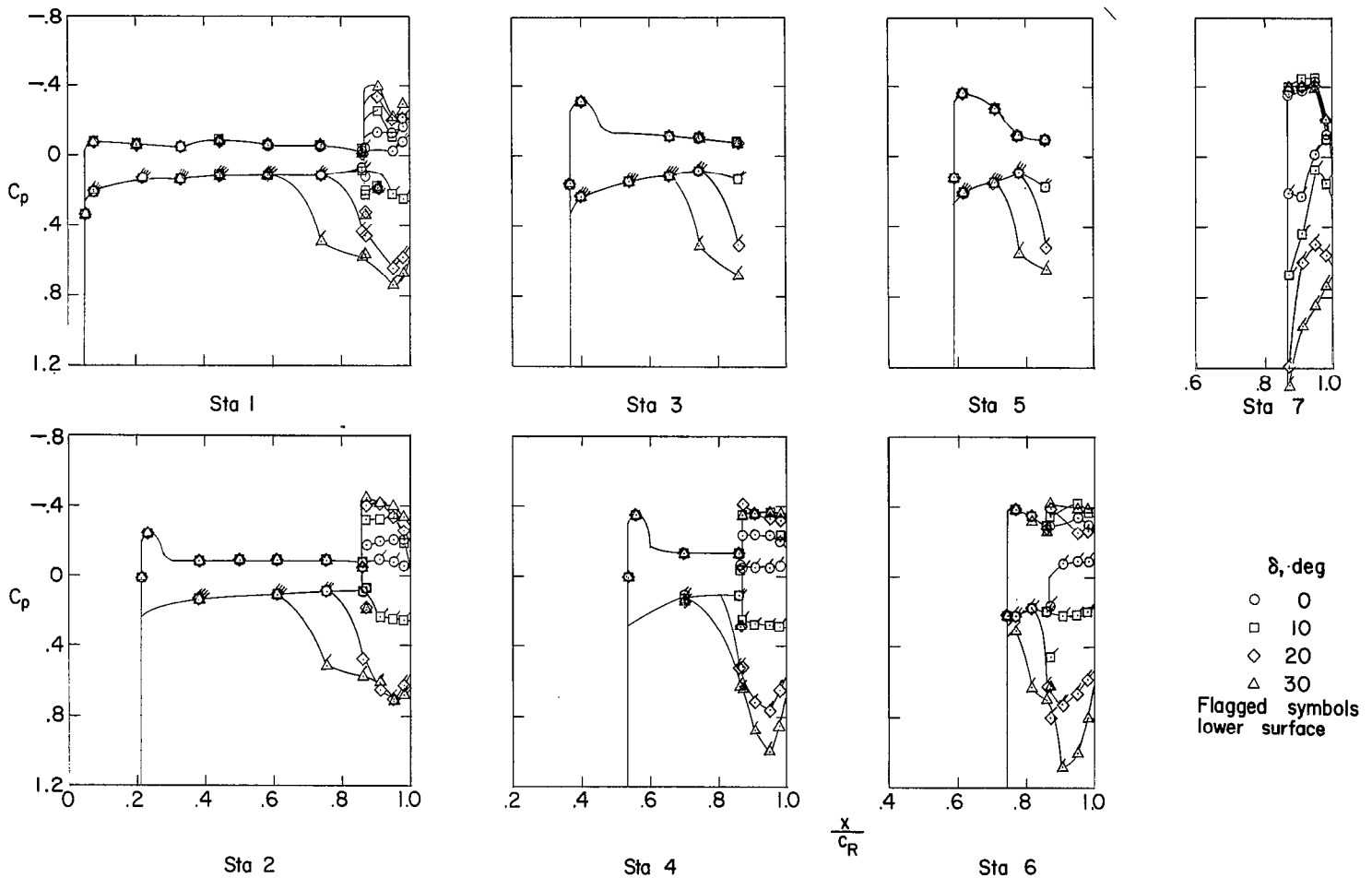

(b) $\alpha = 6^{\circ}$.

Figure 14.- Continued.

[redacted]

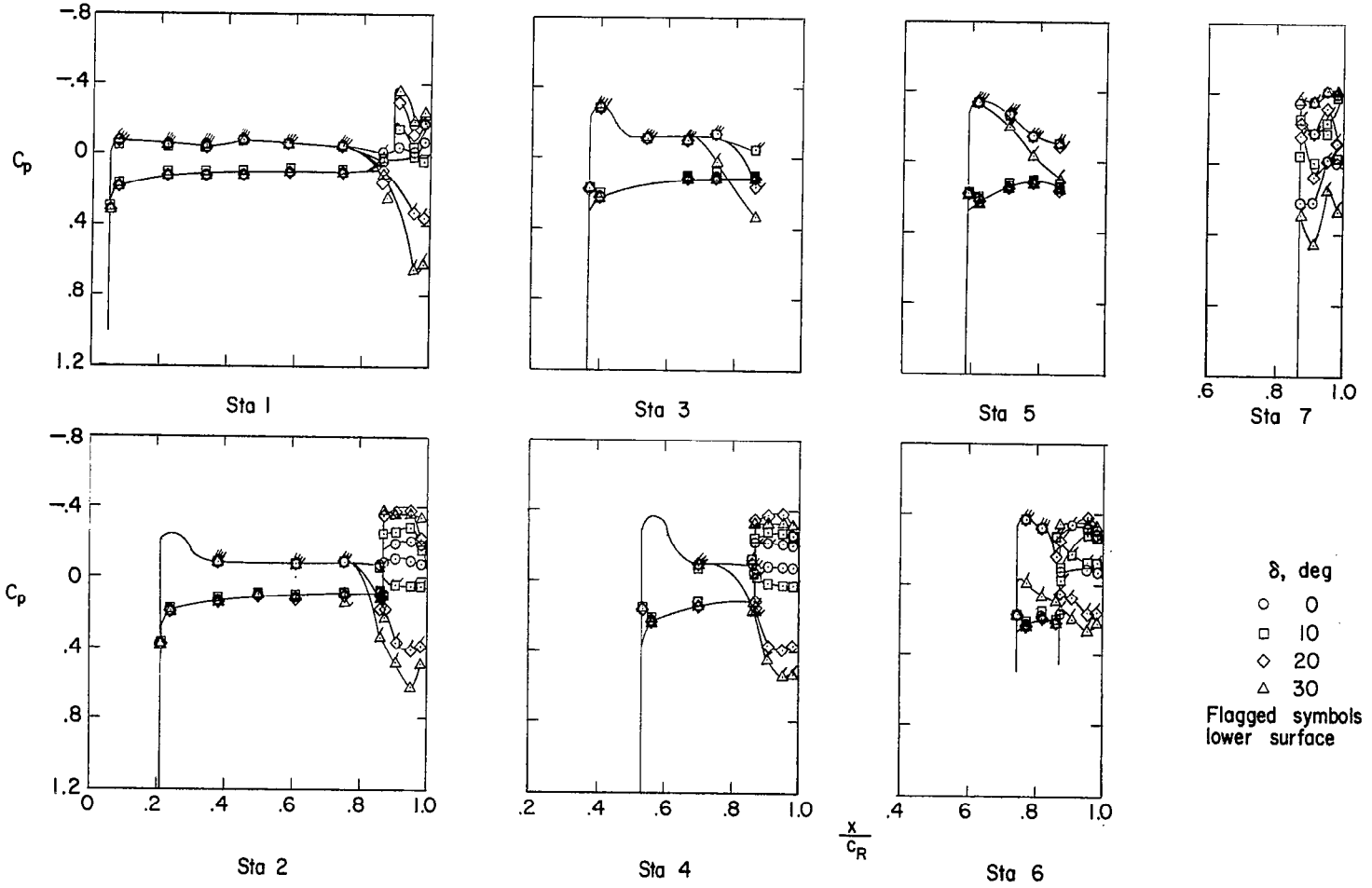

(c) $\alpha = -6^{\circ}$.

Figure 14.- Continued.

[redacted]

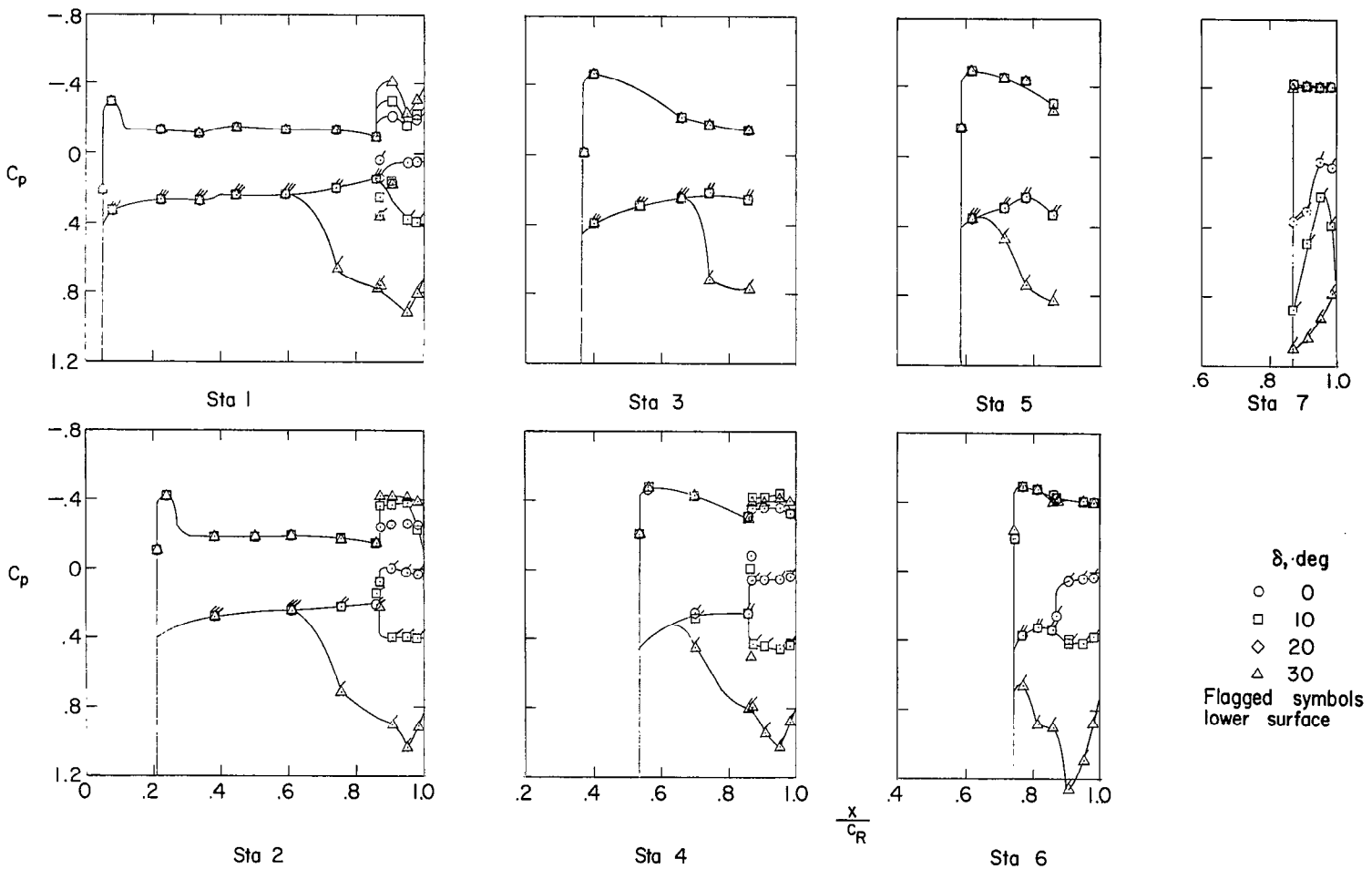

(d) $\alpha = 12^{\circ}$.

Figure 14.- Continued.

[redacted]

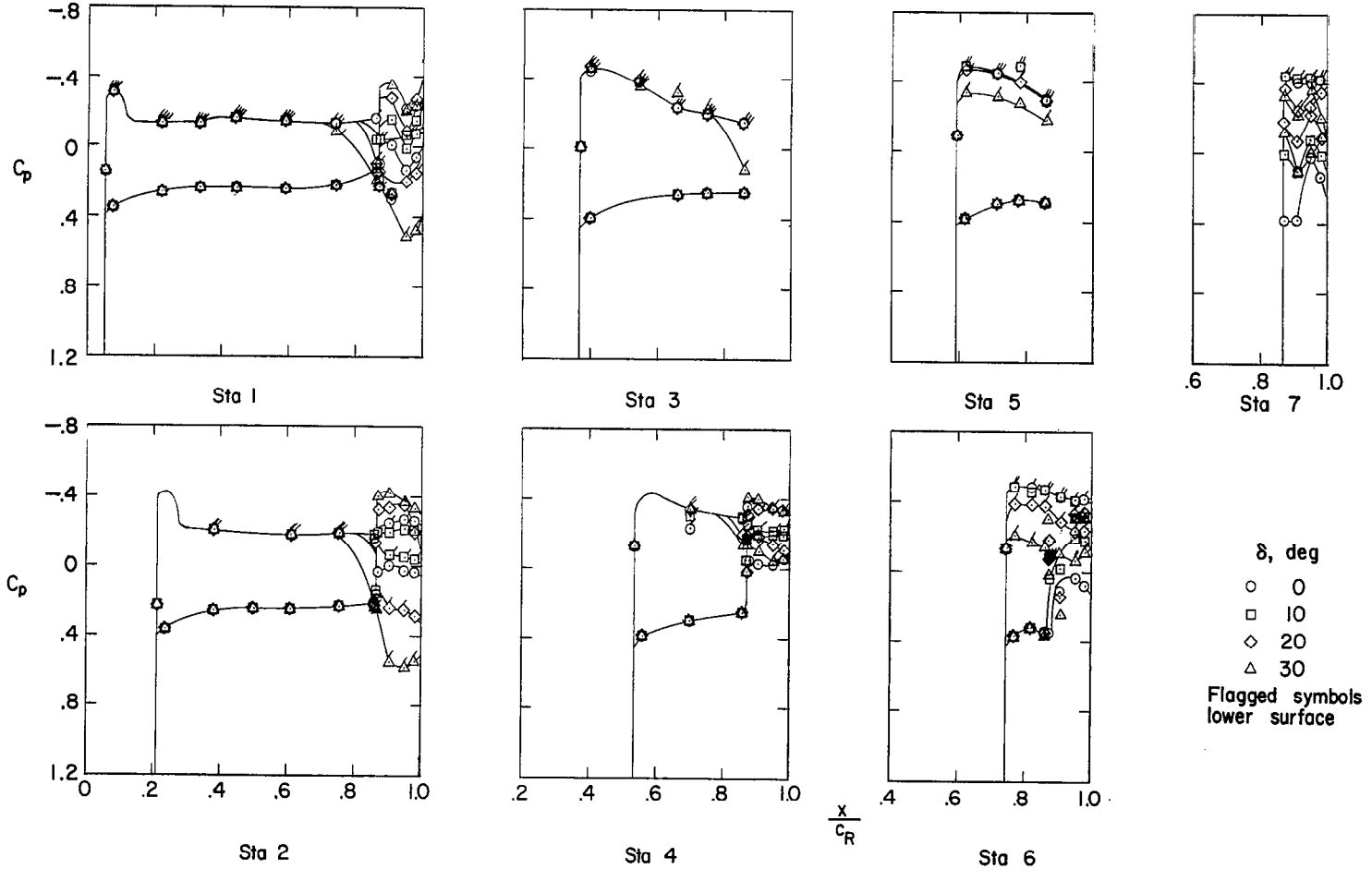

(e) $\alpha = -12^{\circ}$.

Figure 14.- Concluded.

[redacted]

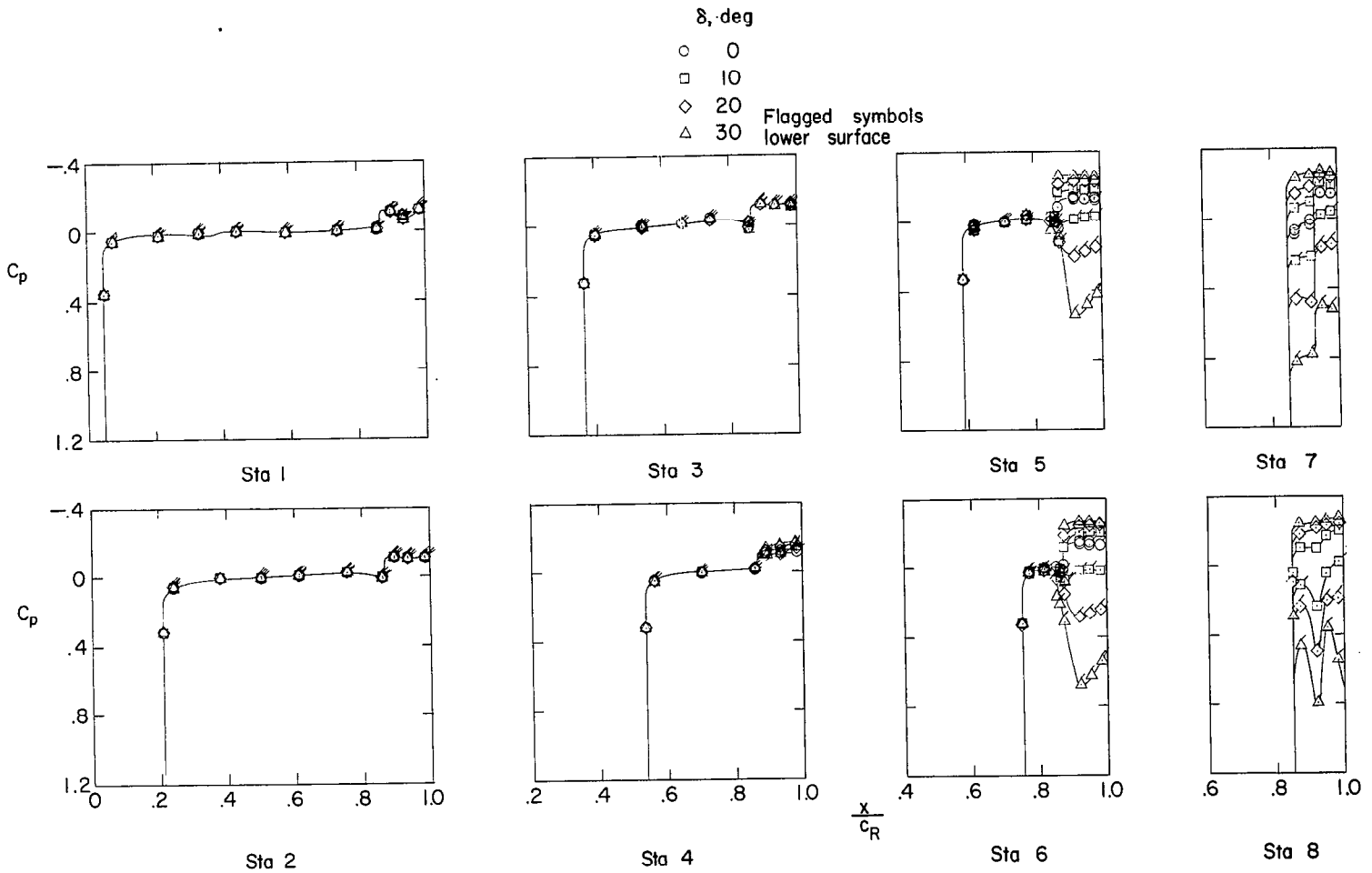

(a) $\alpha = 0^{\circ}$.

Figure 15.- Chordwise pressure distributions for configuration A. $M = 2.01$; $R = 4.2 \times 10^6$.

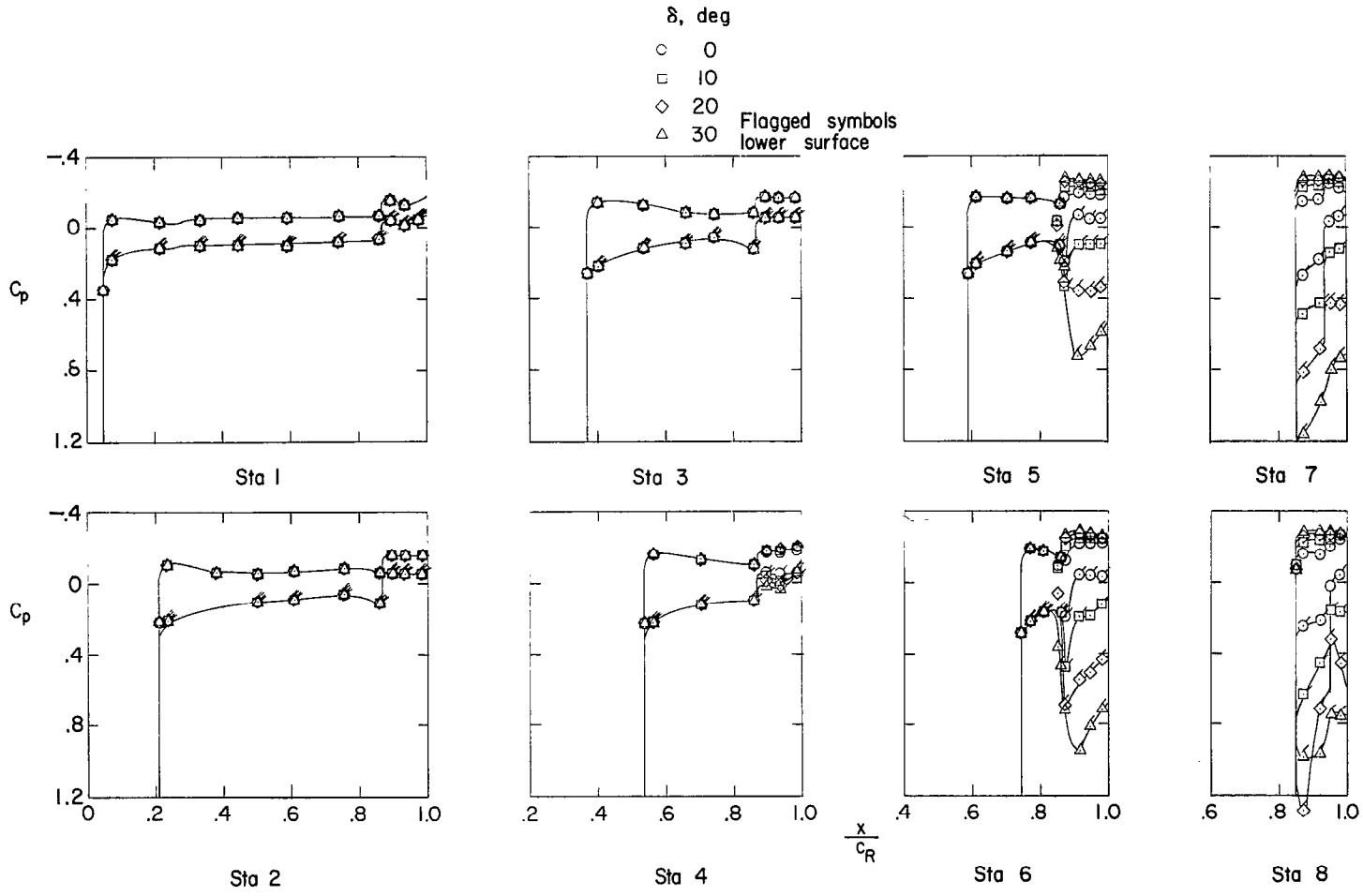

(b) $\alpha = 6^{\circ}$.

Figure 15.- Continued.

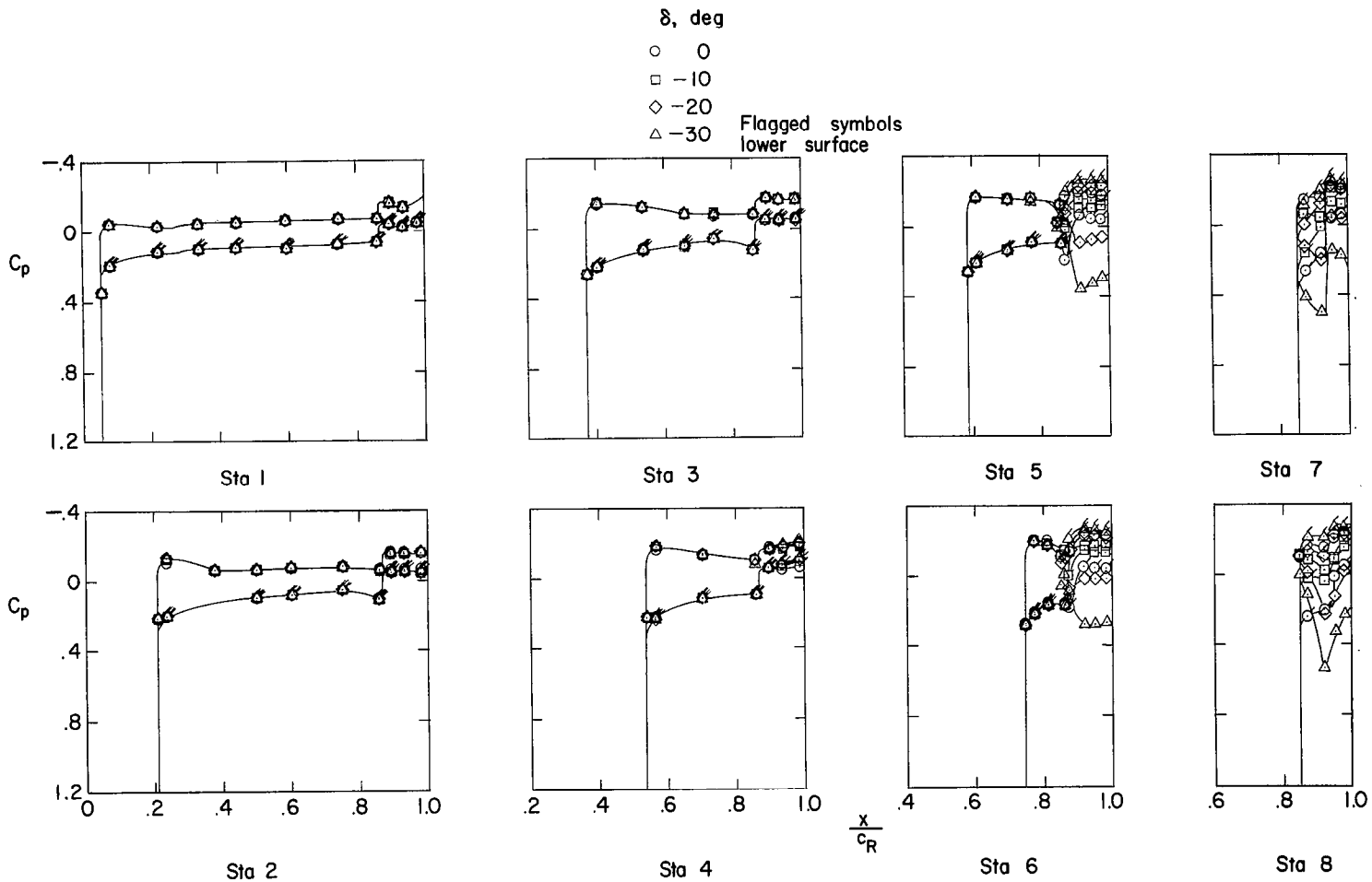

(c) $\alpha = 6^{\circ}$.

Figure 15.- Continued.

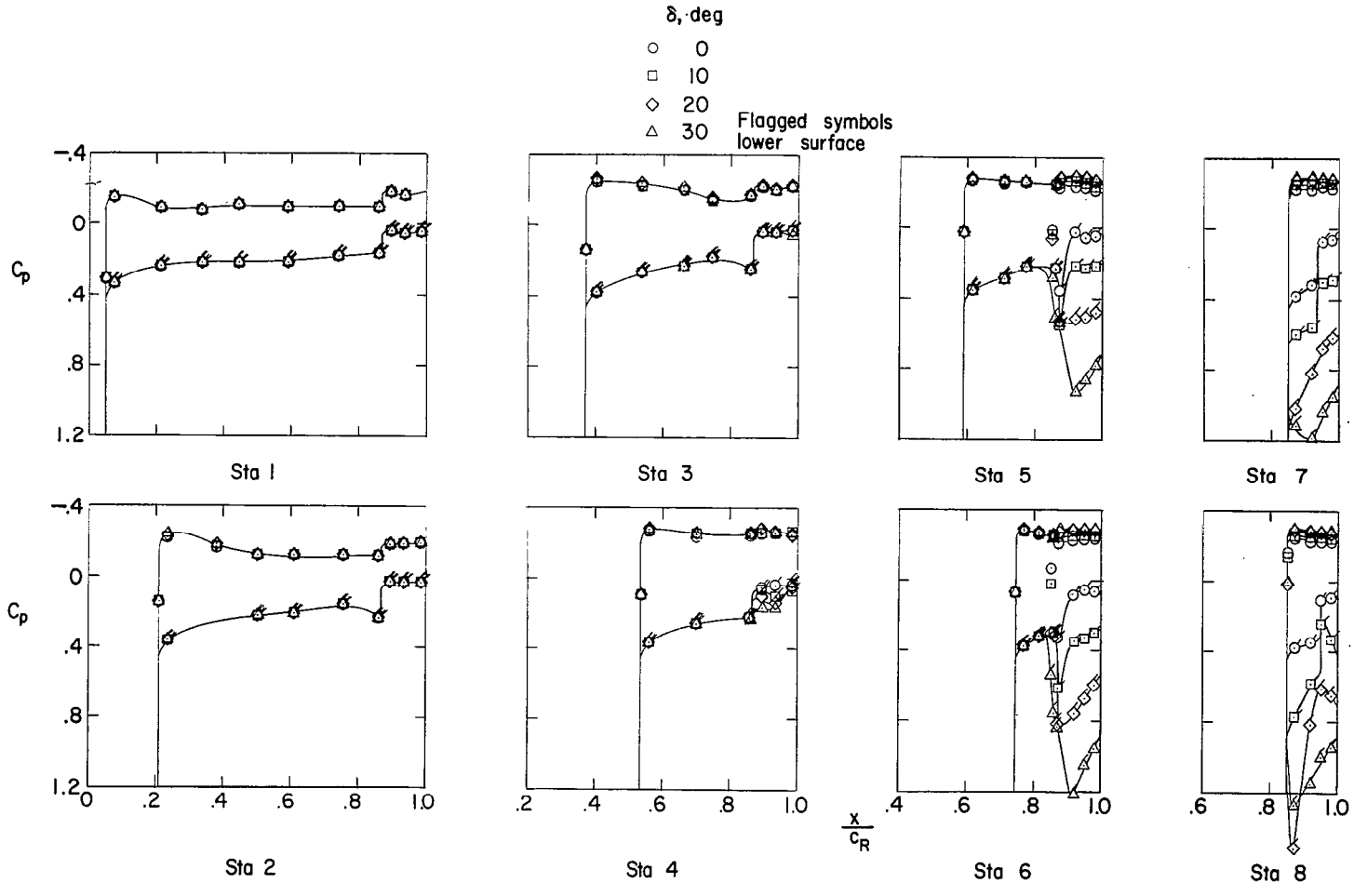

(d) $\alpha = 12^{\circ}$.

Figure 15.- Continued.

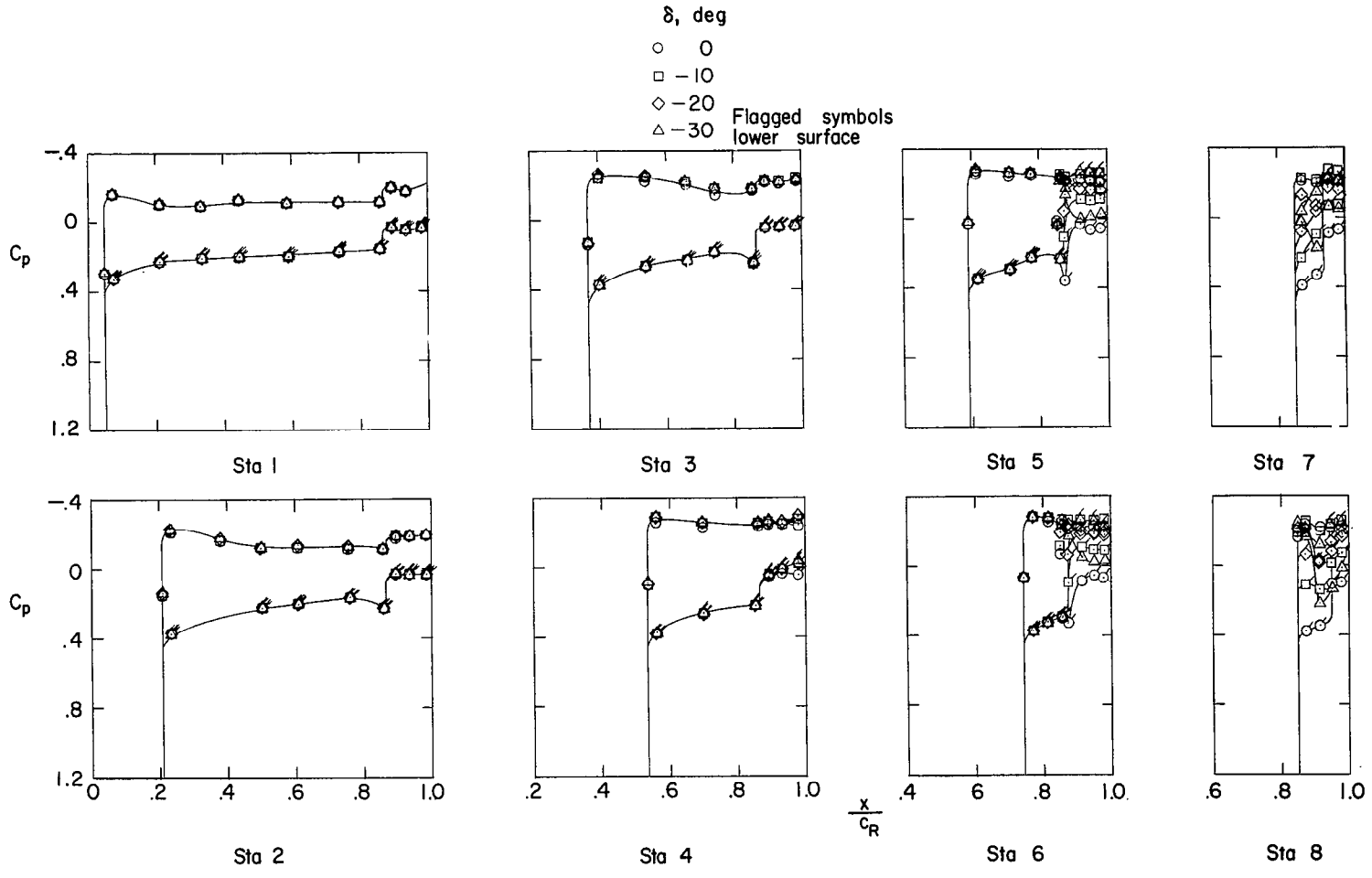

(e) $\alpha = 12^{\circ}$.

Figure 15.- Concluded.

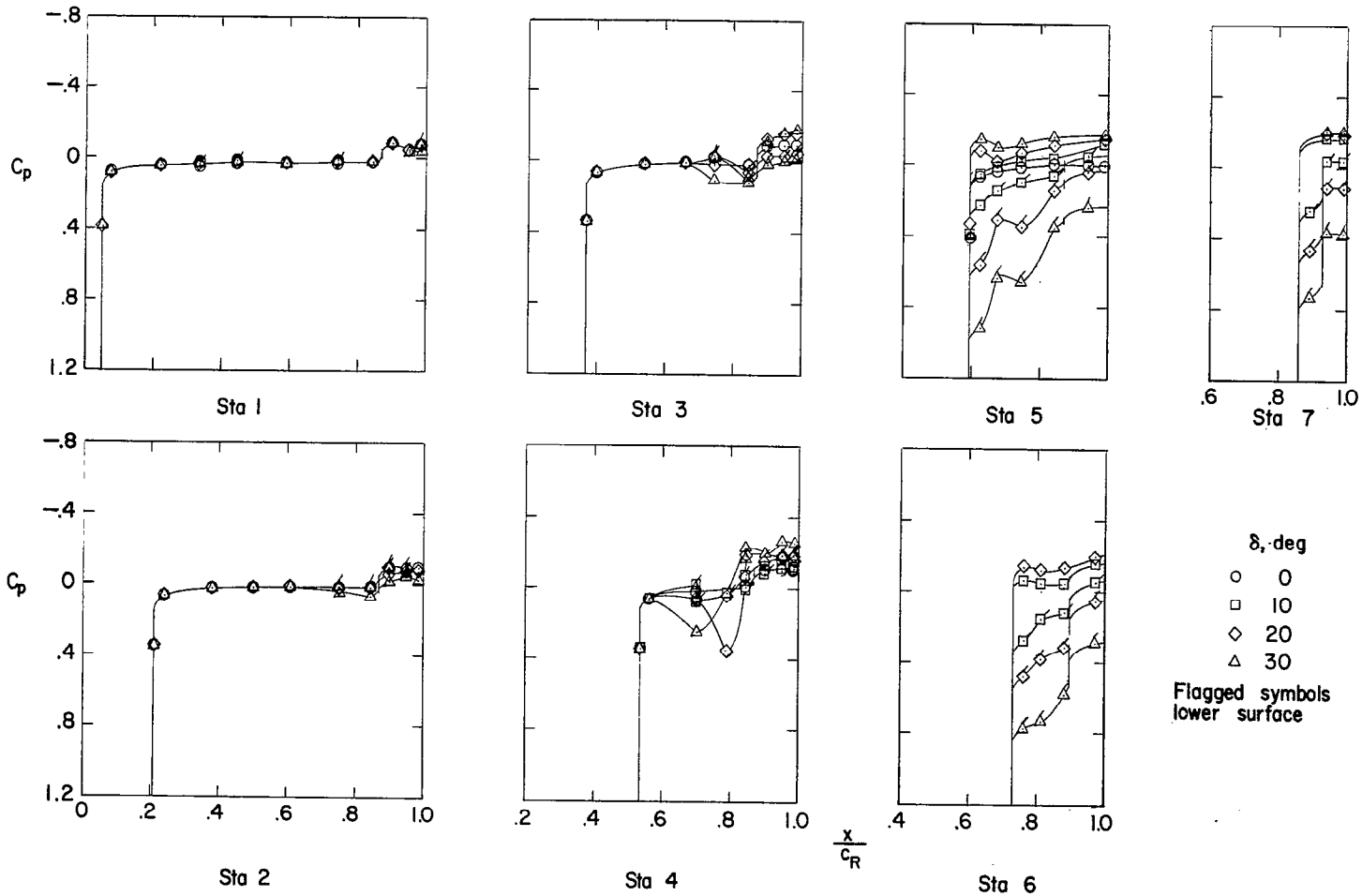

(a) $\alpha = 0^{\circ}$.

Figure 16.- Chordwise pressure distributions for configuration F. $M = 2.01$; $R = 4.2 \times 10^6$.

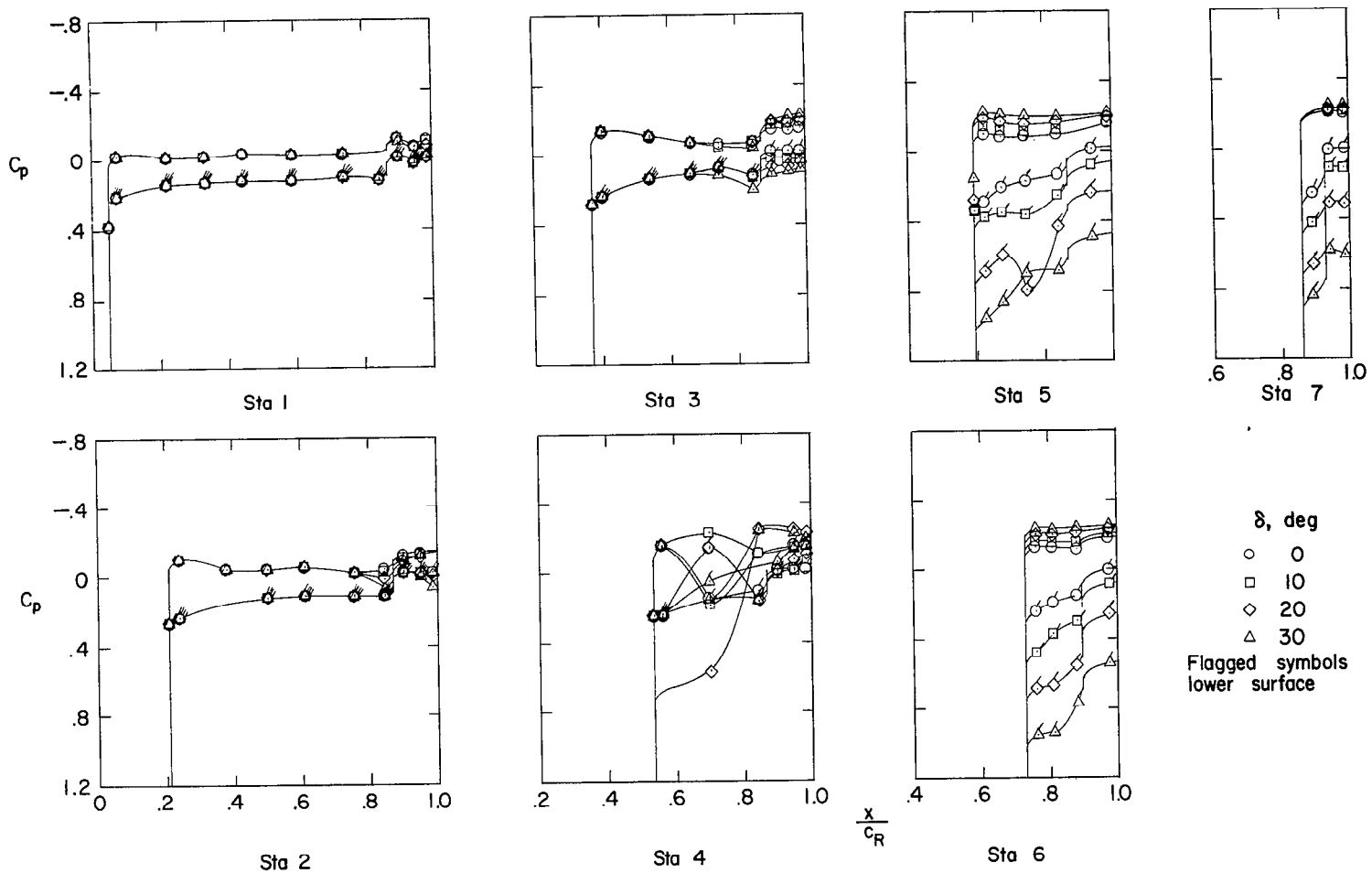

(b) $\alpha = 6^{\circ}$.

Figure 16.- Continued.

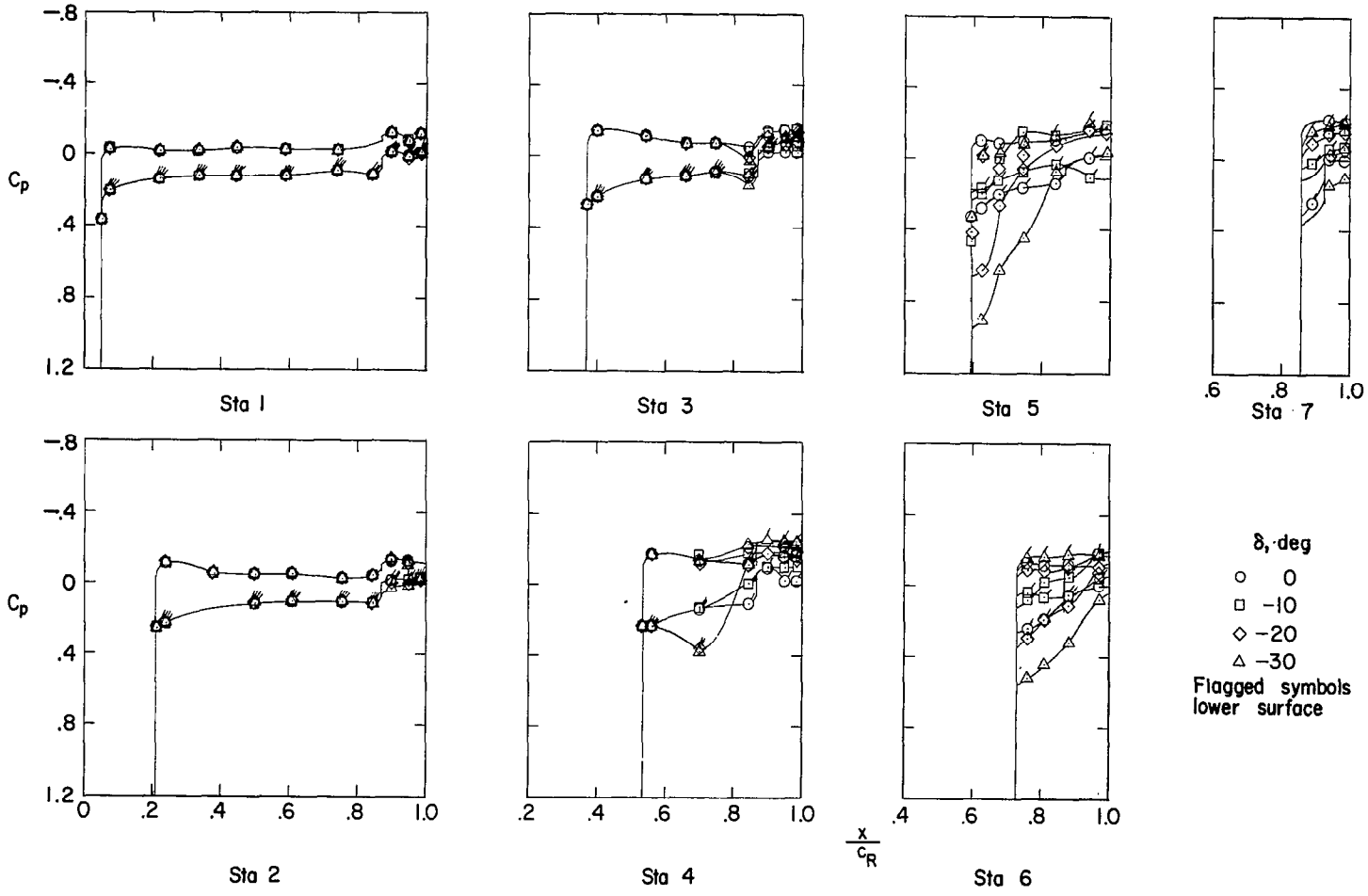

(c) $\alpha = 6^{\circ}$.

Figure 16.- Continued.

[redacted]

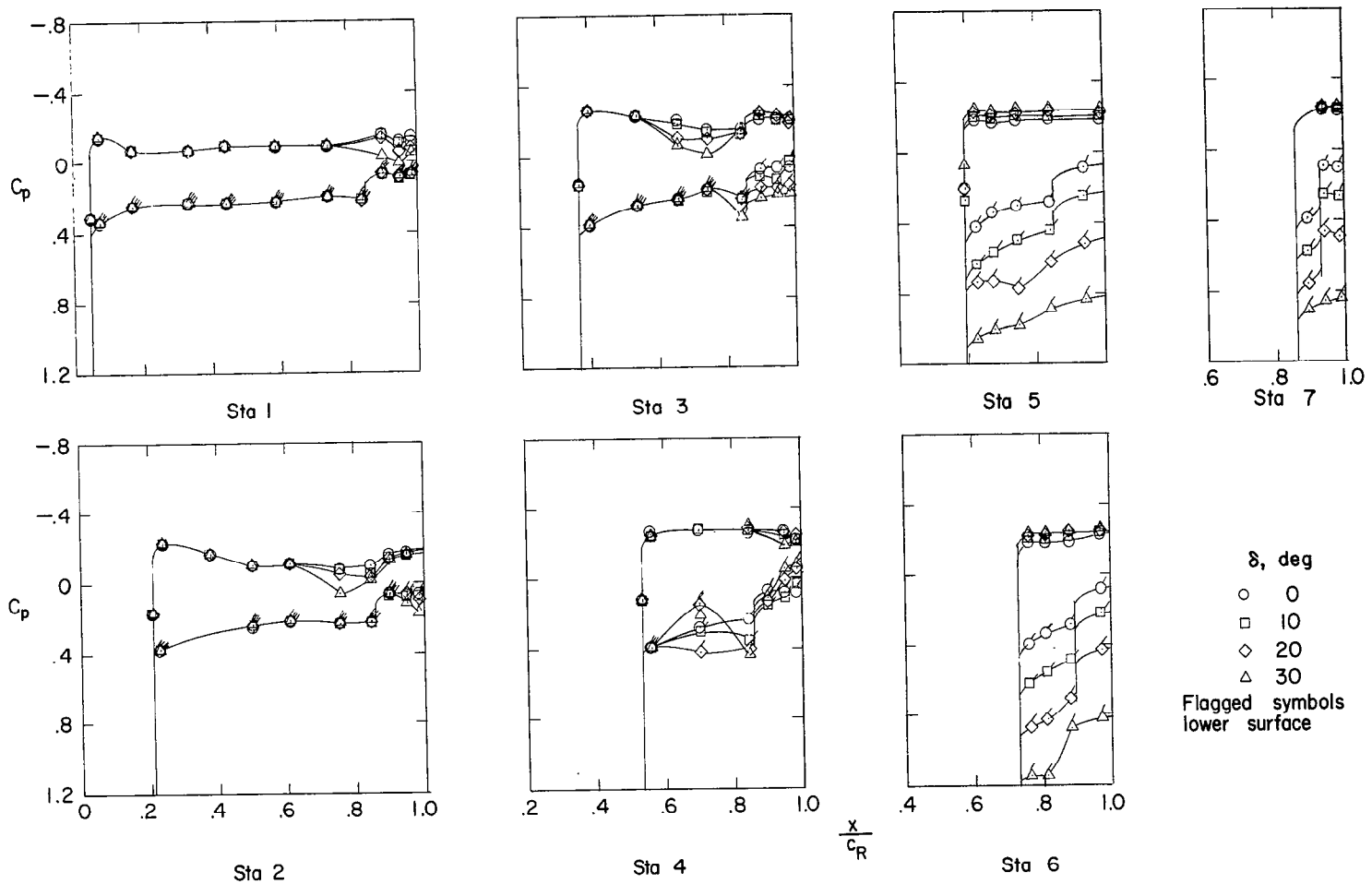

(d) $\alpha = 12^{\circ}$.

Figure 16.- Continued.

[redacted]

[redacted]

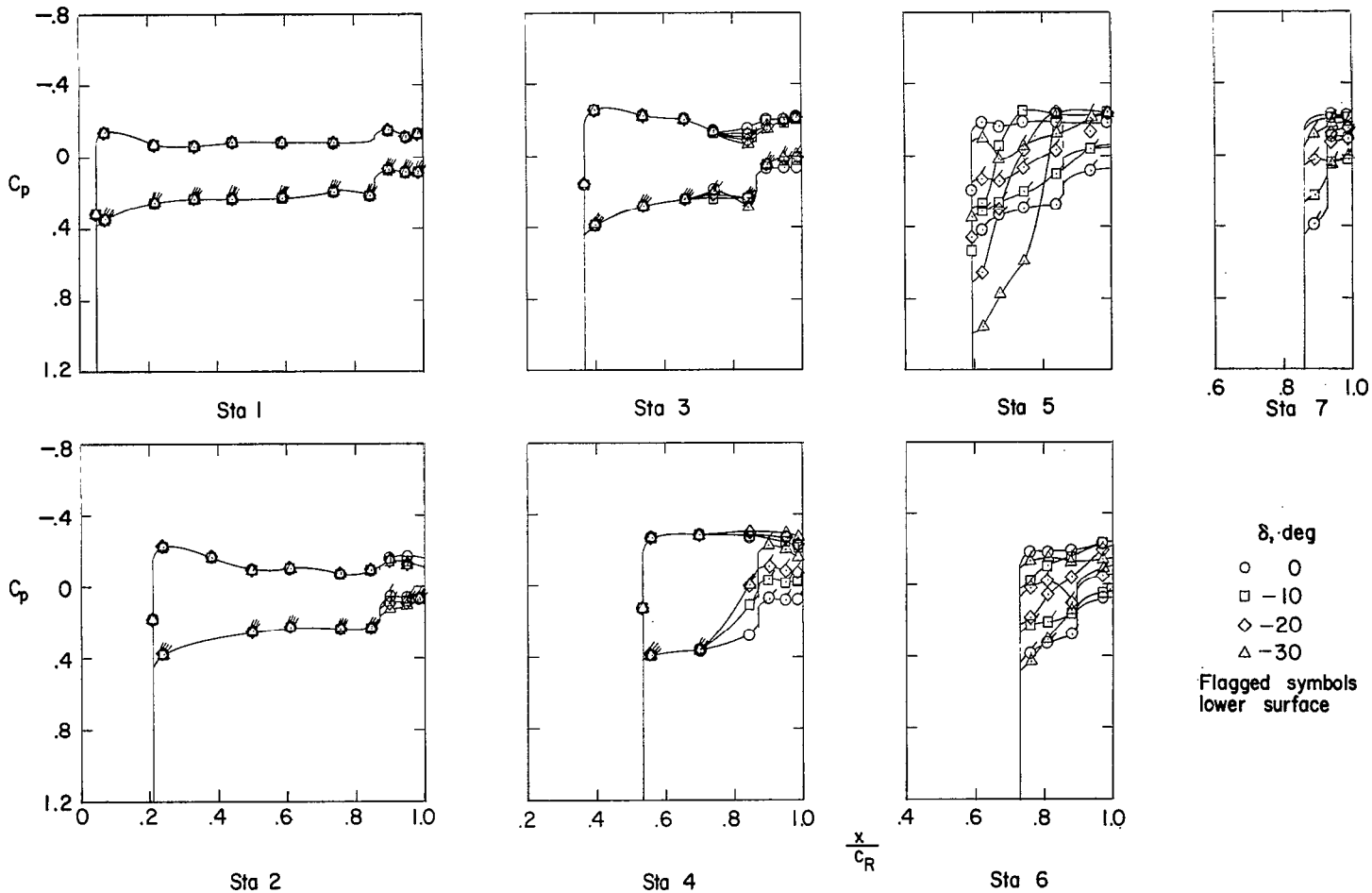

(e) $\alpha = 12^{\circ}$.

Figure 16.- Concluded.

[redacted]

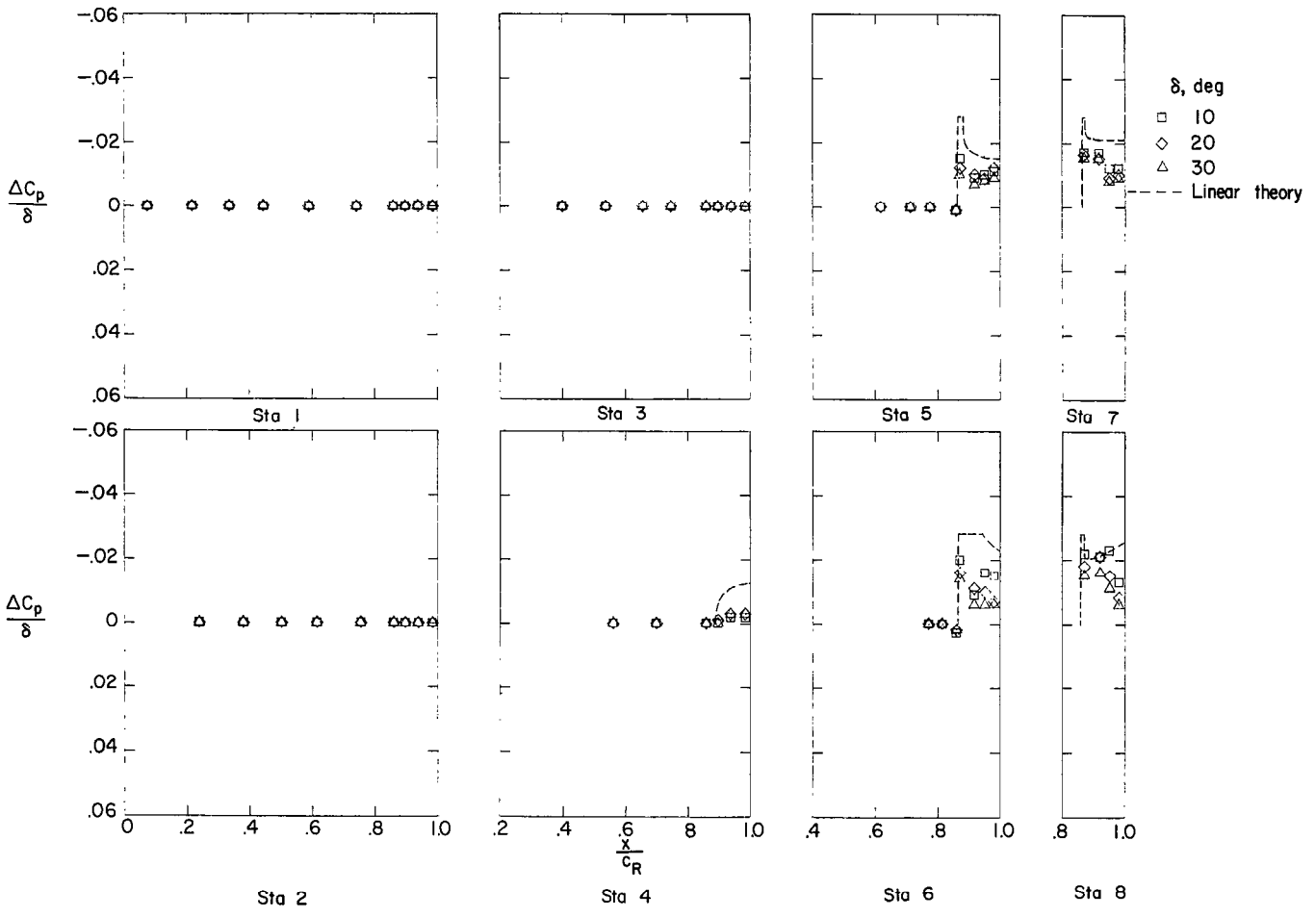

(a) Pressure coefficients due to δ; $\alpha = 0^{\circ}$; upper surface.

Figure 17.- Incremental pressure distributions due to control deflection and angle of attack for configuration A. $M = 1.61$; $R = 4.2 \times 10^{6}$.

[redacted]

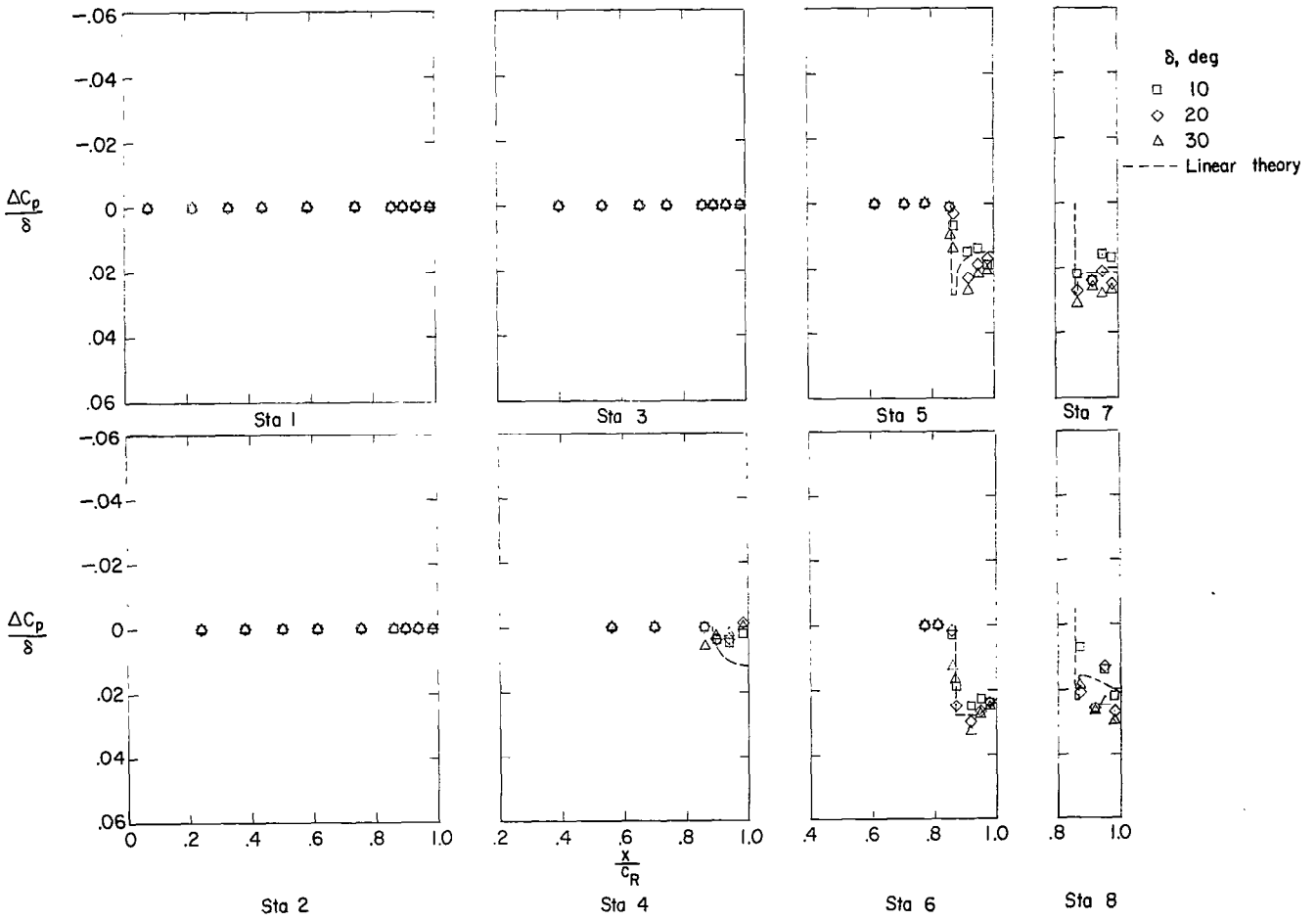

(b) Pressure coefficients due to δ; $\alpha = 0^{\circ}$; lower surface.

Figure 17.- Continued.

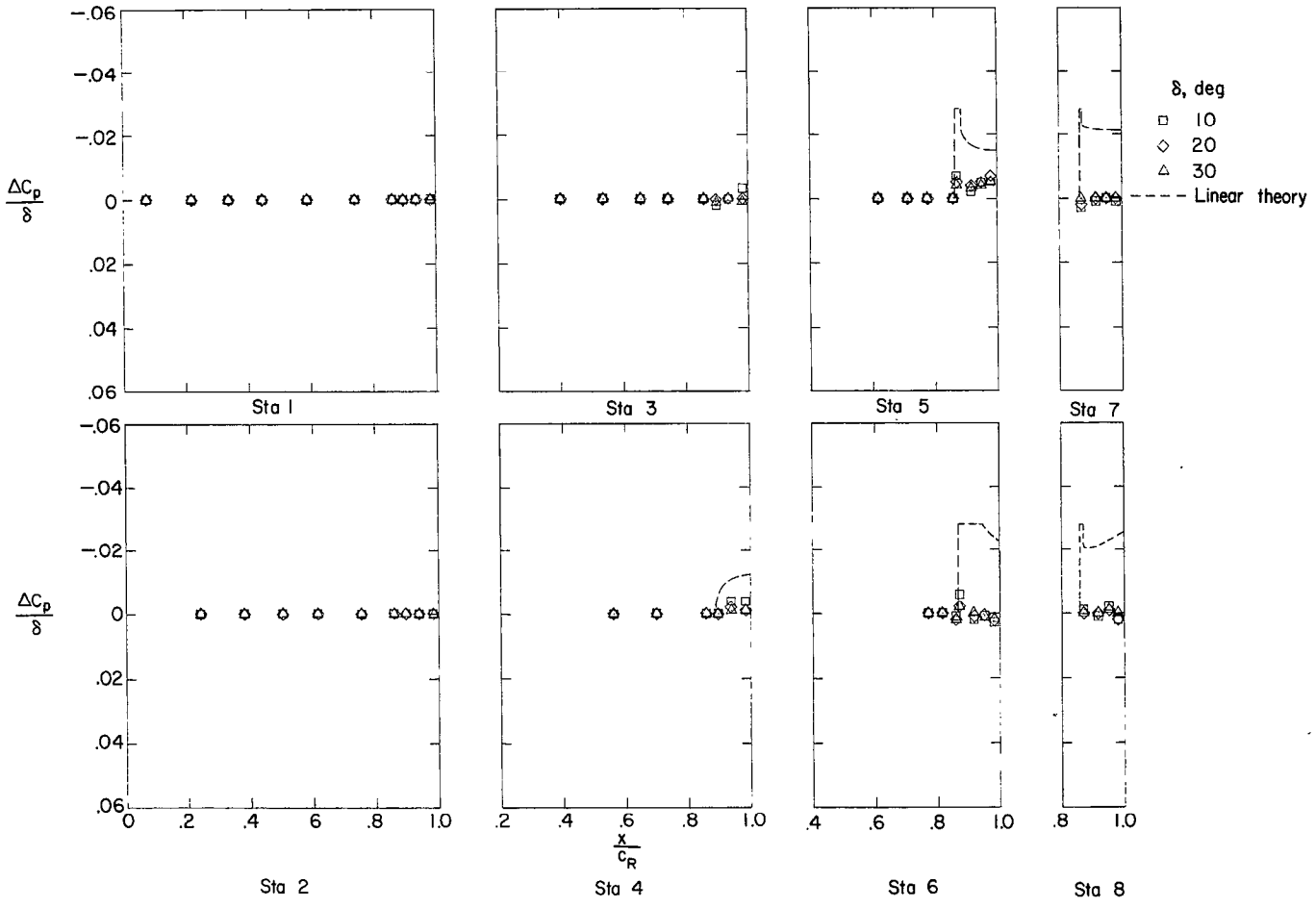

(c) Pressure coefficients due to δ; $\alpha = 12^{\circ}$; upper surface.

Figure 17.- Continued.

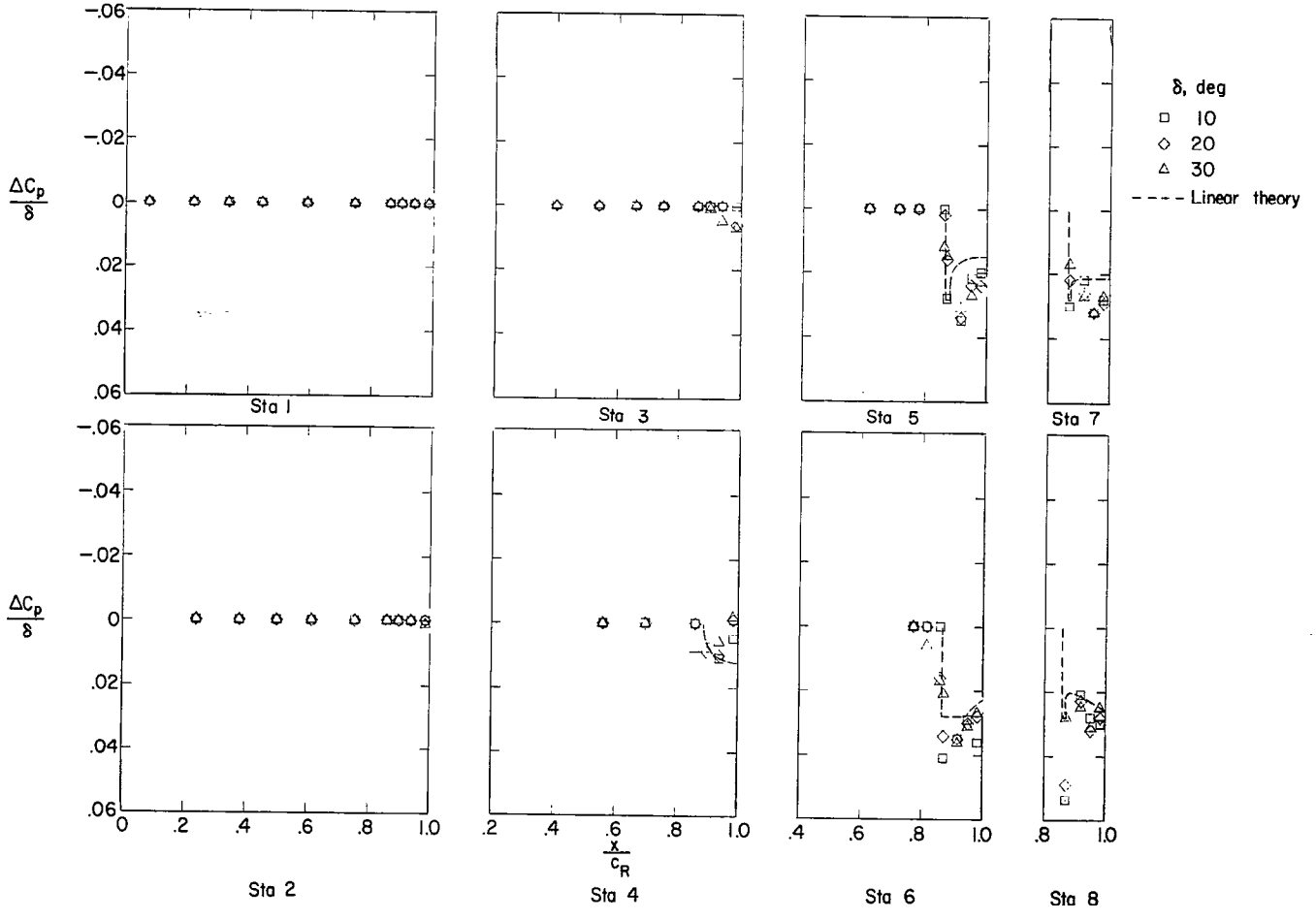

(d) Pressure coefficients due to δ; α = 12°; lower surface.

Figure 17.- Continued.

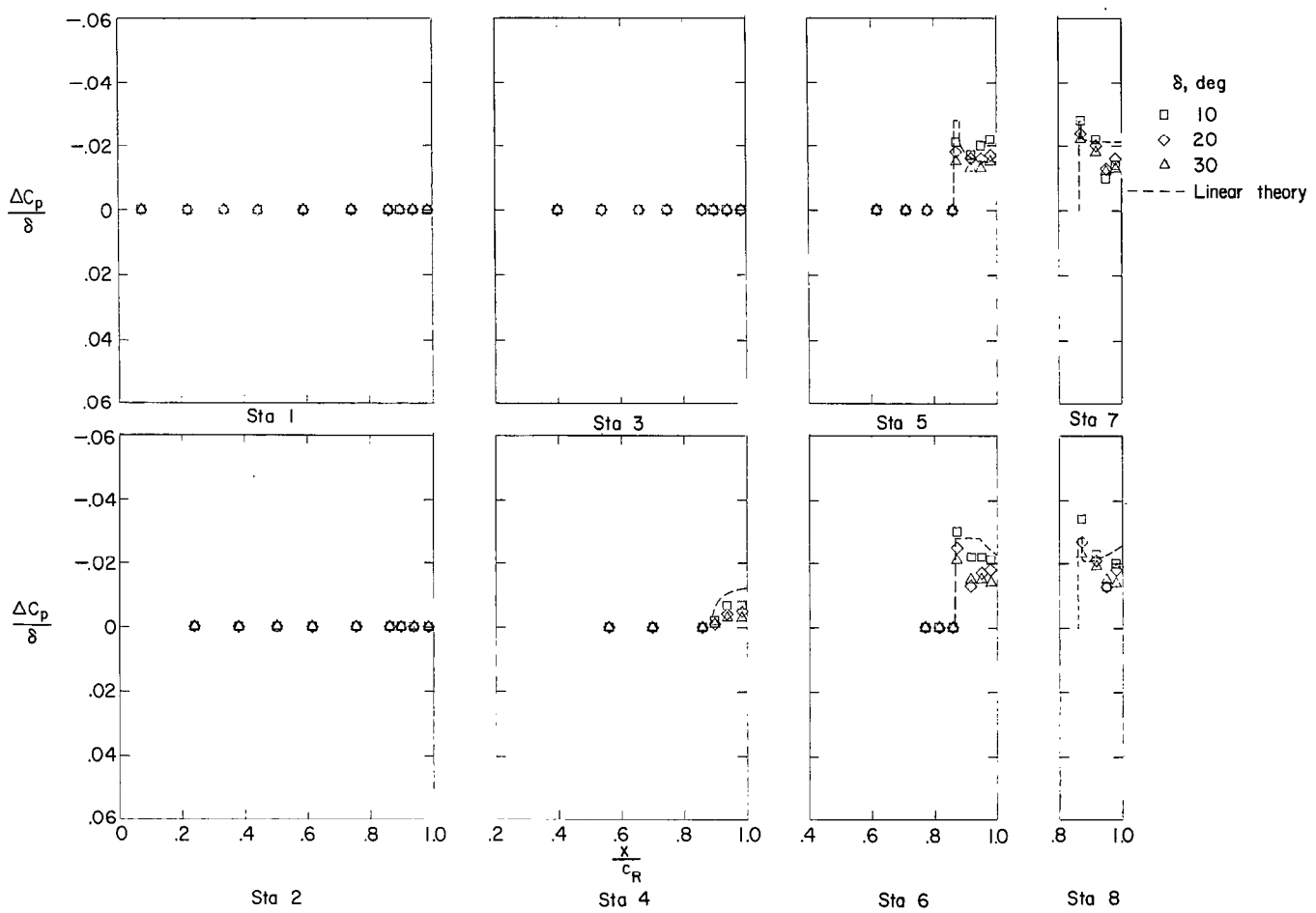

(e) Pressure coefficients due to δ; $\alpha = -12^{\circ}$; upper surface.

Figure 17.- Continued.

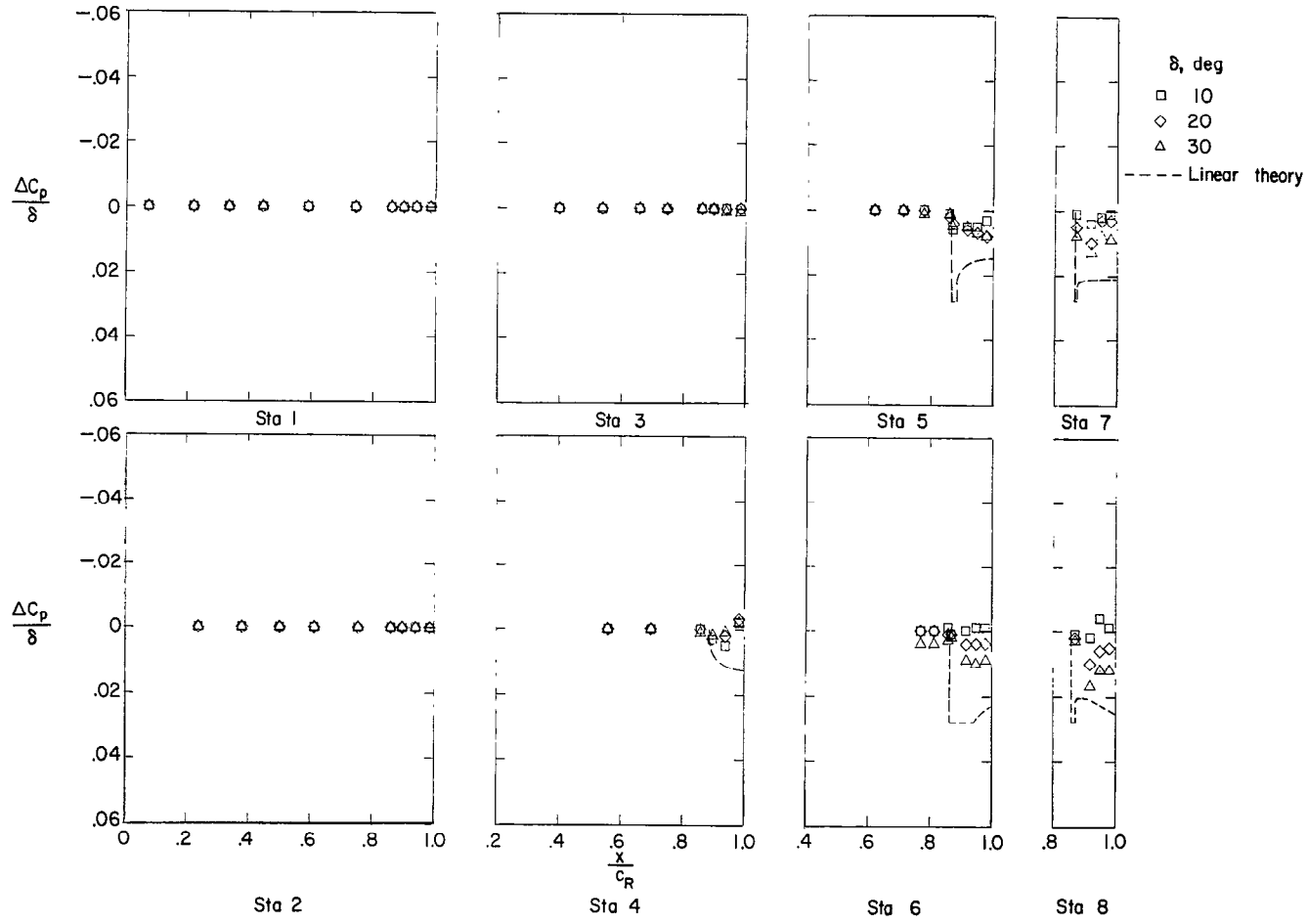

(f) Pressure coefficients due to δ; $\alpha = -12^{\circ}$; lower surface.

Figure 17.- Continued.

[redacted]

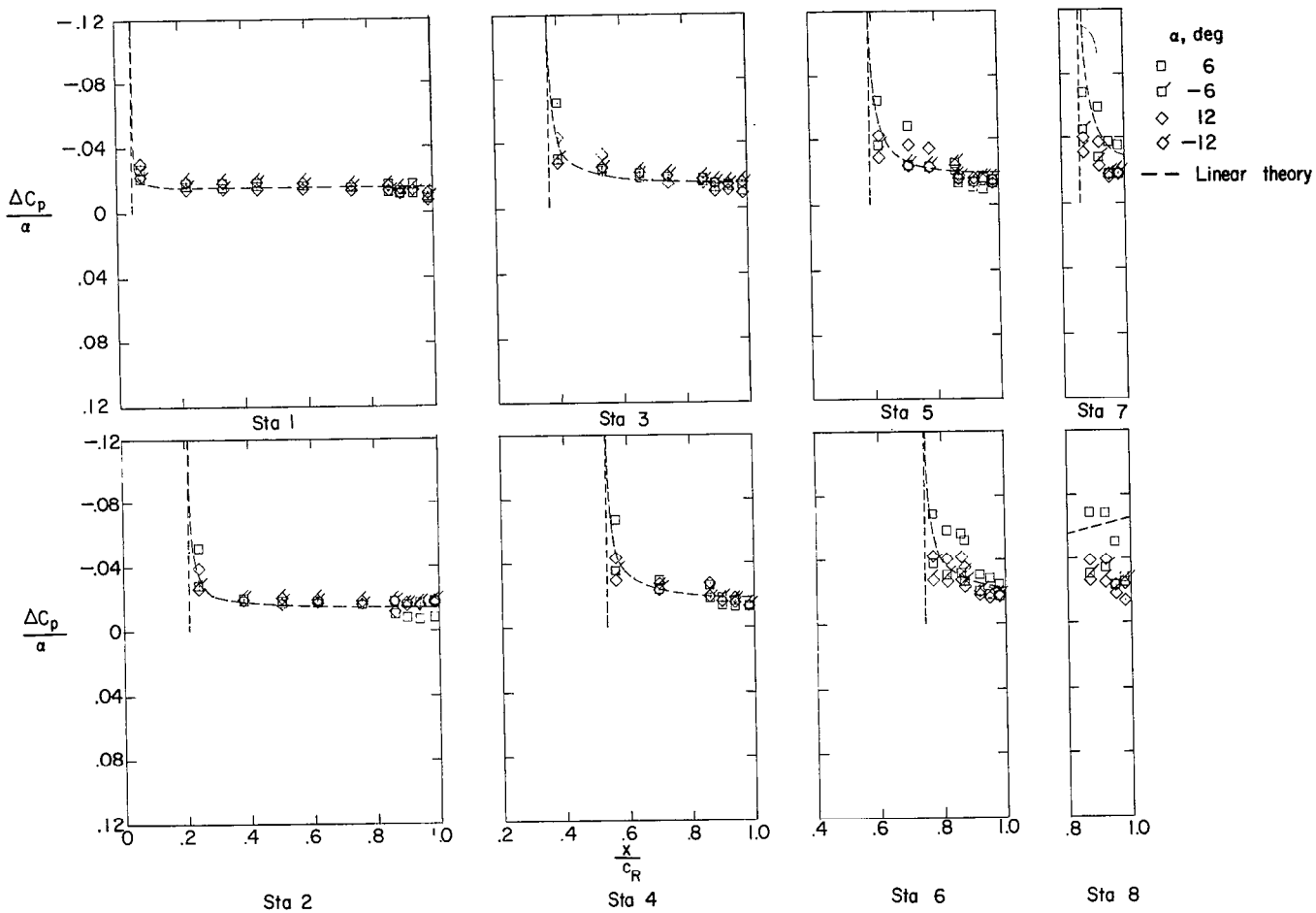

(g) Pressure coefficients due to α; $\delta = 0^{\circ}$; upper surface.

Figure 17.- Continued.

[redacted]

[redacted]

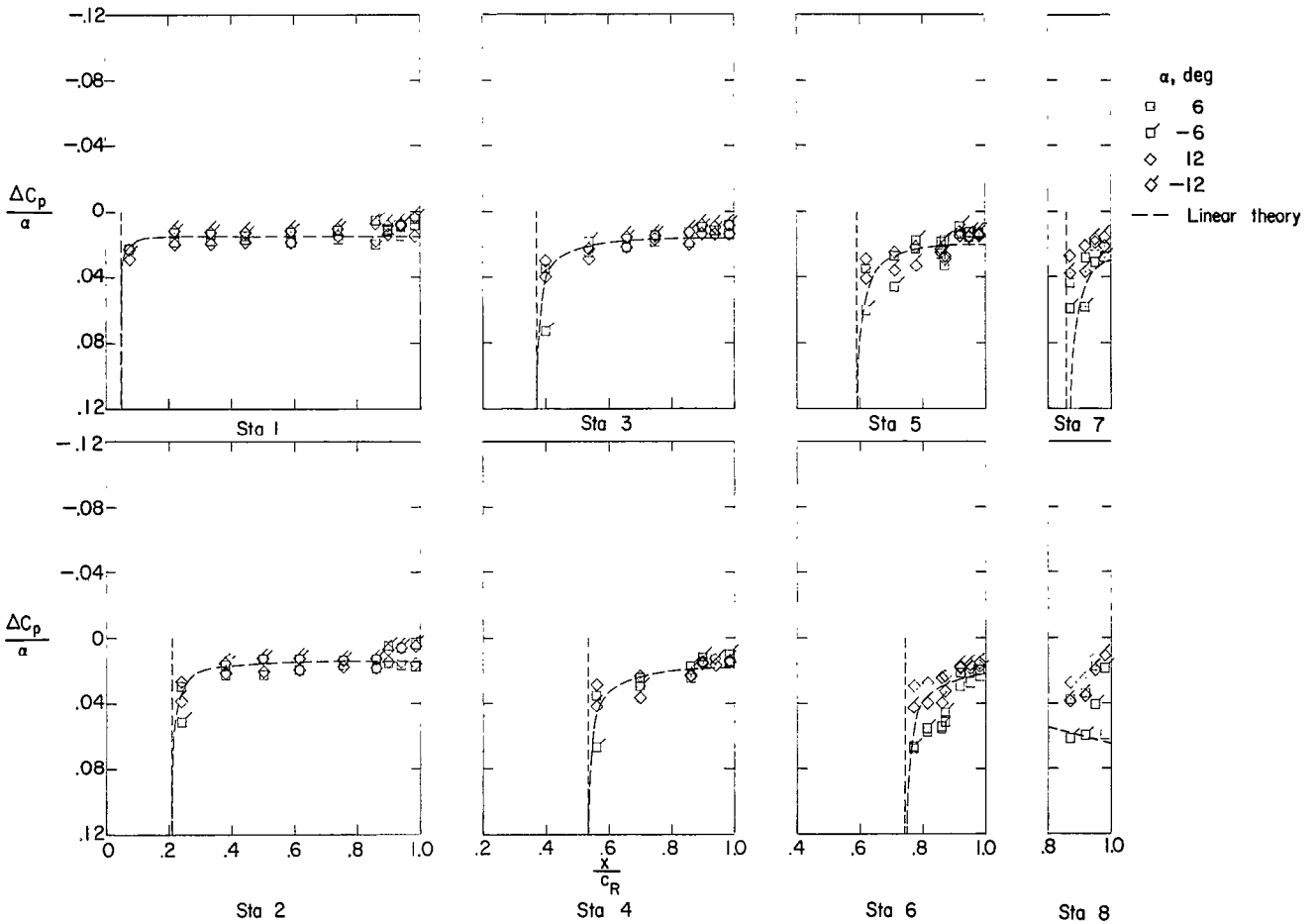

(h) Pressure coefficients due to α; δ = 0°; lower surface.

Figure 17.- Continued.

[redacted]

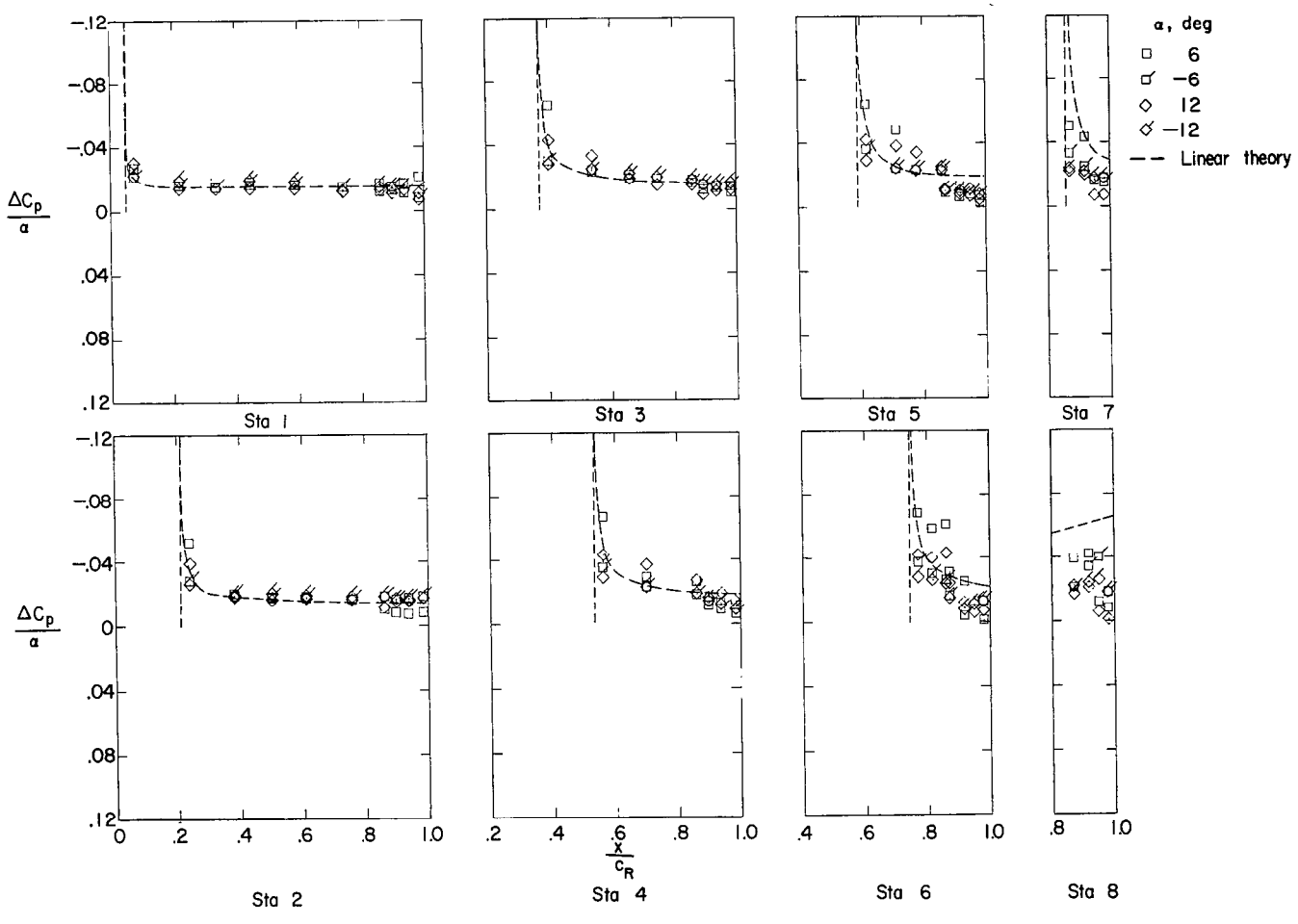

(i) Pressure coefficients due to α; δ = 10°; upper surface.

Figure 17.- Continued.

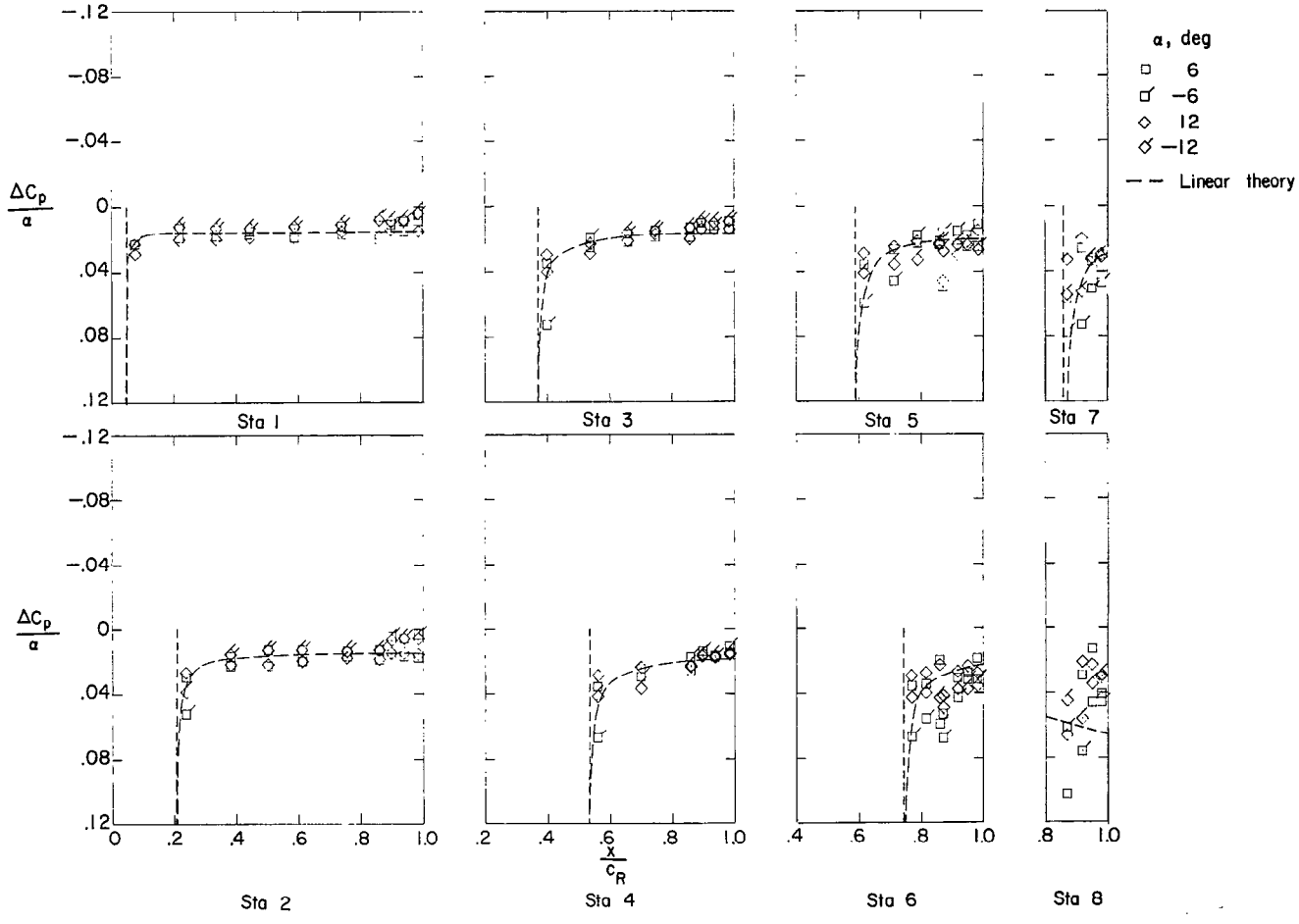

(j) Pressure coefficients due to α; $\delta = 10^{\circ}$; lower surface.

Figure 17.- Continued.

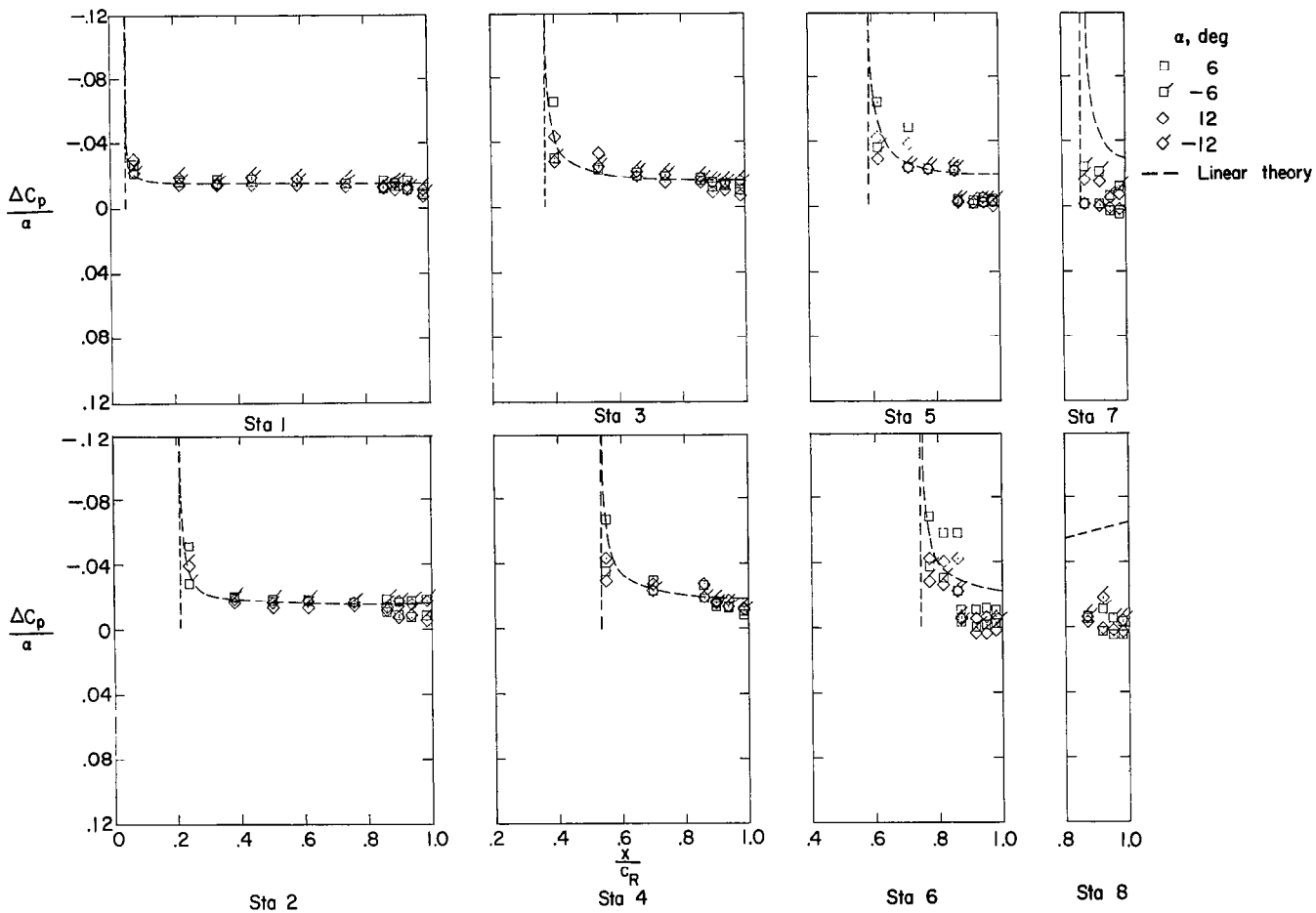

(k) Pressure coefficients due to α; $\delta = 30^{\circ}$; upper surface.

Figure 17.- Continued.

[redacted]

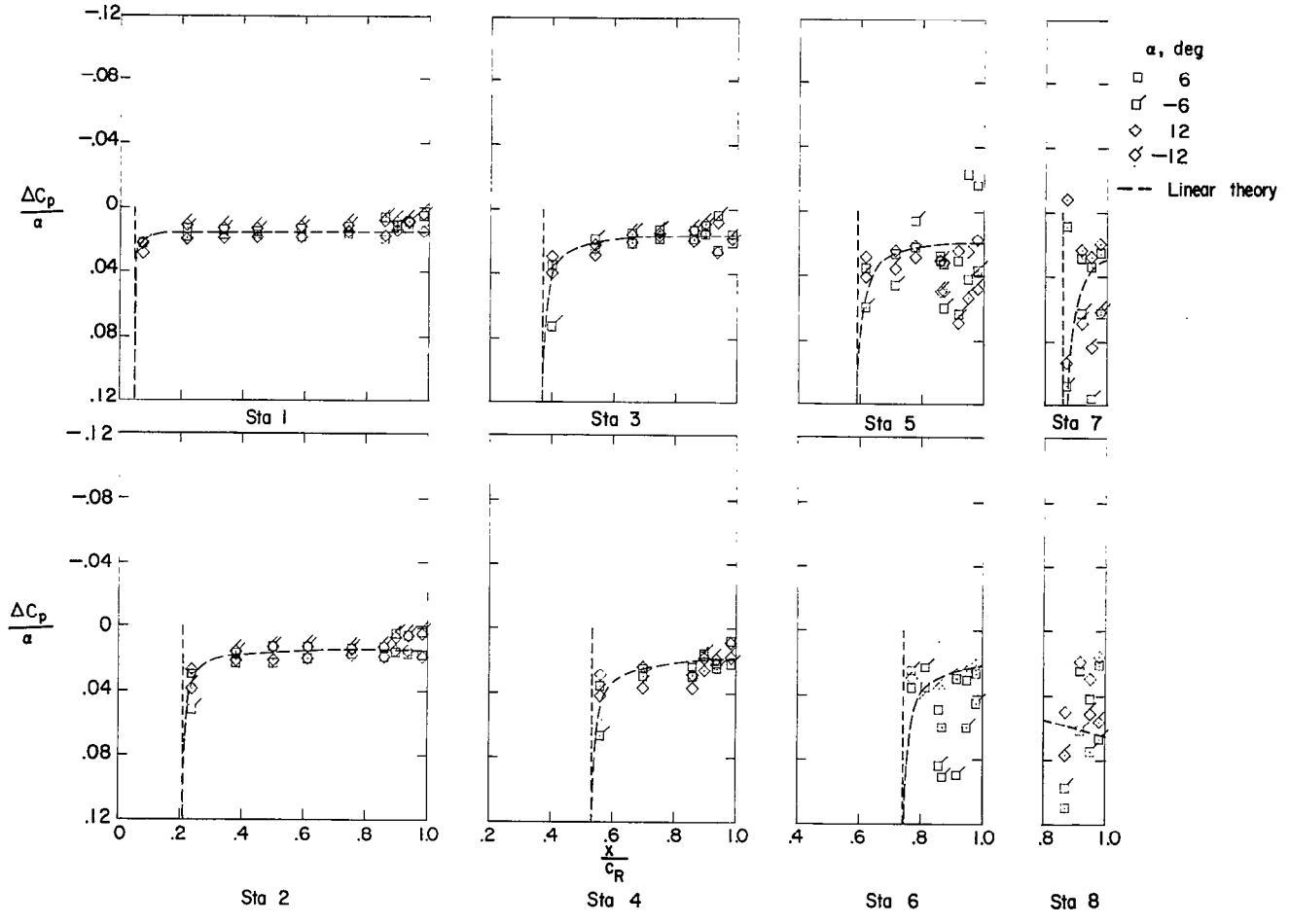

(l) Pressure coefficients due to α; δ = 30°; lower surface.

Figure 17.- Continued.

[redacted]

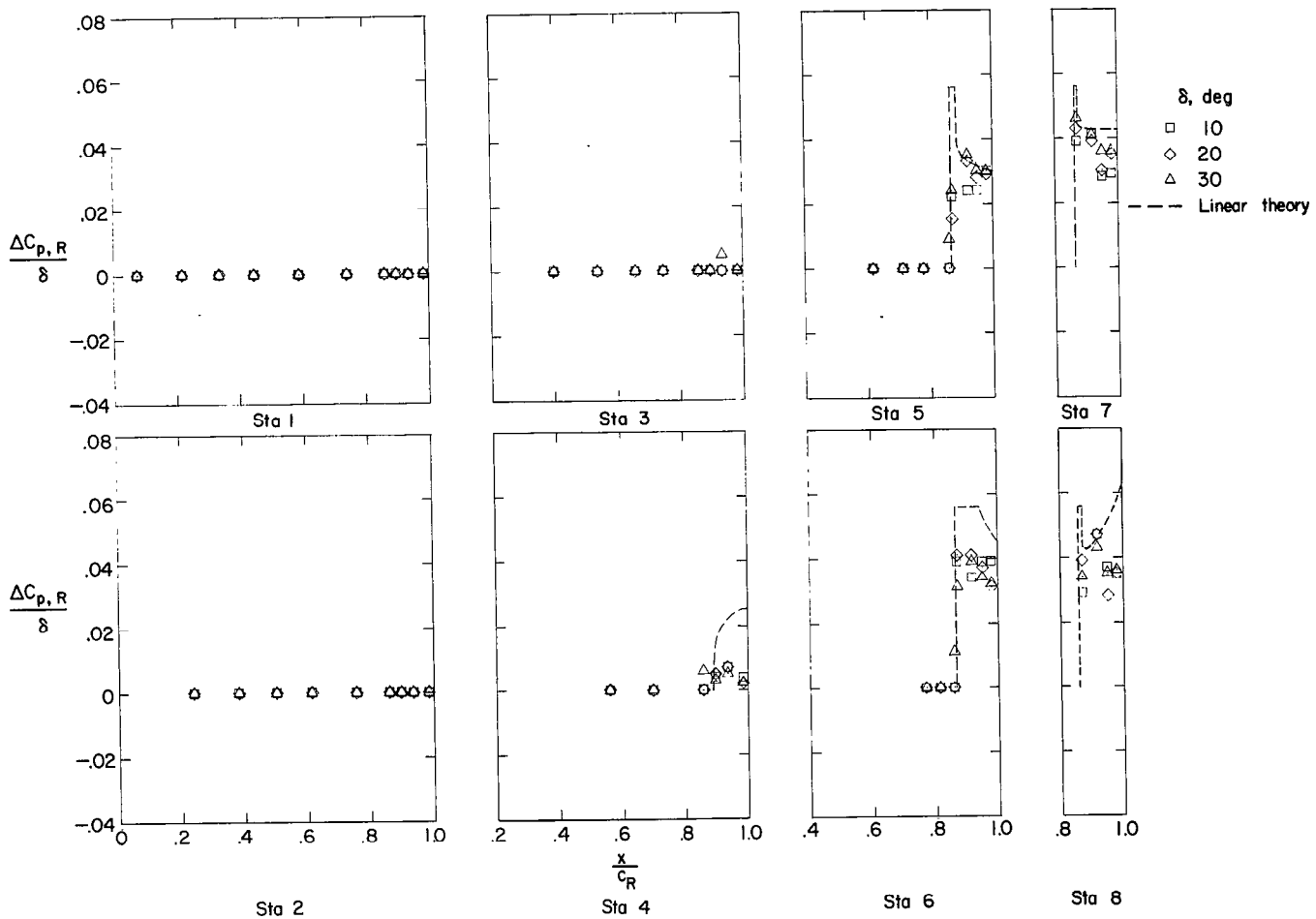

(m) Resultant pressure coefficients due to δ; $\alpha = 0^{\circ}$.

Figure 17.- Continued.

[redacted]

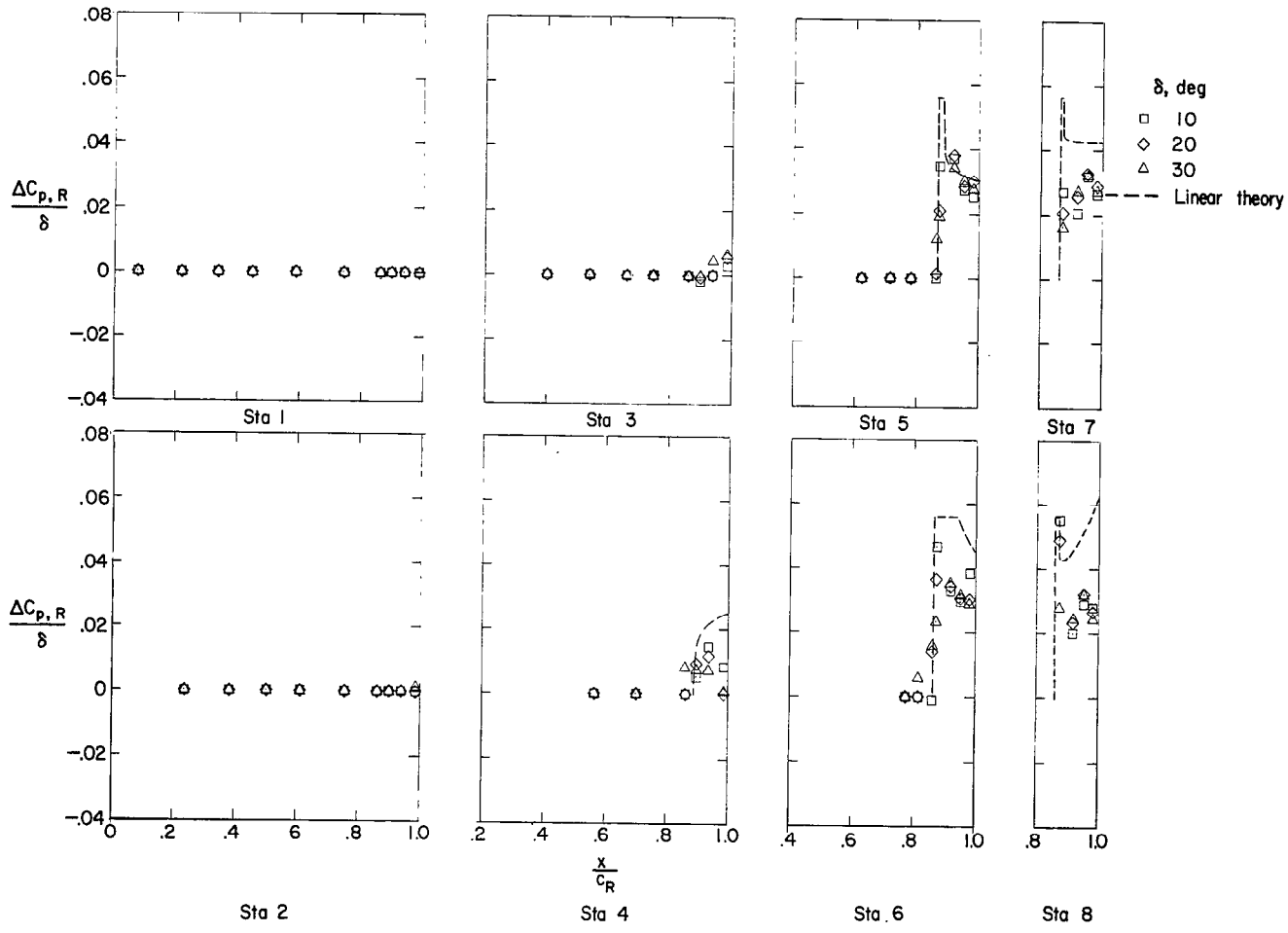

(n) Resultant pressure coefficients due to δ; $\alpha = 12^{\circ}$.

Figure 17.- Continued.

[redacted]

[redacted]

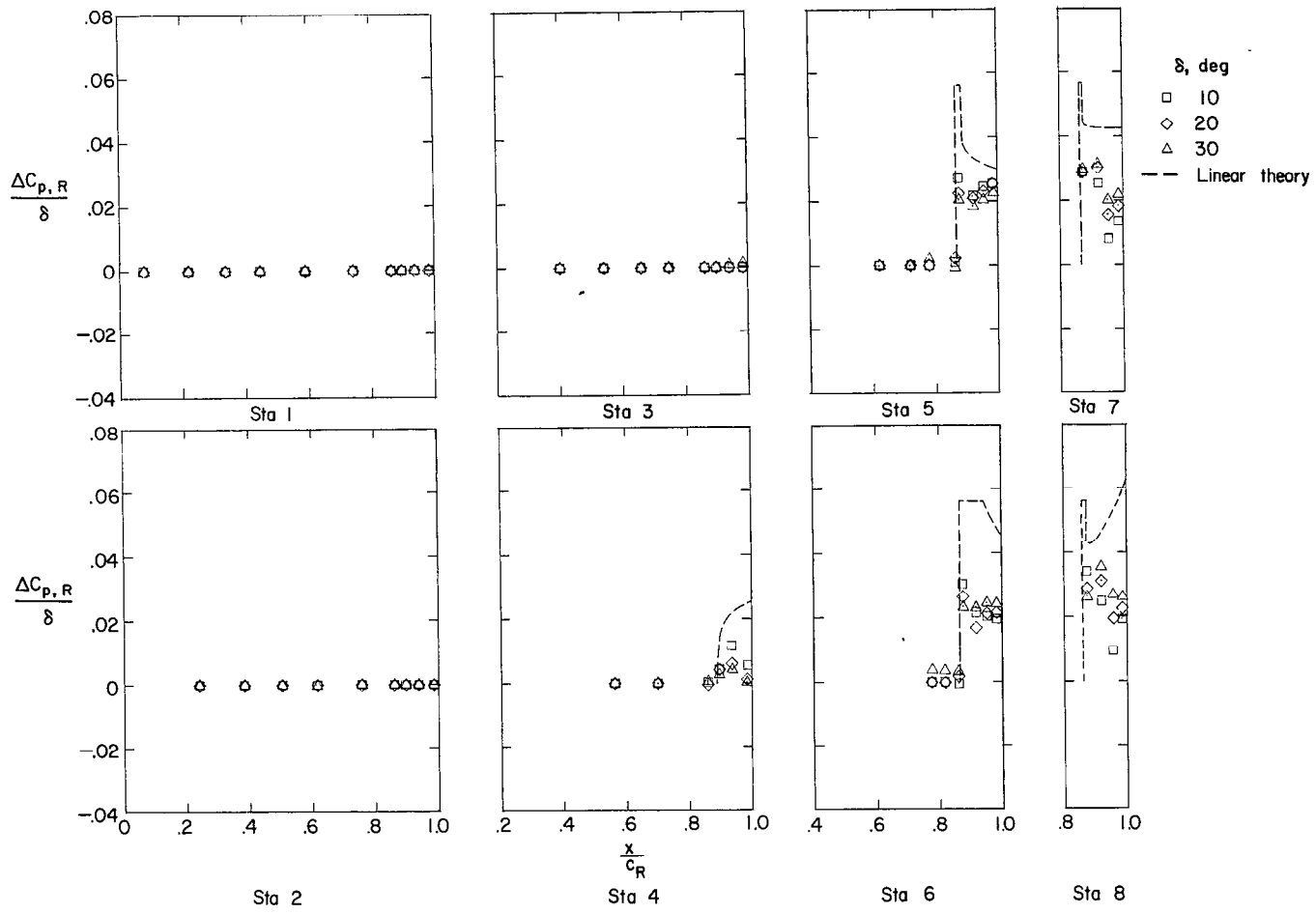

(o) Resultant pressure coefficients due to δ; $\alpha = -12^{\circ}$.

Figure 17.- Continued.

[redacted]

[redacted]

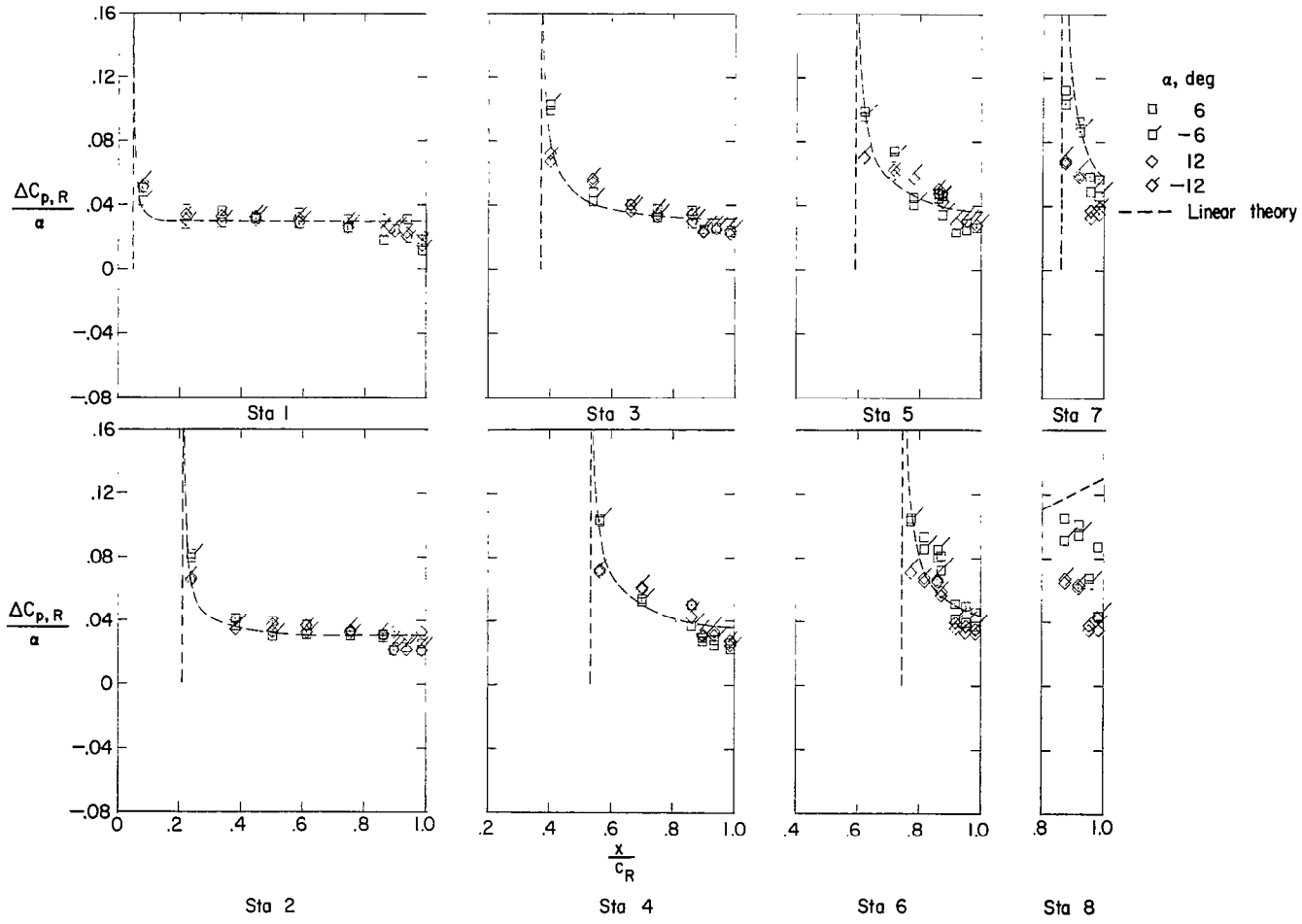

(p) Resultant pressure coefficients due to α; $\delta = 0^{\circ}$.

Figure 17.- Continued.

[redacted]

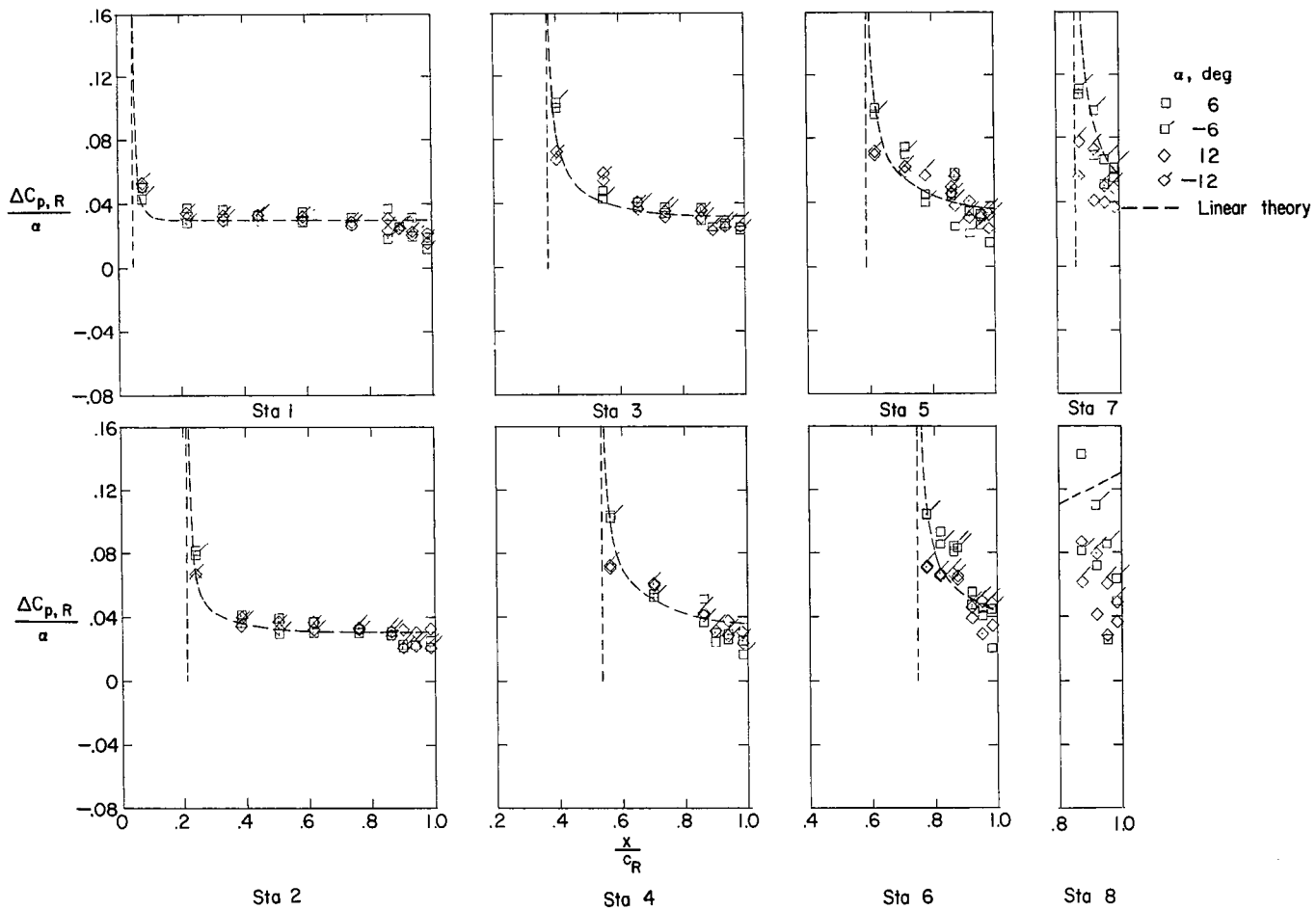

(q) Resultant pressure coefficients due to α; $\delta = 10^{\circ}$.

Figure 17.- Continued.

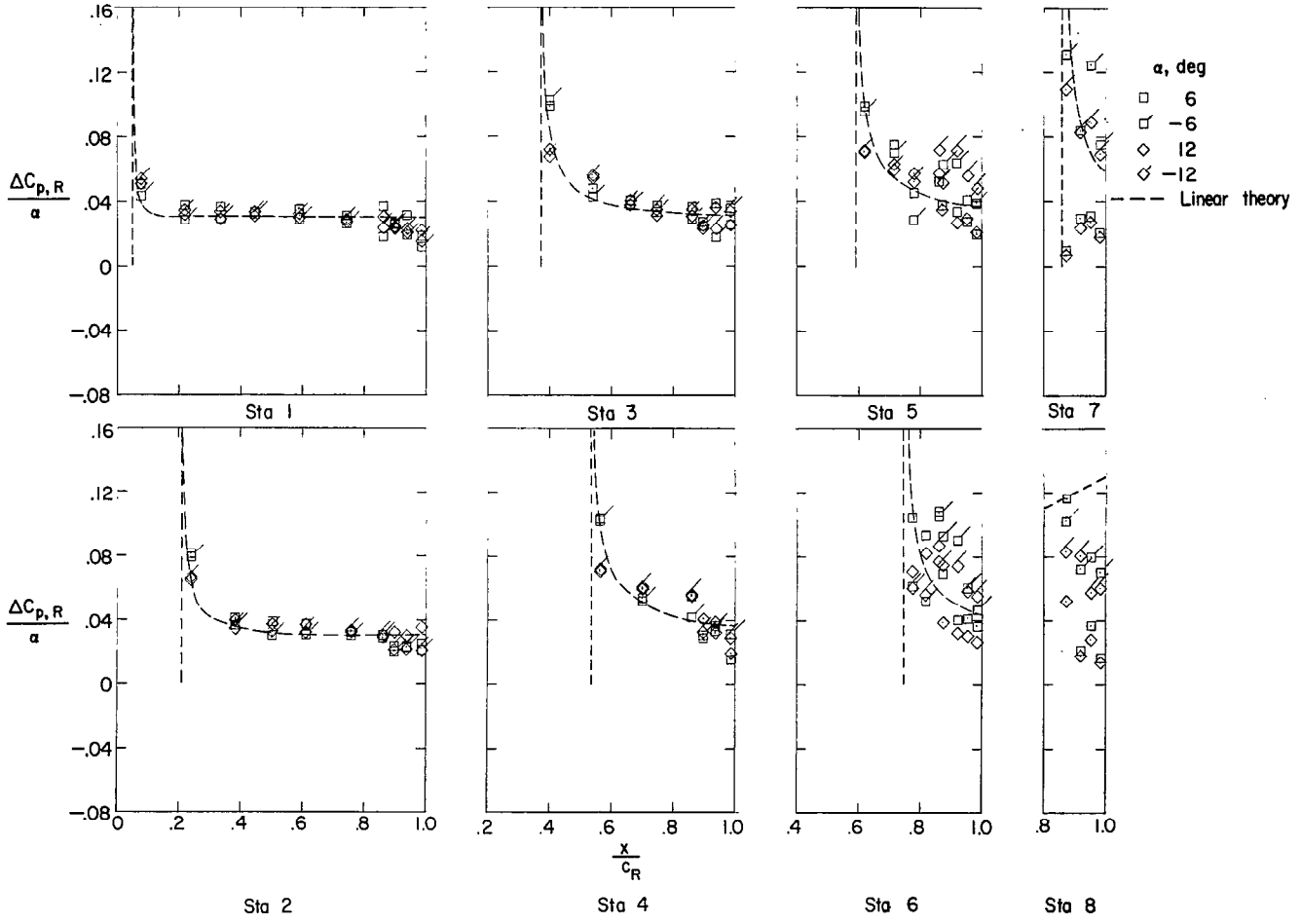

(r) Resultant pressure coefficients due to α; $\delta = 30^{\circ}$.

Figure 17.- Concluded.

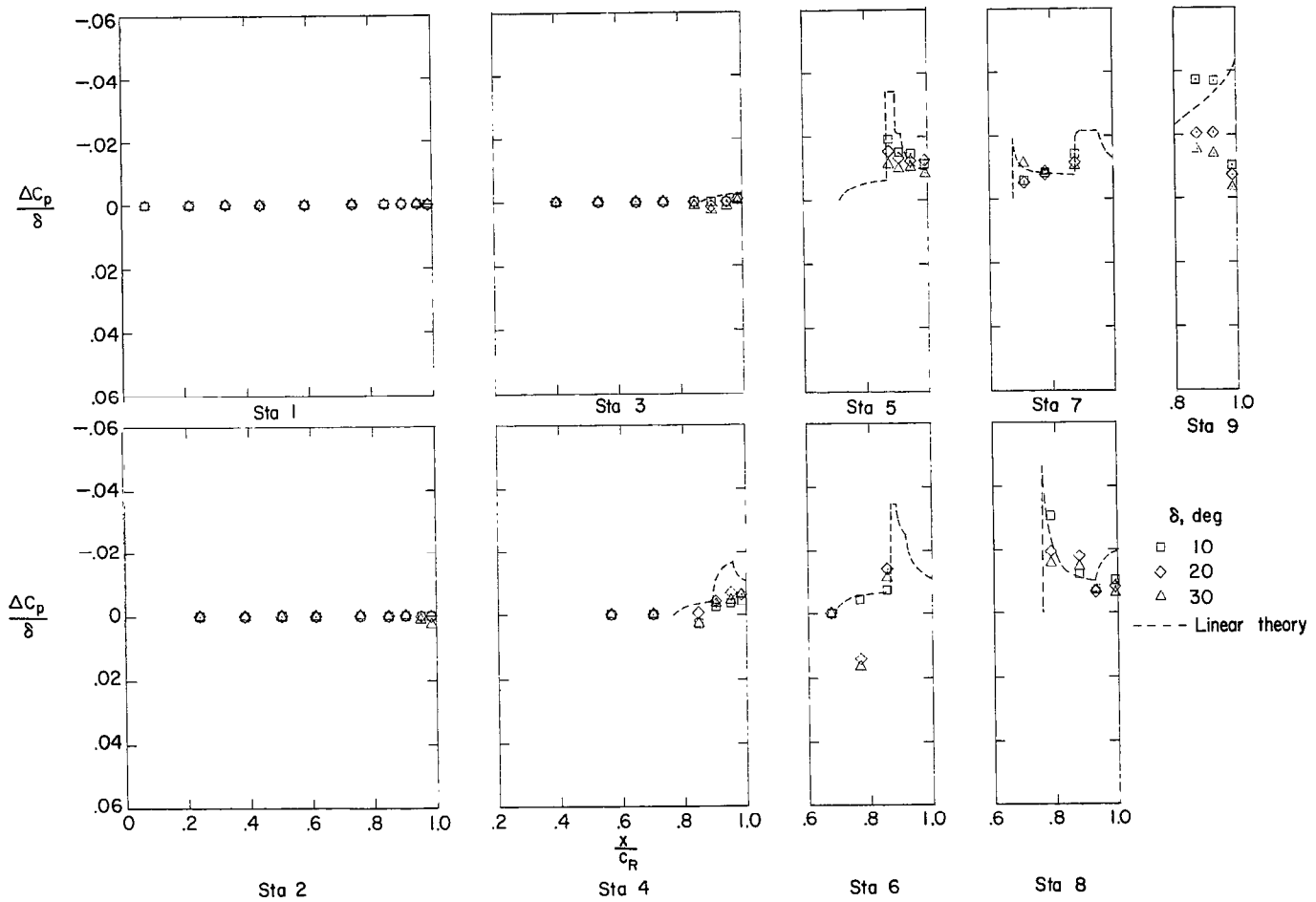

(a) Pressure coefficients due to δ; $\alpha = 0^{\circ}$; upper surface.

Figure 18.- Incremental pressure distributions due to control deflection and angle of attack for configuration C. $M = 1.61$; $R = 4.2 \times 10^{6}$.

[redacted]

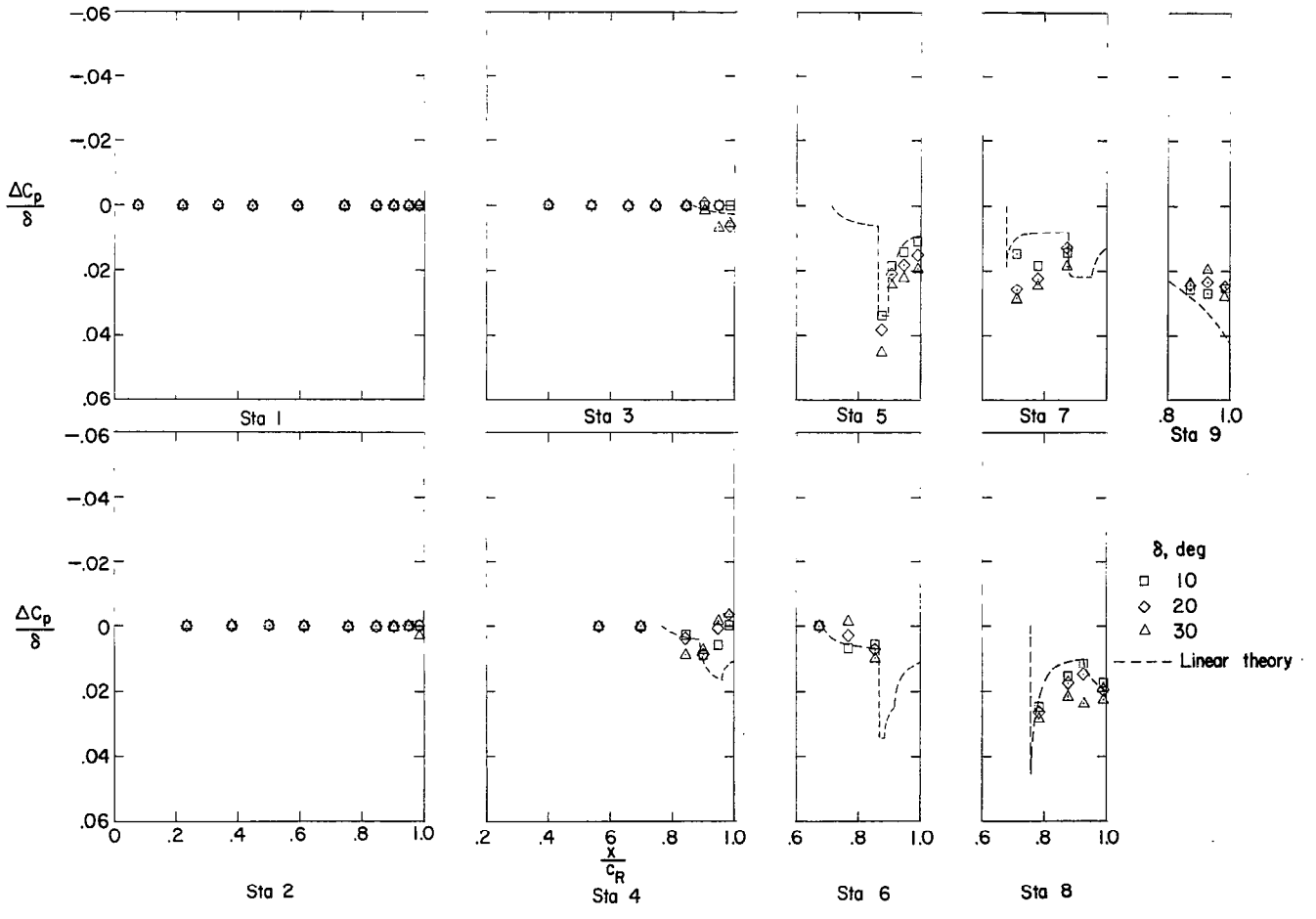

(b) Pressure coefficients due to δ; α = 0°; lower surface.

Figure 18.- Continued.

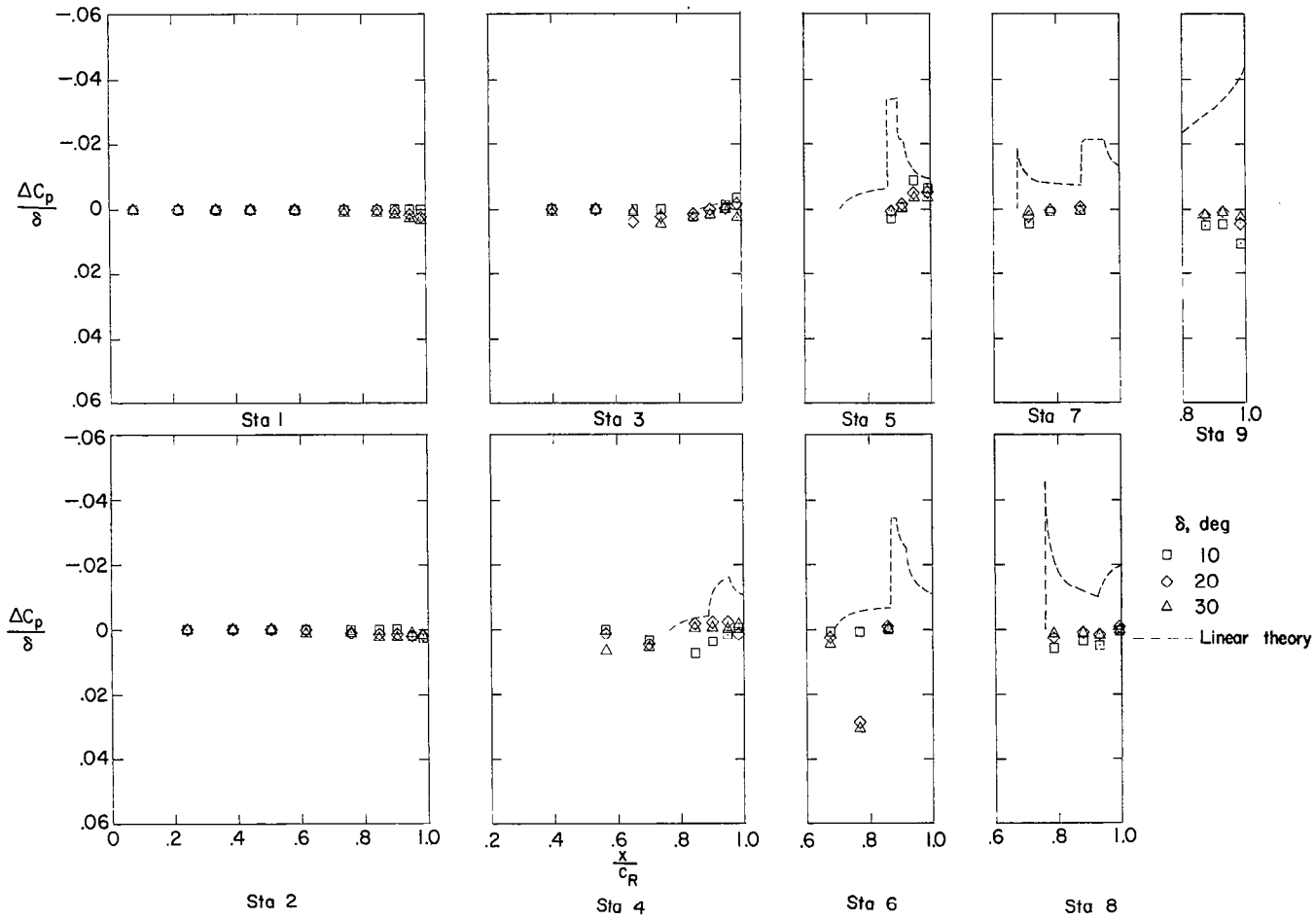

(c) Pressure coefficients due to δ; $\alpha = 12^{\circ}$; upper surface.

Figure 18.- Continued.

[redacted]

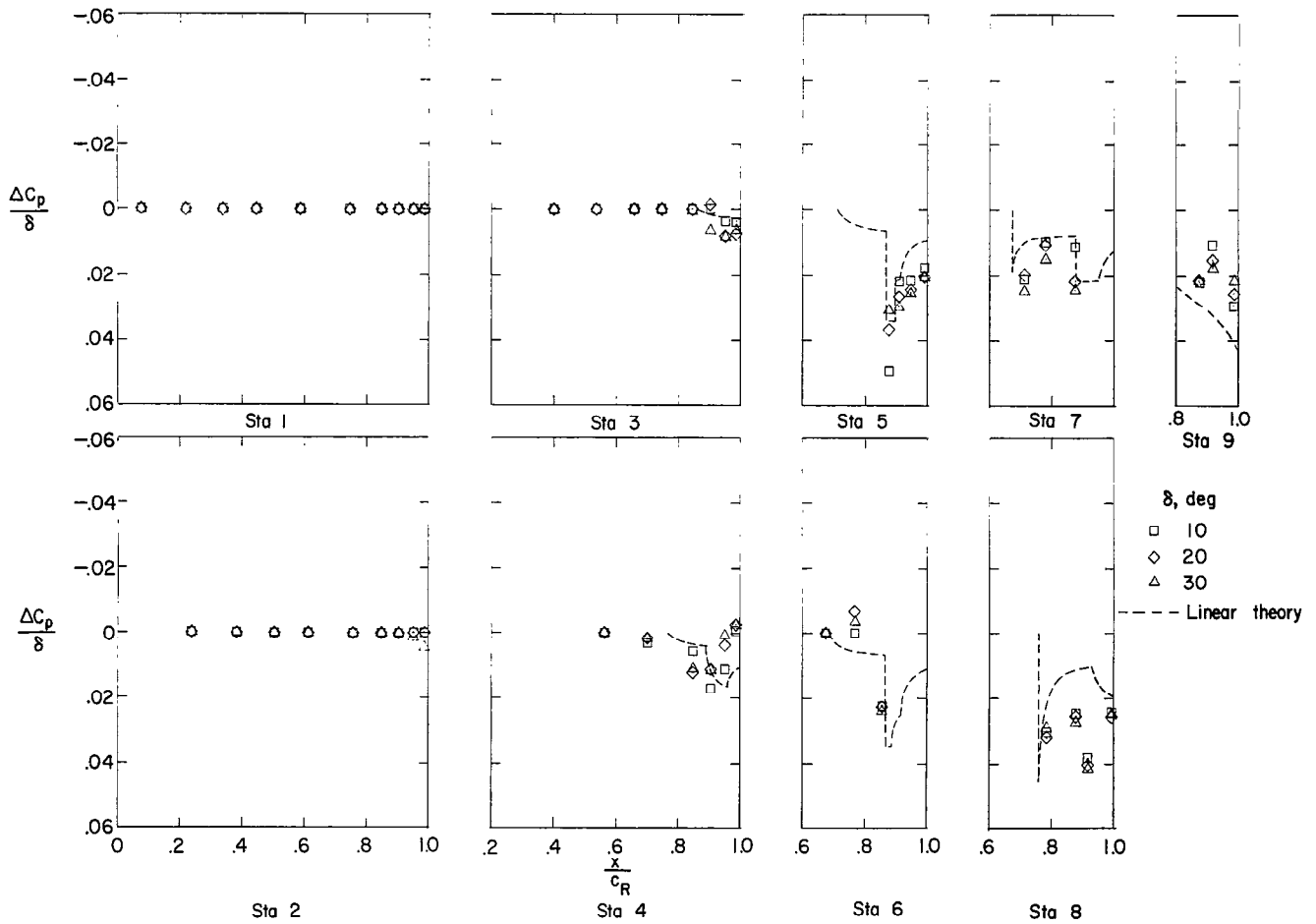

(d) Pressure coefficients due to δ; $\alpha = 12^{\circ}$; lower surface.

Figure 18.- Continued.

[redacted]

[redacted]

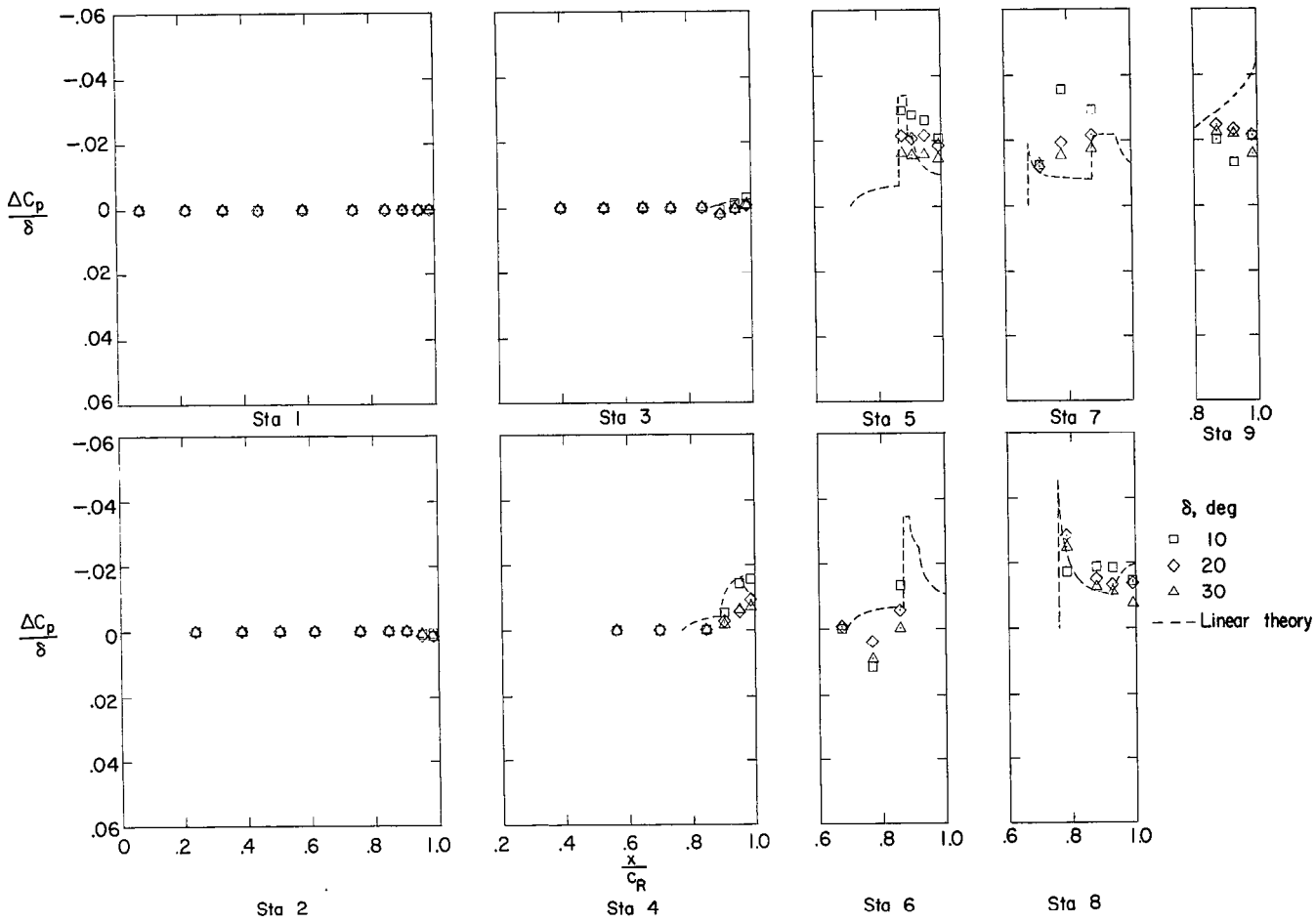

(e) Pressure coefficients due to δ; $\alpha = -12^{\circ}$; upper surface.

Figure 18.- Continued.

[redacted]

[redacted]

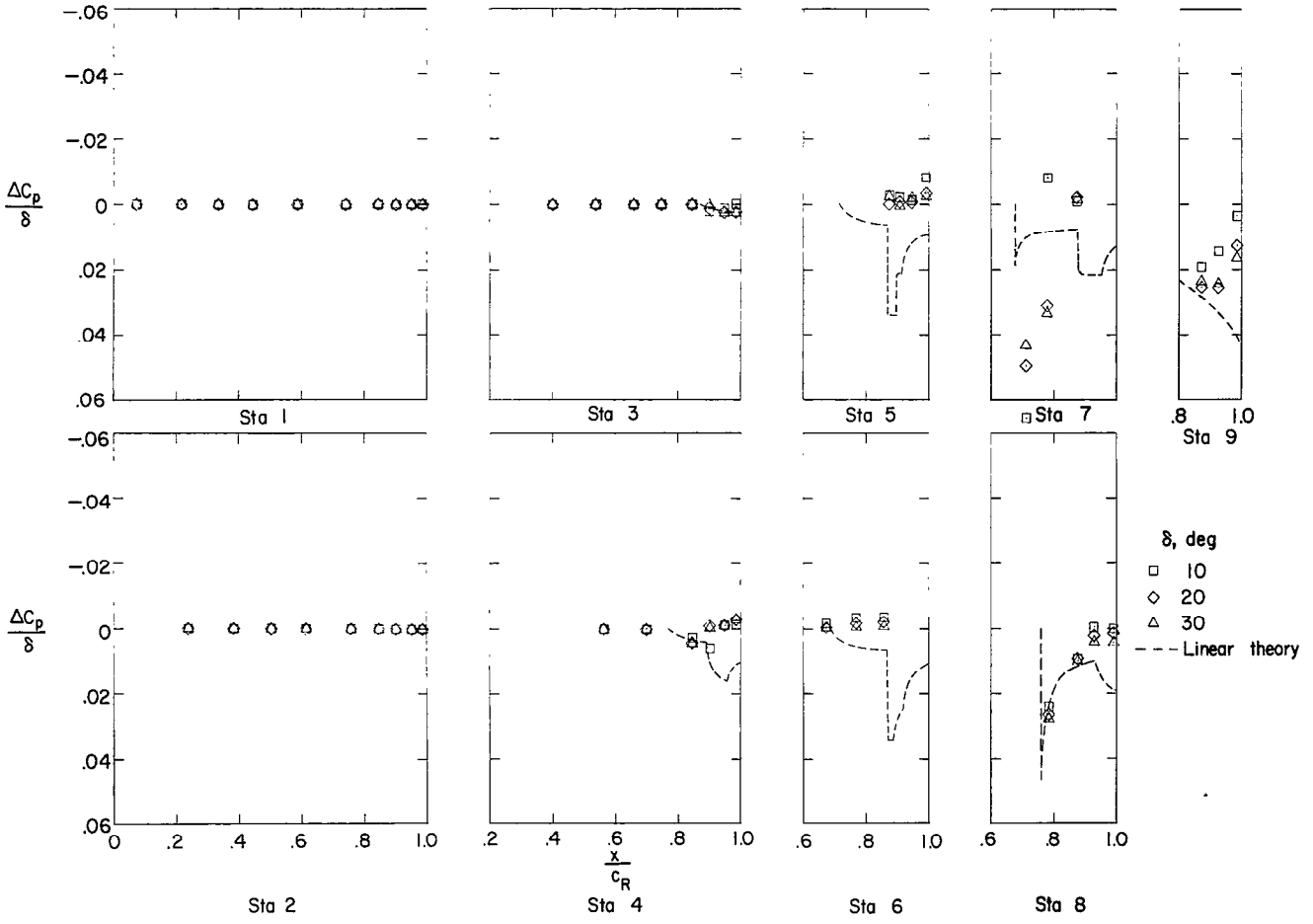

(f) Pressure coefficients due to δ; $\alpha = -12^{\circ}$; lower surface.

Figure 18.- Continued.

[redacted]

[redacted]

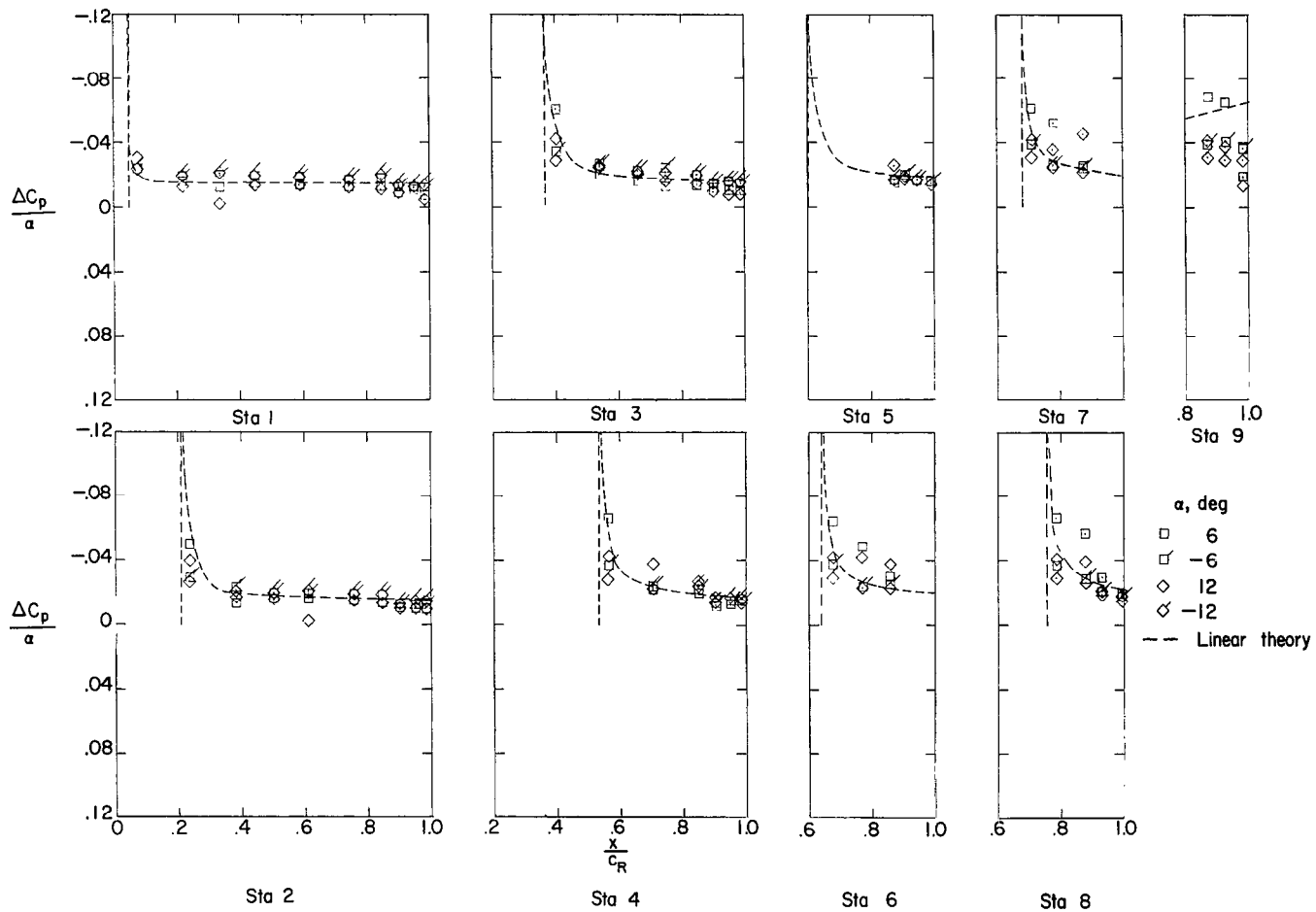

(g) Pressure coefficients due to α; $\delta = 0^{\circ}$; upper surface.

Figure 18.- Continued.

[redacted]

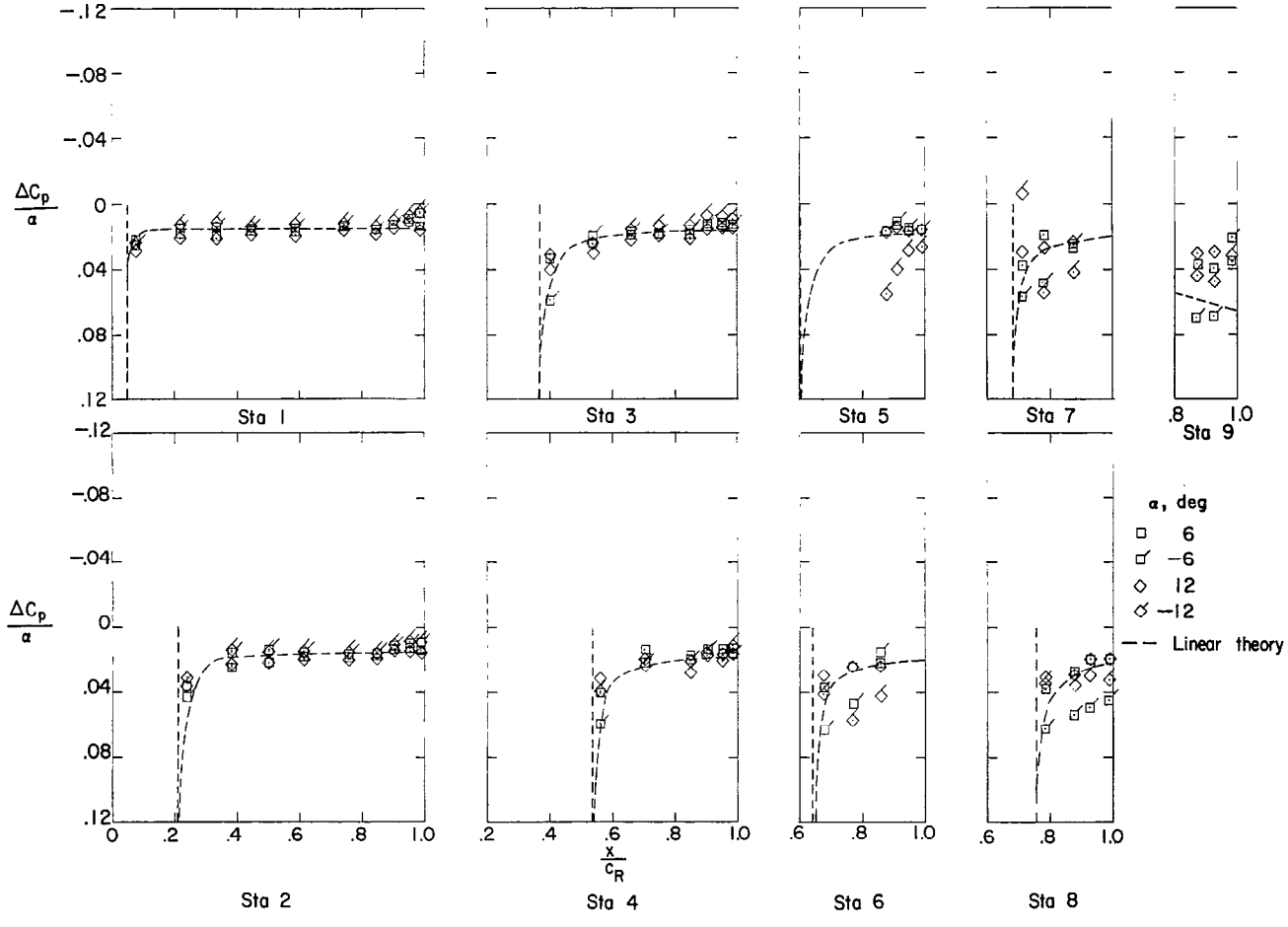

(h) Pressure coefficients due to α; $\delta = 0^{\circ}$; lower surface.

Figure 18.- Continued.

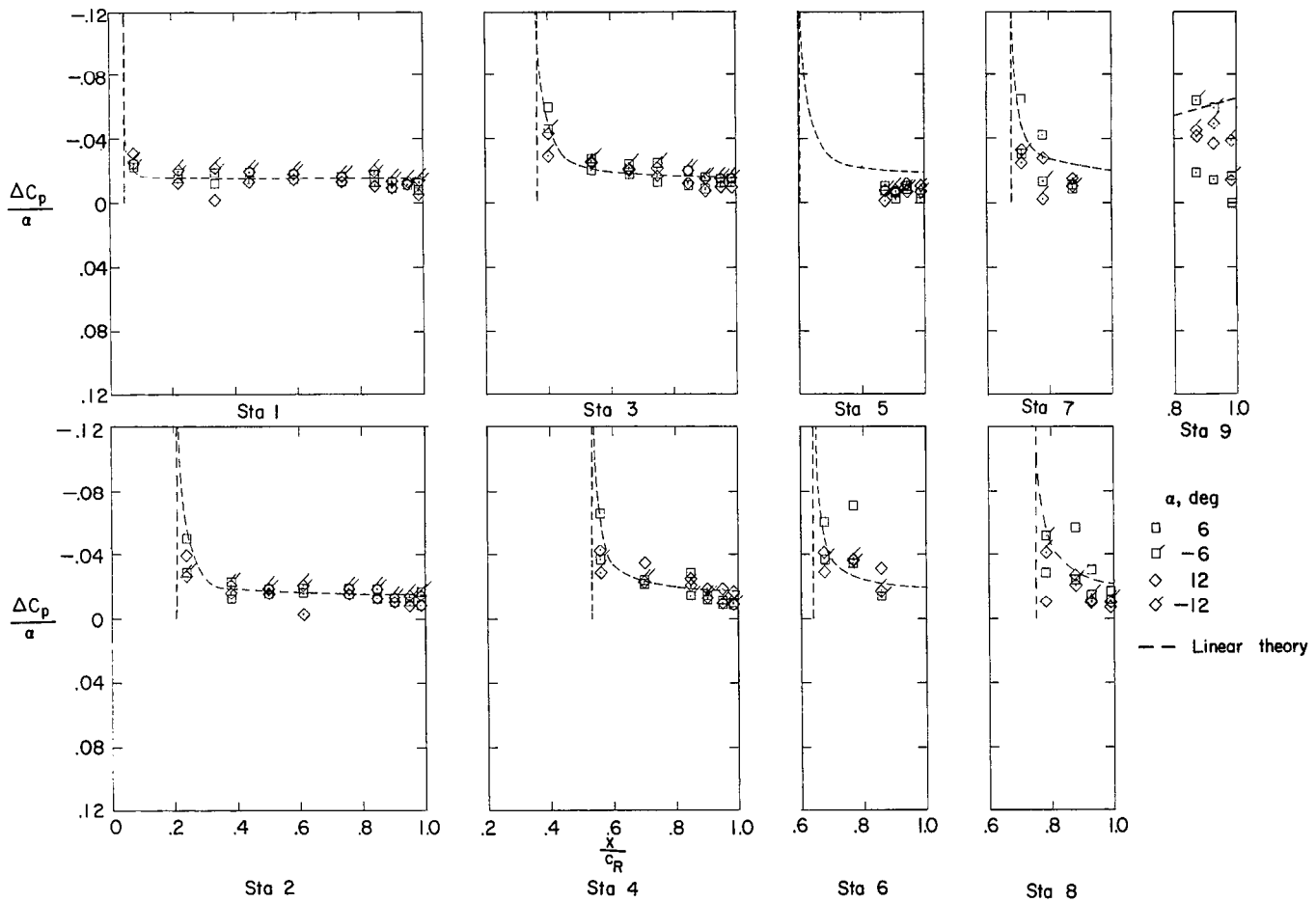

(i) Pressure coefficients due to α; δ = 10°; upper surface.

Figure 18.- Continued.

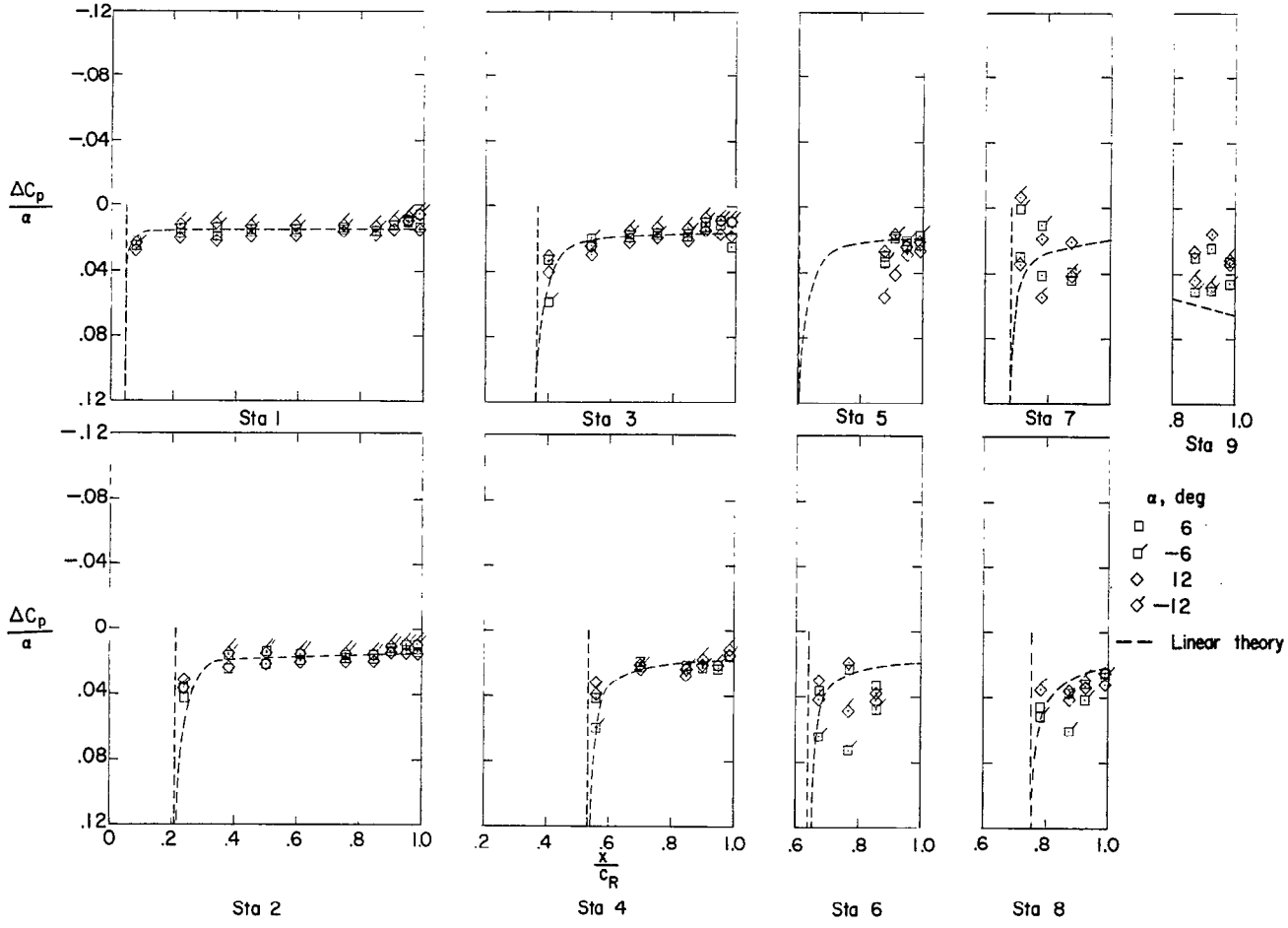

(j) Pressure coefficients due to α; $\delta = 10^{\circ}$; lower surface.

Figure 18.- Continued.

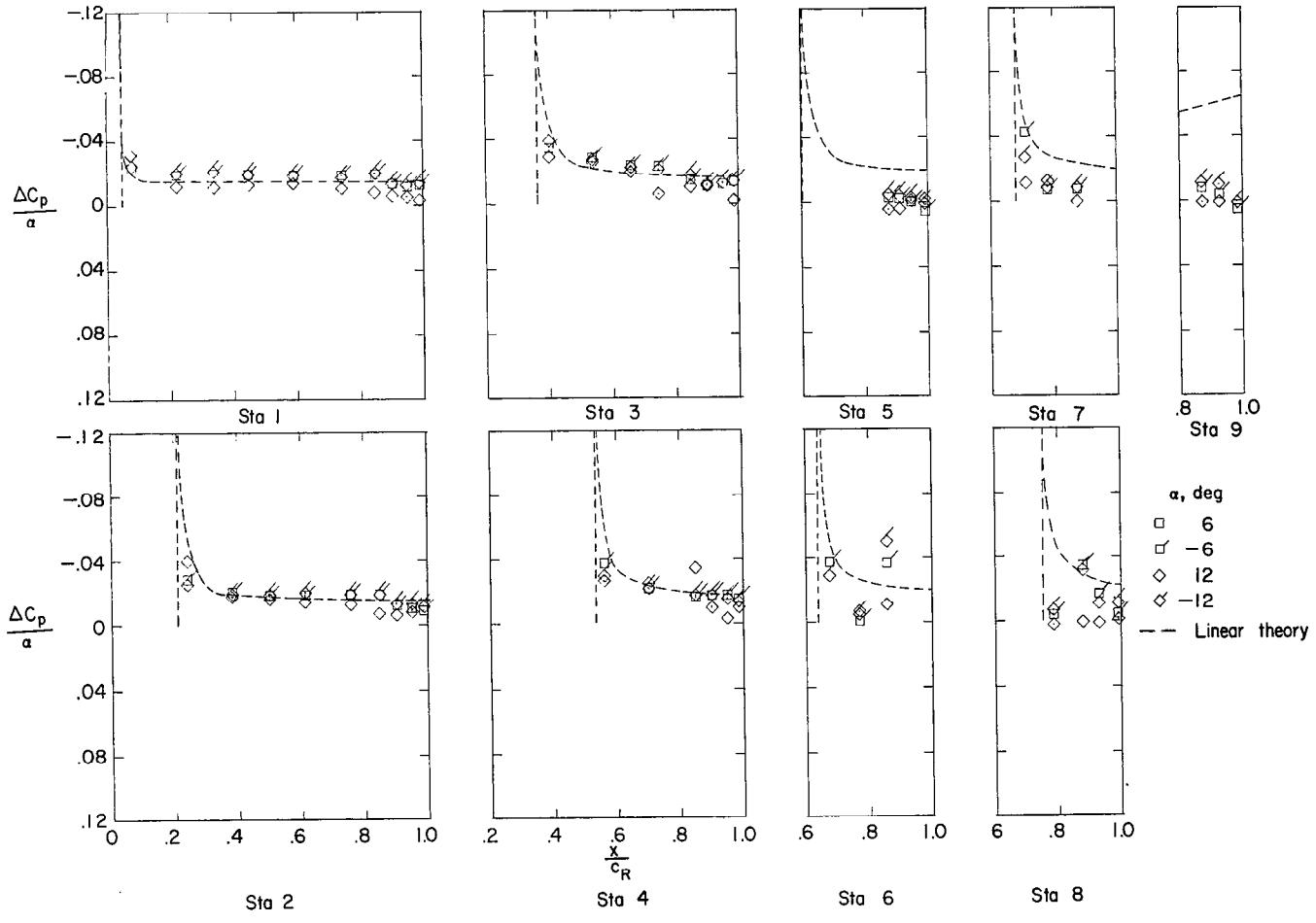

(k) Pressure coefficients due to α; δ = 30°; upper surface.

Figure 18.- Continued.

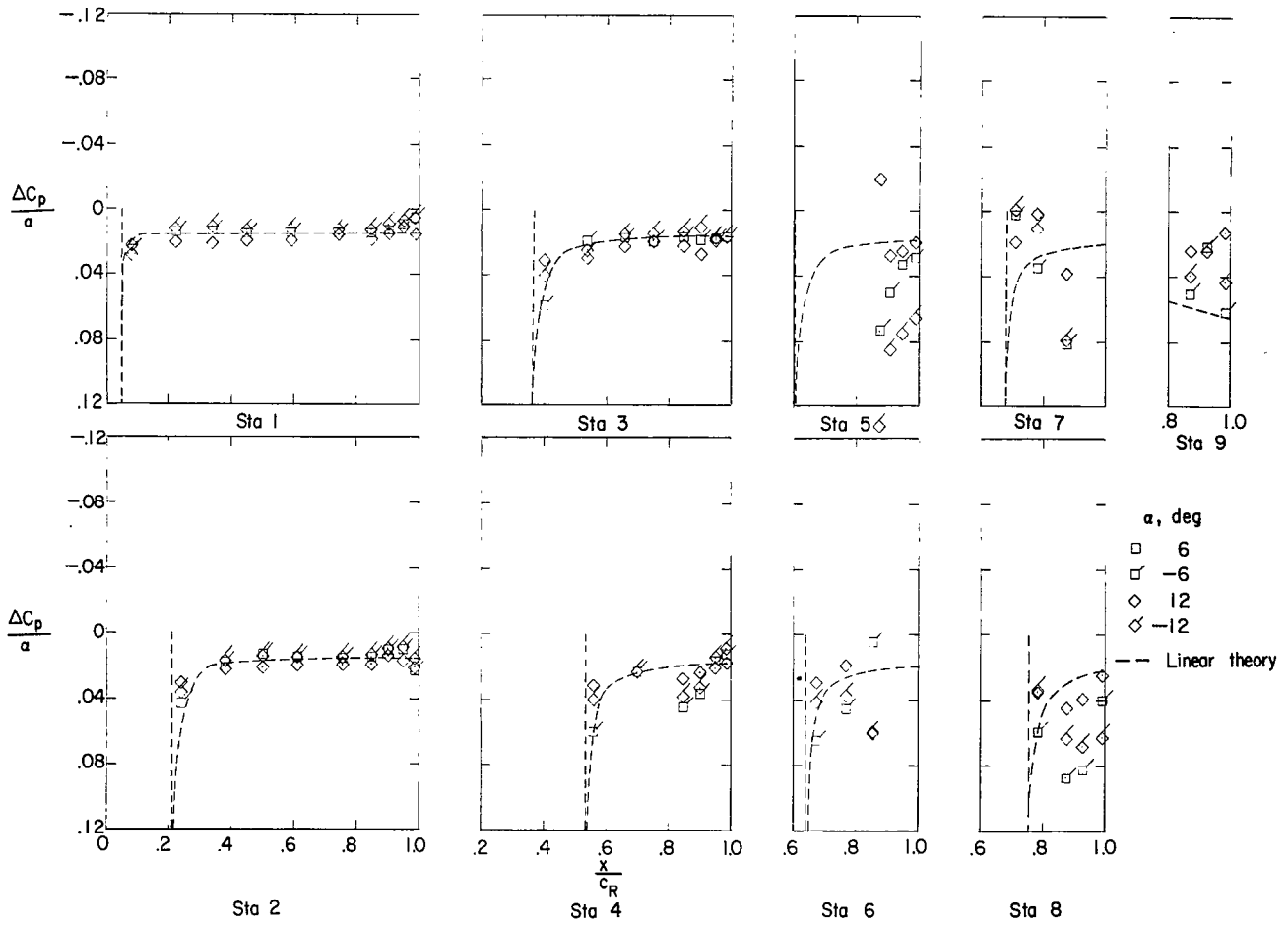

(*l*) Pressure coefficients due to α; δ = 30°; lower surface.

Figure 18.- Continued.

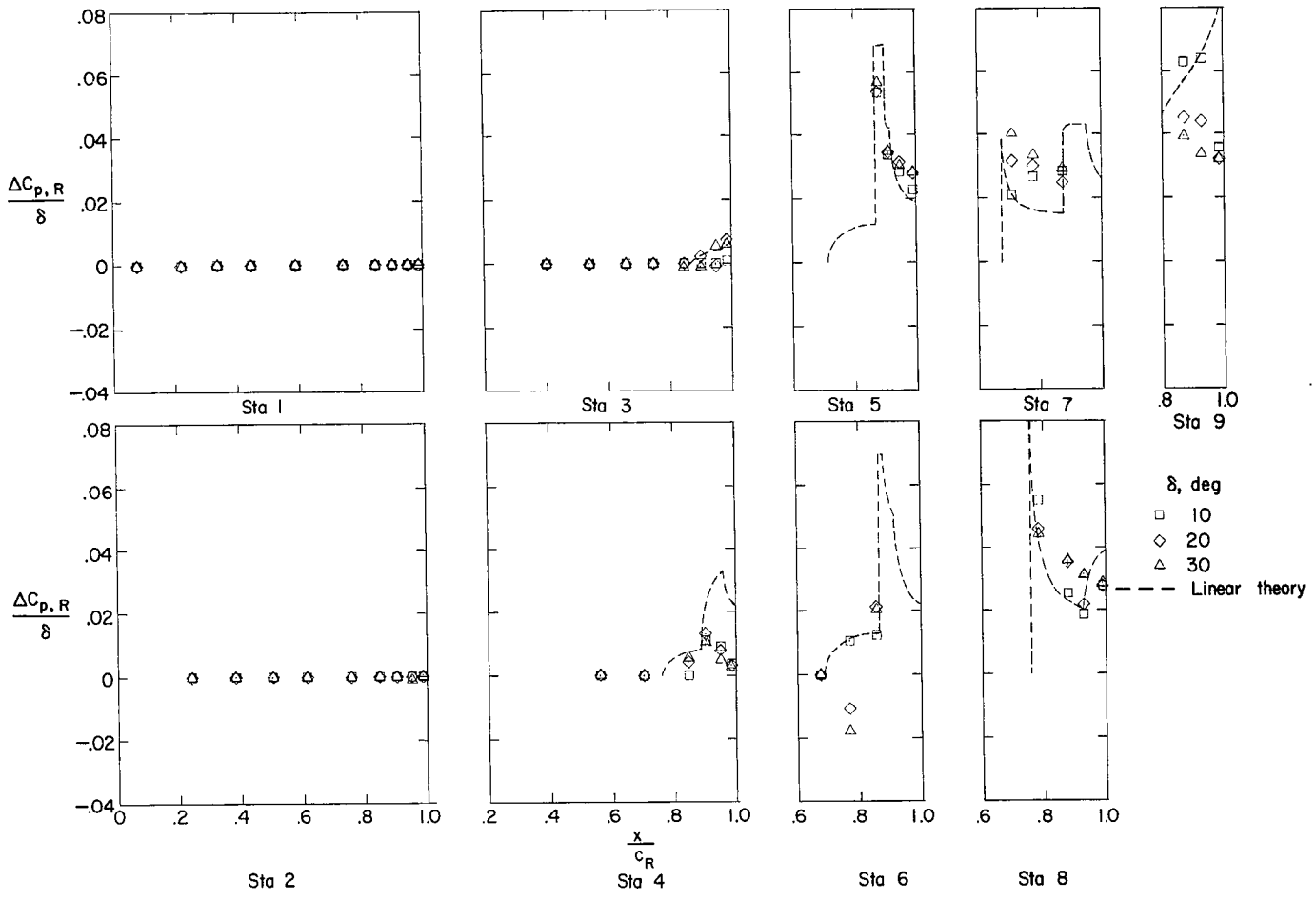

(m) Resultant pressure coefficients due to δ; $\alpha = 0^{\circ}$.

Figure 18.- Continued.

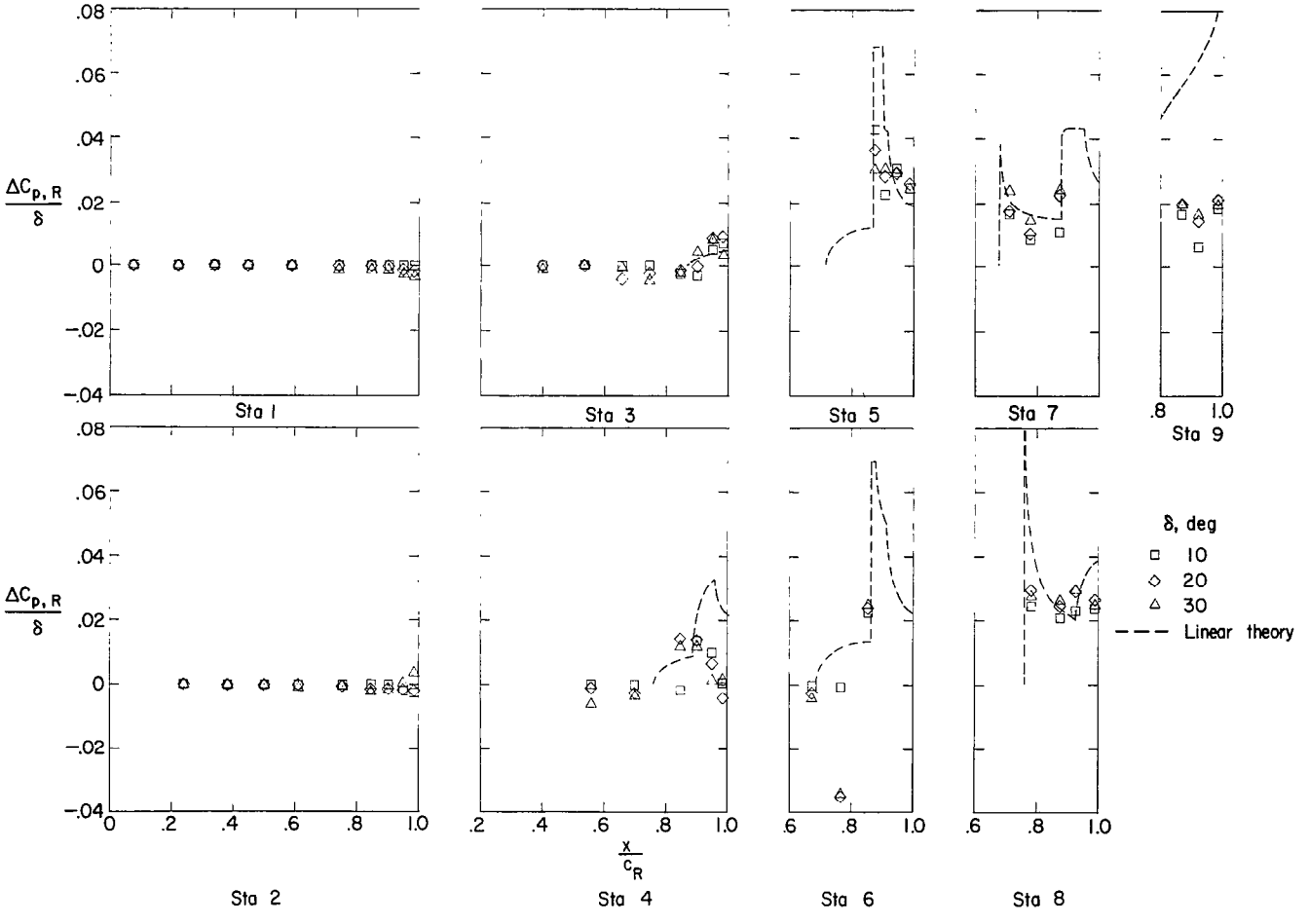

(n) Resultant pressure coefficients due to δ; $\alpha = 12^{\circ}$.

Figure 18.- Continued.

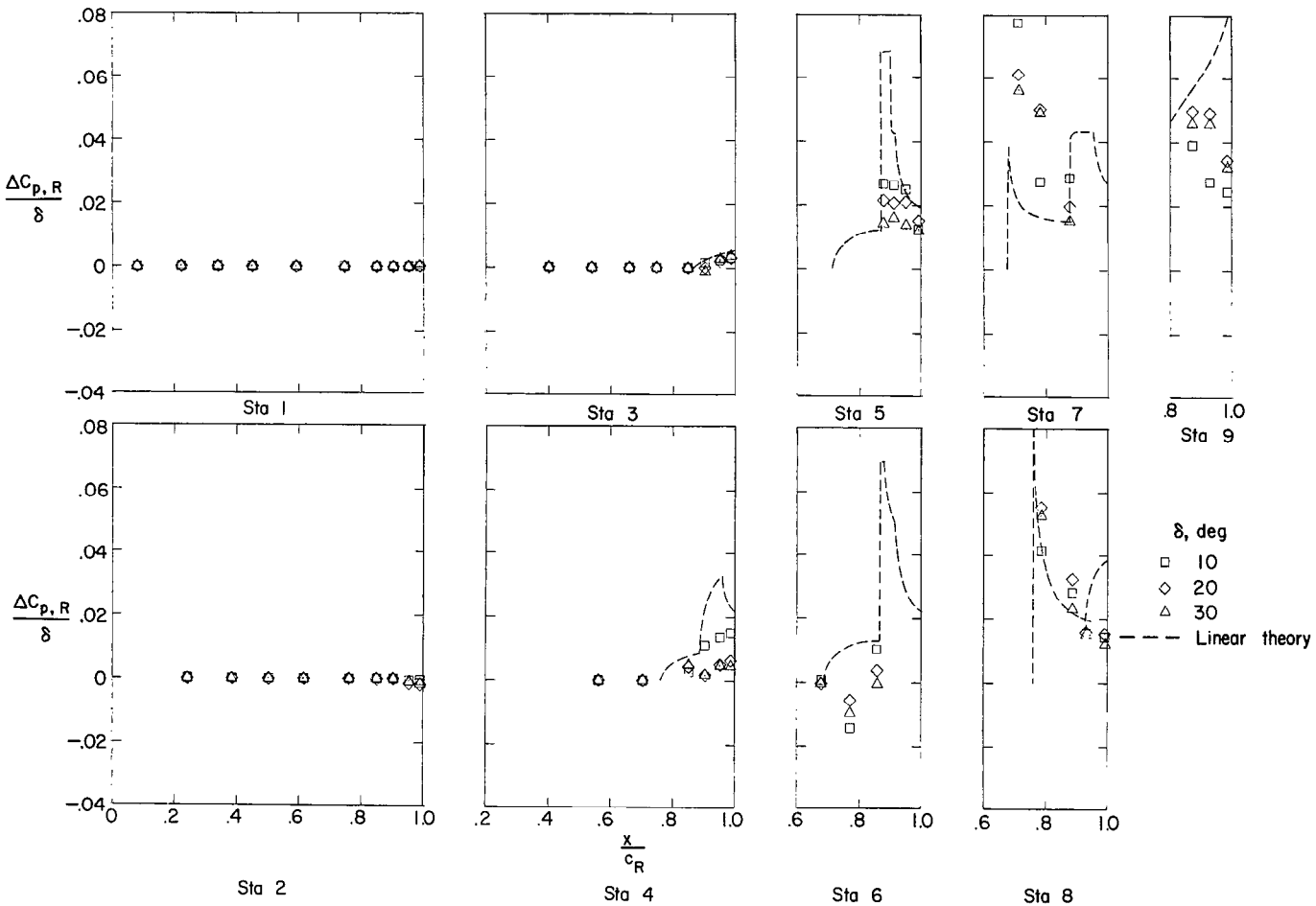

(o) Resultant pressure coefficients due to δ; $\alpha = -12^{\circ}$.

Figure 18.- Continued.

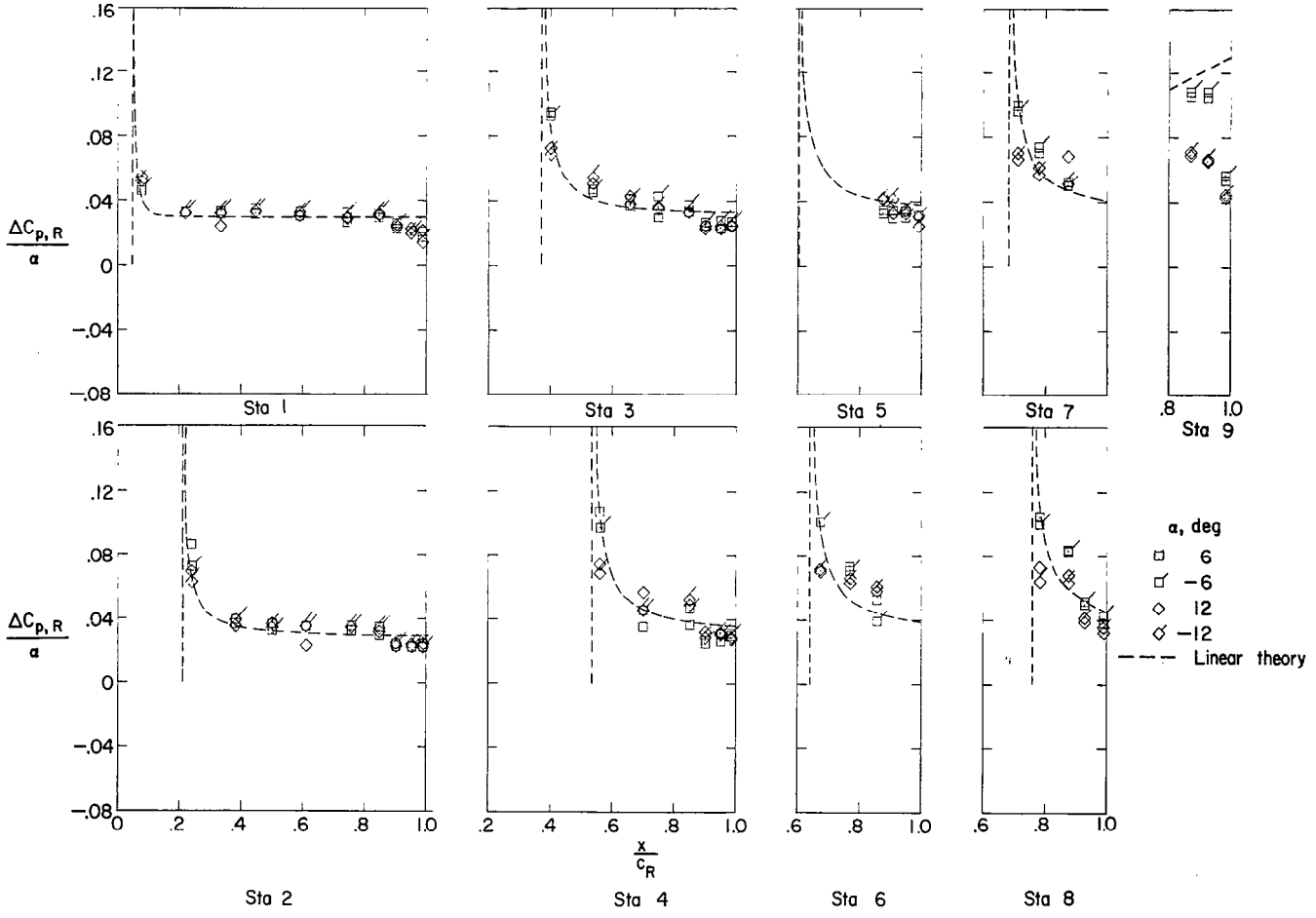

(p) Resultant pressure coefficients due to α; $\delta = 0^{\circ}$.

Figure 18.- Continued.

[redacted]

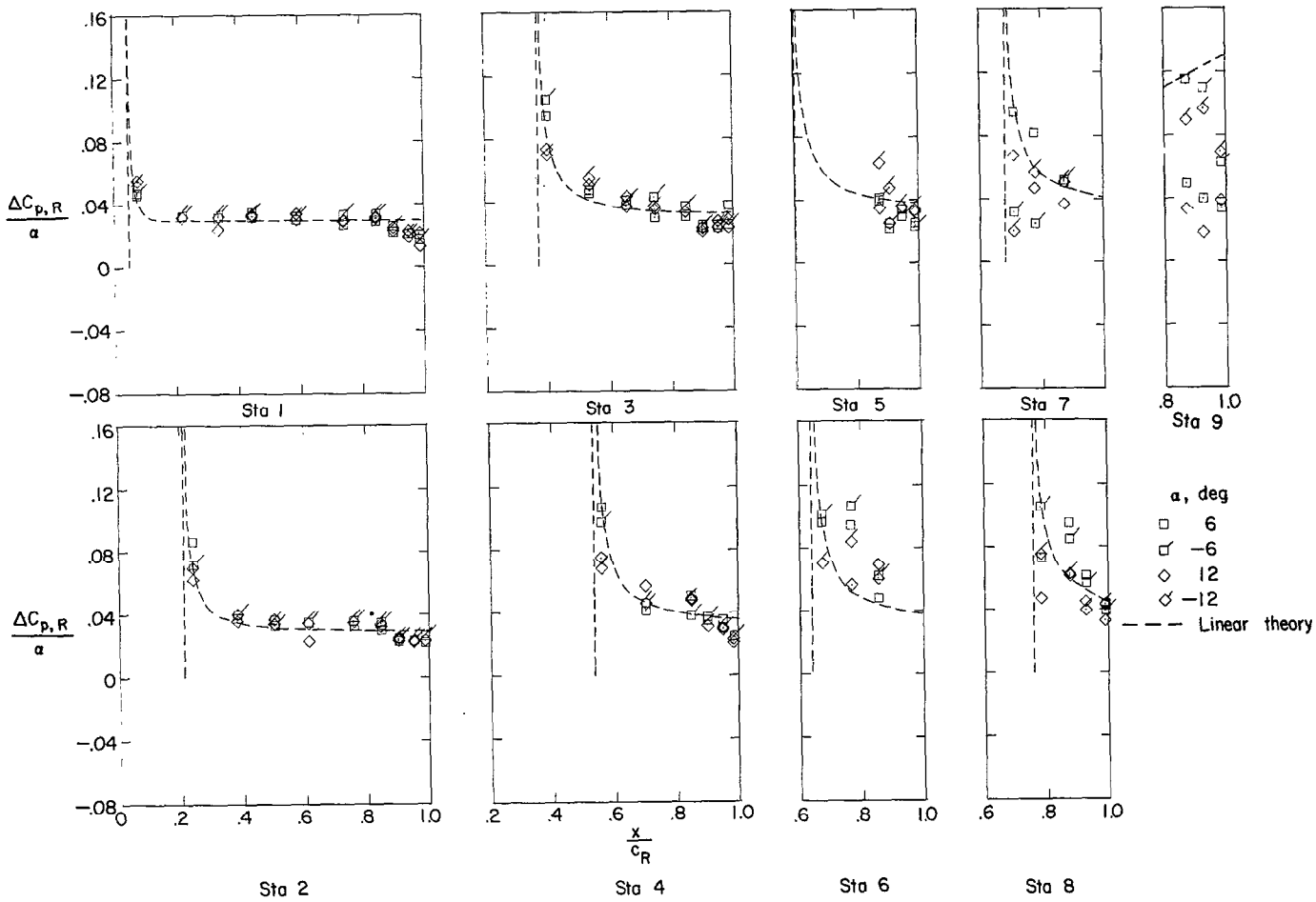

(q) Resultant pressure coefficients due to α; $\delta = 10^{\circ}$.

Figure 18.- Continued.

[redacted]

[redacted]

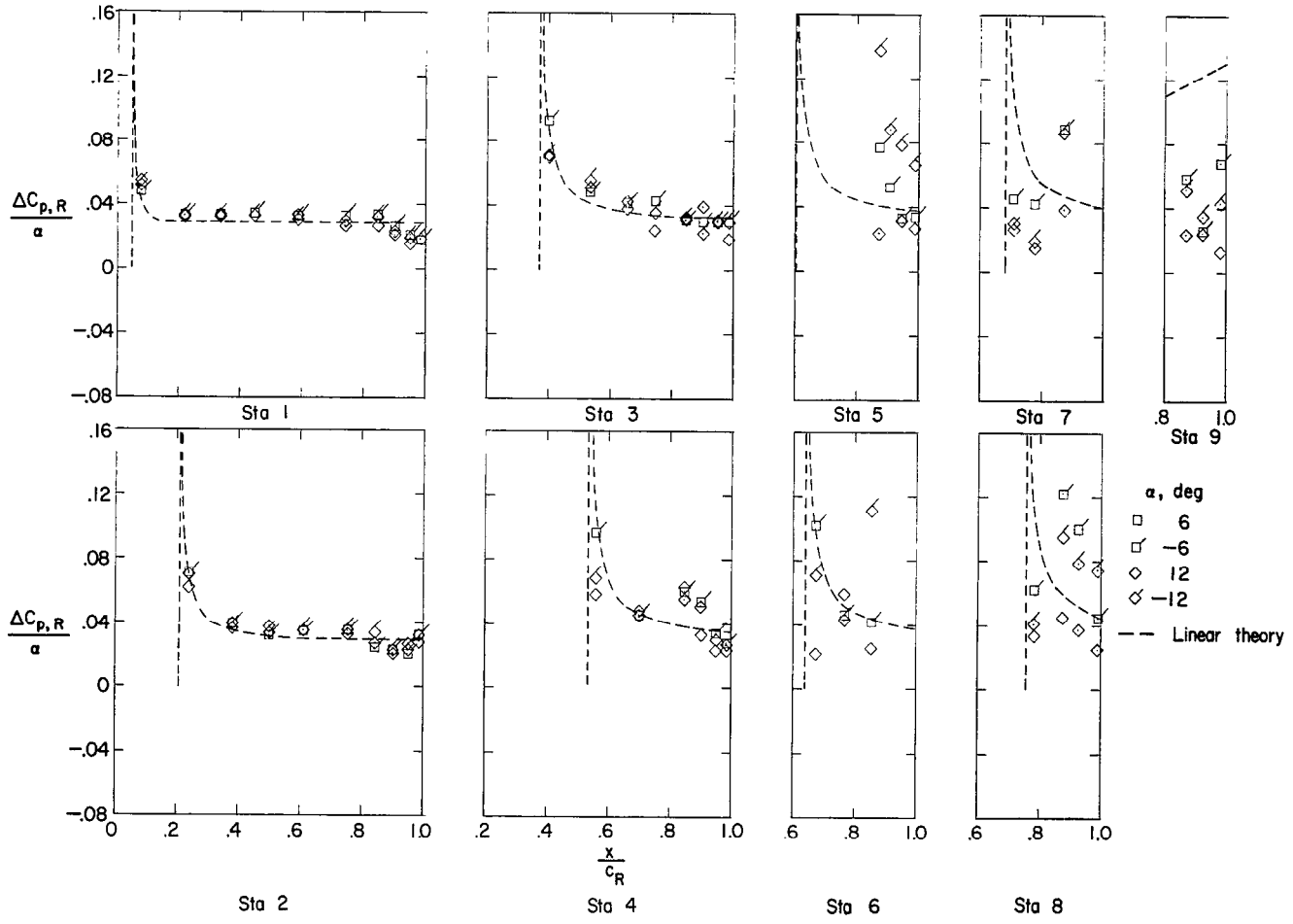

(r) Resultant pressure coefficients due to α; $\delta = 30^{\circ}$.

Figure 18.- Concluded.

[redacted]

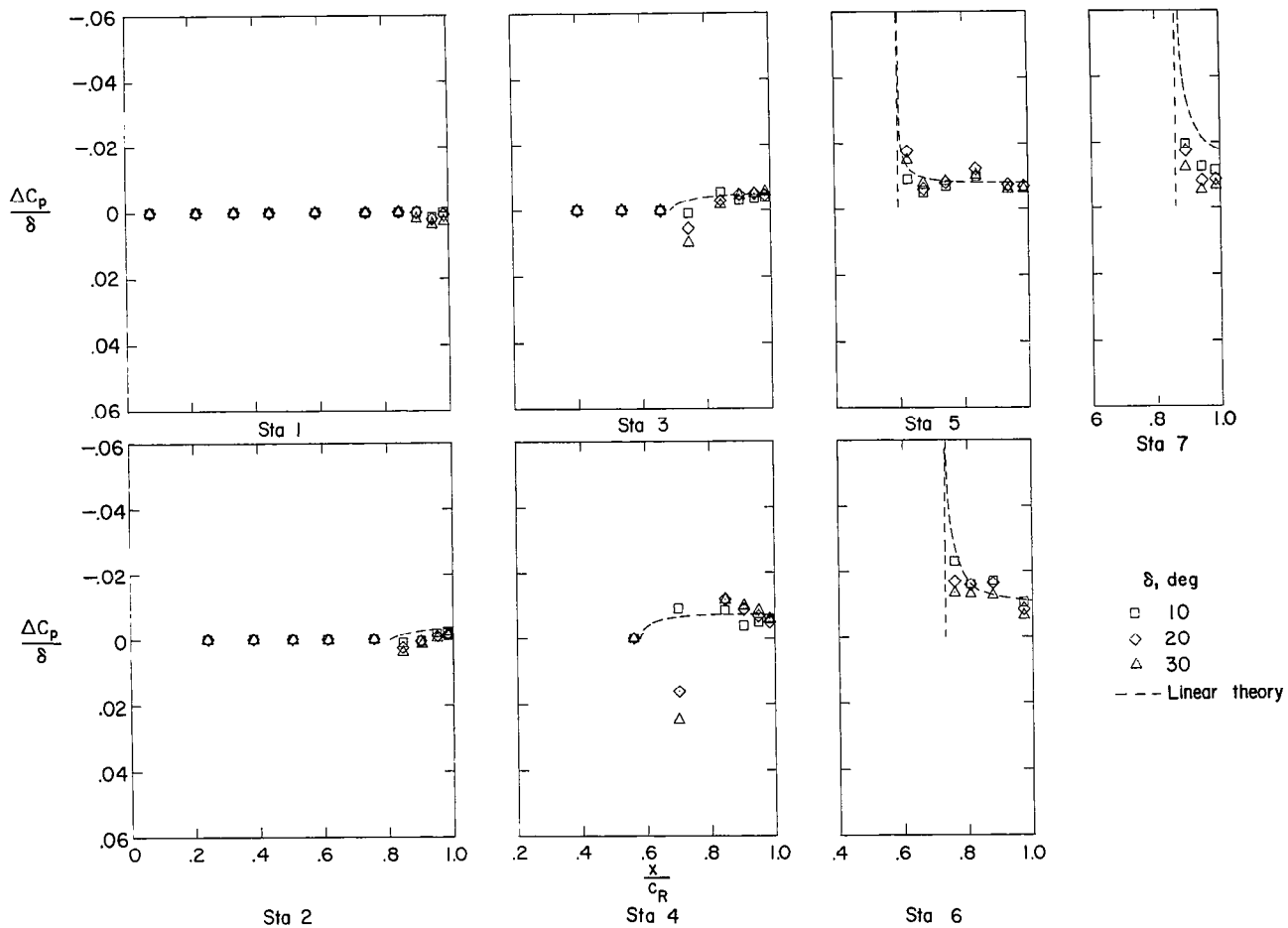

(a) Pressure coefficients due to δ; $\alpha = 0^{\circ}$; upper surface.

Figure 19.- Incremental pressure distributions due to control deflection and angle of attack for configuration F. $M = 1.61$; $R = 4.2 \times 10^6$.

[redacted]

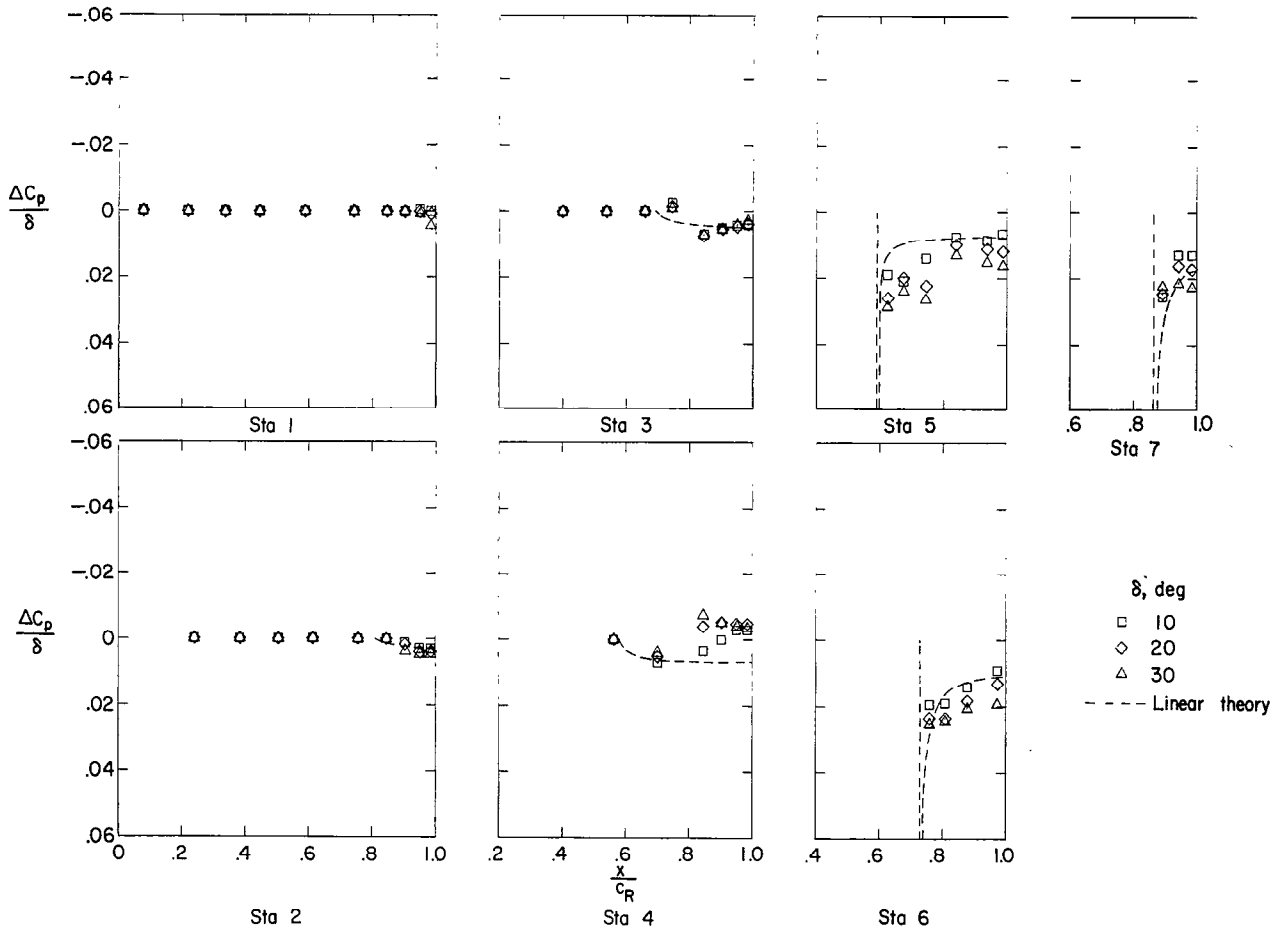

(b) Pressure coefficients due to δ; $\alpha = 0^{\circ}$; lower surface.

Figure 19.- Continued.

[redacted]

[redacted]

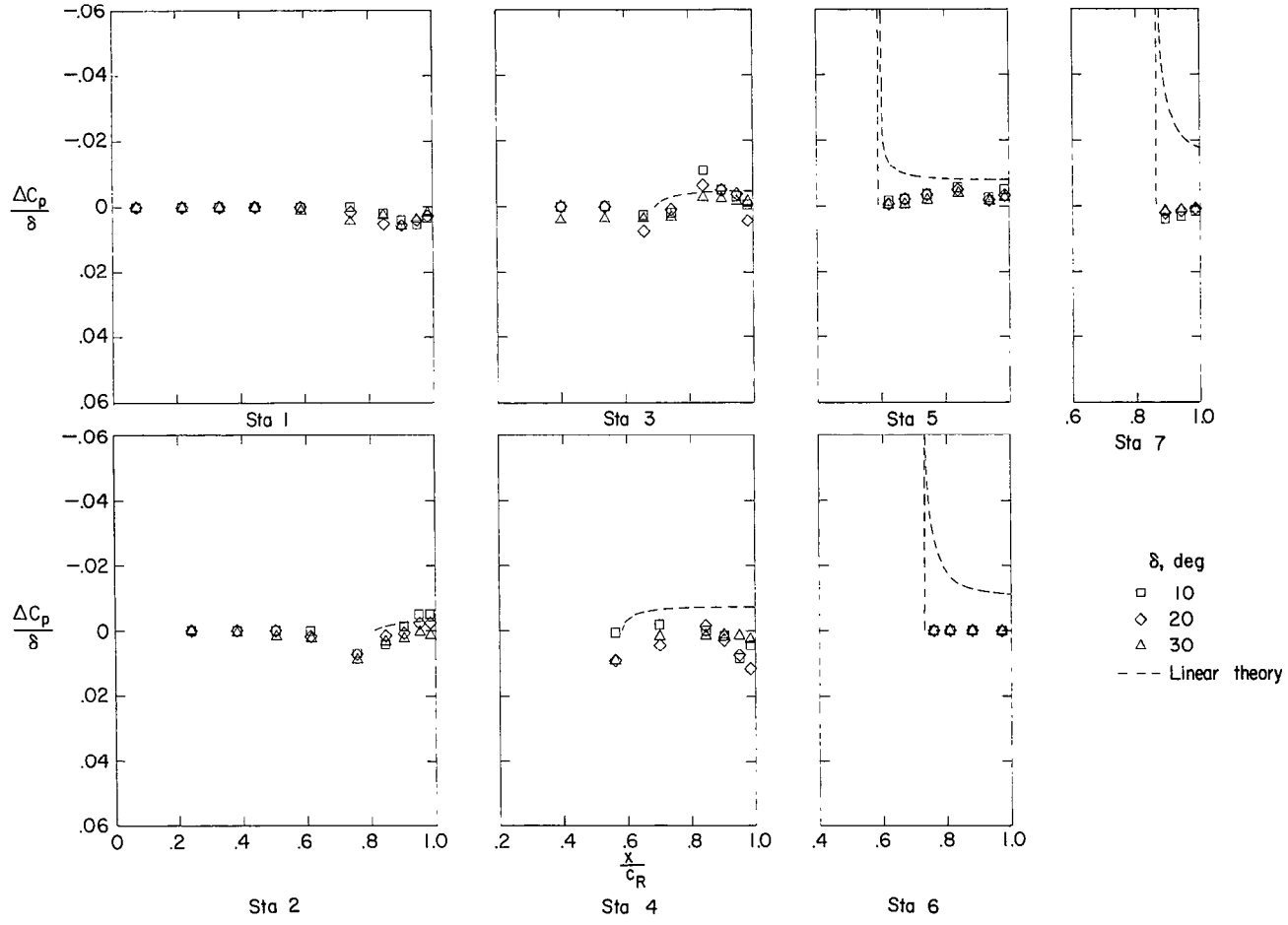

(c) Pressure coefficients due to δ; $\alpha = 12^{\circ}$; upper surface.

Figure 19.- Continued.

[redacted]

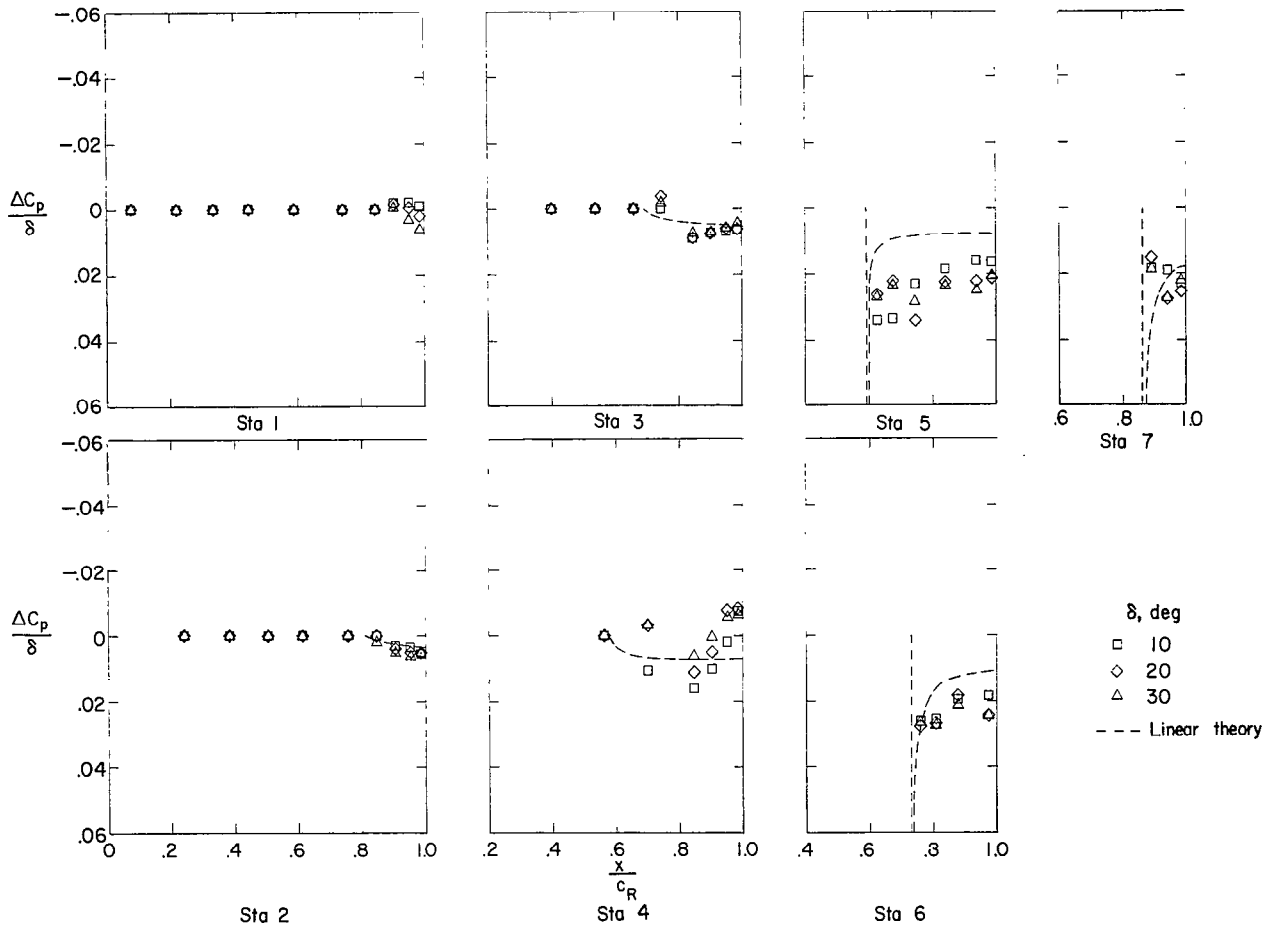

(d) Pressure coefficients due to δ; $\alpha = 12^{\circ}$; lower surface.

Figure 19.- Continued.

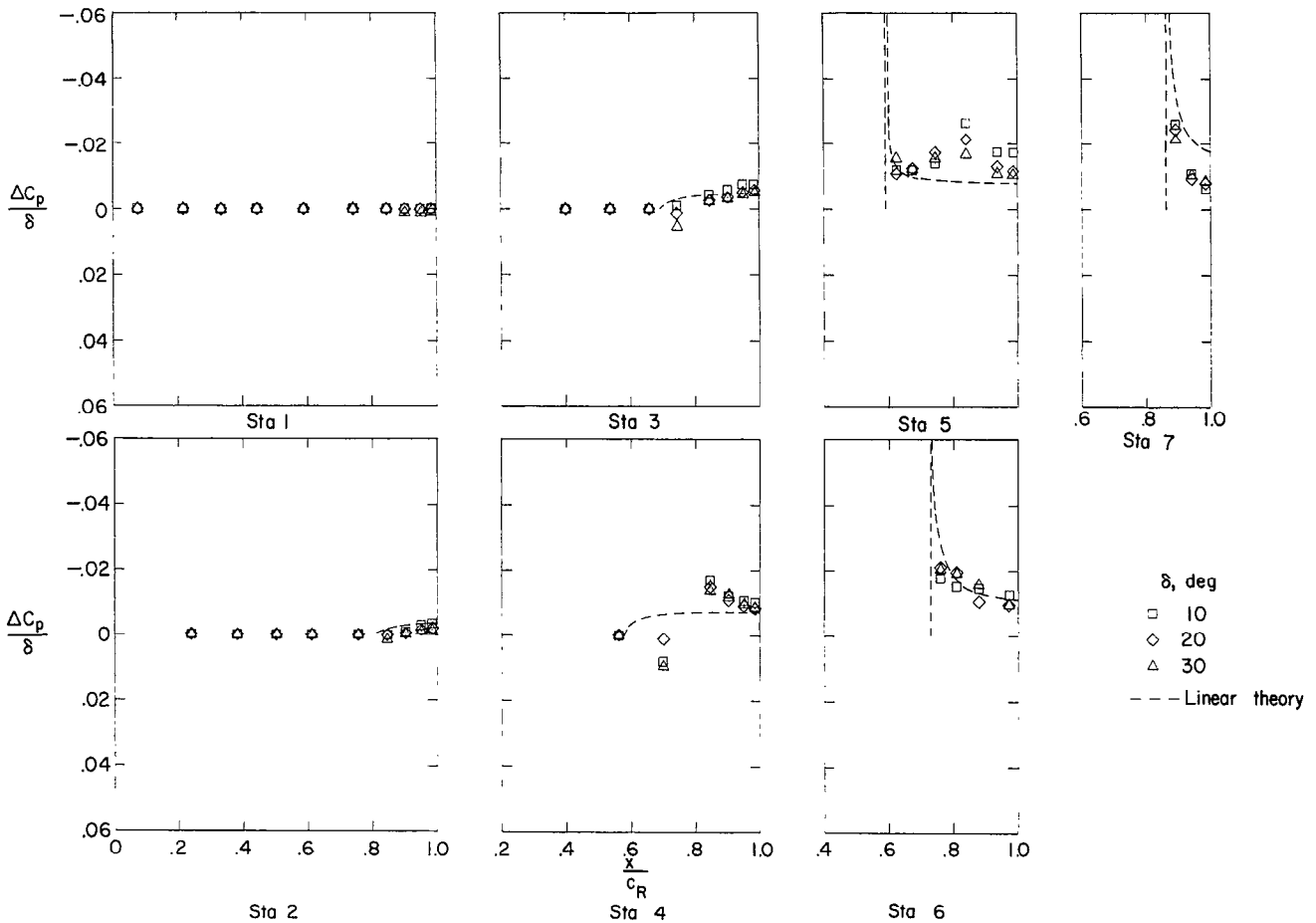

(e) Pressure coefficients due to δ; α = -12°; upper surface.

Figure 19.- Continued.

[redacted]

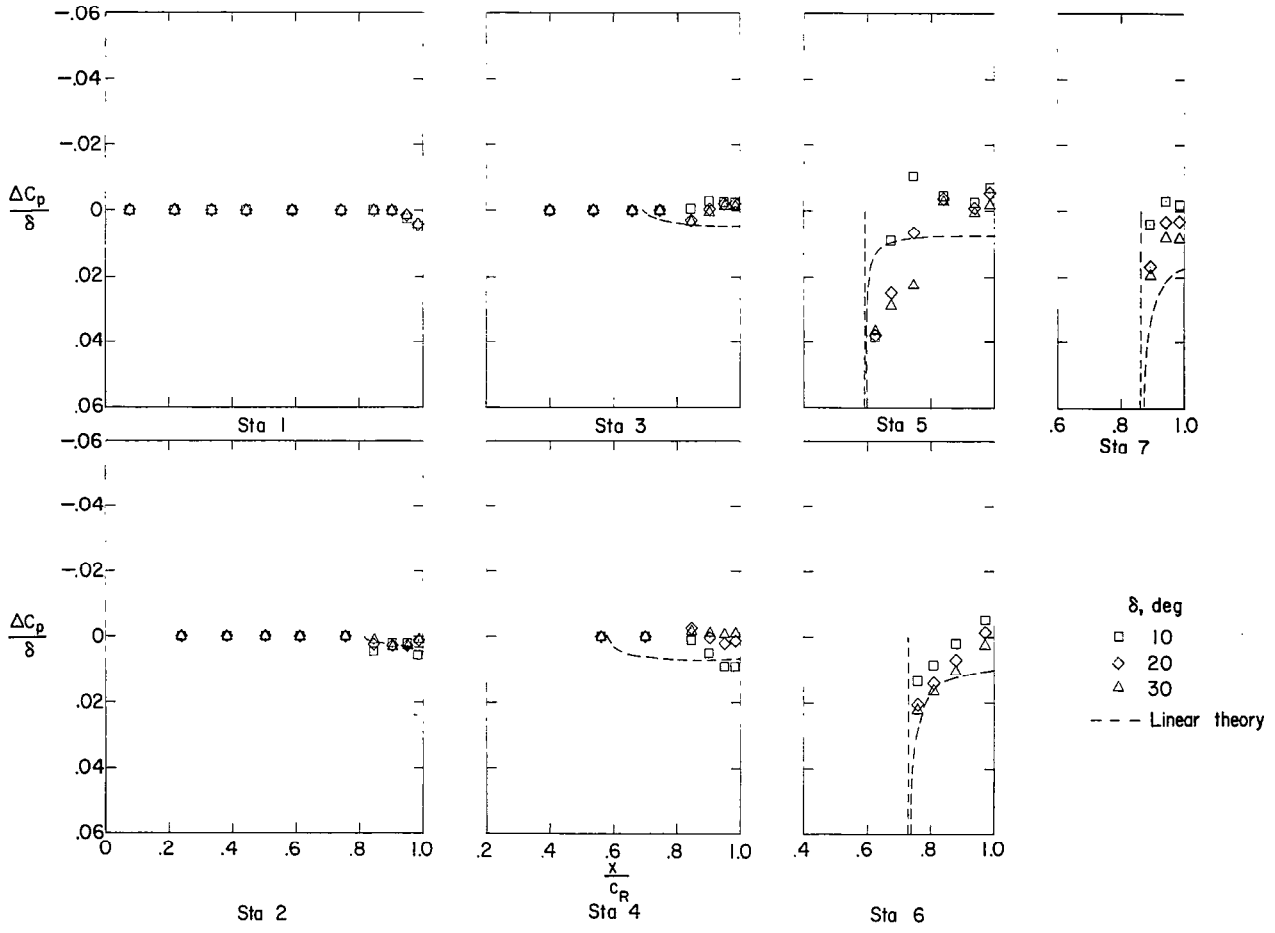

(f) Pressure coefficients due to δ; $\alpha = -12^{\circ}$; lower surface.

Figure 19.- Continued.

[redacted]

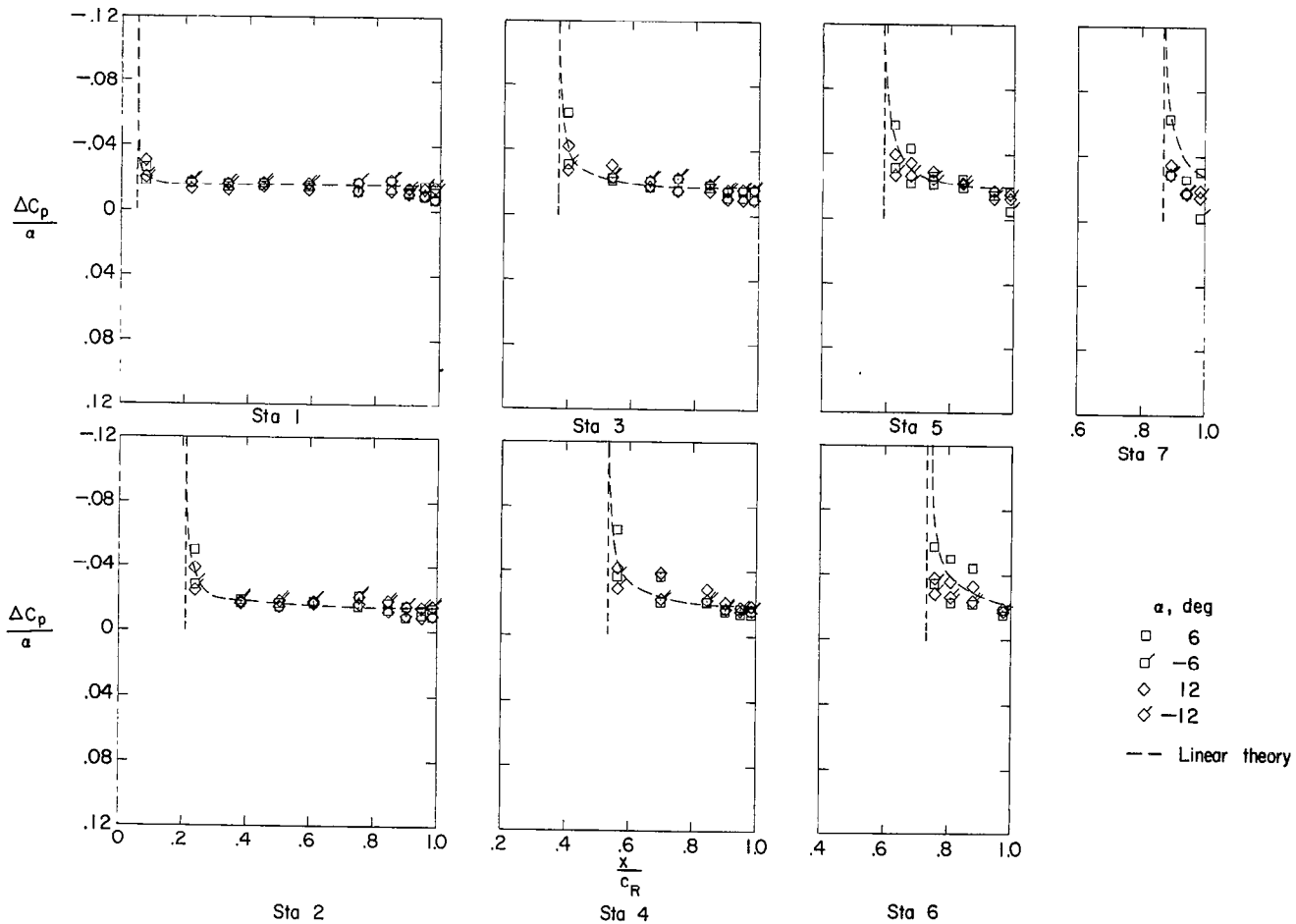

(g) Pressure coefficients due to α; δ = 0°; upper surface.

Figure 19.- Continued.

[redacted]

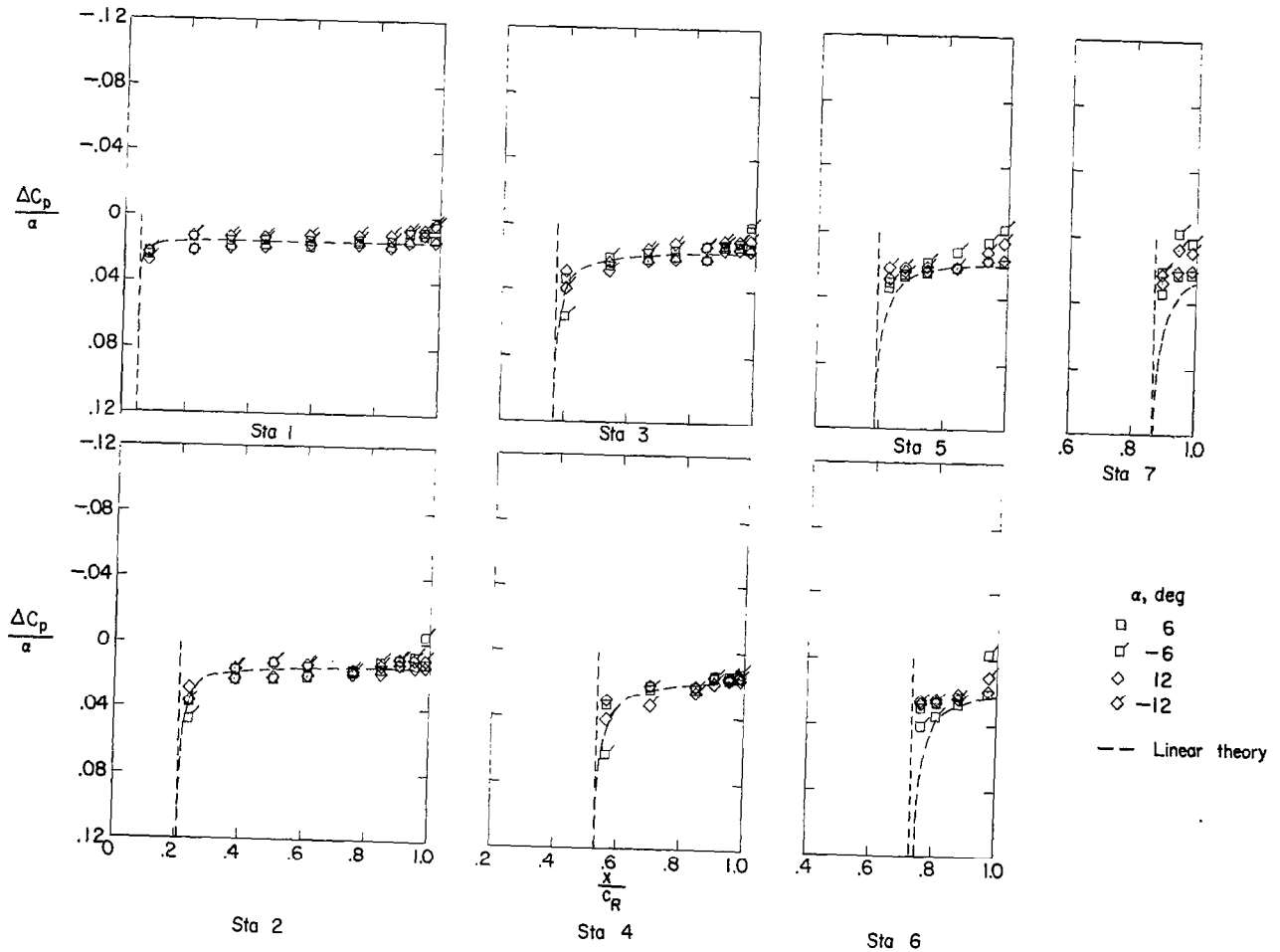

(h) Pressure coefficients due to α; δ = 0°; lower surface.

Figure 19.- Continued.

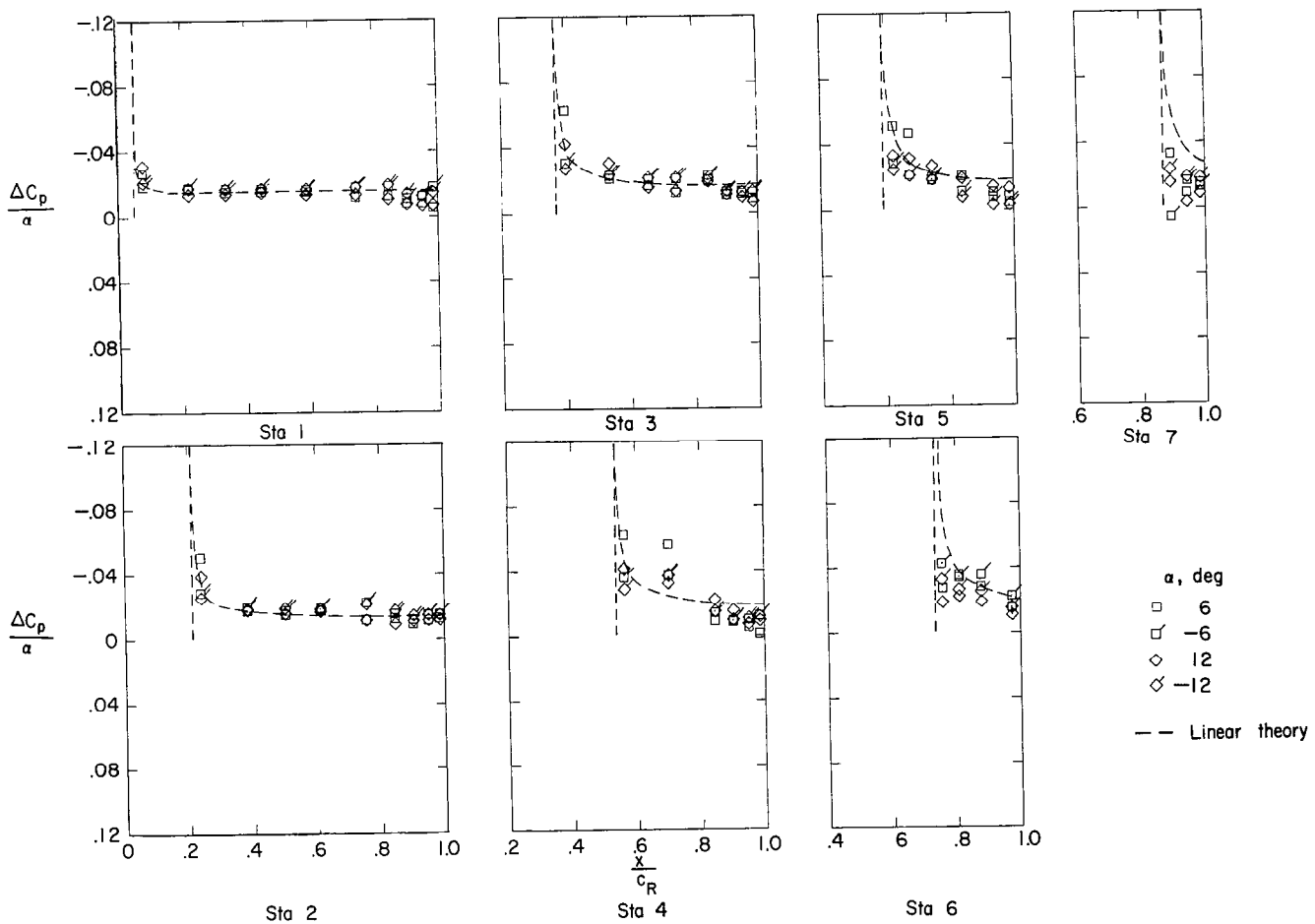

(i) Pressure coefficients due to α; δ = 10°; upper surface.

Figure 19.- Continued.

[redacted]

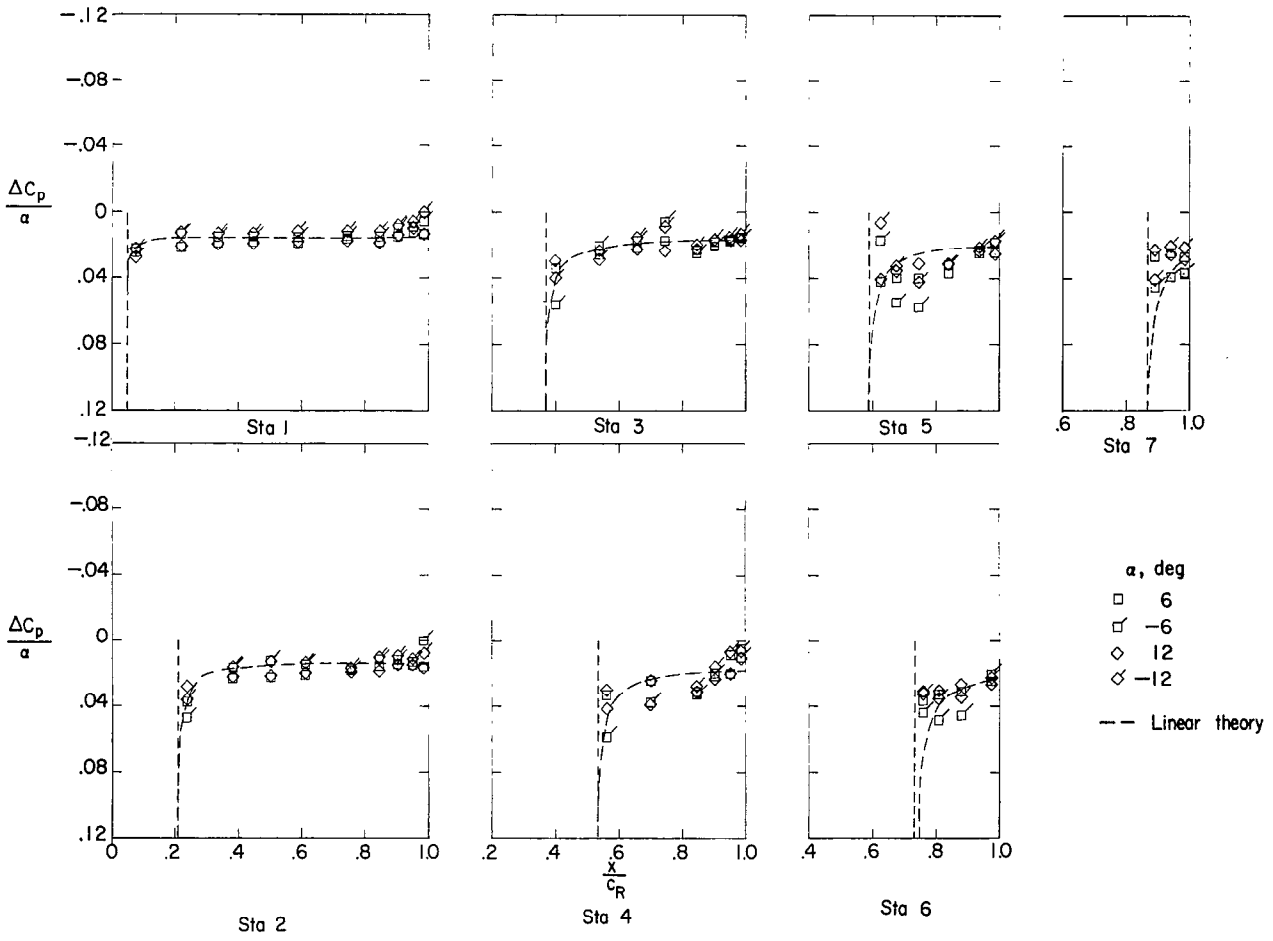

(j) Pressure coefficients due to α; δ = 10°; lower surface.

Figure 19.- Continued.

[redacted]

[redacted]

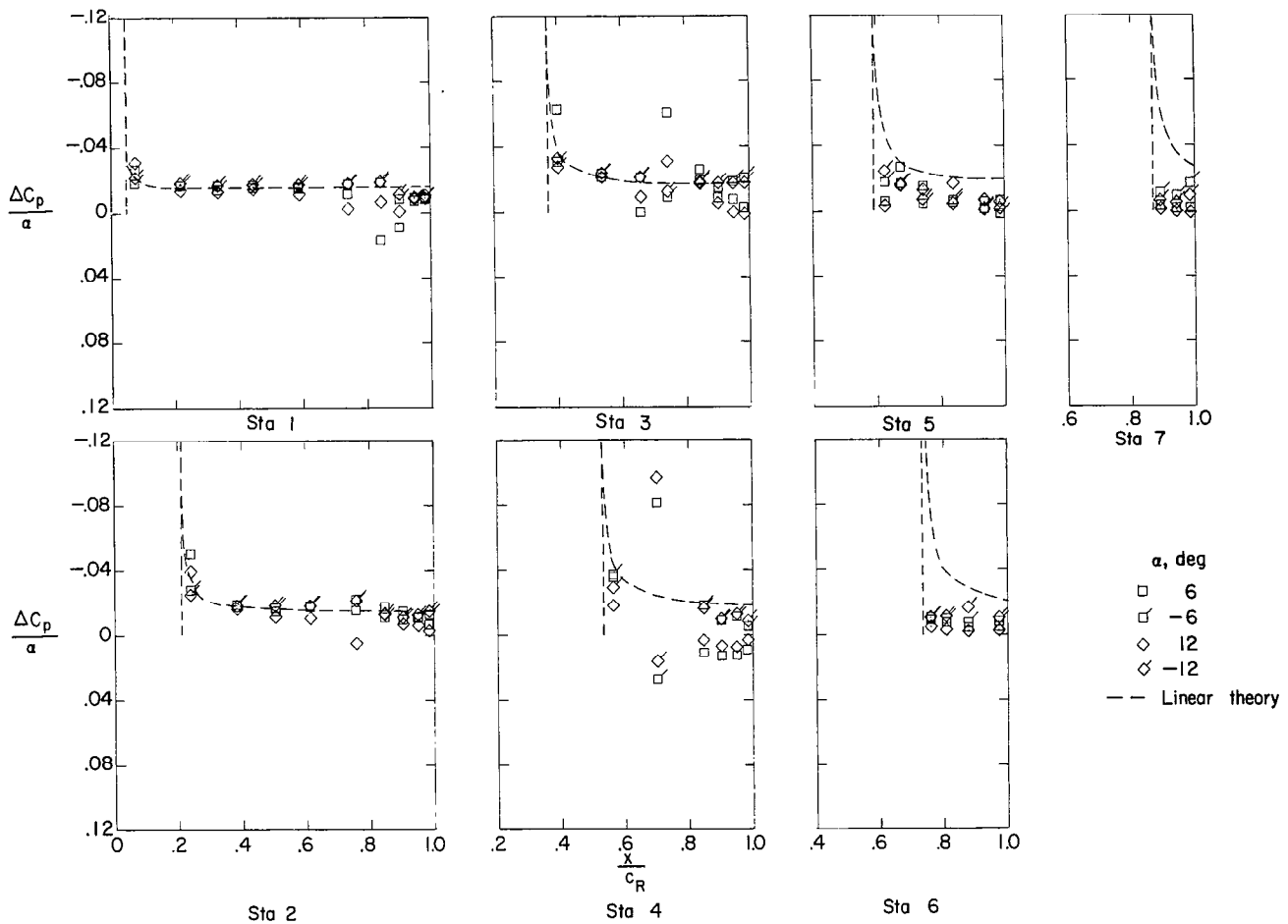

(k) Pressure coefficients due to α; $\delta = 30^{\circ}$; upper surface.

Figure 19.- Continued.

[redacted]

[redacted]

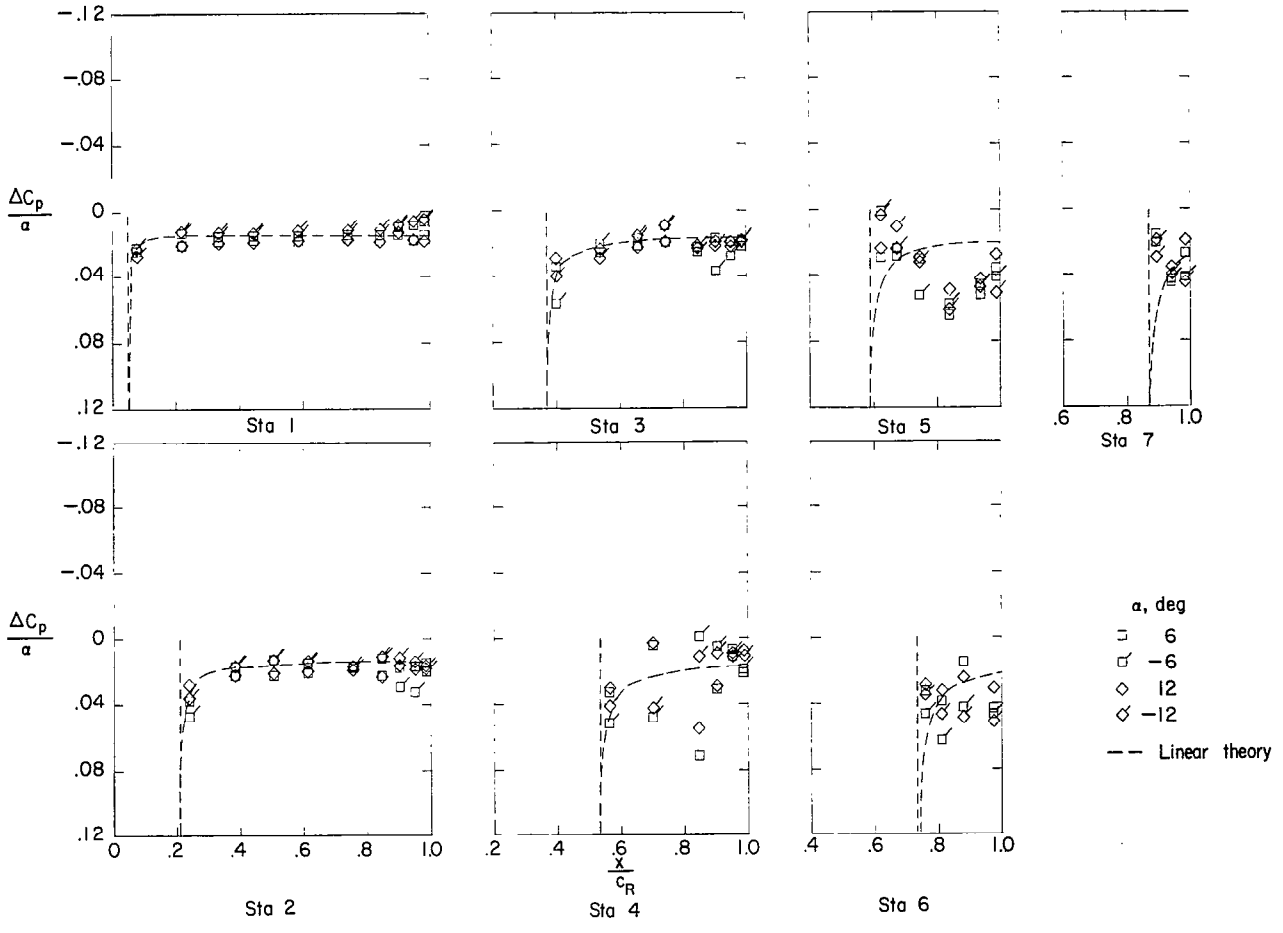

(l) Pressure coefficients due to α; δ = 30°; lower surface.

Figure 19.- Continued.

[redacted]

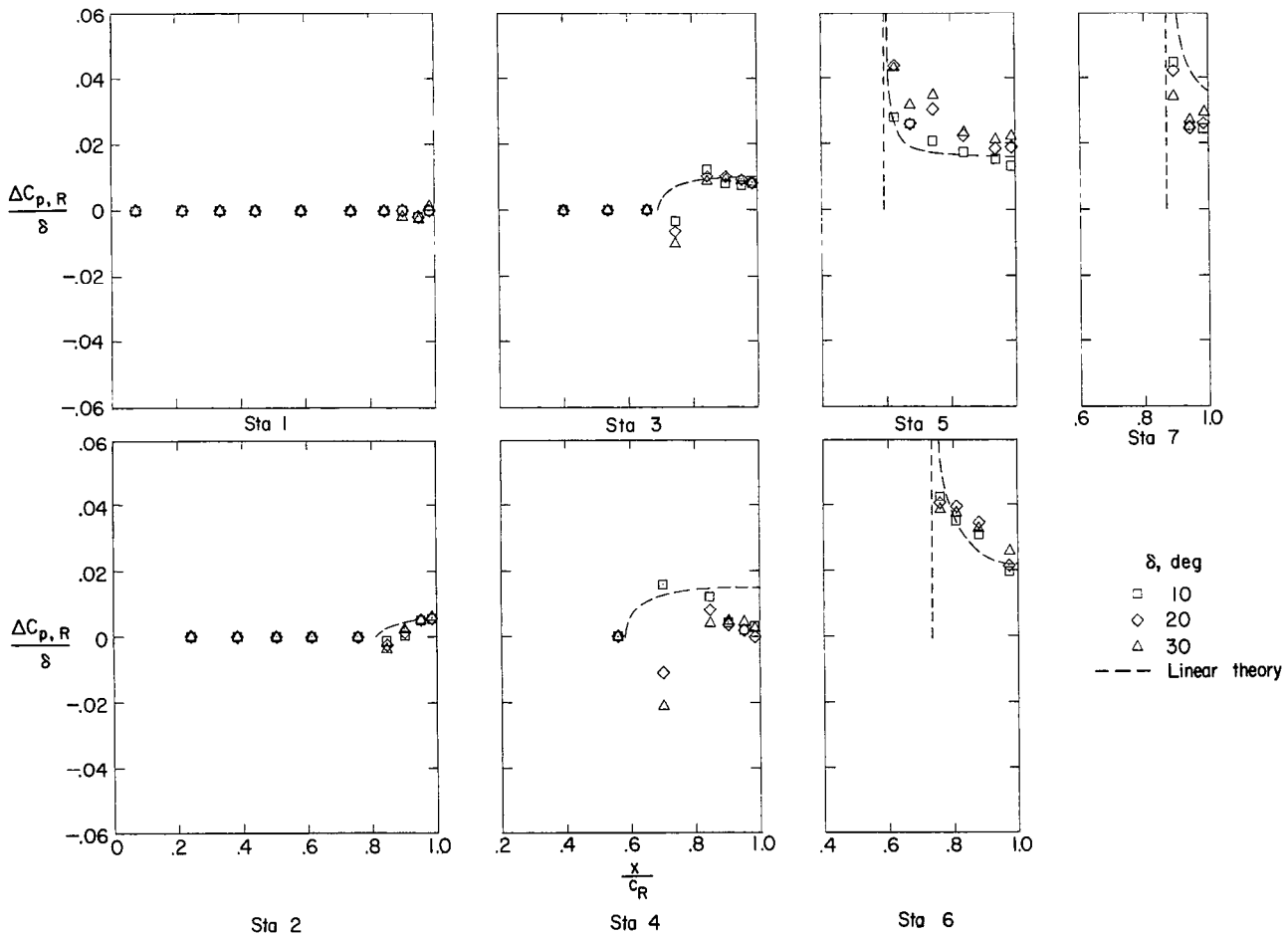

(m) Resultant pressure coefficients due to δ; $\alpha = 0^{\circ}$.

Figure 19.- Continued.

[redacted]

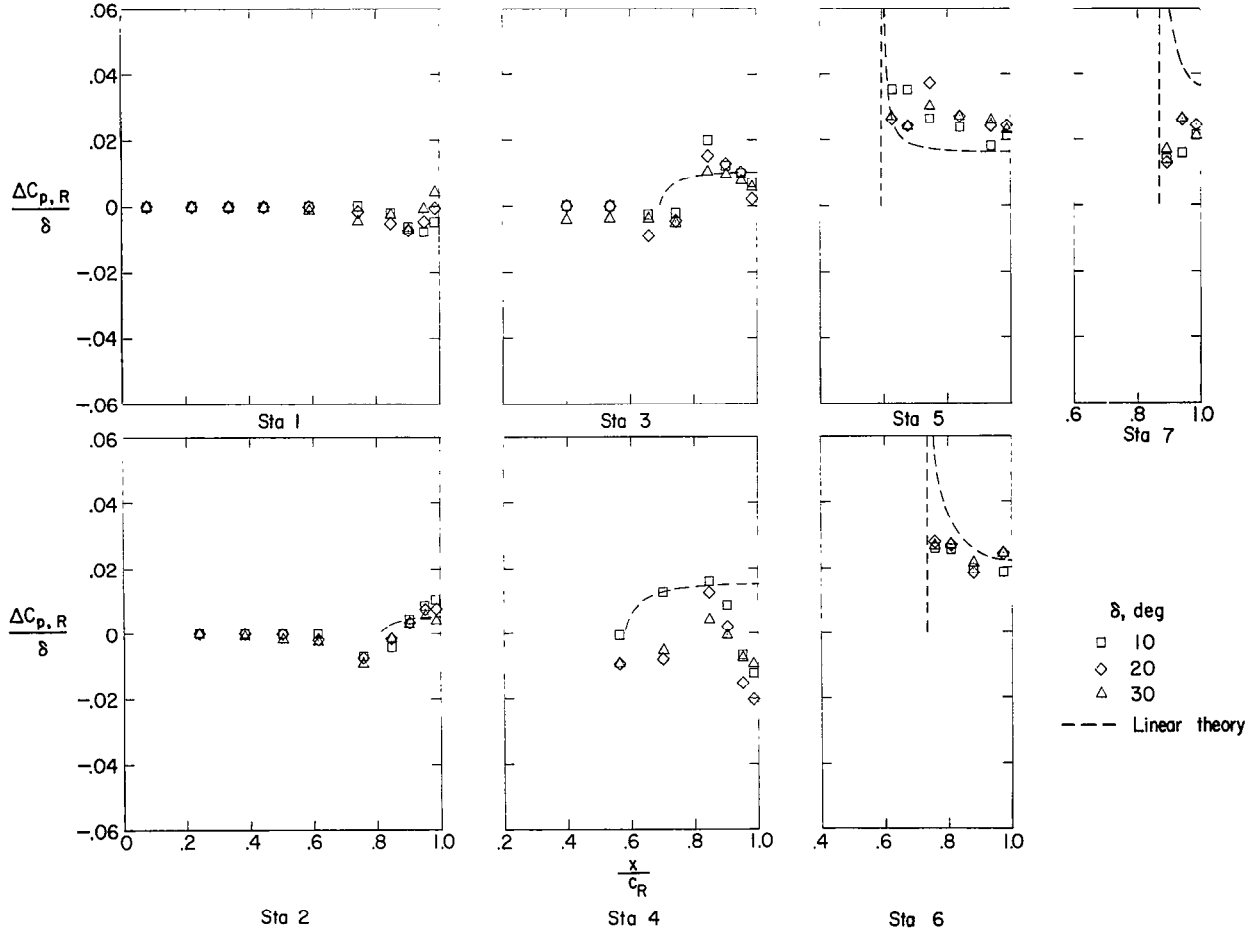

(n) Resultant pressure coefficients due to δ; $\alpha = 12^{\circ}$.

Figure 19.- Continued.

[redacted]

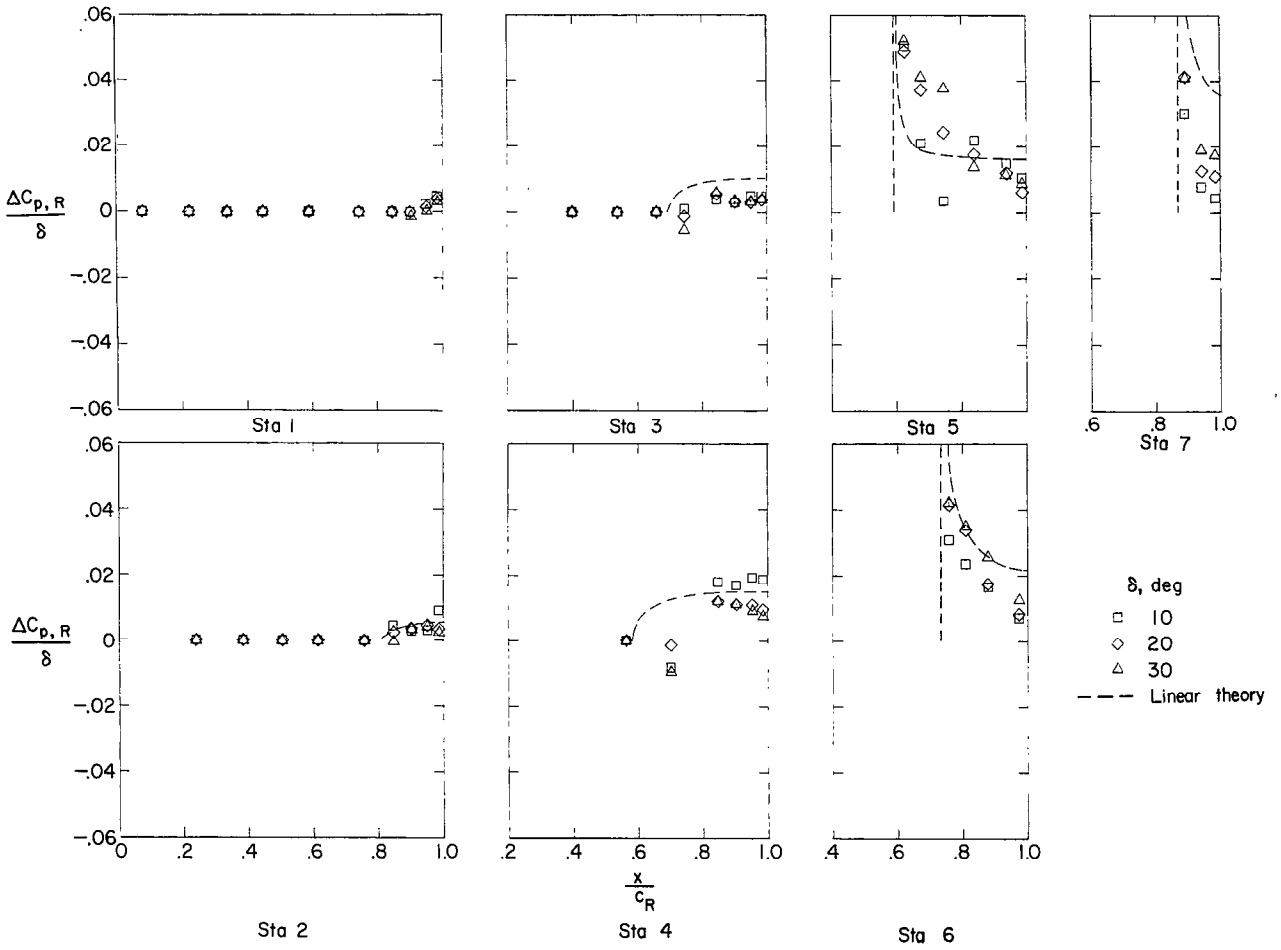

(o) Resultant pressure coefficients due to δ; $\alpha = -12^{\circ}$.

Figure 19.- Continued.

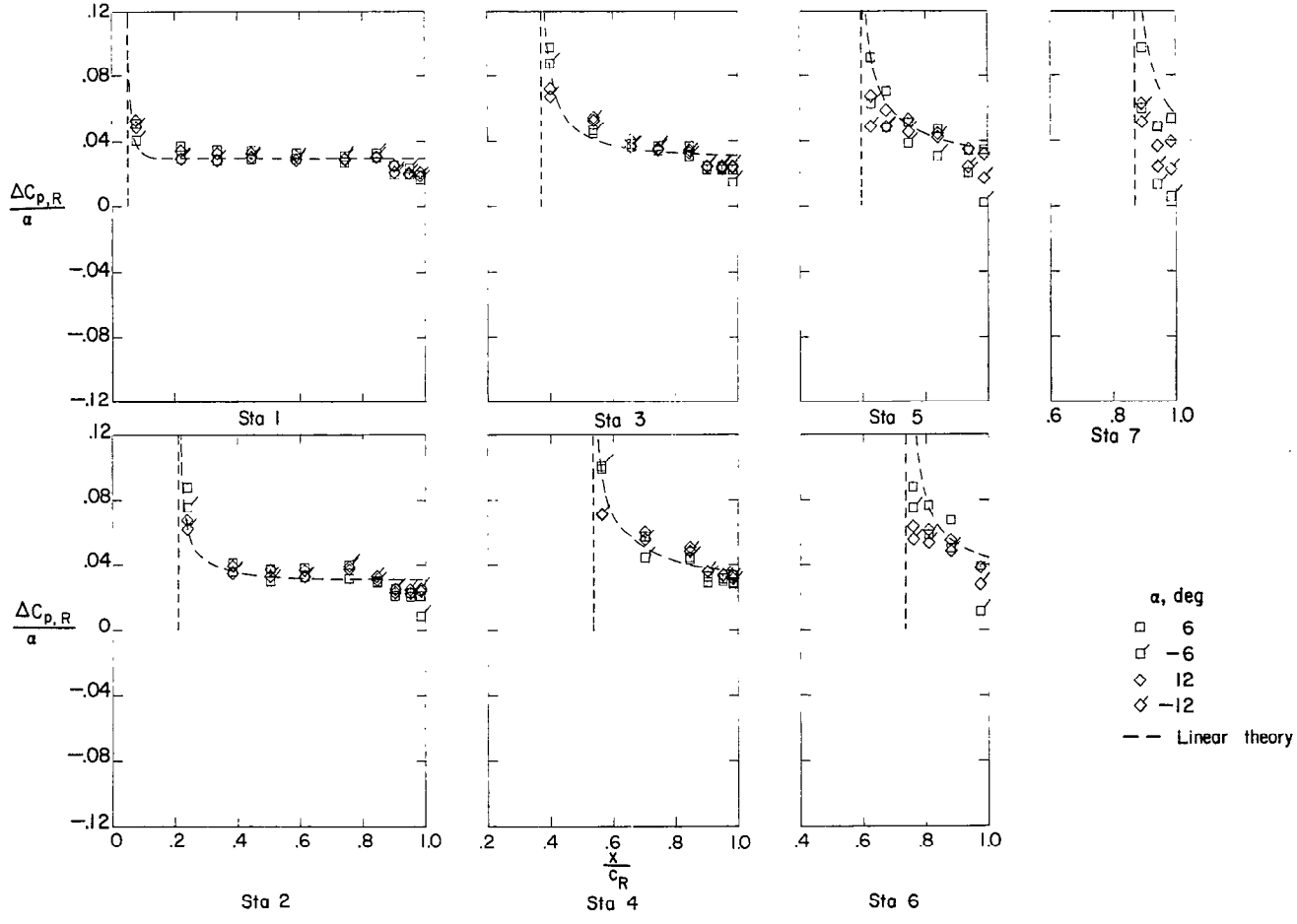

(p) Resultant pressure coefficients due to α; $\delta = 0^{\circ}$.

Figure 19.- Continued.

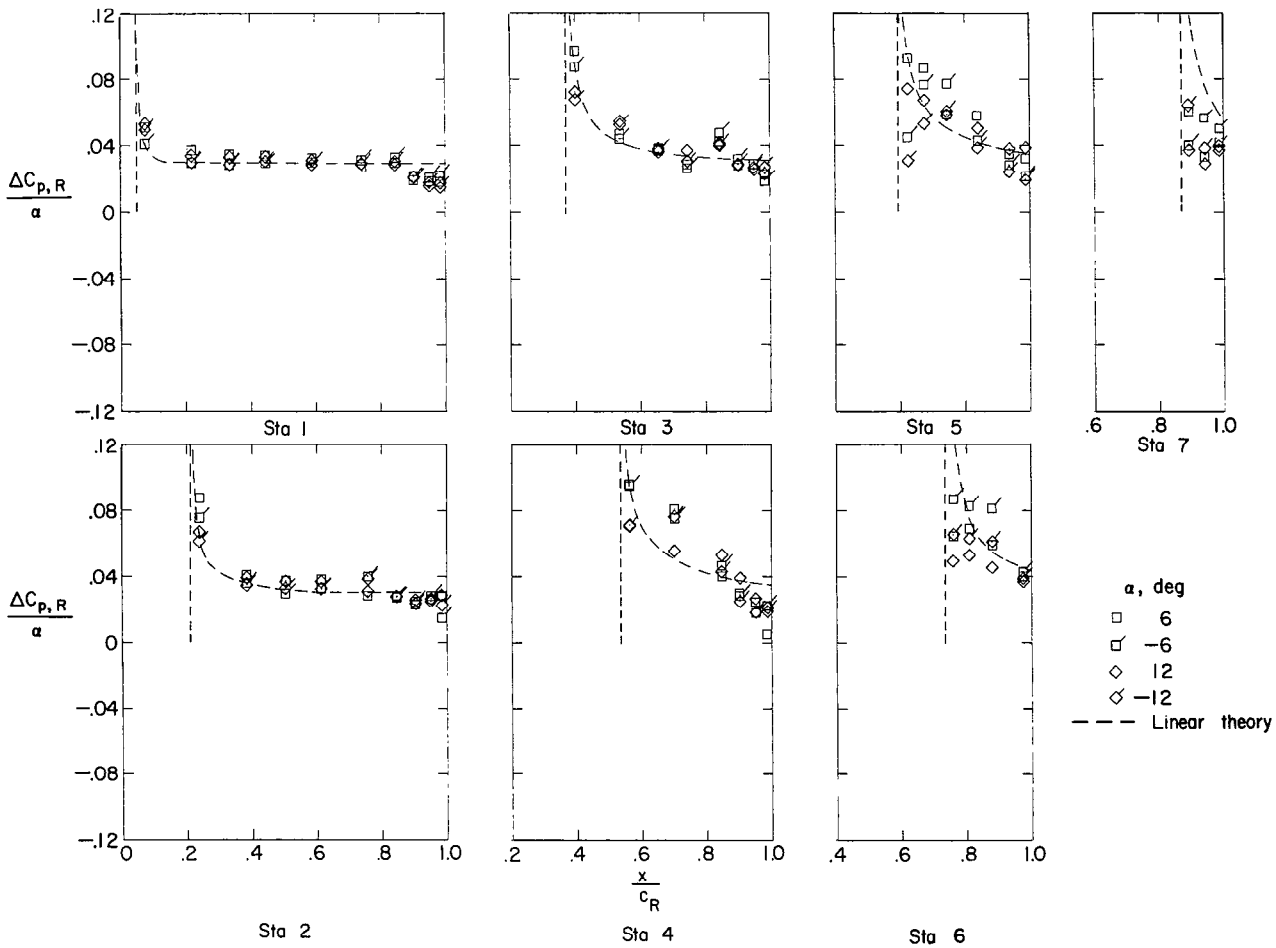

(q) Resultant pressure coefficients due to α; $\delta = 10^{\circ}$.

Figure 19.- Continued.

[redacted]

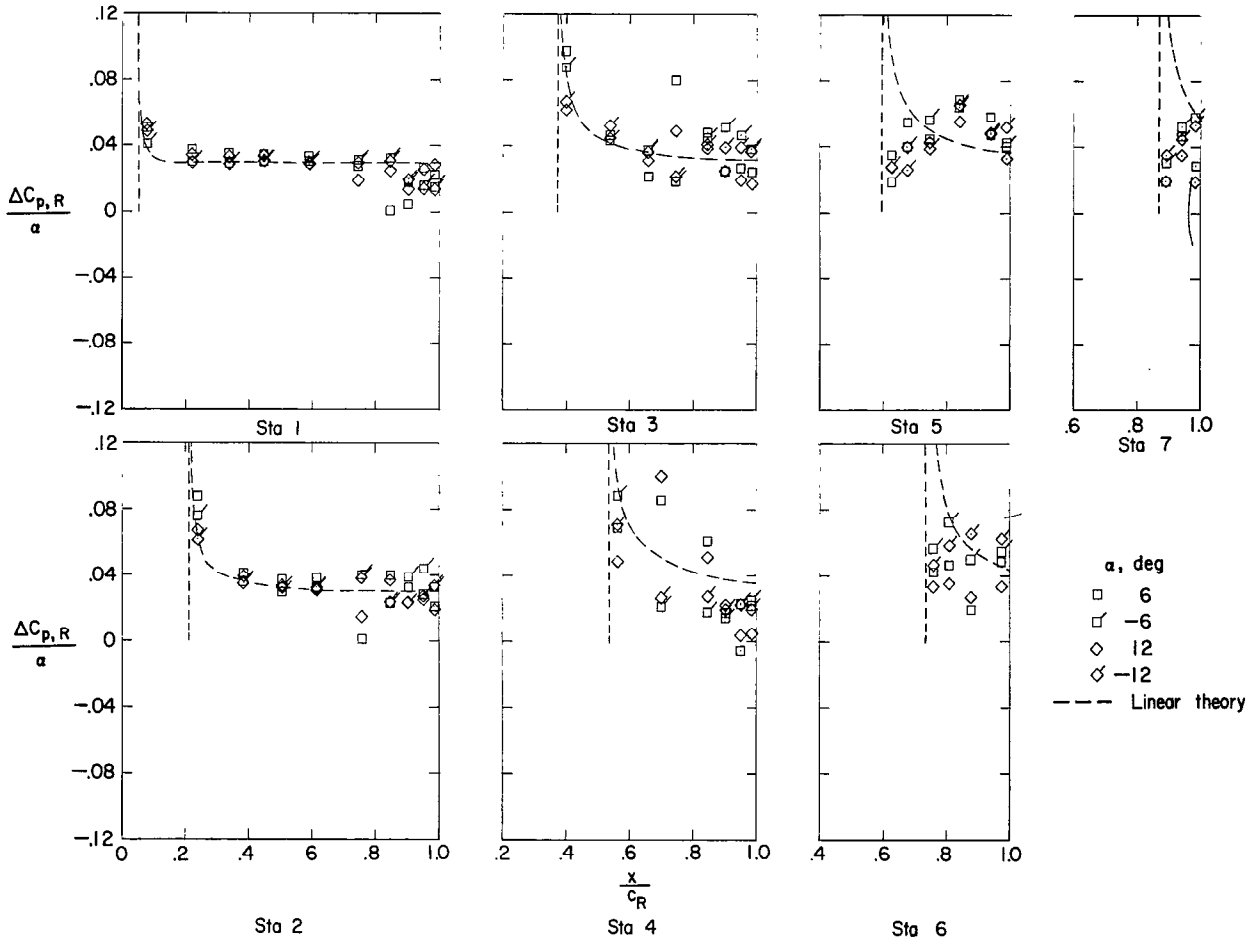

(r) Resultant pressure coefficients due to α; $\delta = 30^{\circ}$.

Figure 19.- Concluded.

[redacted]

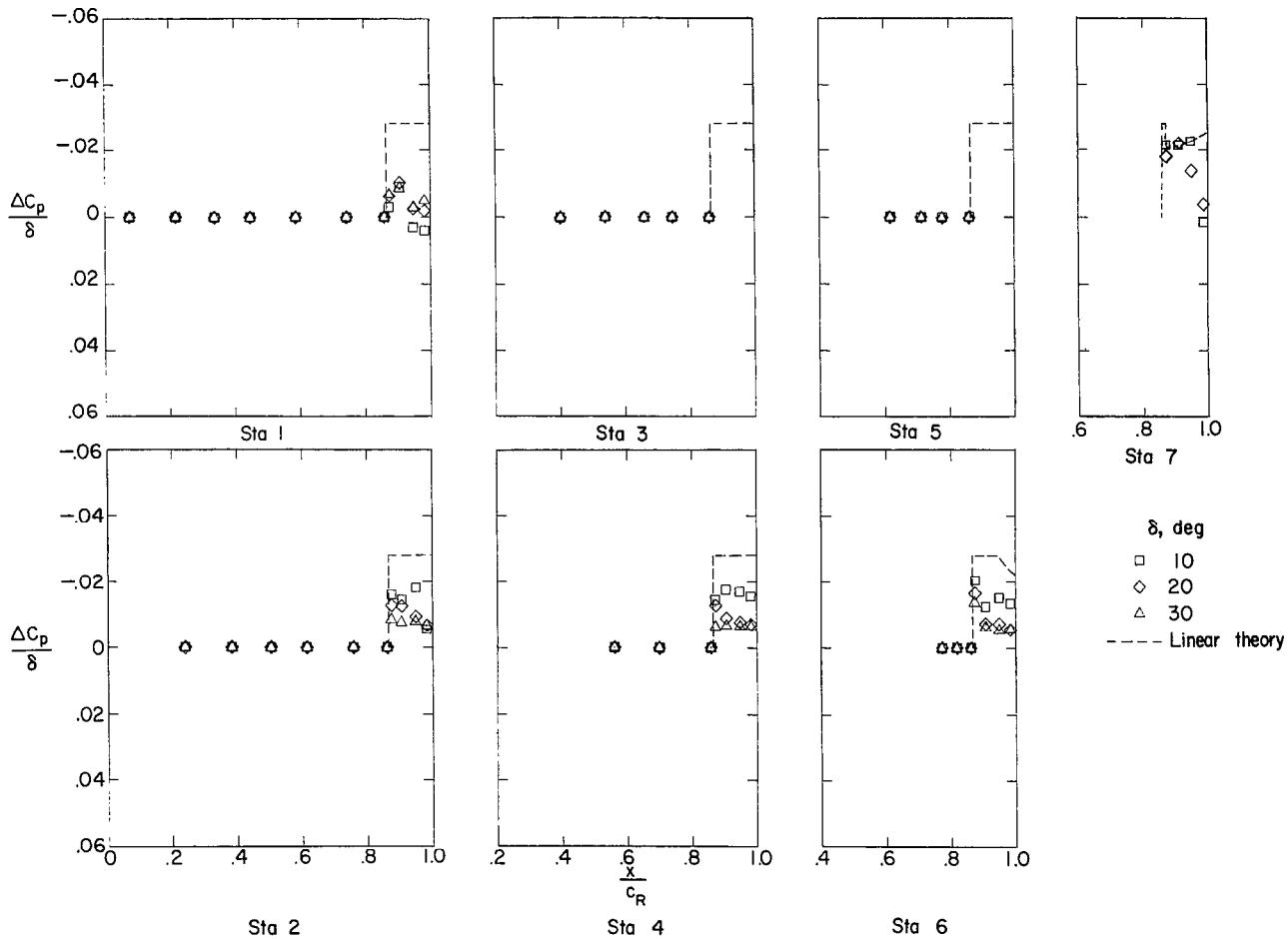

(a) Pressure coefficients due to δ; $\alpha = 0^{\circ}$; upper surface.

Figure 20.- Incremental pressure distributions due to control deflection and angle of attack for configuration J. $M = 1.61$; $R = 4.2 \times 10^{6}$.

[redacted]

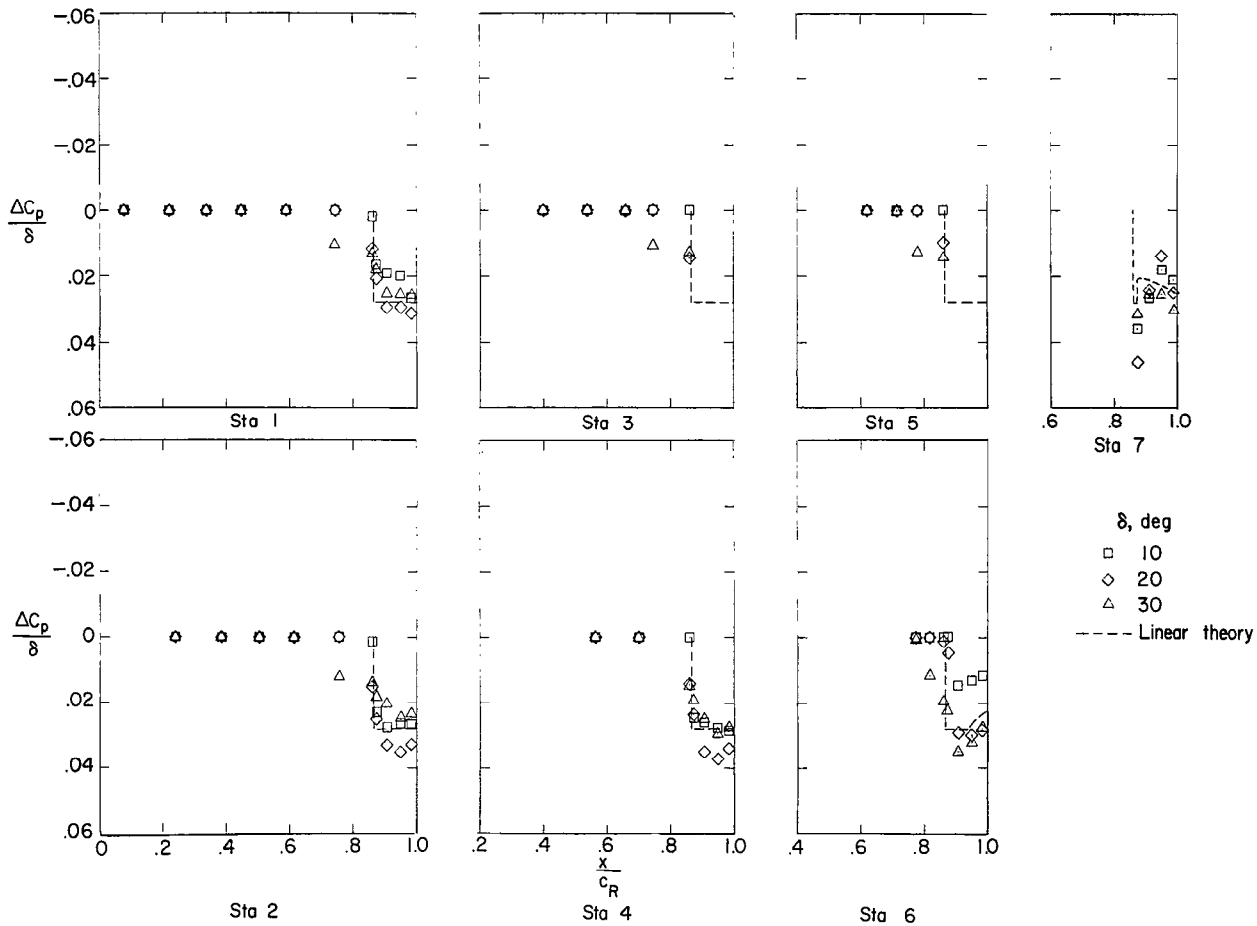

(b) Pressure coefficients due to δ; $\alpha = 0^{\circ}$; lower surface.

Figure 20.- Continued.

[redacted]

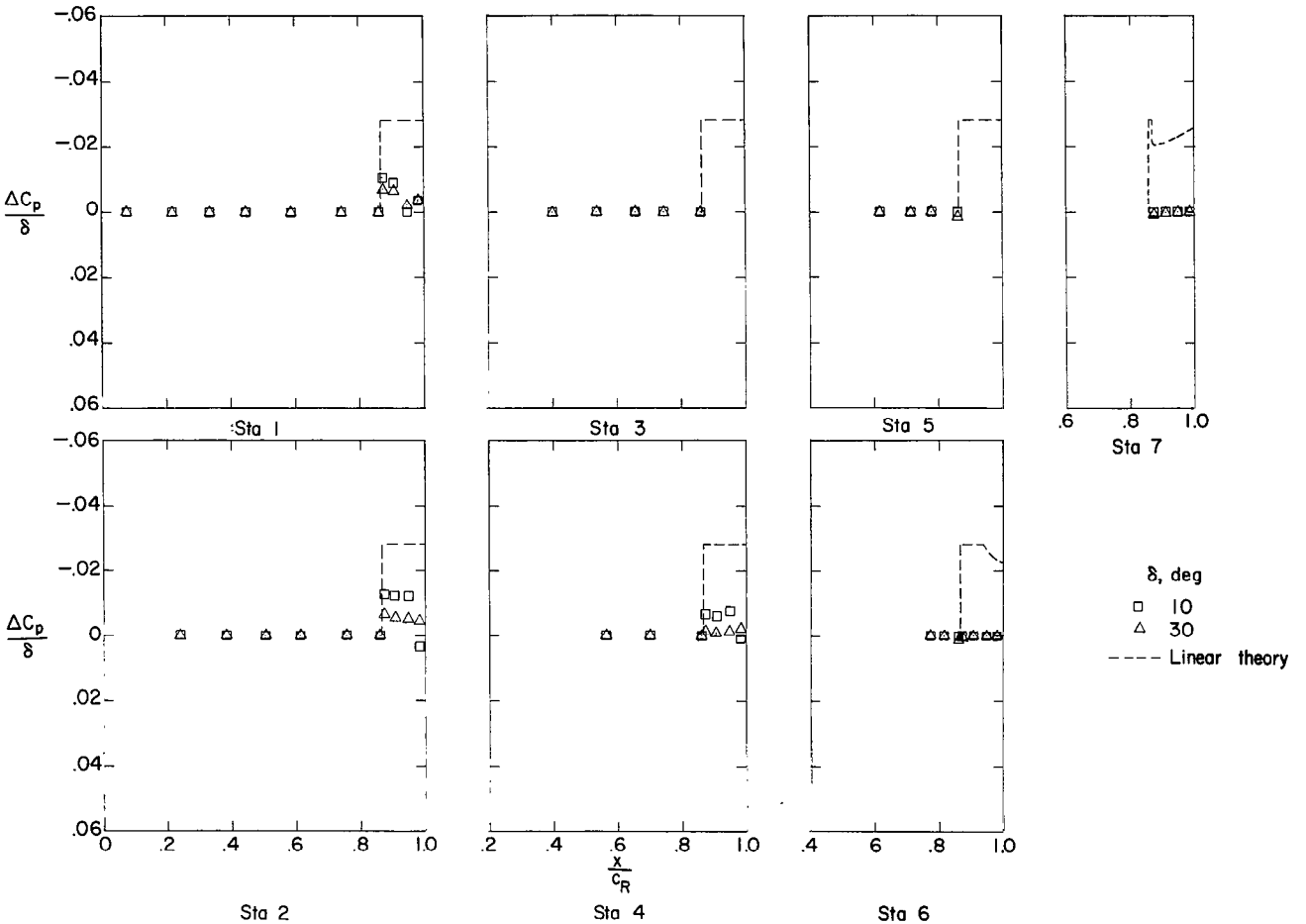

(c) Pressure coefficients due to δ; $\alpha = 12^{\circ}$; upper surface.

Figure 20.- Continued.

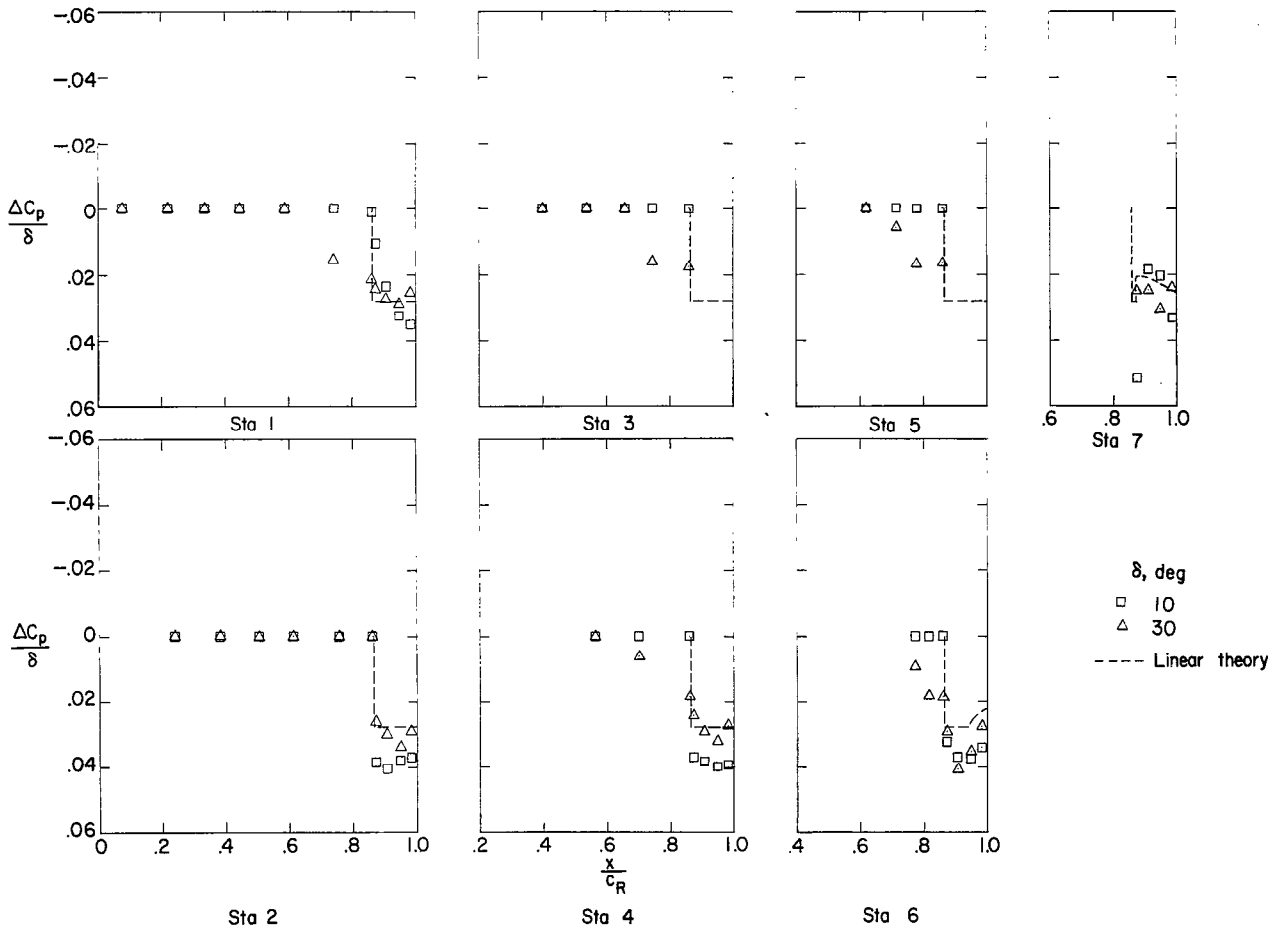

(d) Pressure coefficients due to δ; α = 12°; lower surface.

Figure 20.- Continued.

[redacted]

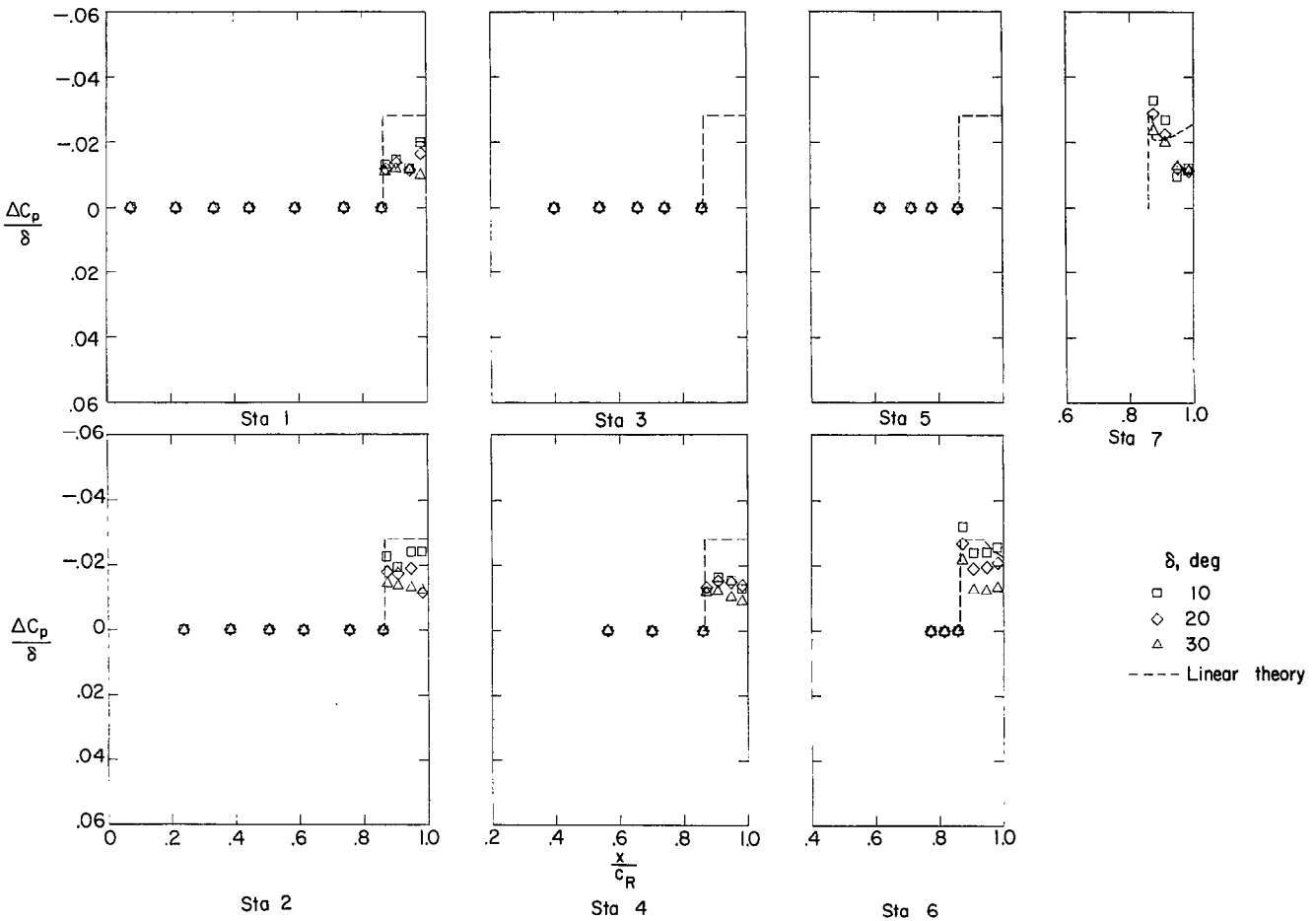

(e) Pressure coefficients due to δ; $\alpha = -12^{\circ}$; upper surface.

Figure 20.- Continued.

[redacted]

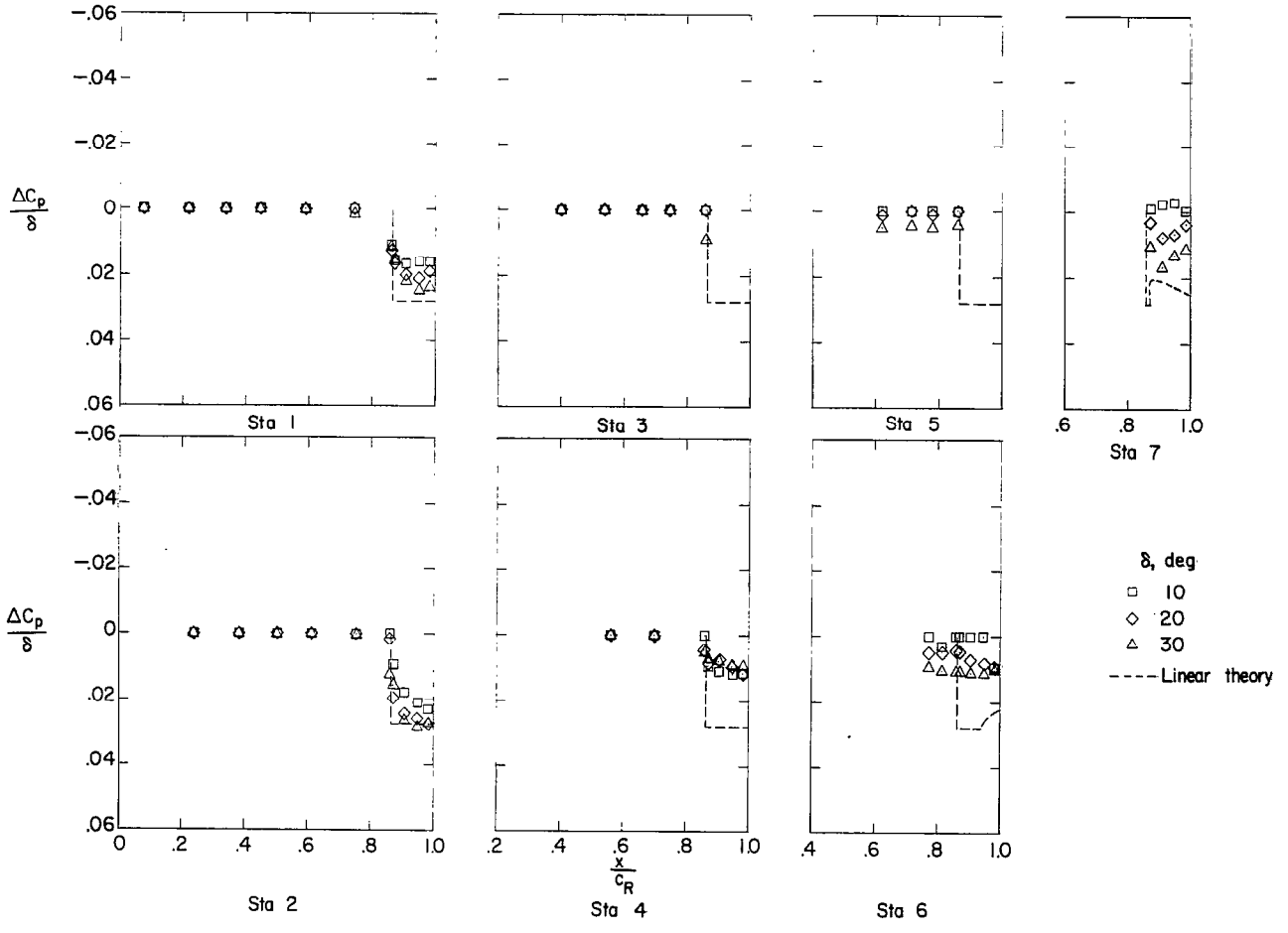

(f) Pressure coefficients due to δ; $\alpha = -12^{\circ}$; lower surface.

Figure 20.- Continued.

[redacted]

[redacted]

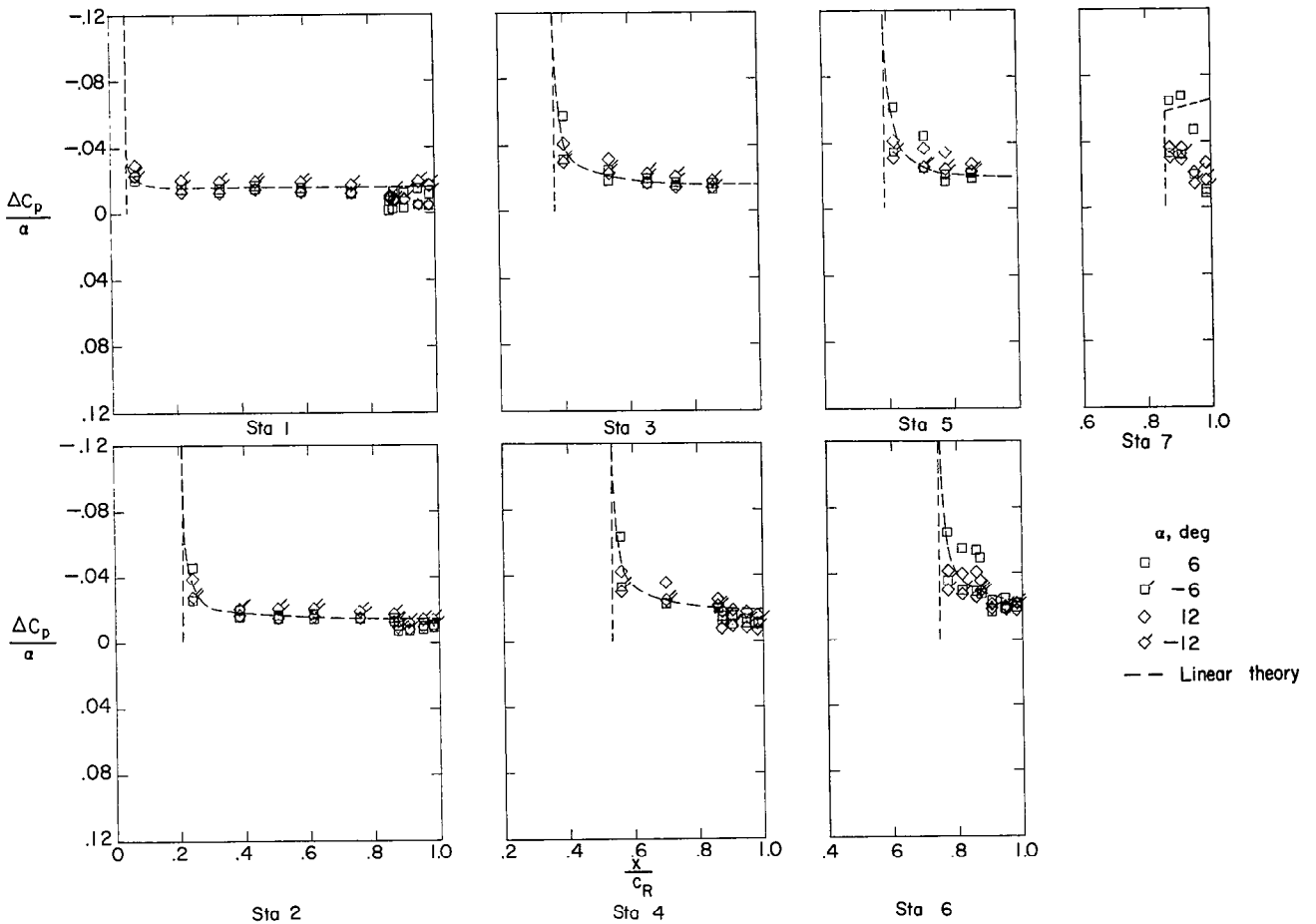

(g) Pressure coefficients due to α; $\delta = 0^{\circ}$; upper surface.

Figure 20.- Continued.

[redacted]

[redacted]

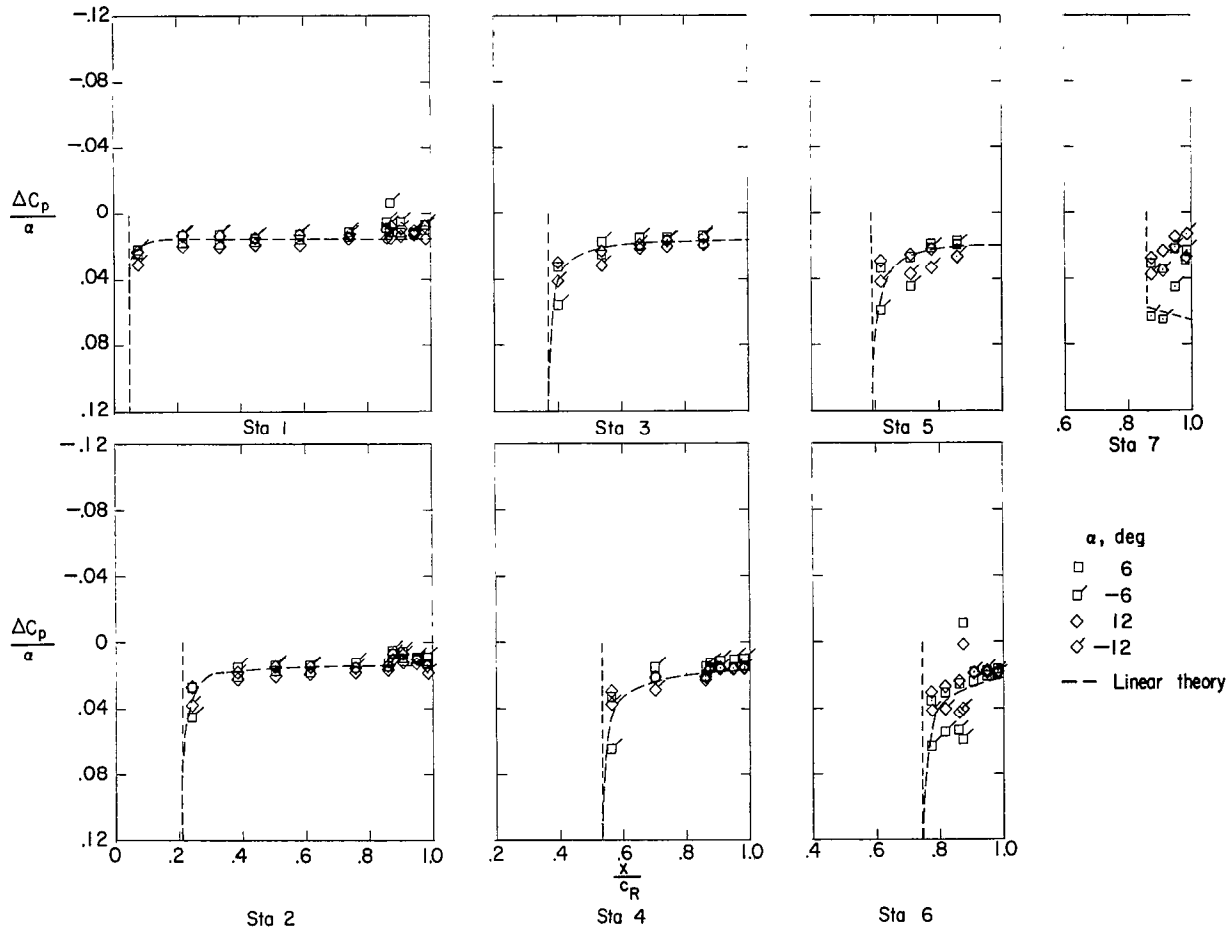

(h) Pressure coefficients due to α; $\delta = 0^{\circ}$; lower surface.

Figure 20.- Continued.

[redacted]

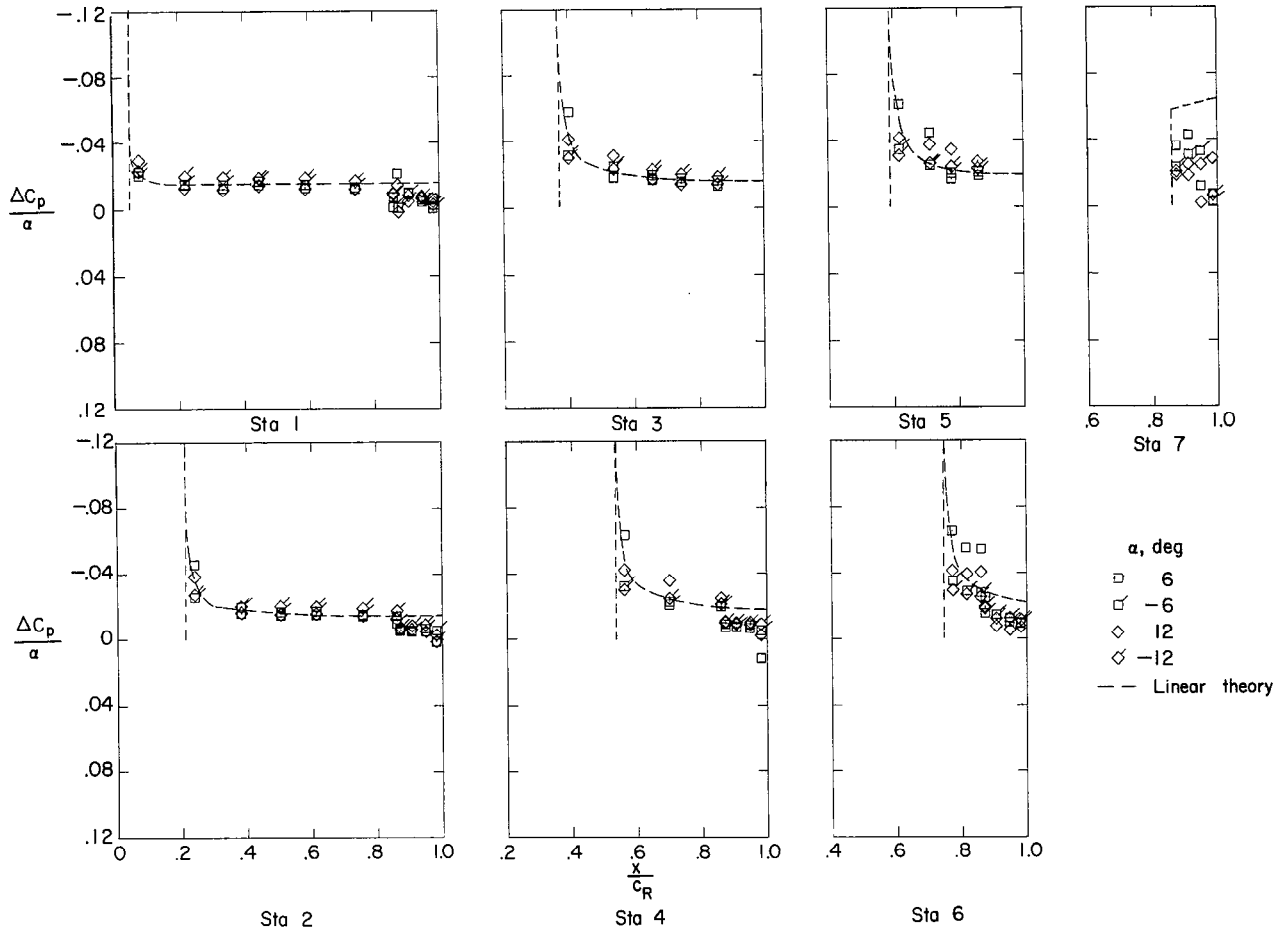

(i) Pressure coefficients due to α; $\delta = 10^{\circ}$; upper surface.

Figure 20.- Continued.

[redacted]

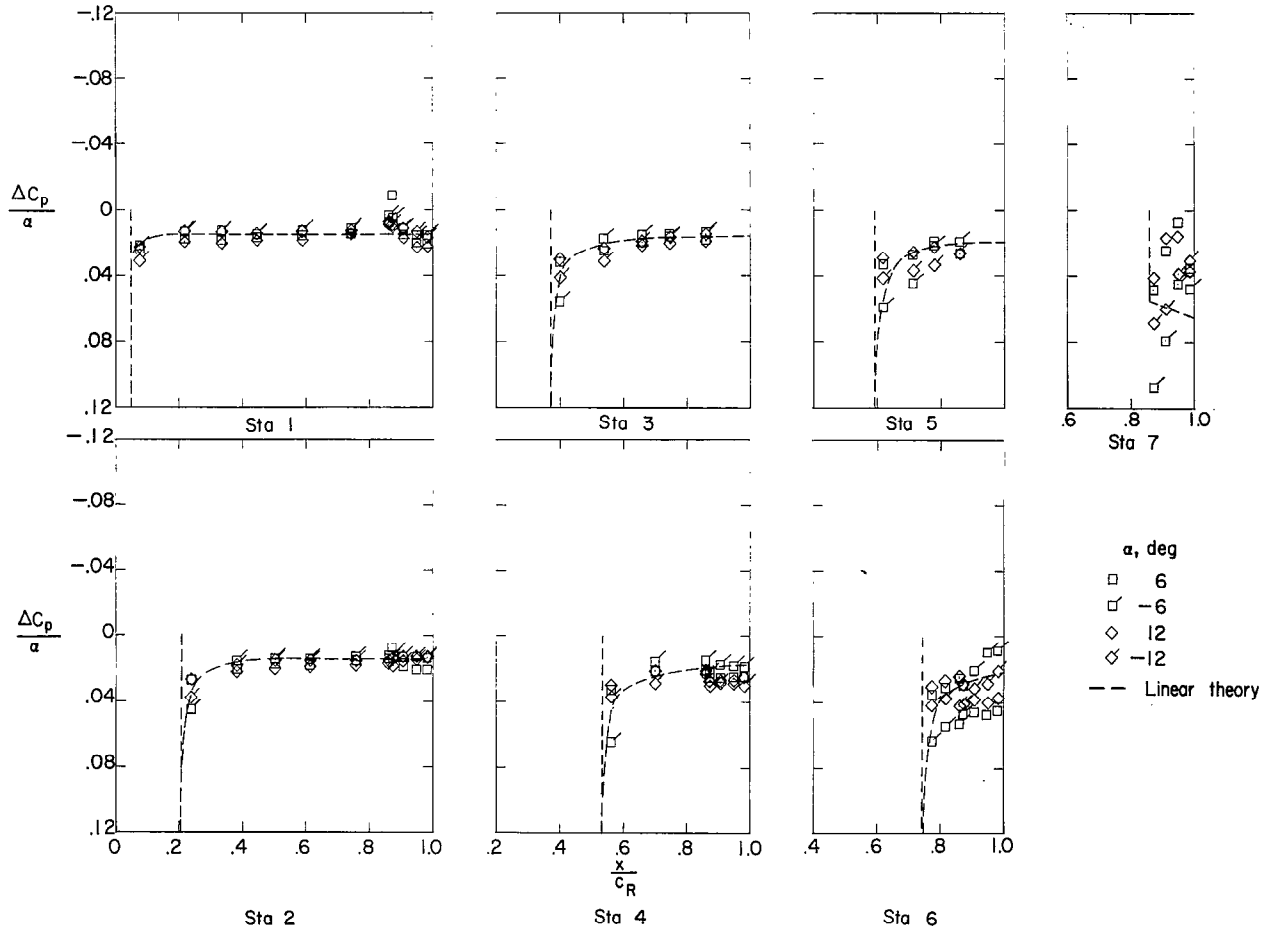

(j) Pressure coefficients due to α; δ = 10°; lower surface.

Figure 20.- Continued.

[redacted]

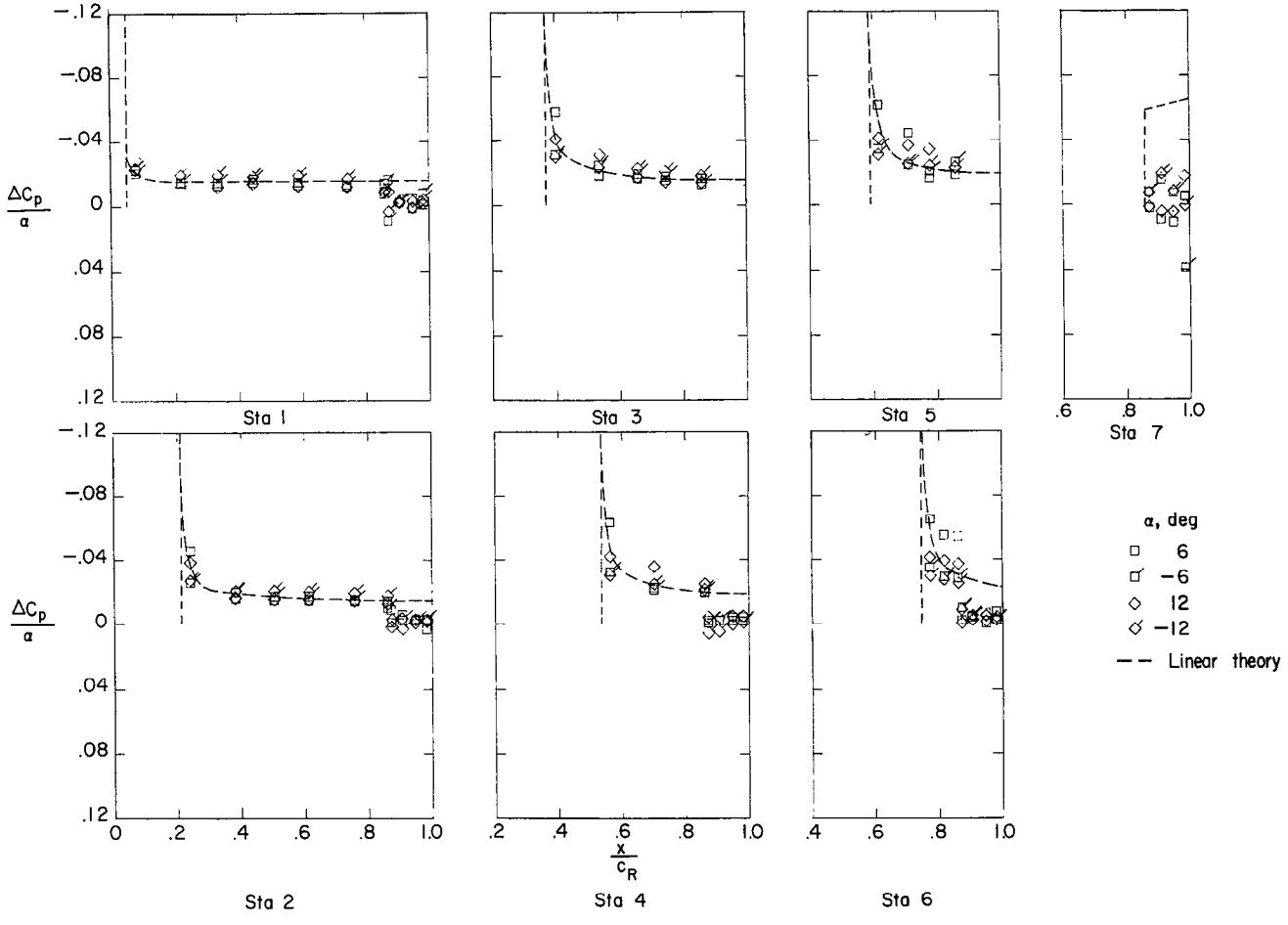

(k) Pressure coefficients due to α; $\delta = 30^{\circ}$; upper surface.

Figure 20.- Continued.

[redacted]

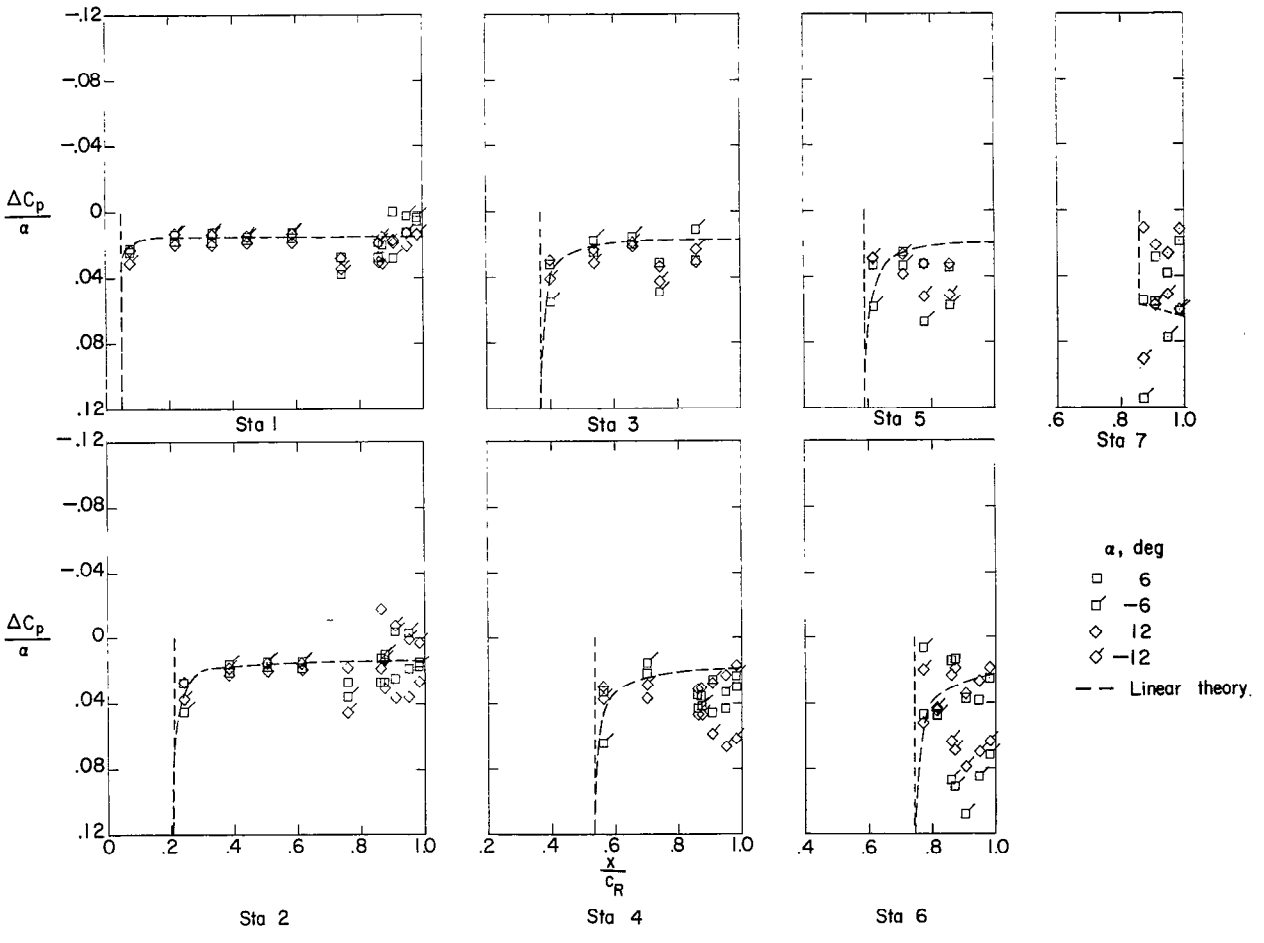

(*l*) Pressure coefficients due to α; δ = 30°; lower surface.

Figure 20.- Continued.

[redacted]

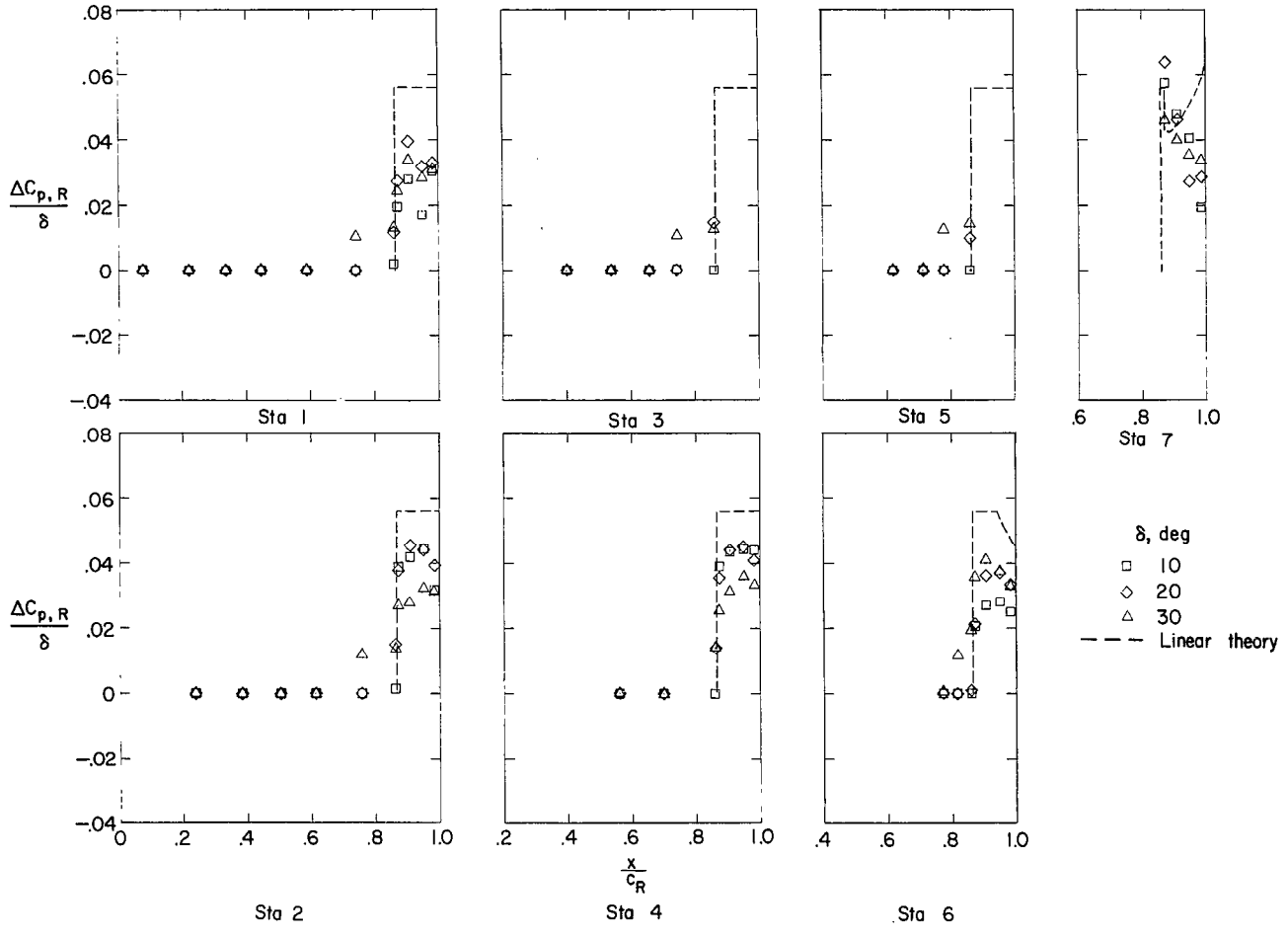

(m) Resultant pressure coefficients due to δ; $\alpha = 0^{\circ}$.

Figure 20.- Continued.

[redacted]

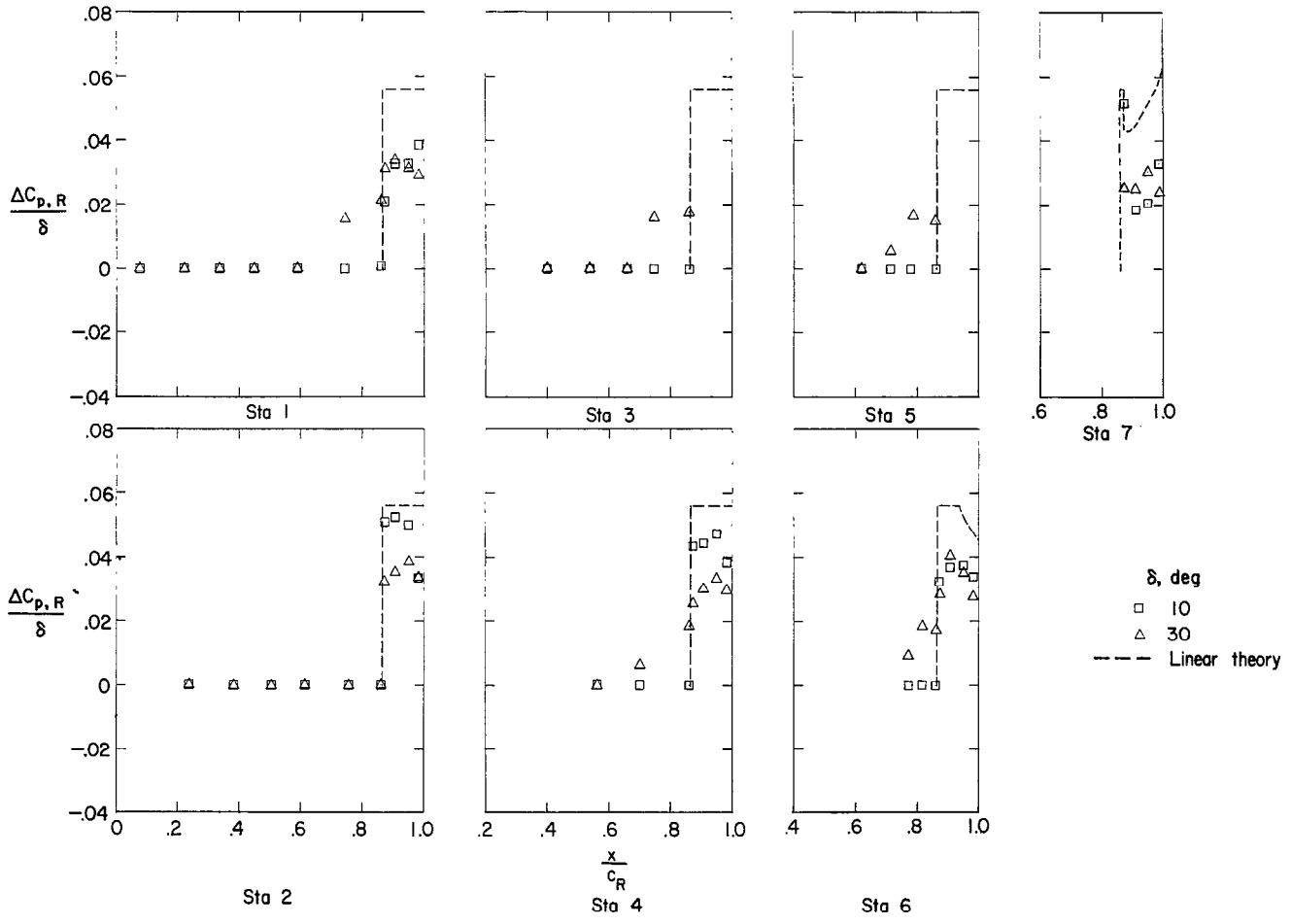

(n) Resultant pressure coefficients due to δ; $\alpha = 12^{\circ}$.

Figure 20.- Continued.

[redacted]

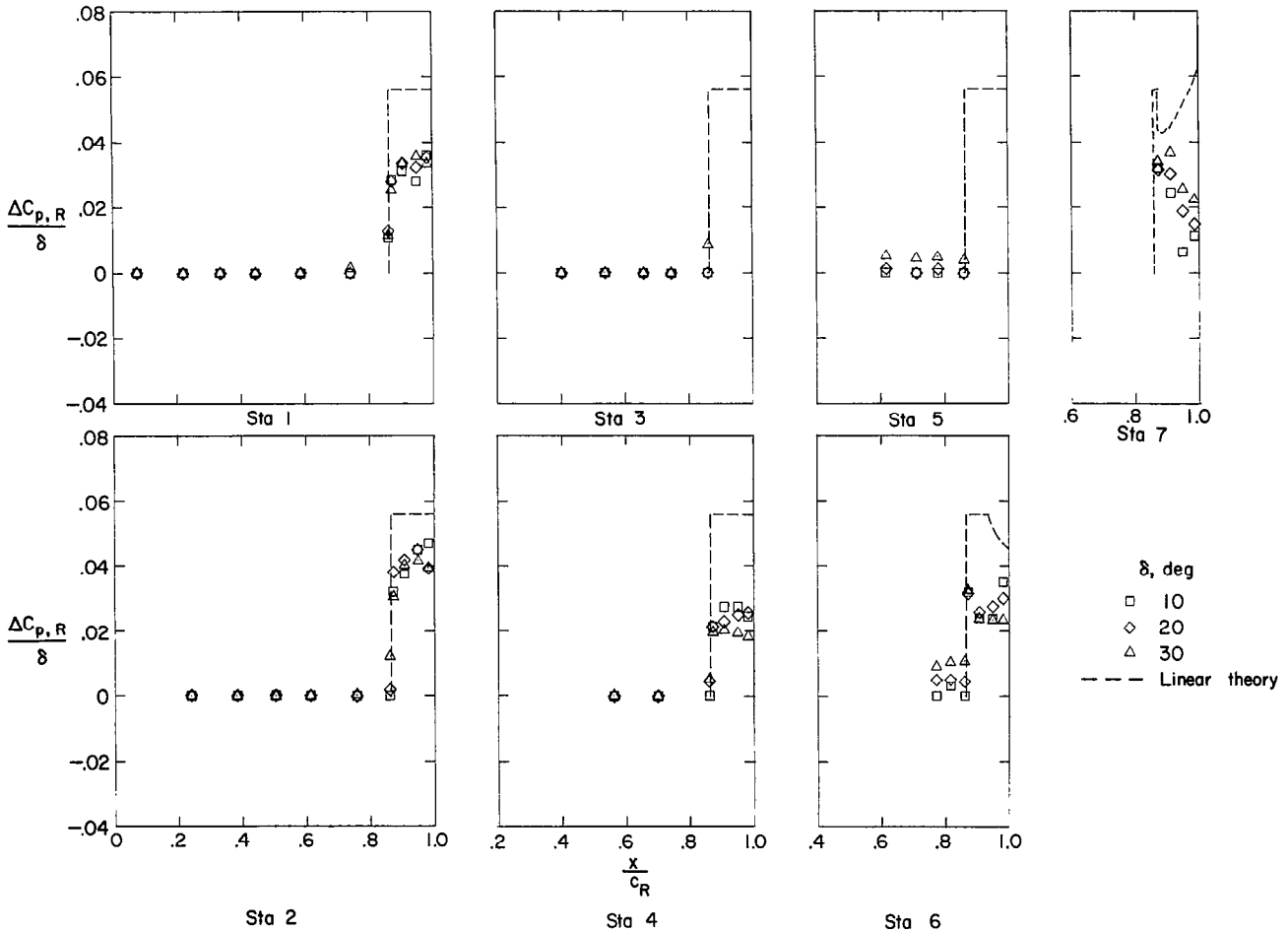

(o) Resultant pressure coefficients due to δ; $\alpha = -12^{\circ}$.

Figure 20.- Continued.

[redacted]

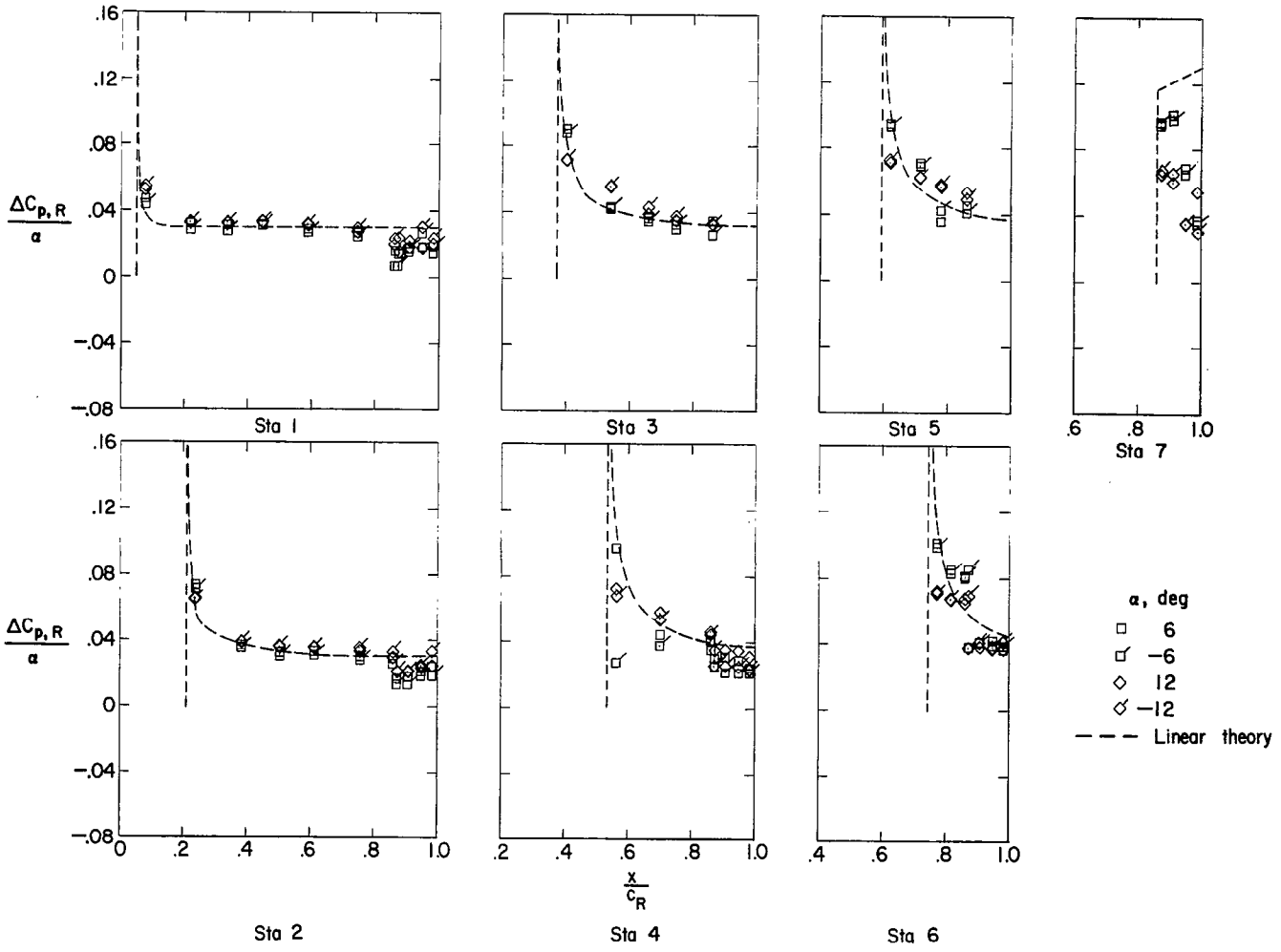

(p) Resultant pressure coefficients due to α; $\delta = 0^{\circ}$.

Figure 20.- Continued.

[redacted]

[redacted]

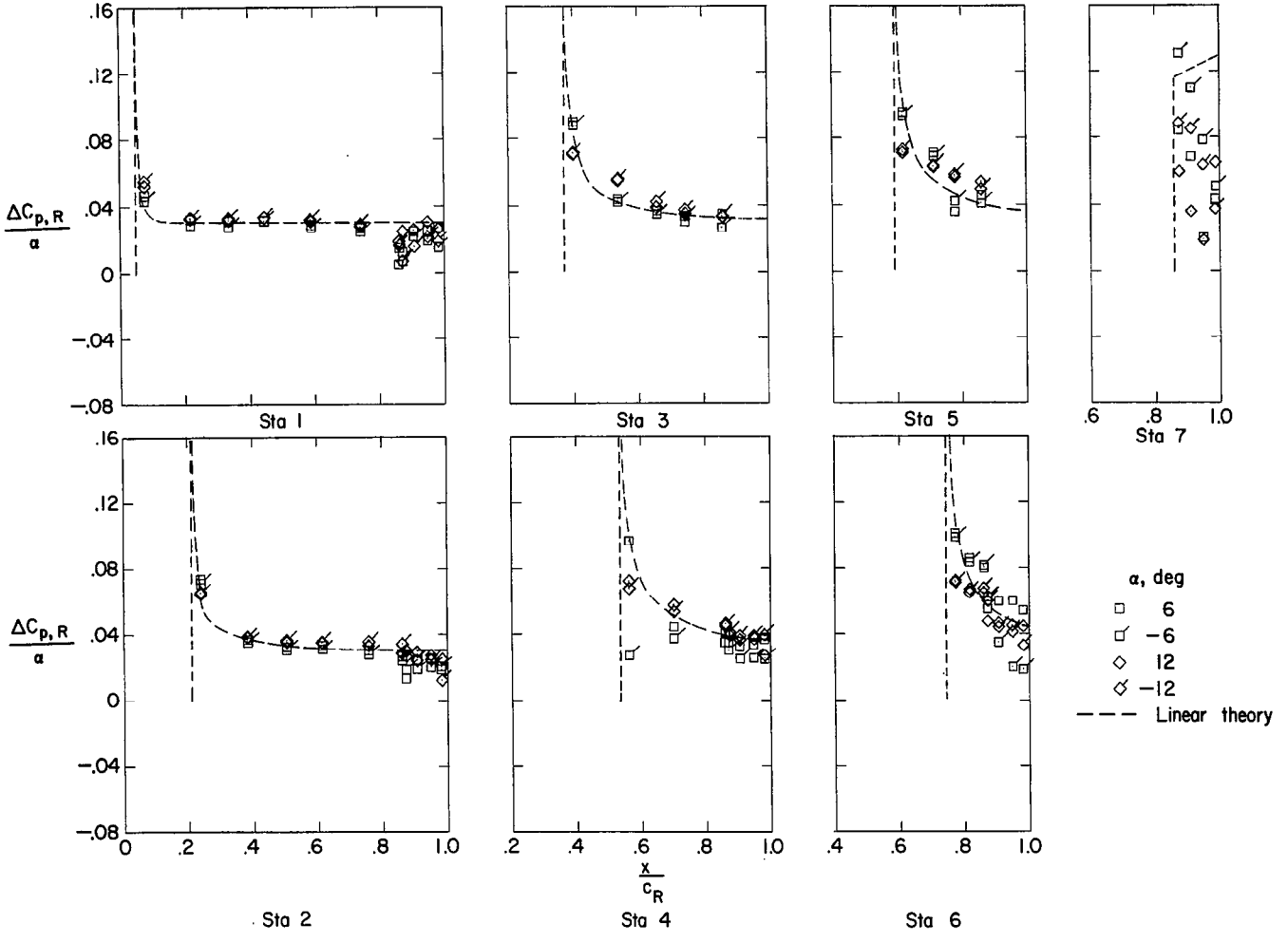

(q) Resultant pressure coefficients due to α; $\delta = 10^{\circ}$.

Figure 20.- Continued.

[redacted]

[redacted]

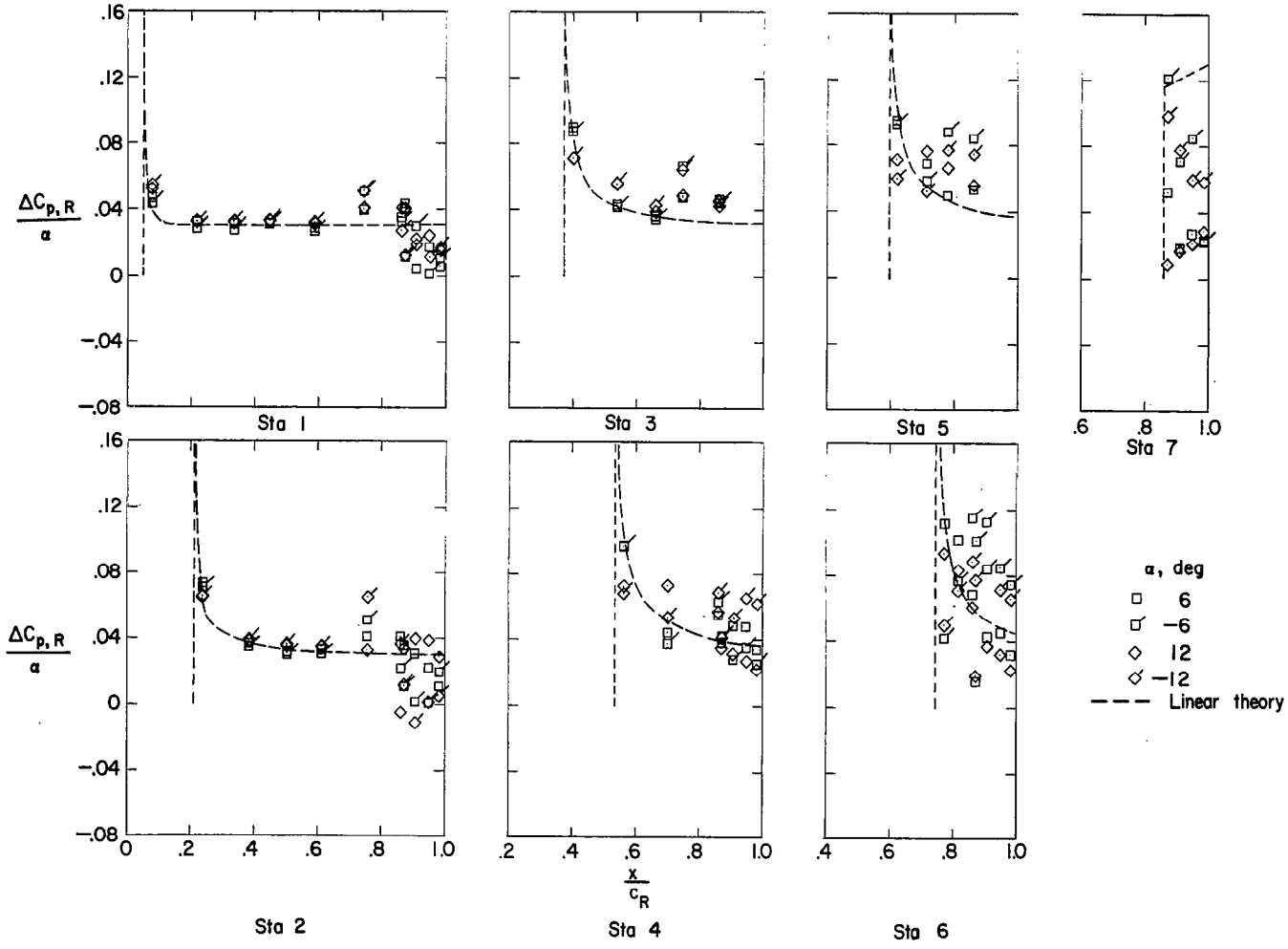

(r) Resultant pressure coefficients due to α; $\delta = 30^{\circ}$.

Figure 20.- Concluded.

[redacted]

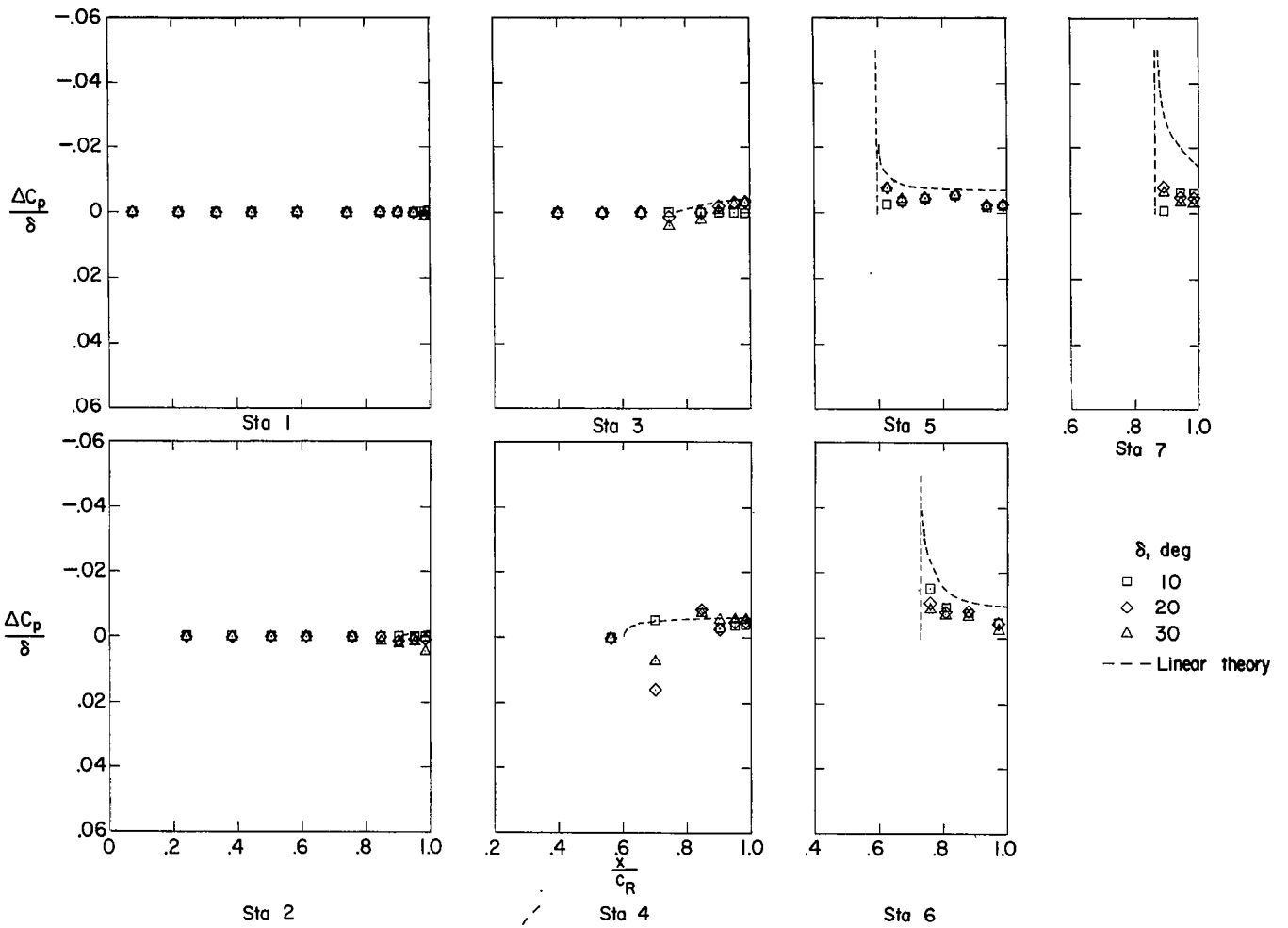

(a) Pressure coefficients due to δ; $\alpha = 0^{\circ}$; upper surface.

Figure 21.- Incremental pressure distributions due to control deflection and angle of attack for configuration F. $M = 2.01$; $R = 4.2 \times 10^{6}$.

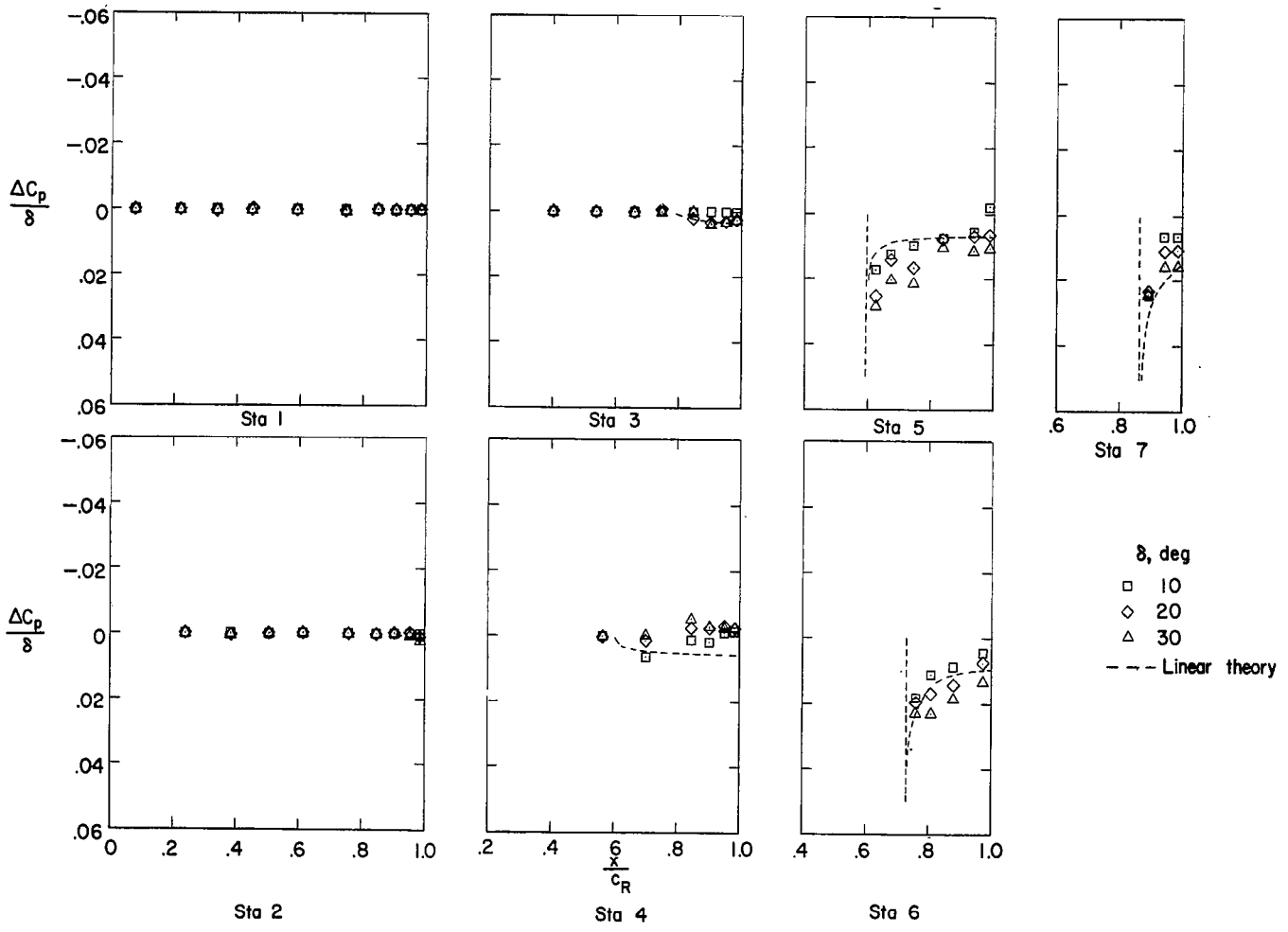

(b) Pressure coefficients due to δ; $\alpha = 0^{\circ}$; lower surface.

Figure 21.- Continued.

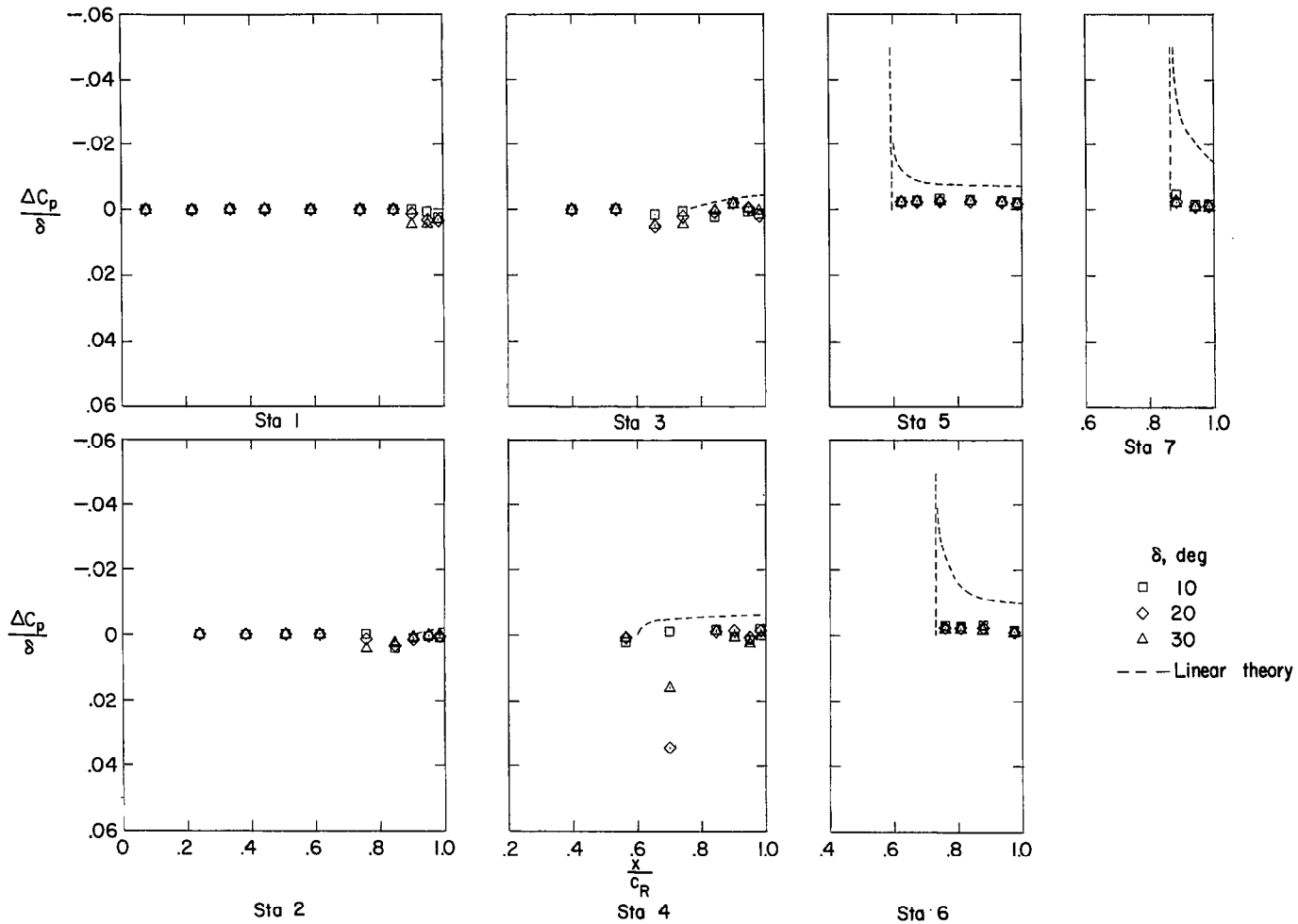

(c) Pressure coefficients due to δ; $\alpha = 12^{\circ}$; upper surface.

Figure 21.- Continued.

[redacted]

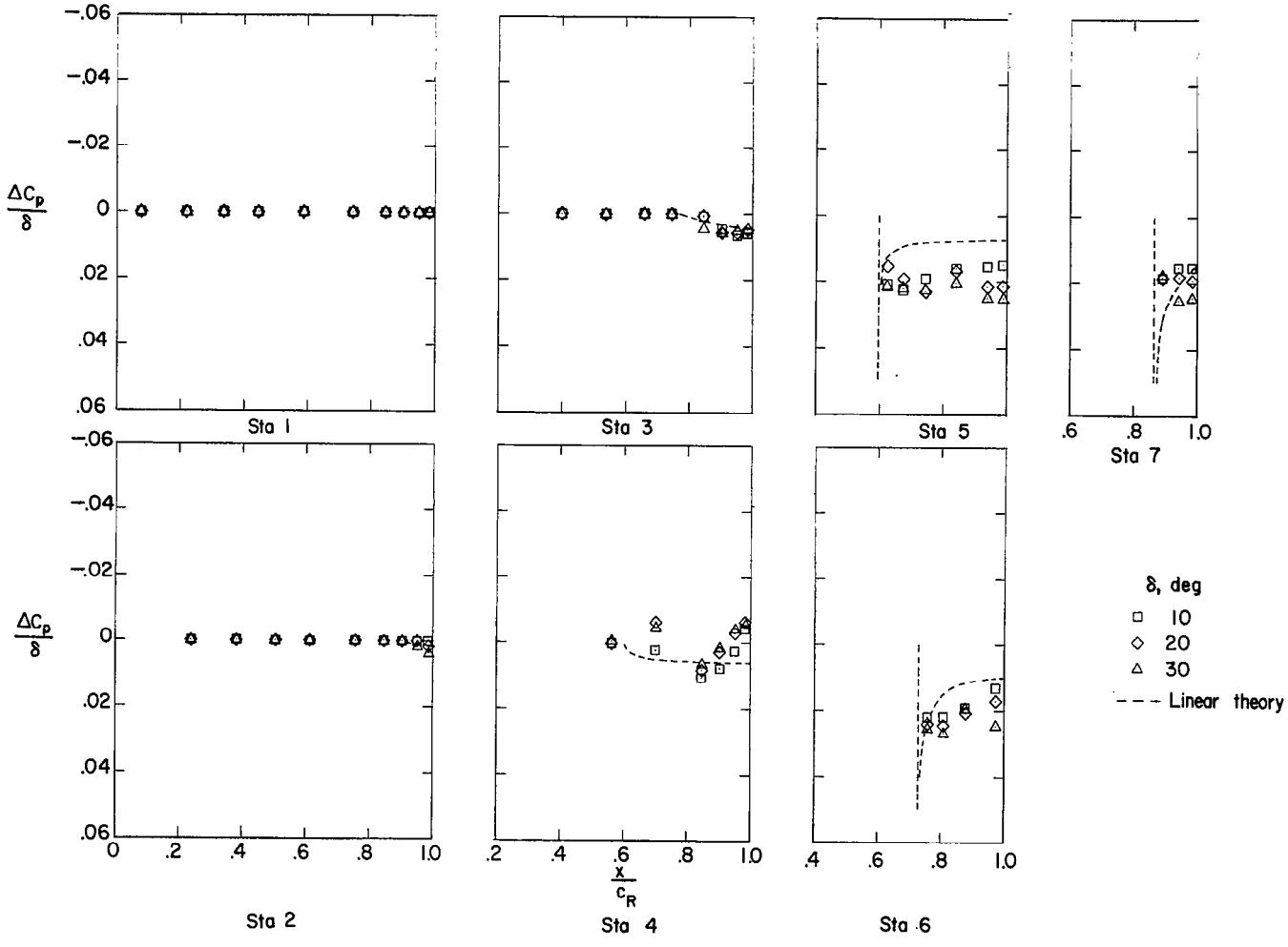

(d) Pressure coefficients due to δ; $\alpha = 12^{\circ}$; lower surface.

Figure 21.- Continued.

[redacted]

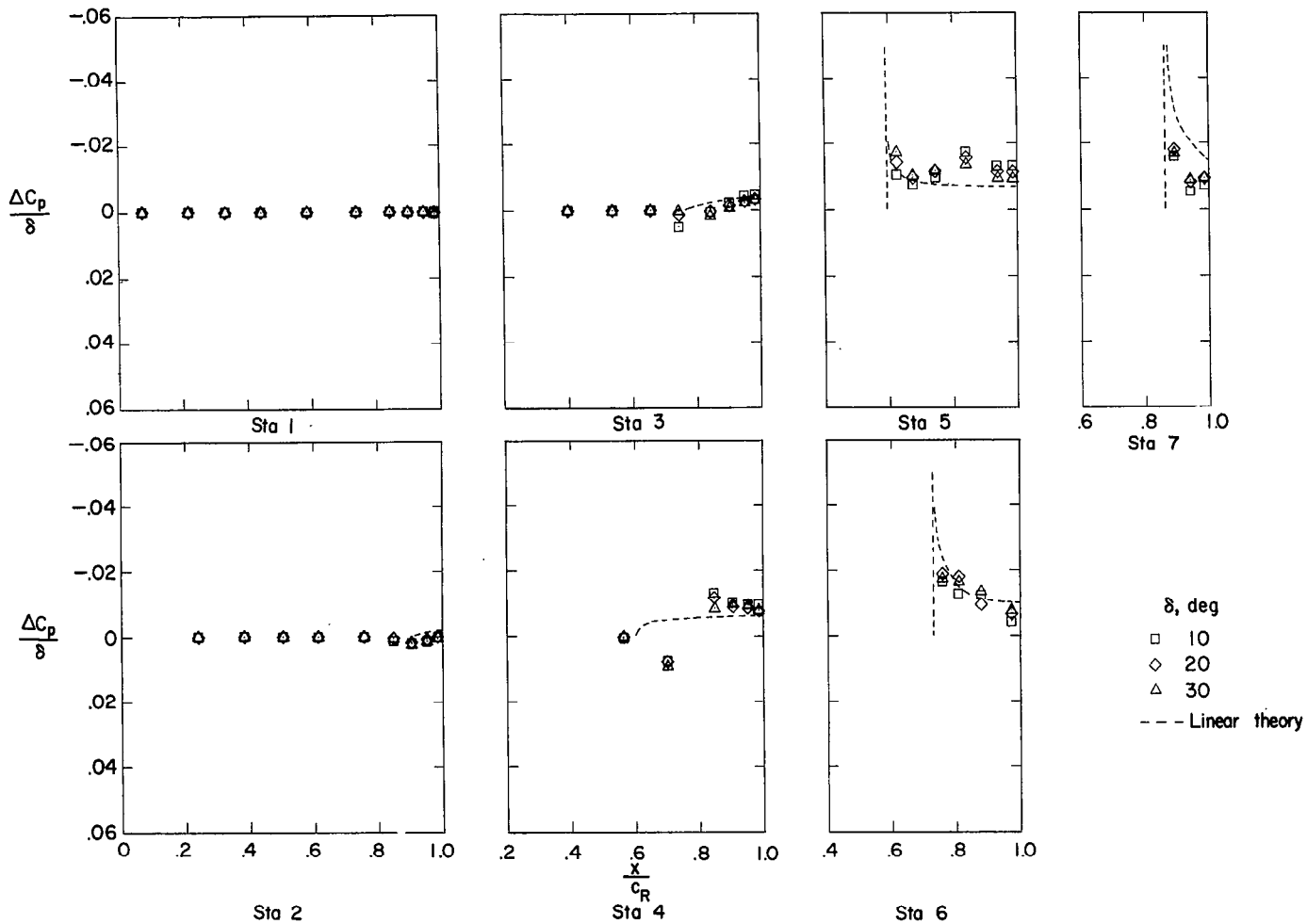

(e) Pressure coefficients due to δ; $\alpha = -12^{\circ}$; upper surface.

Figure 21.- Continued.

[redacted]

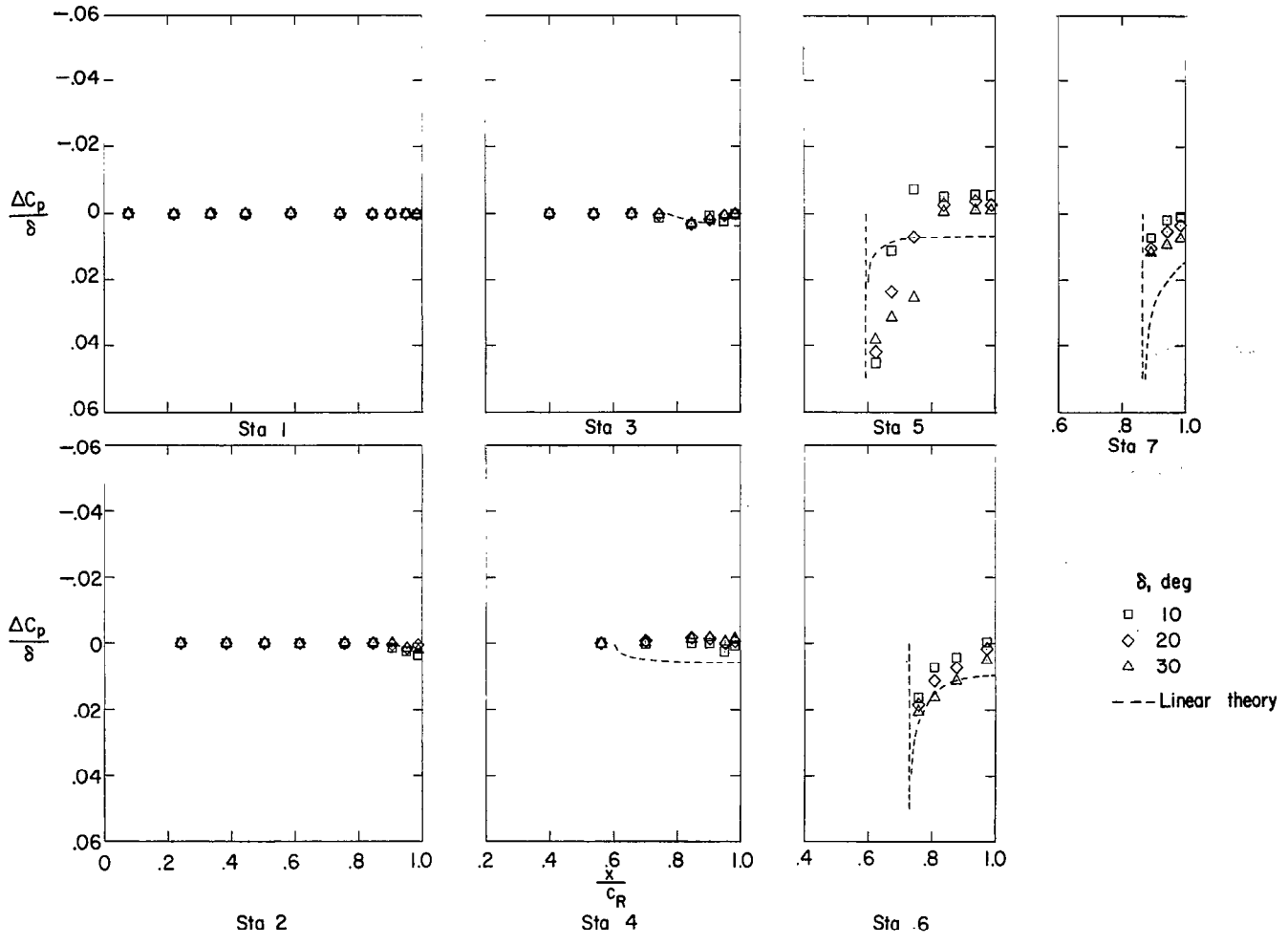

(f) Pressure coefficients due to δ; $\alpha = -12^{\circ}$; lower surface.

Figure 21.- Continued.

[redacted]

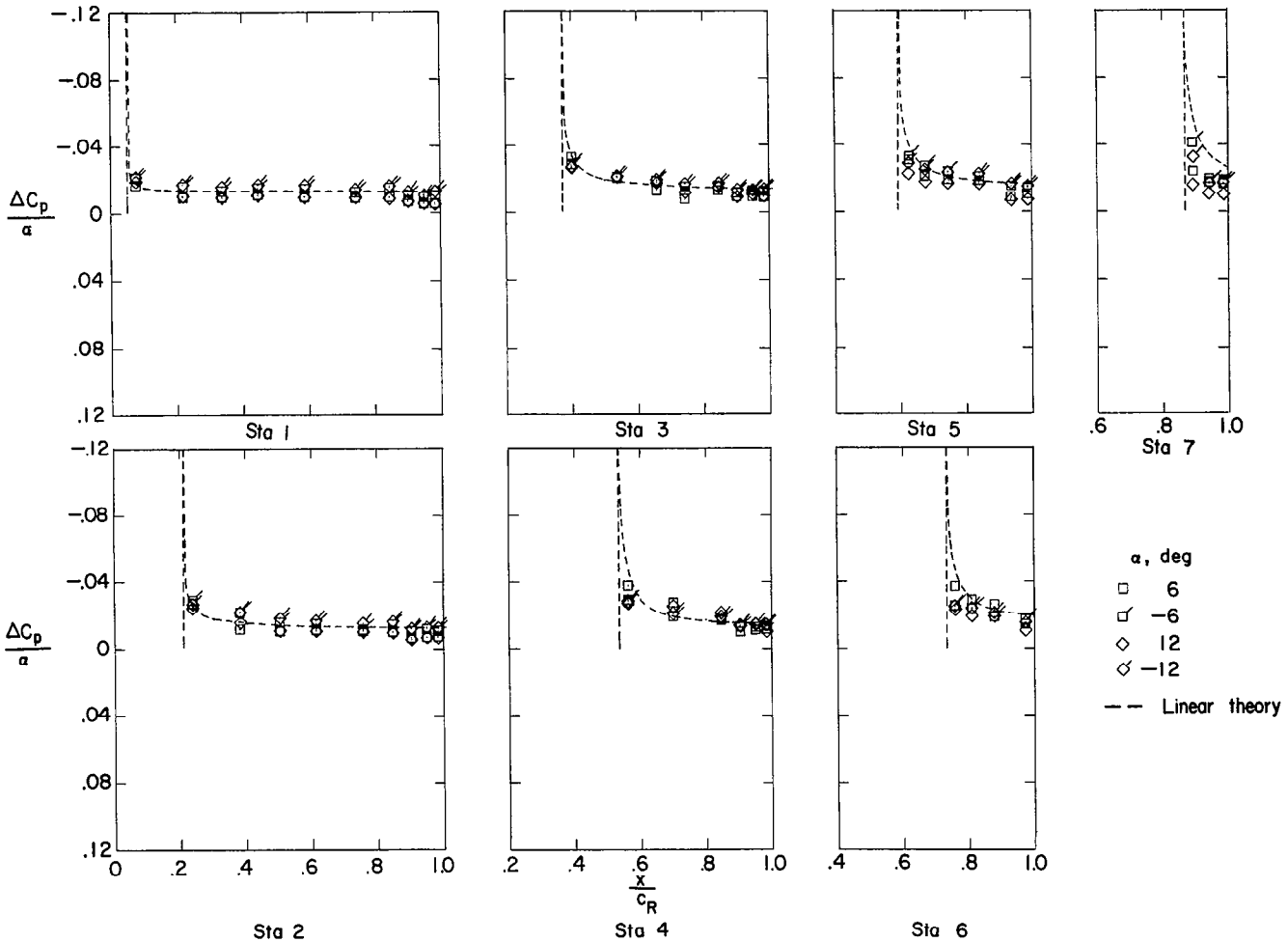

(g) Pressure coefficients due to α; $\delta = 0^{\circ}$; upper surface.

Figure 21.- Continued.

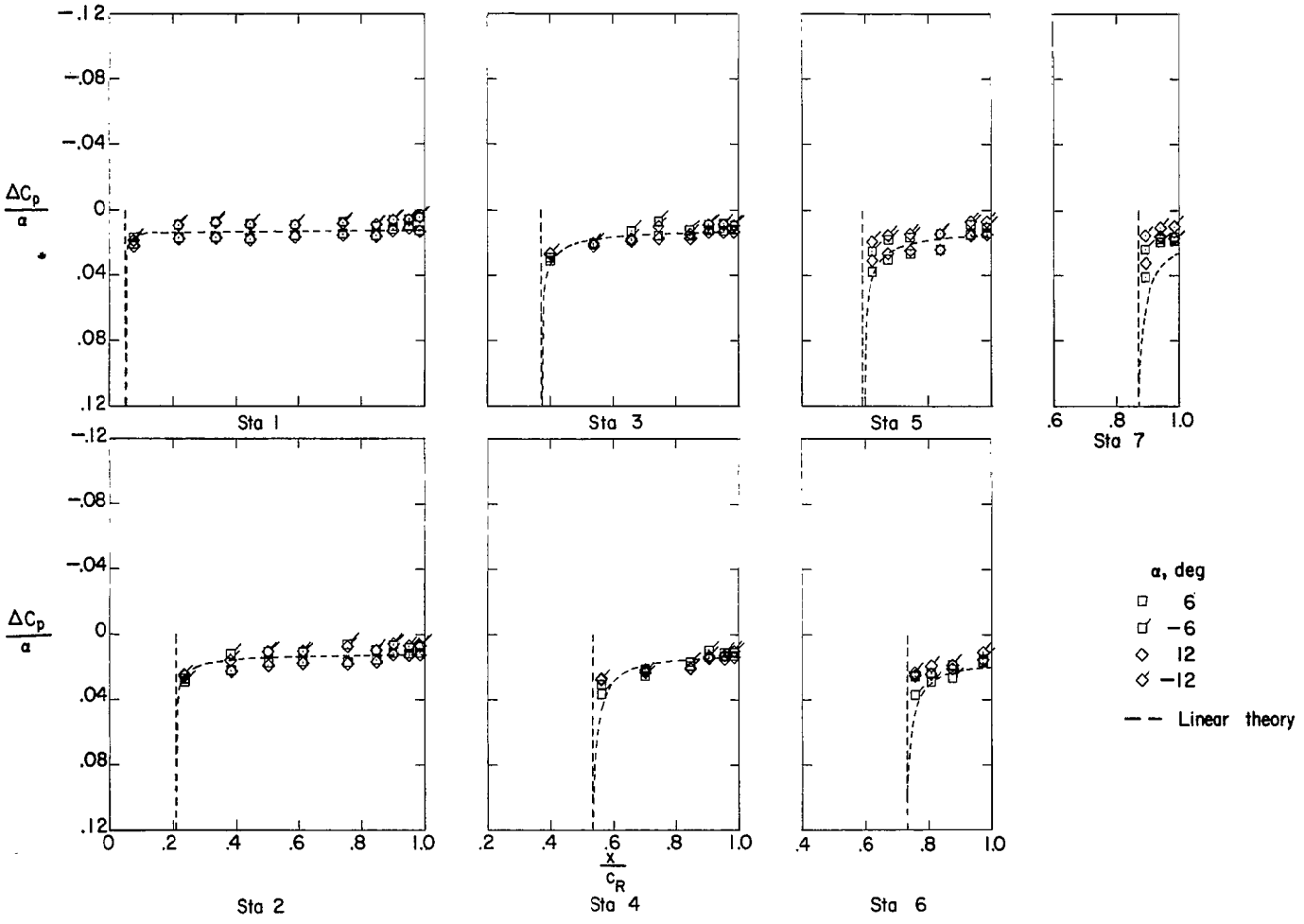

(h) Pressure coefficients due to α; $\delta = 0^{\circ}$; lower surface.

Figure 21.- Continued.

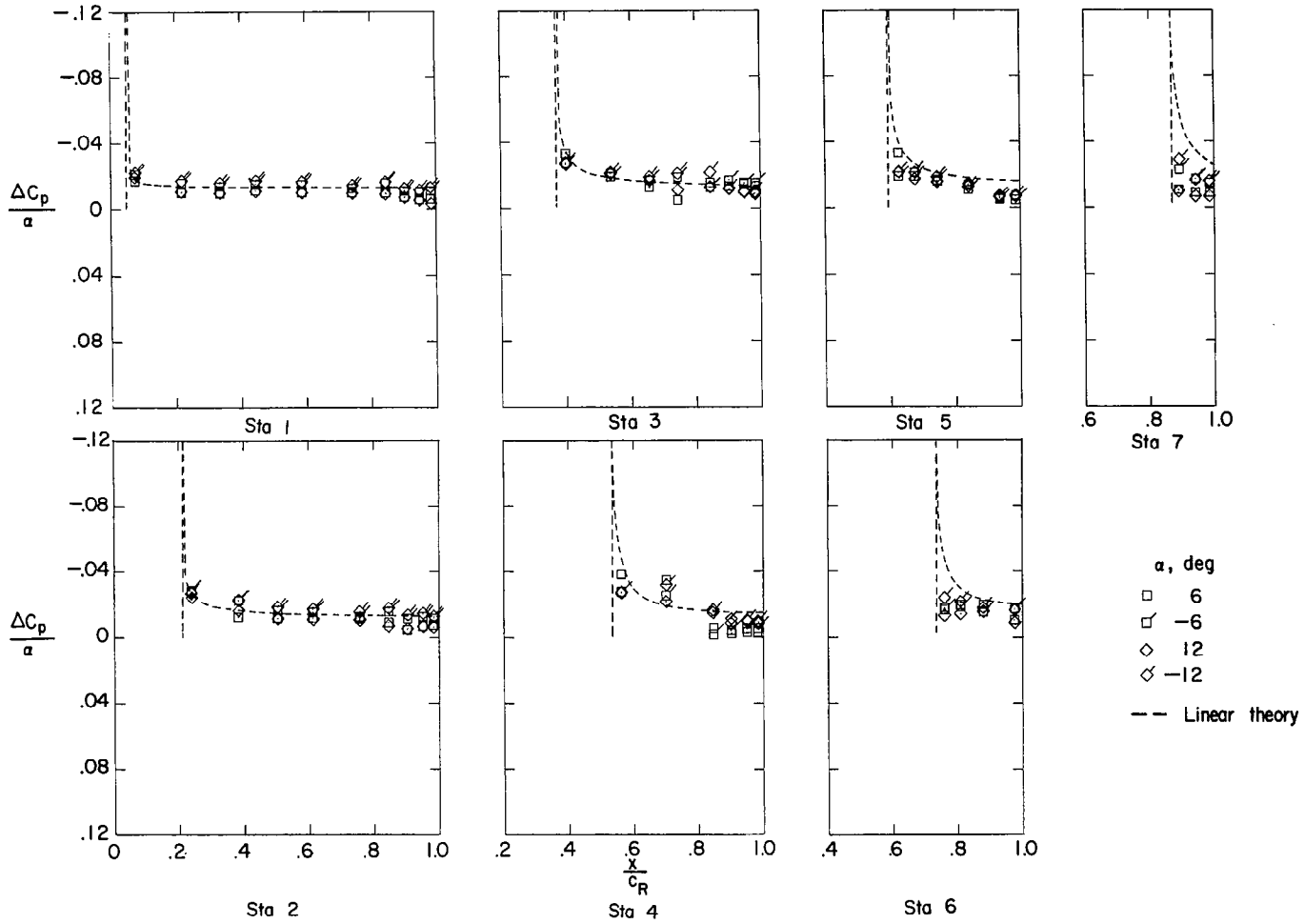

(i) Pressure coefficients due to α; $\delta = 10^{\circ}$; upper surface.

Figure 21.- Continued.

[redacted]

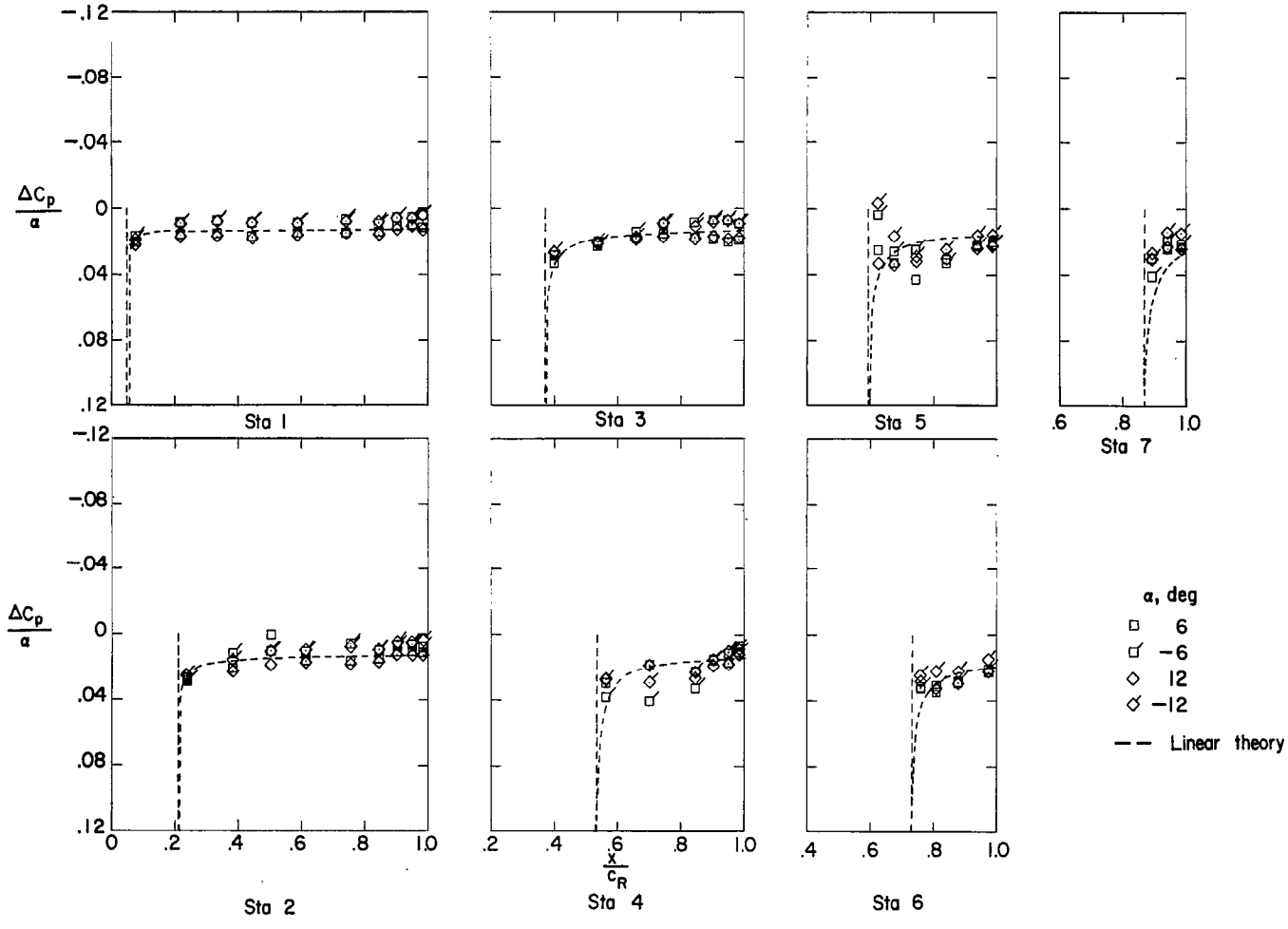

(j) Pressure coefficients due to α; $\delta = 10^{\circ}$; lower surface.

Figure 21.- Continued.

[redacted]

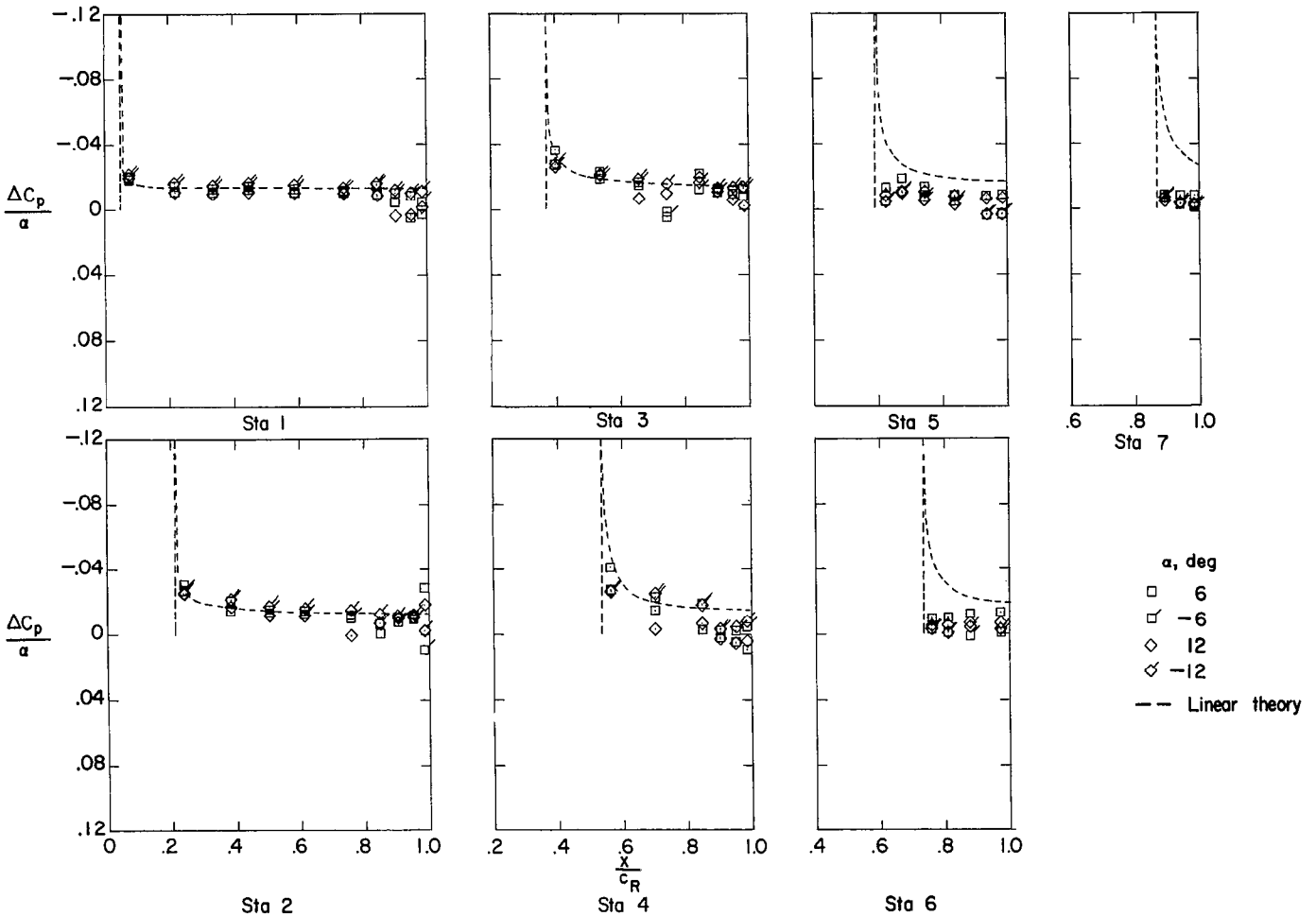

(k) Pressure coefficients due to α; $\delta = 30^{\circ}$; upper surface.

Figure 21.- Continued.

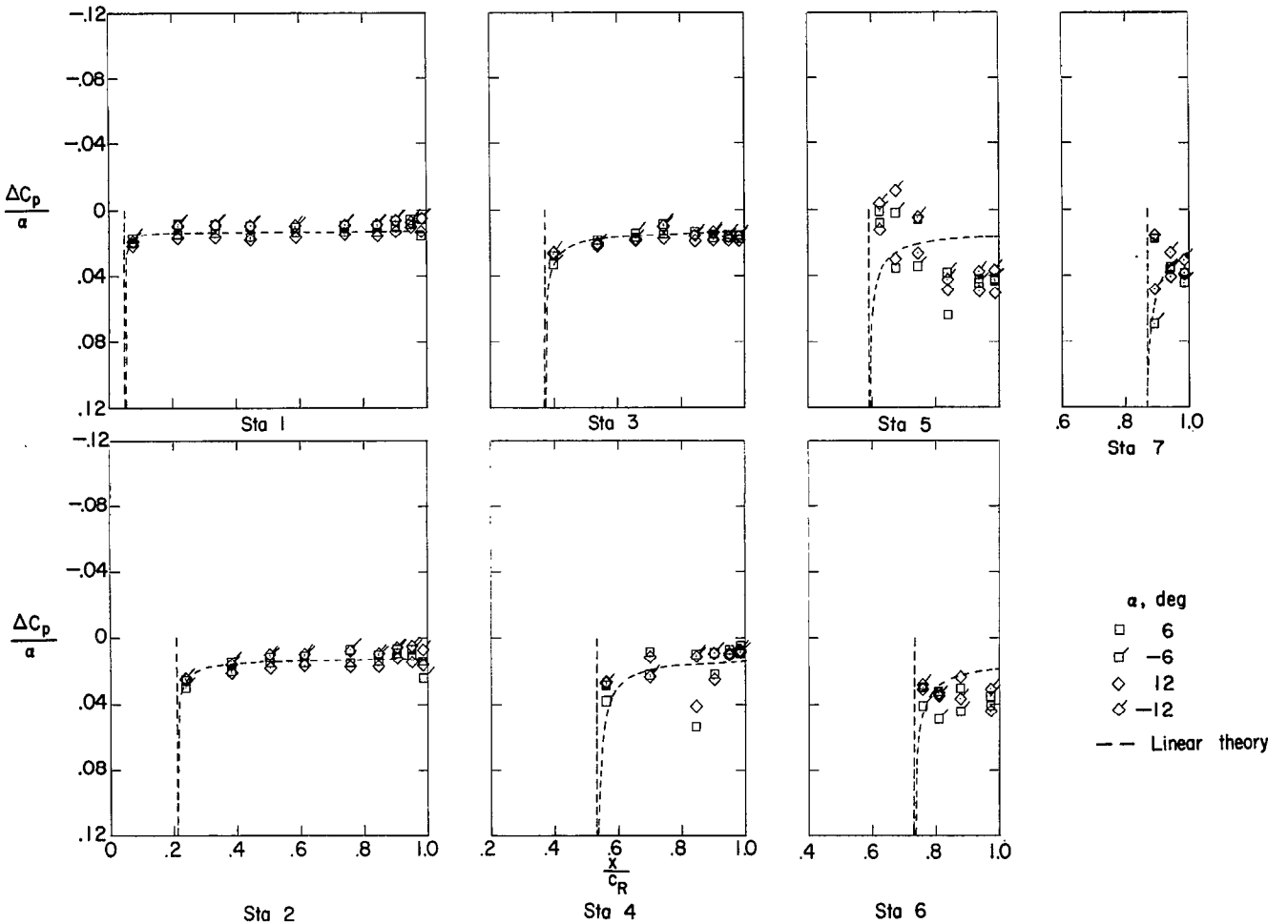

(*l*) Pressure coefficients due to α; δ = 30°; lower surface.

Figure 21.- Continued.

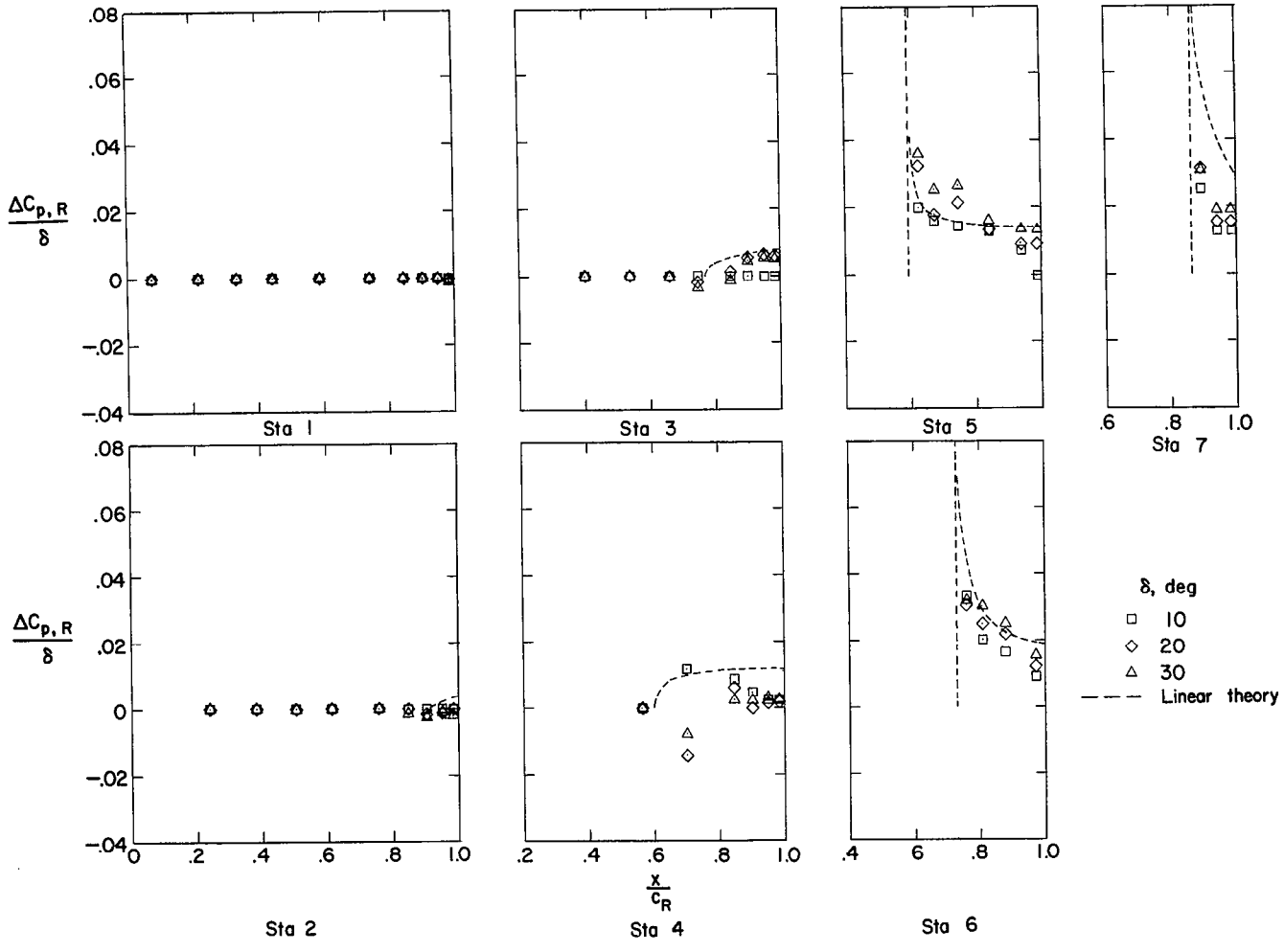

(m) Resultant pressure coefficients due to δ; $\alpha = 0^{\circ}$.

Figure 21.- Continued.

[redacted]

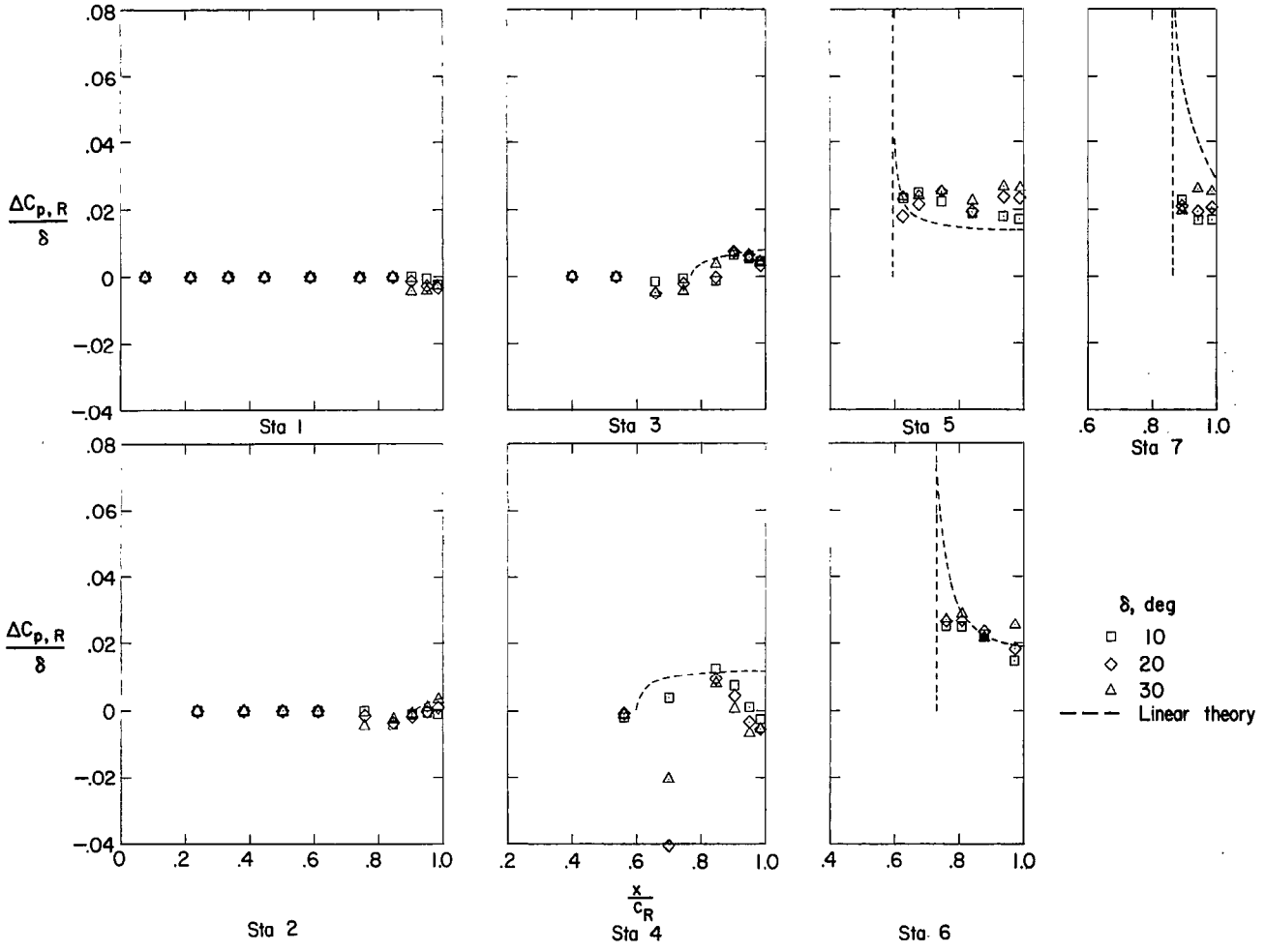

(n) Resultant pressure coefficients due to δ; $\alpha = 12^{\circ}$.

Figure 21.- Continued.

[redacted]

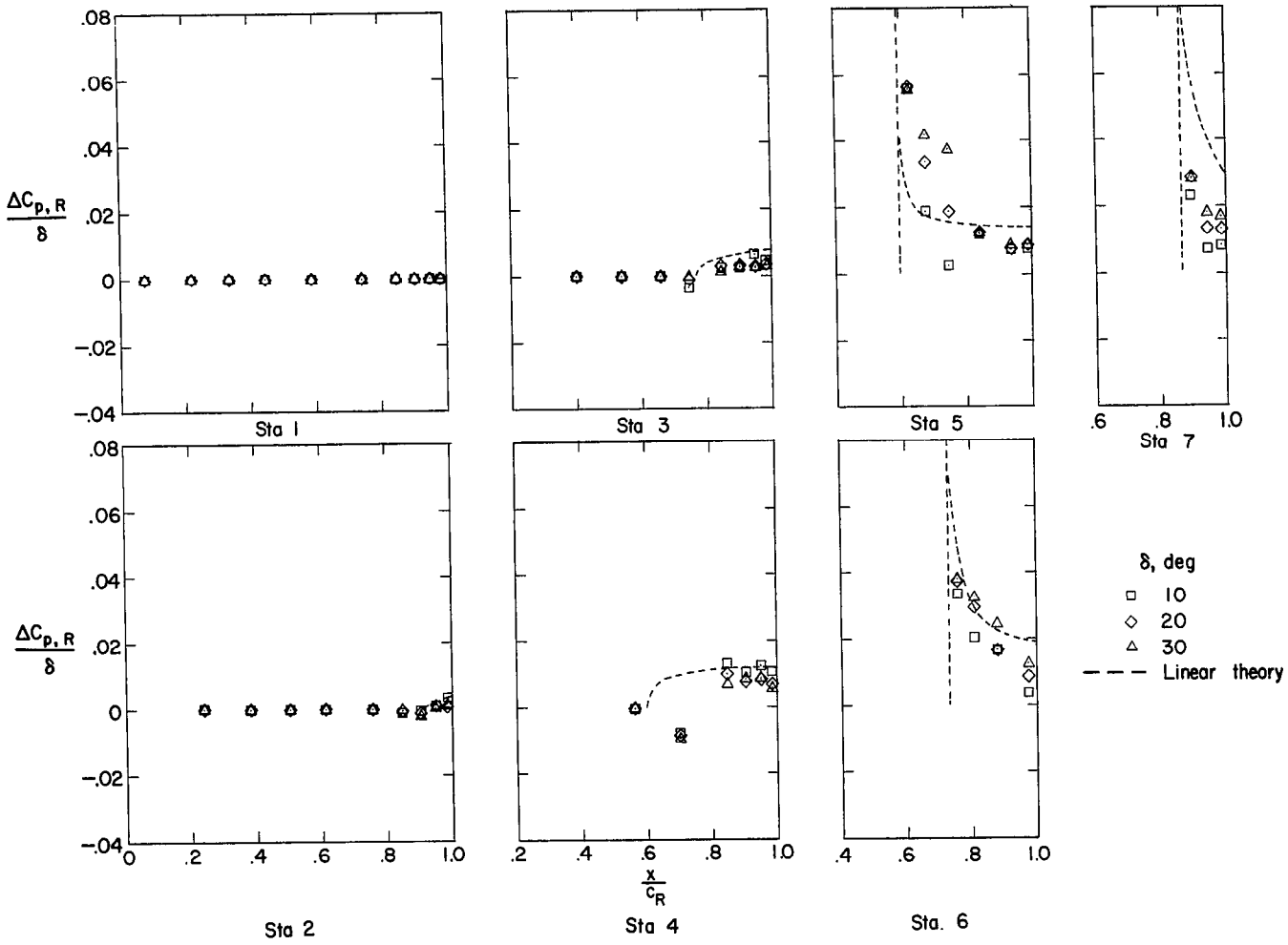

(o) Resultant pressure coefficients due to δ; $\alpha = -12^{\circ}$.

Figure 21.- Continued.

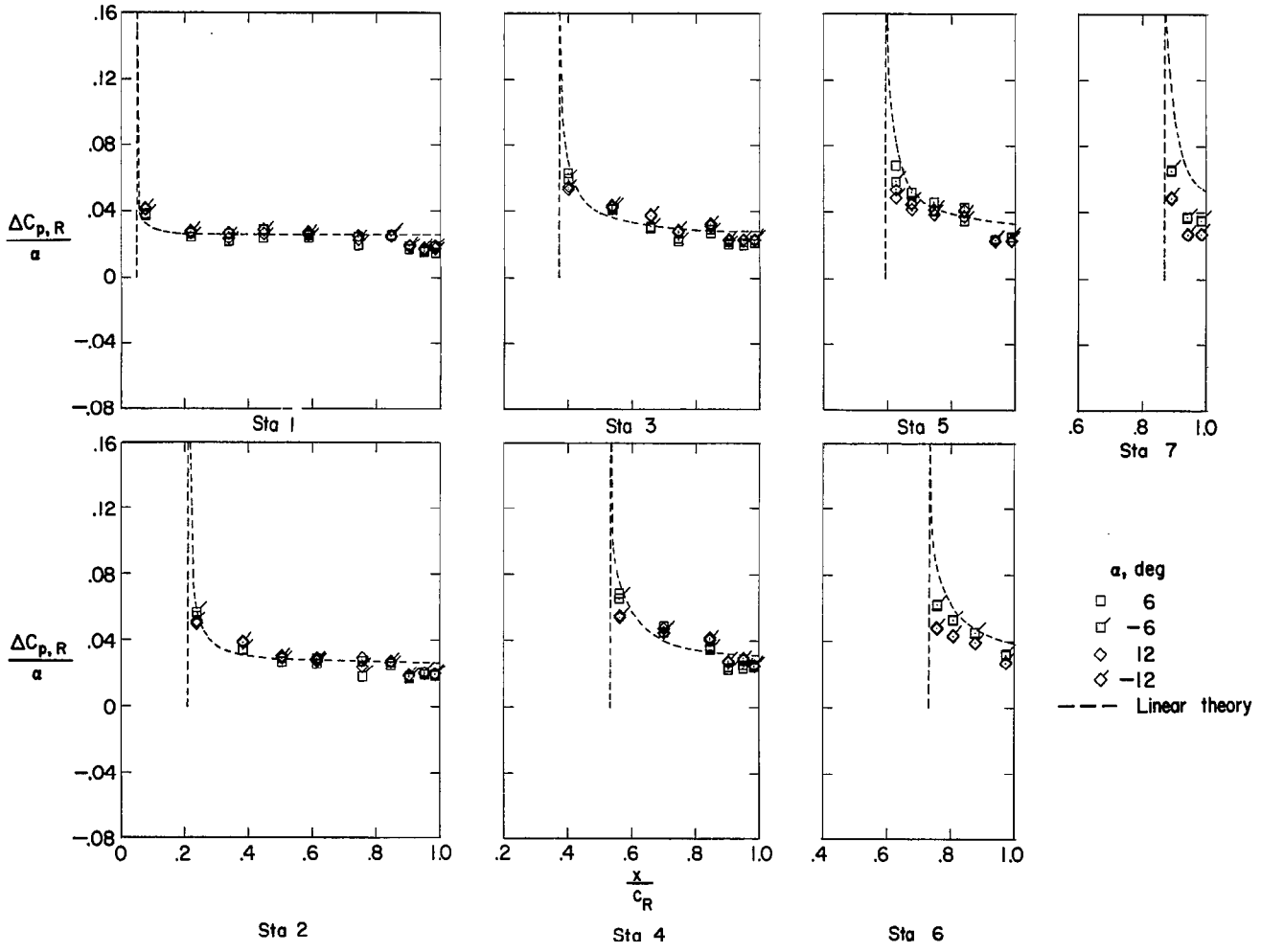

(p) Resultant pressure coefficients due to α; $\delta = 0^{\circ}$.

Figure 21.- Continued.

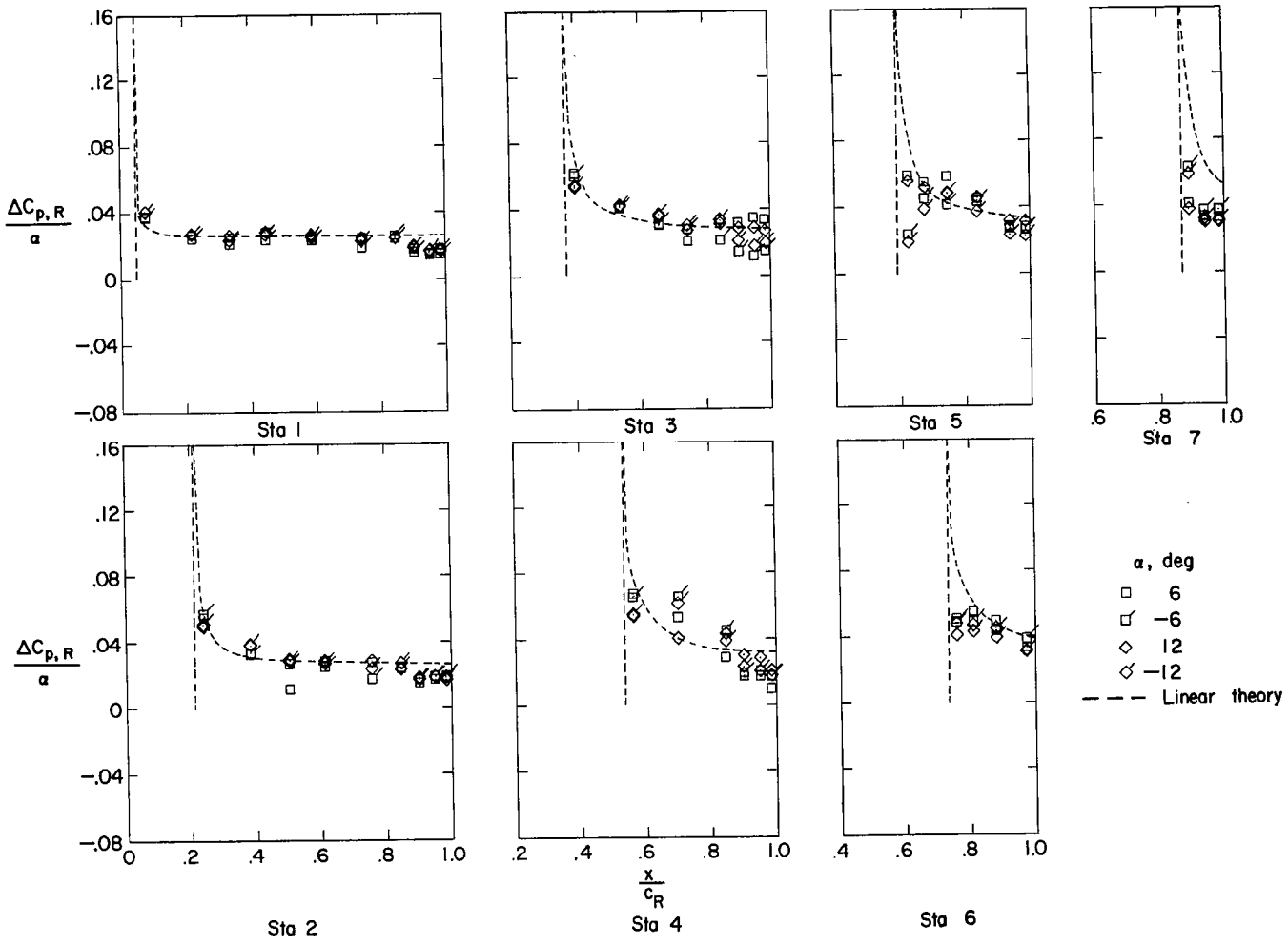

(q) Resultant pressure coefficients due to α; $\delta = 10^{\circ}$.

Figure 21.- Continued.

[redacted]

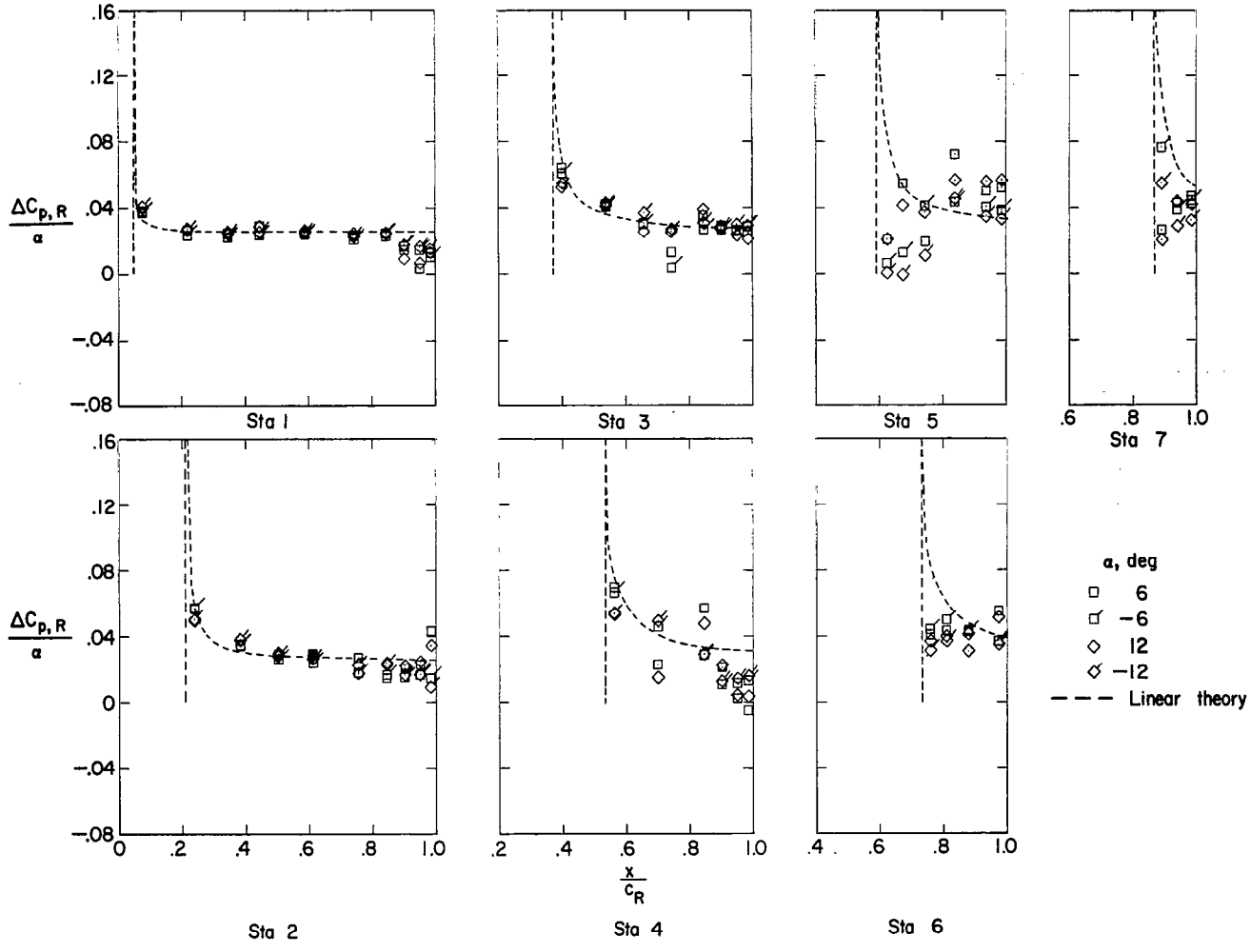

(r) Resultant pressure coefficients due to α; $\delta = 30^{\circ}$.

Figure 21.- Concluded.

[redacted]

[redacted]

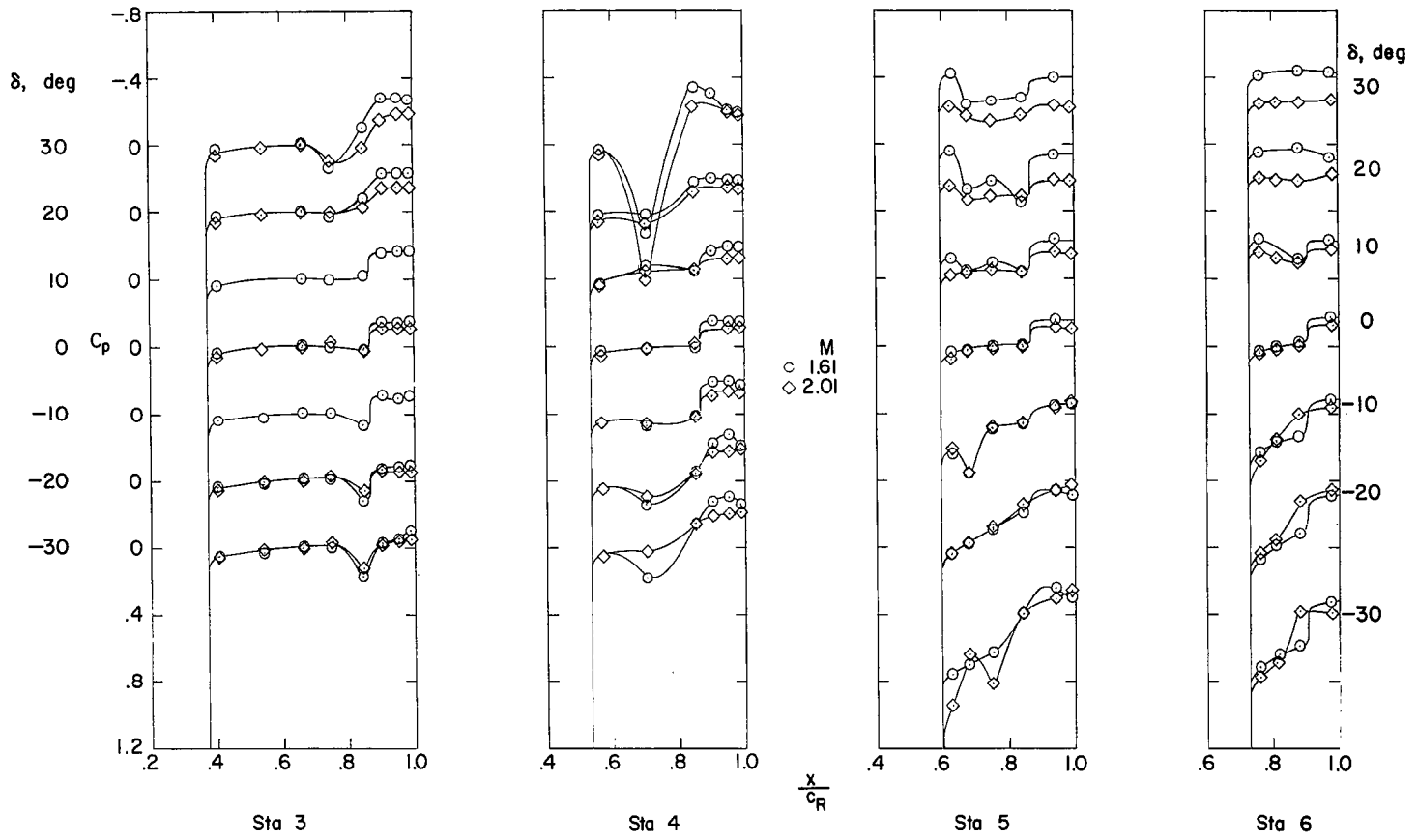

(a) $\alpha = 0^{\circ}$.

Figure 22.- Effect of Mach number on the upper-surface pressure distributions of configuration E. $R = 4.2 \times 10^6$.

[redacted]

[redacted]

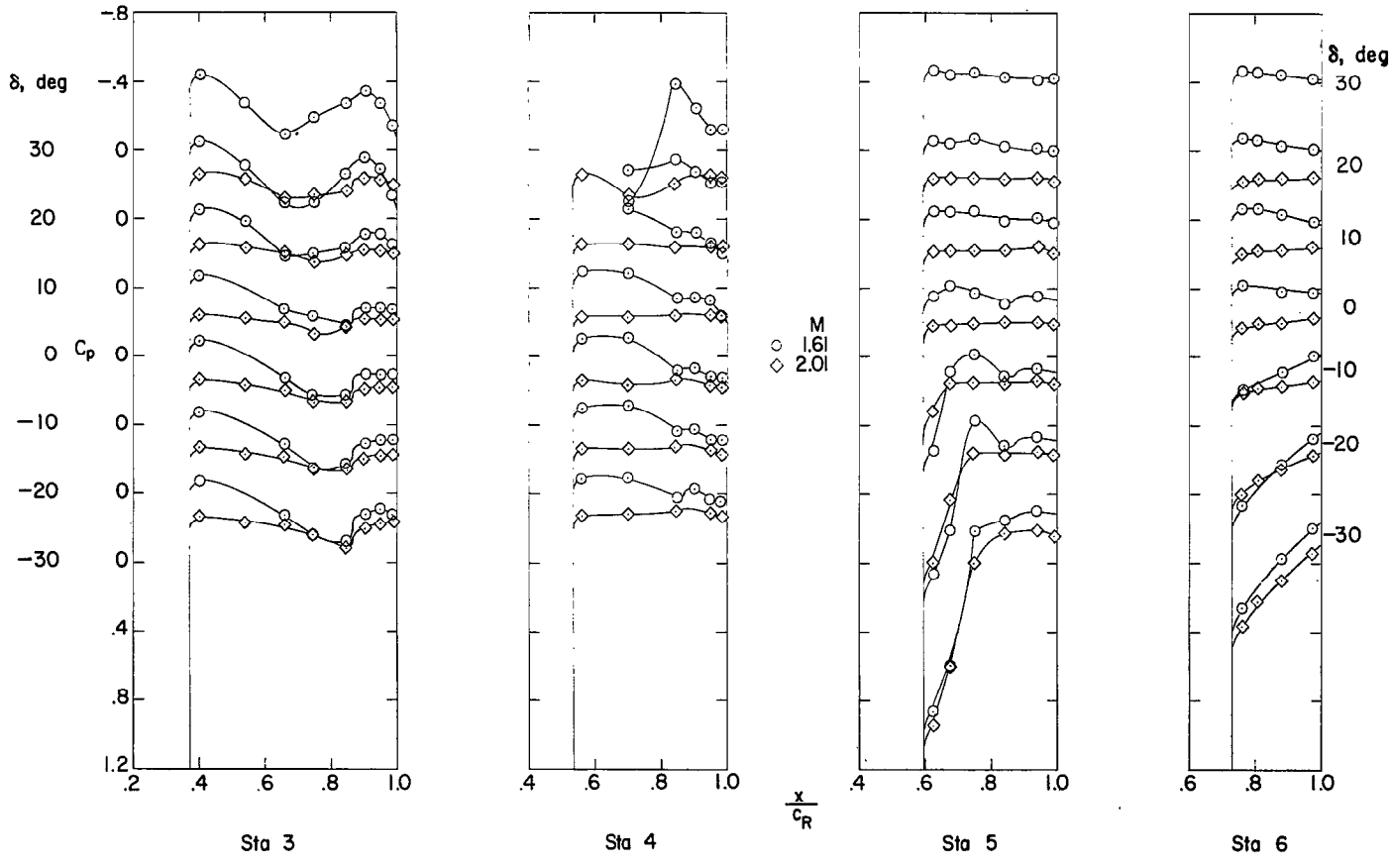

(b) $\alpha = 12^{\circ}$.

Figure 22.- Continued.

[redacted]

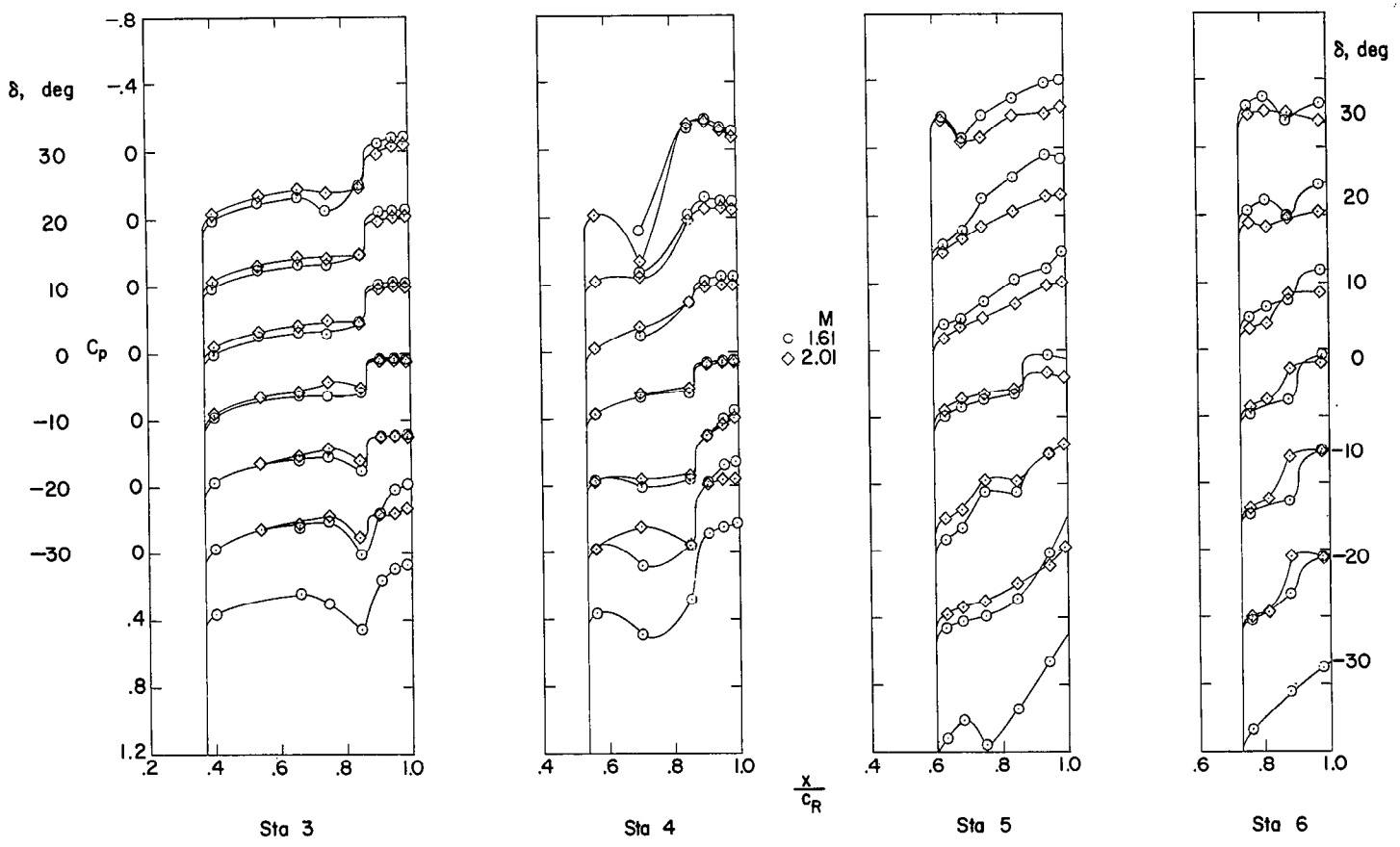

(c) $\alpha = -12^{\circ}$.

Figure 22.- Concluded.

[redacted]

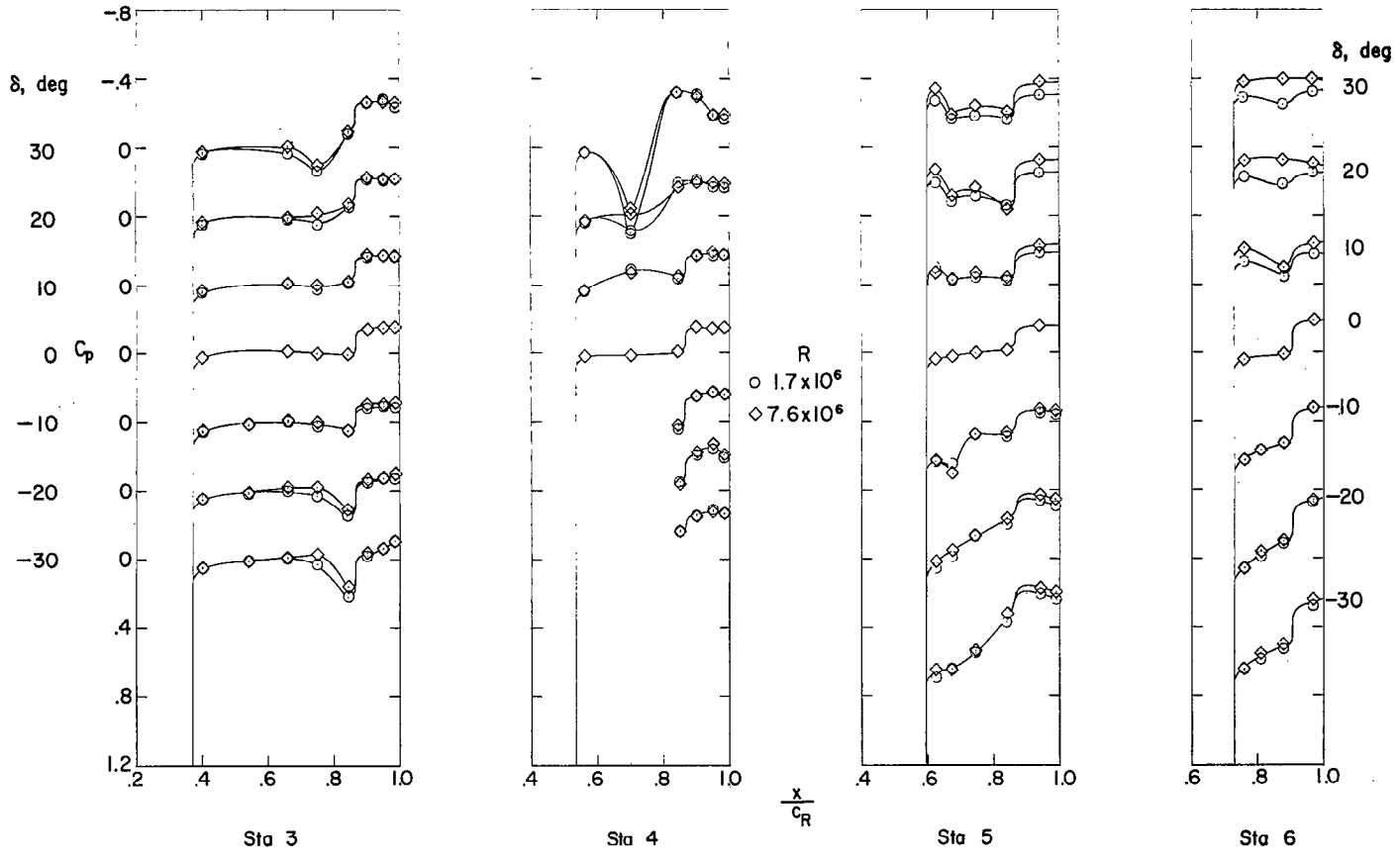

(a) $\alpha = 0^{\circ}$.

Figure 23.- Effect of Reynolds number on the upper-surface pressure distributions of configuration E. M = 1.61.

[redacted]

[redacted]

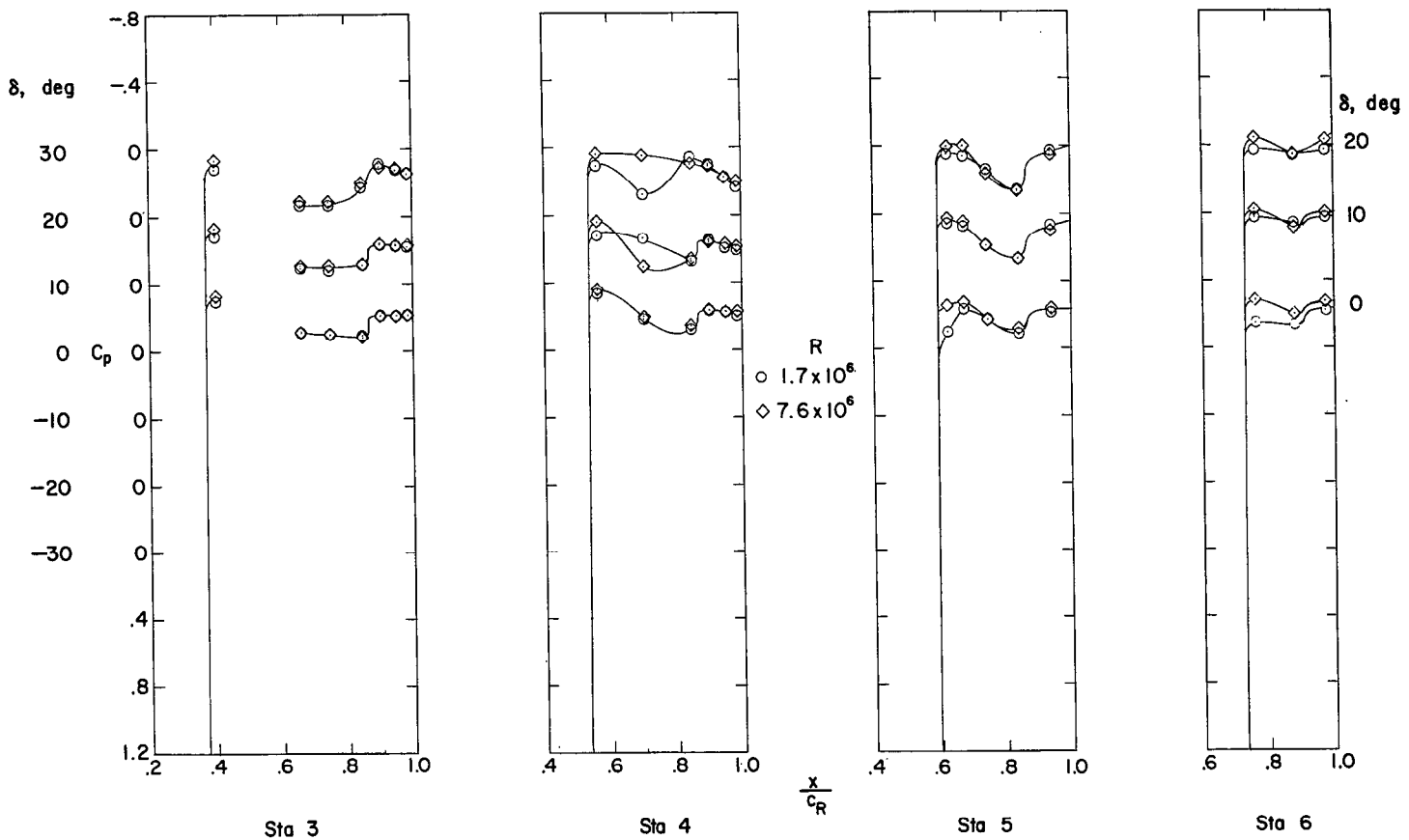

(b) $\alpha = 6^{\circ}$.

Figure 23.- Continued.

[redacted]

[redacted]

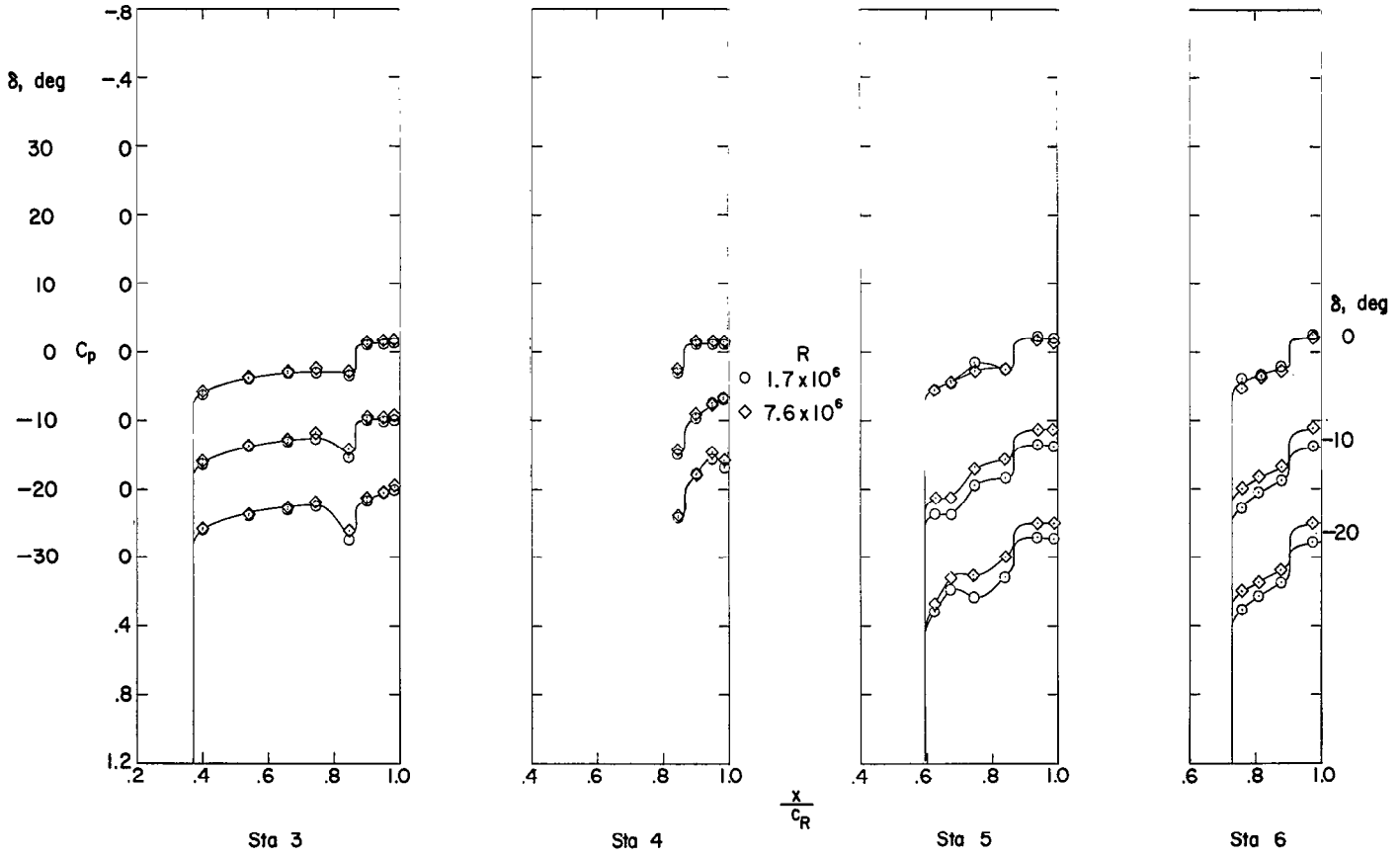

(c) $\alpha = -6^{\circ}$.

Figure 23.- Concluded.

[redacted]

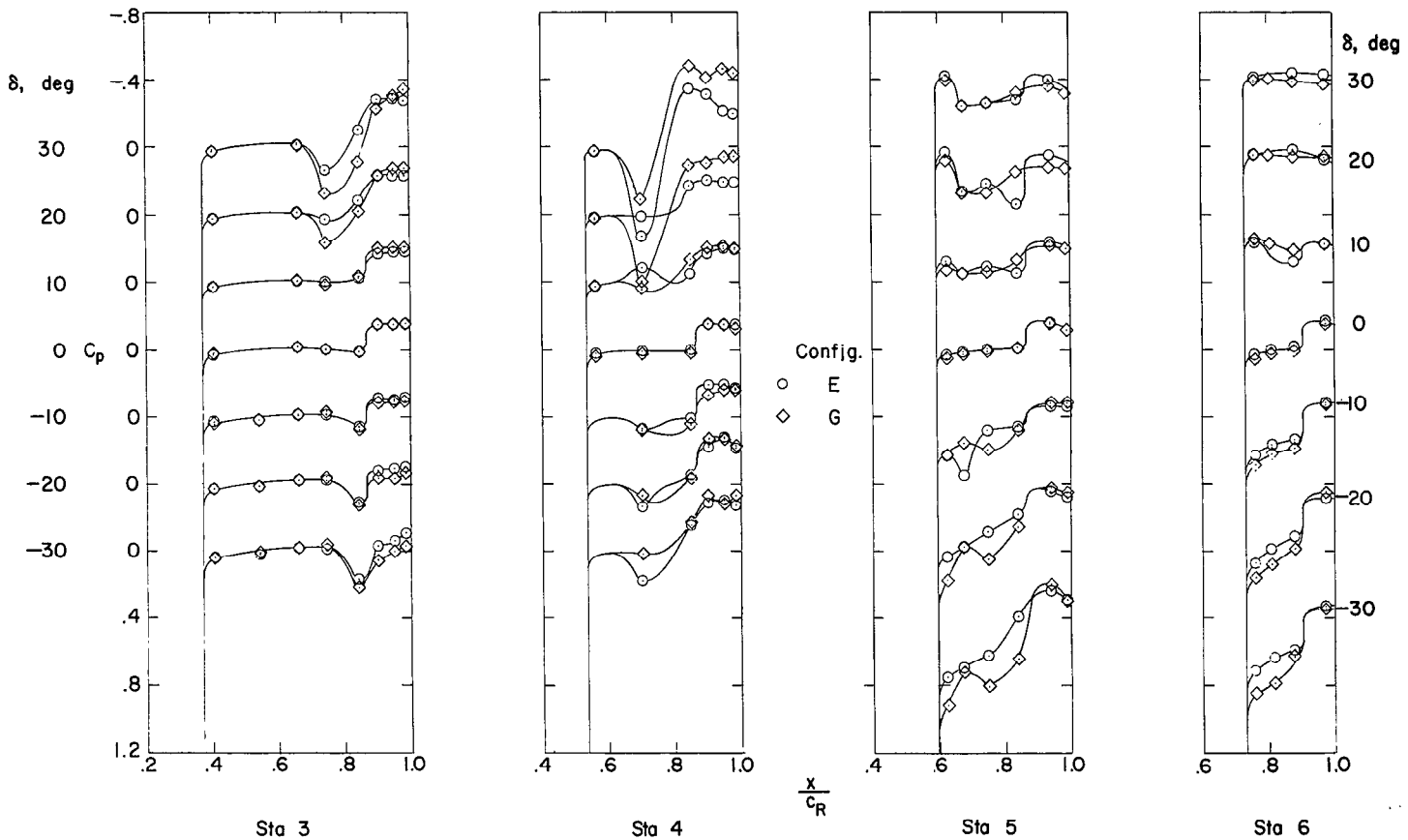

(a) $\alpha = 0^{\circ}$.

Figure 24.- Effect of hinge-line location on the upper-surface pressure distributions of the half-delta tip controls. $M = 1.61$; $R = 4.2 \times 10^6$.

[redacted]

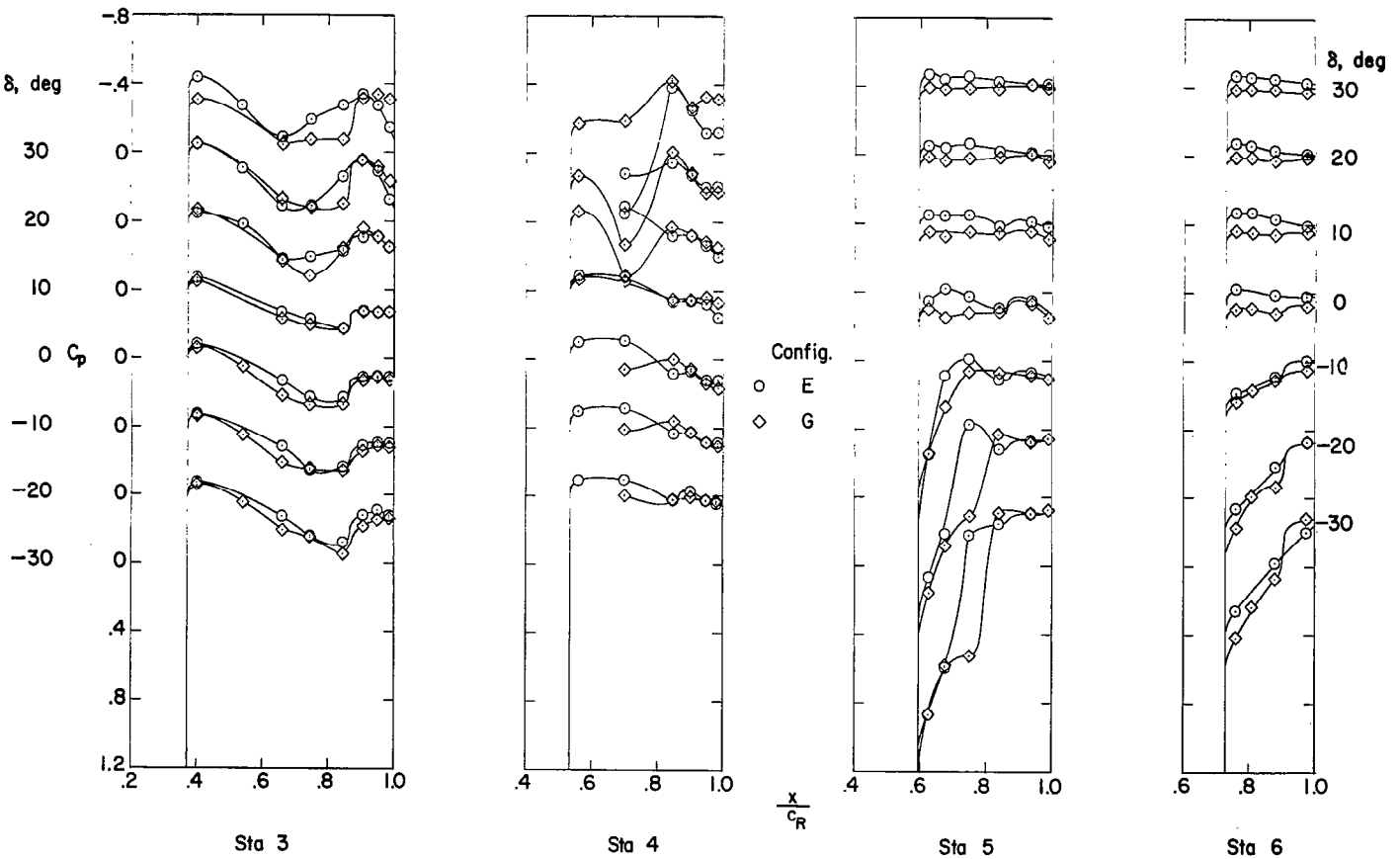

(b) $\alpha = 12^{\circ}$.

Figure 24.- Continued.

[redacted]

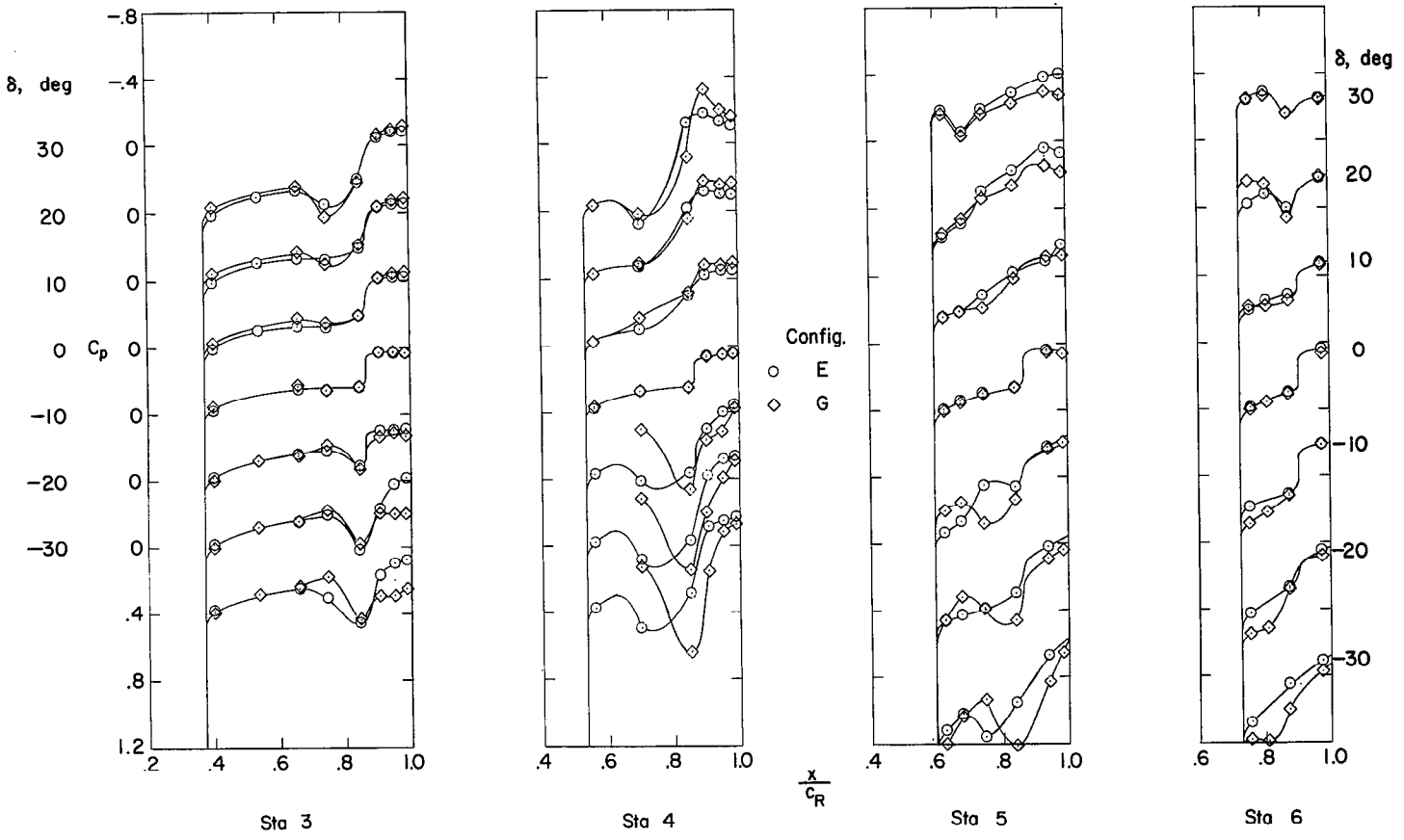

(c) $\alpha = -12^{\circ}$.

Figure 24.- Concluded.

[redacted]

[redacted]

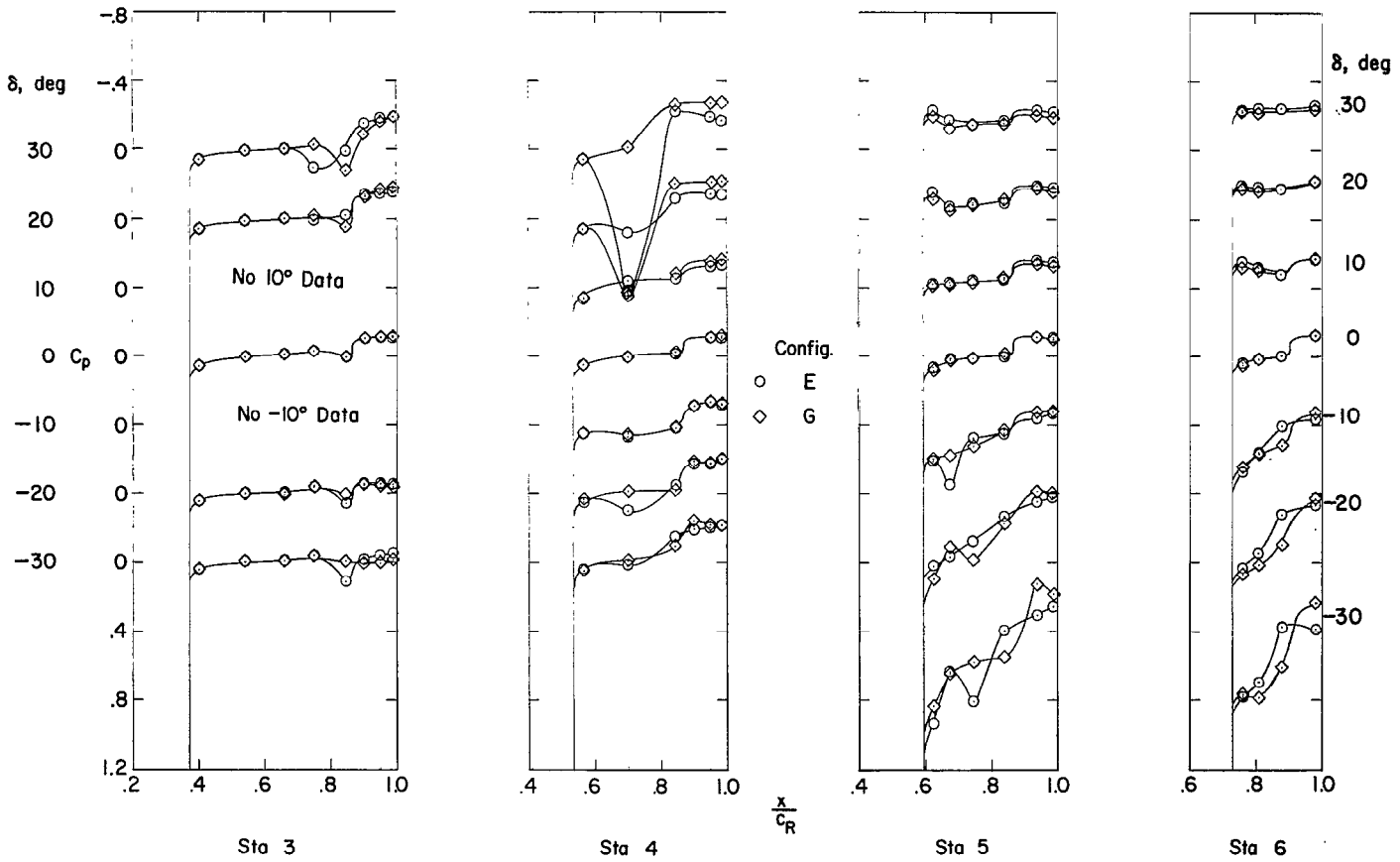

(a) $\alpha = 0^{\circ}$.

Figure 25.- Effect of hinge-line location on the upper-surface pressure distributions of the half-delta tip controls. $M = 2.01$; $R = 4.2 \times 10^{6}$.

[redacted]

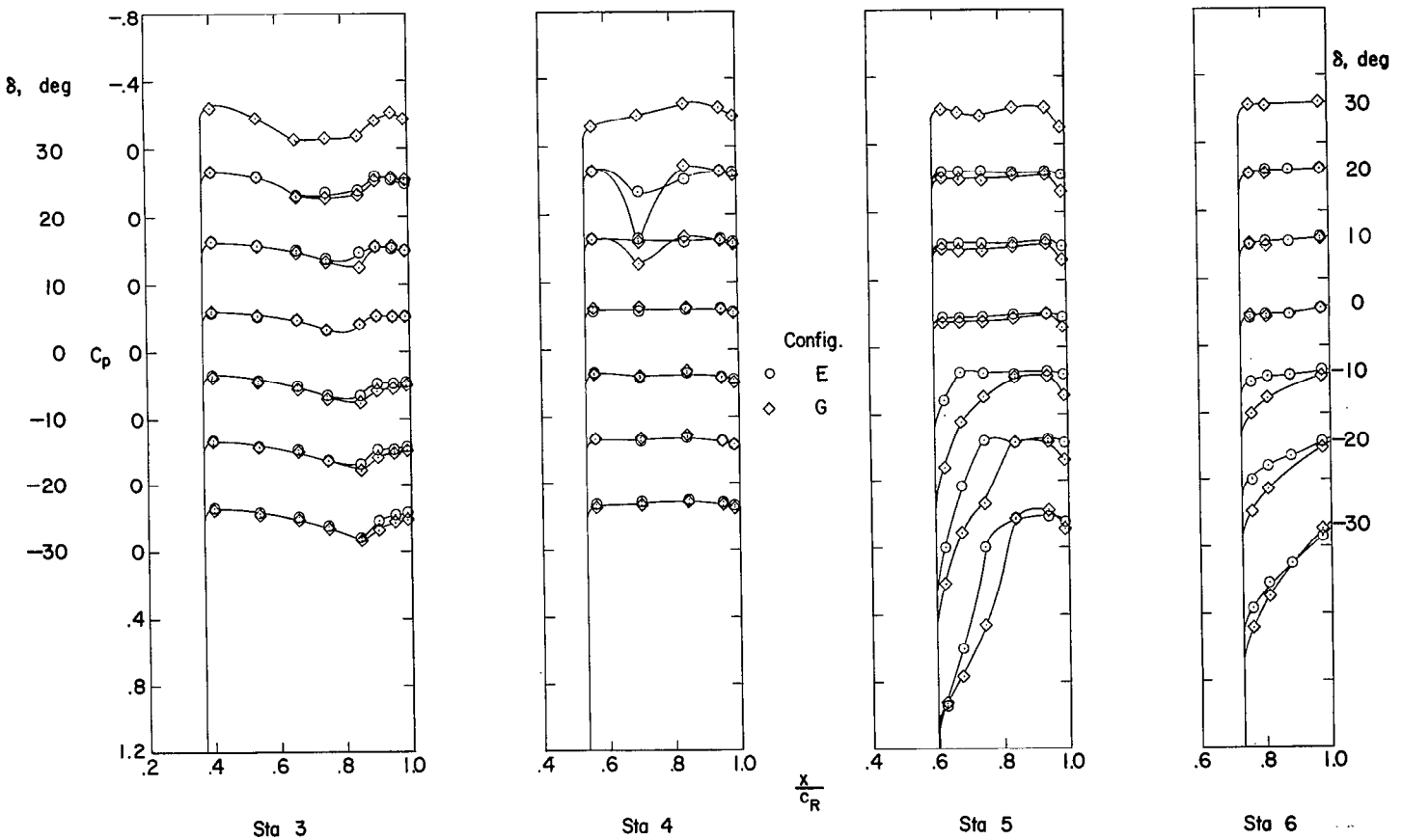

(b) $\alpha = 12^{\circ}$.

Figure 25.- Continued.

[redacted]

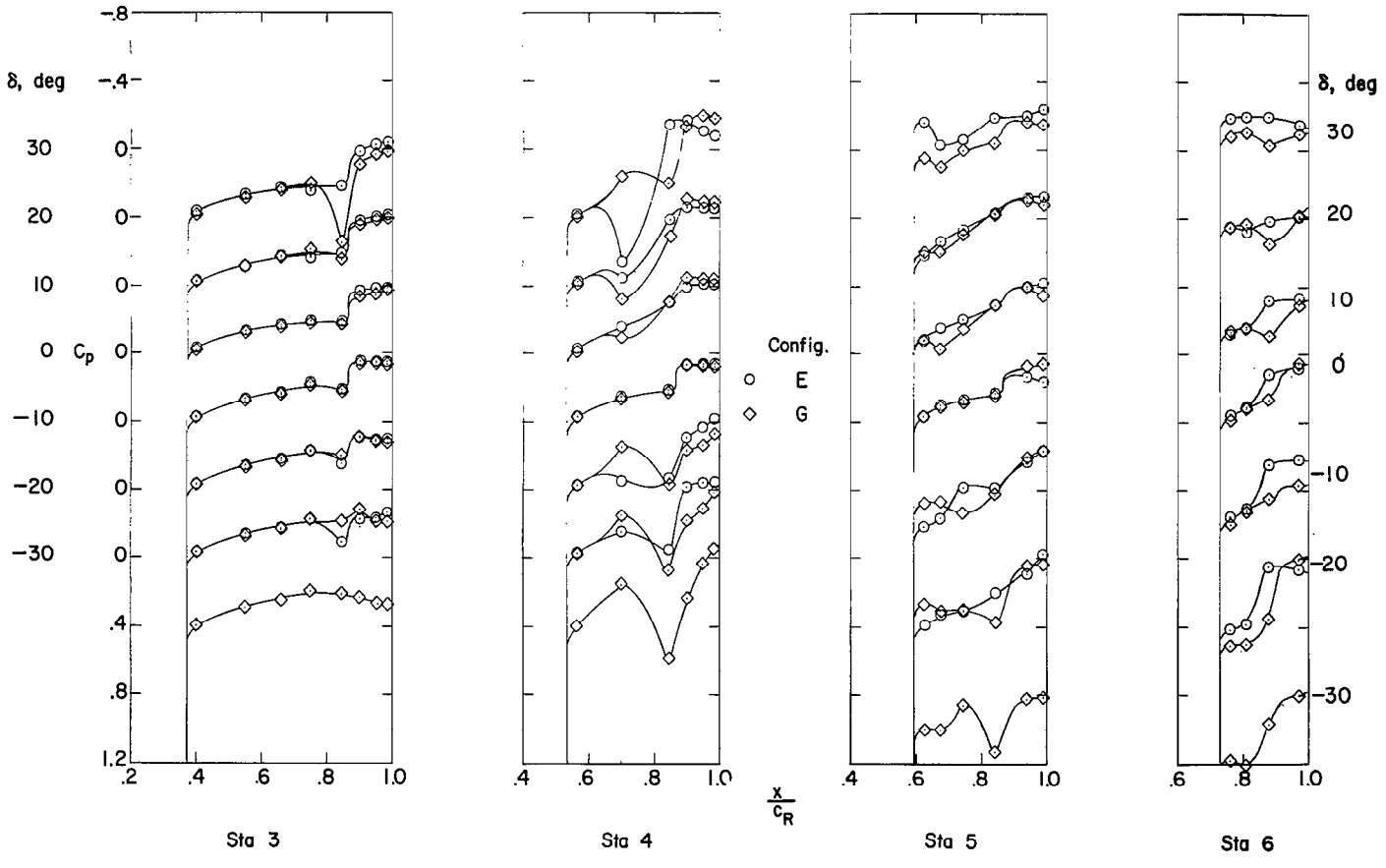

(c) $\alpha = -12^{\circ}$.

Figure 25.- Concluded.

[redacted]

[redacted]

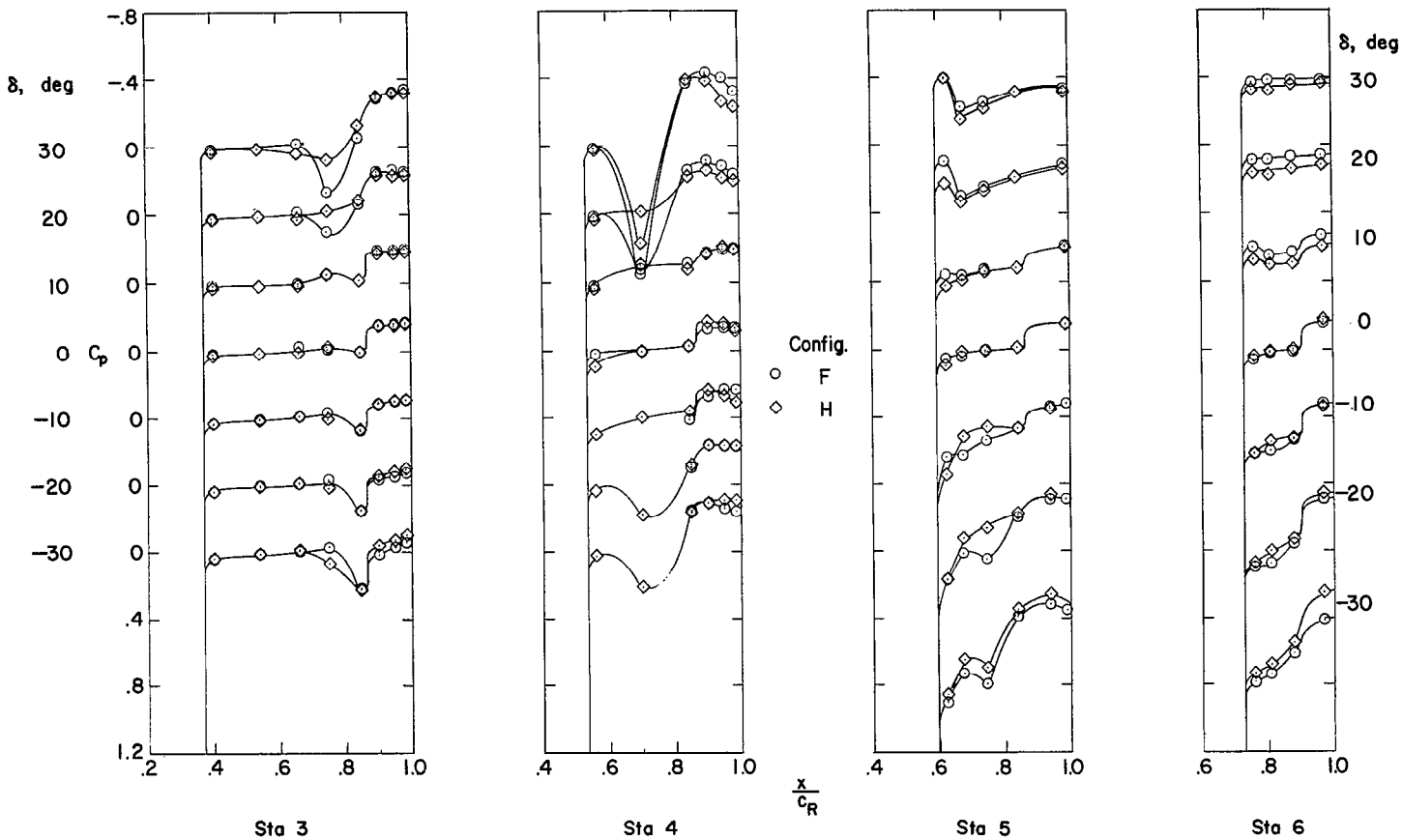

(a) $\alpha = 0^{\circ}$.

Figure 26.- Effect of offsetting a half-delta tip control with respect to the wing on the upper-surface pressure distributions. $M = 1.61$; $R = 4.2 \times 10^6$.

[redacted]

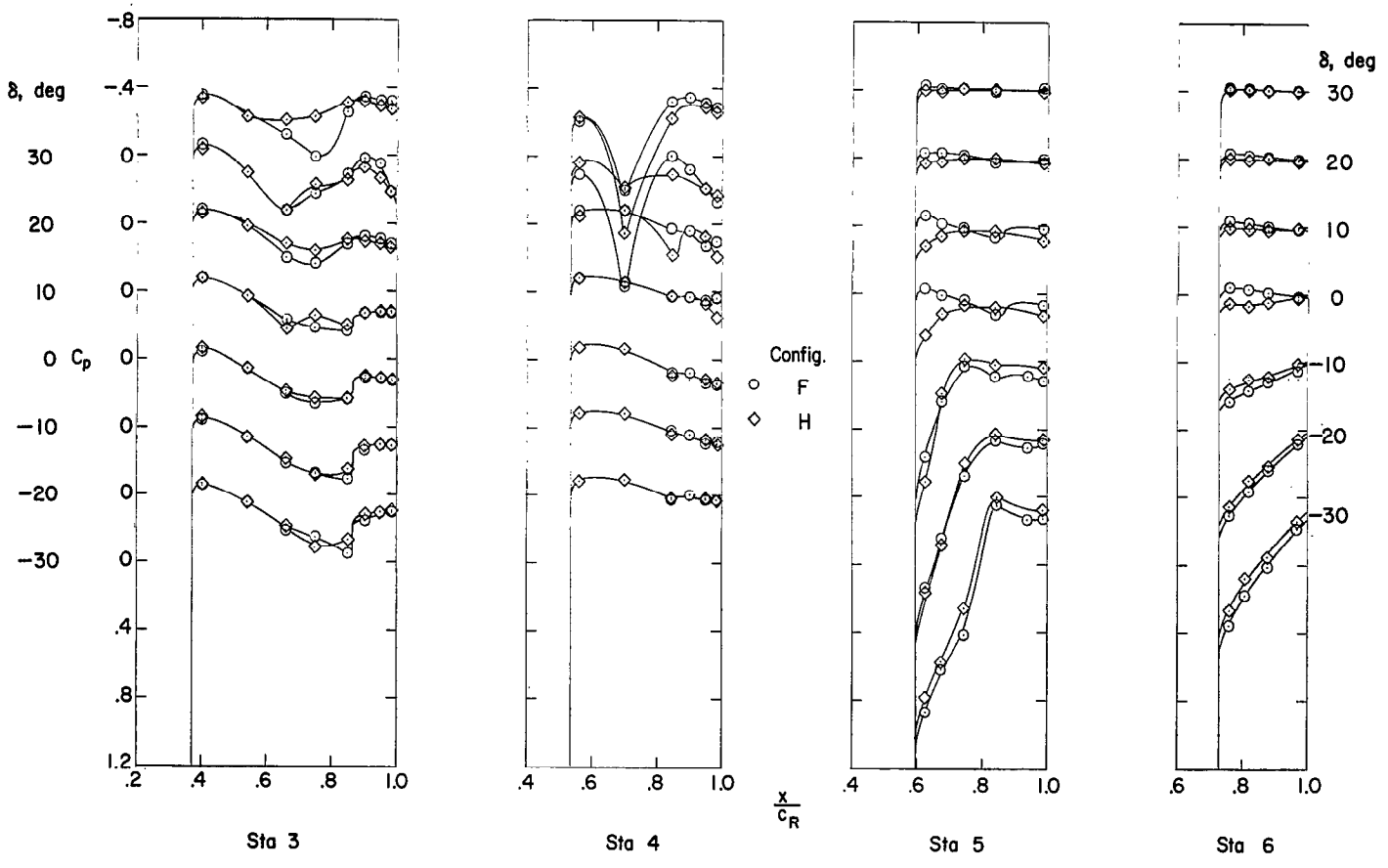

(b) $\alpha = 12^{\circ}$.

Figure 26.- Continued.

[redacted]

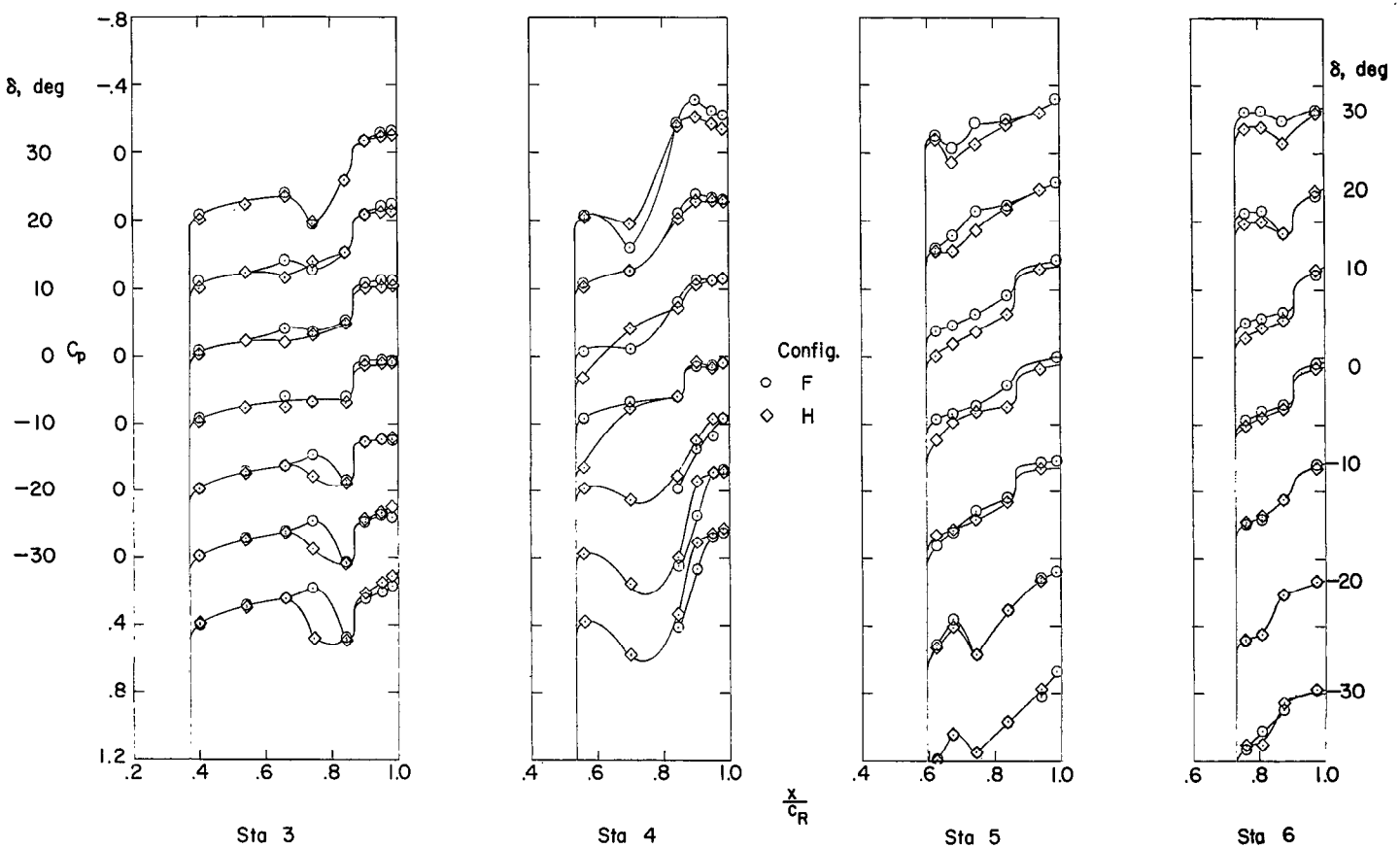

(c) $\alpha = -12^{\circ}$.

Figure 26.- Concluded.

[redacted]

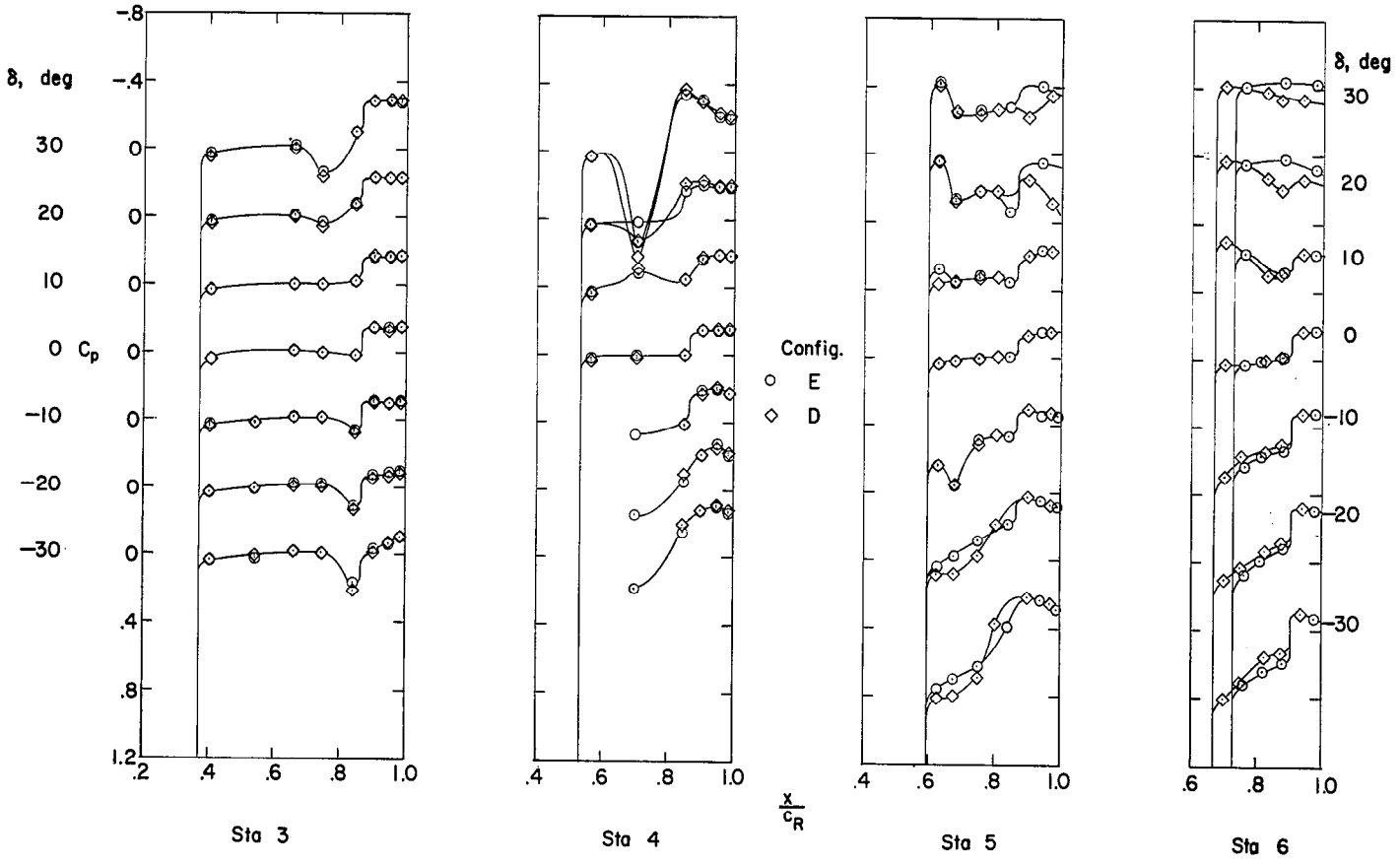

(a) $\alpha = 0^{\circ}$.

Figure 27.- Effect of modifying the control plan form of a tip control on the upper-surface pressure distributions. $M = 1.61$; $R = 4.2 \times 10^6$.

[redacted]

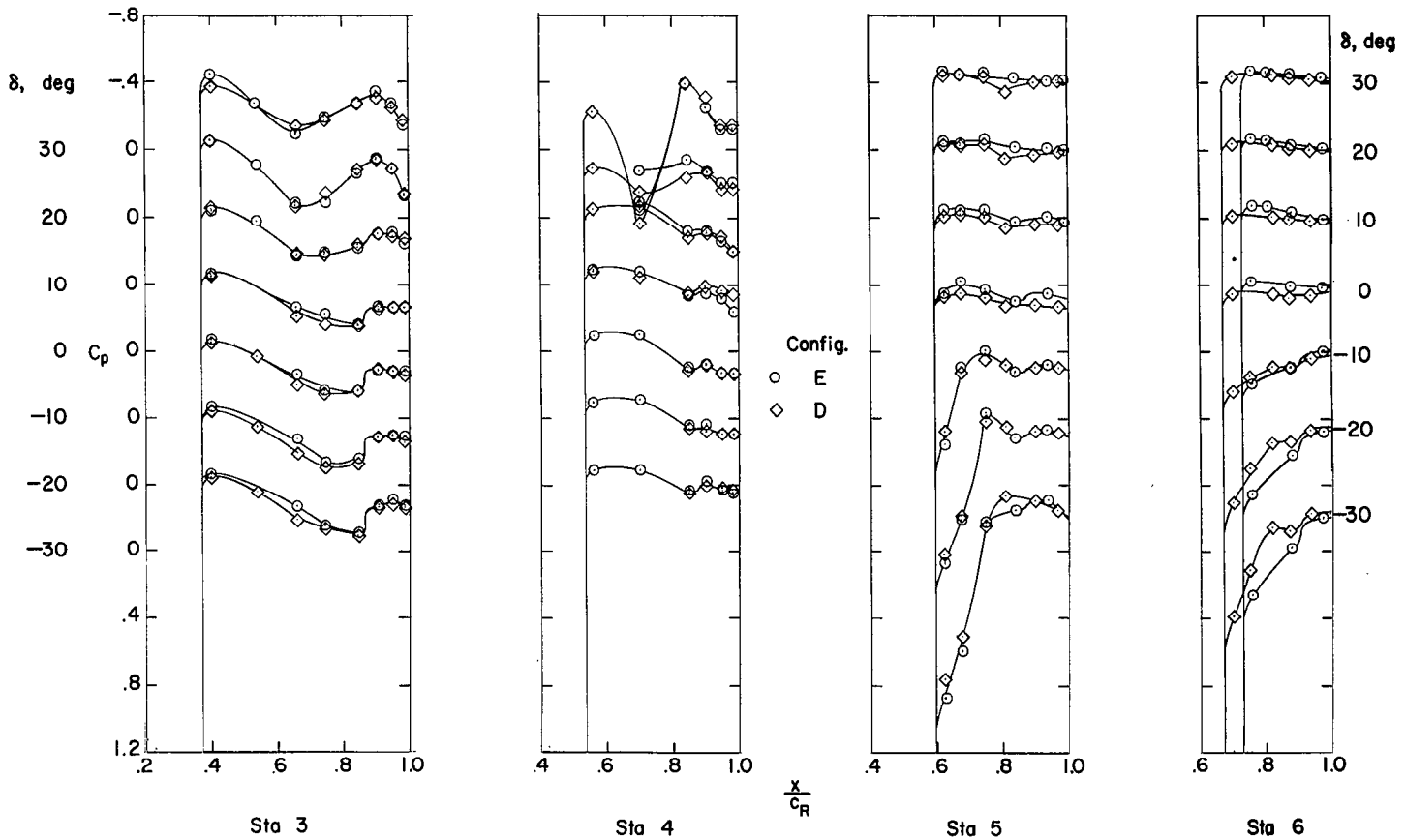

(b) $\alpha = 12^{\circ}$.

Figure 27.- Continued.

[redacted]

[redacted]

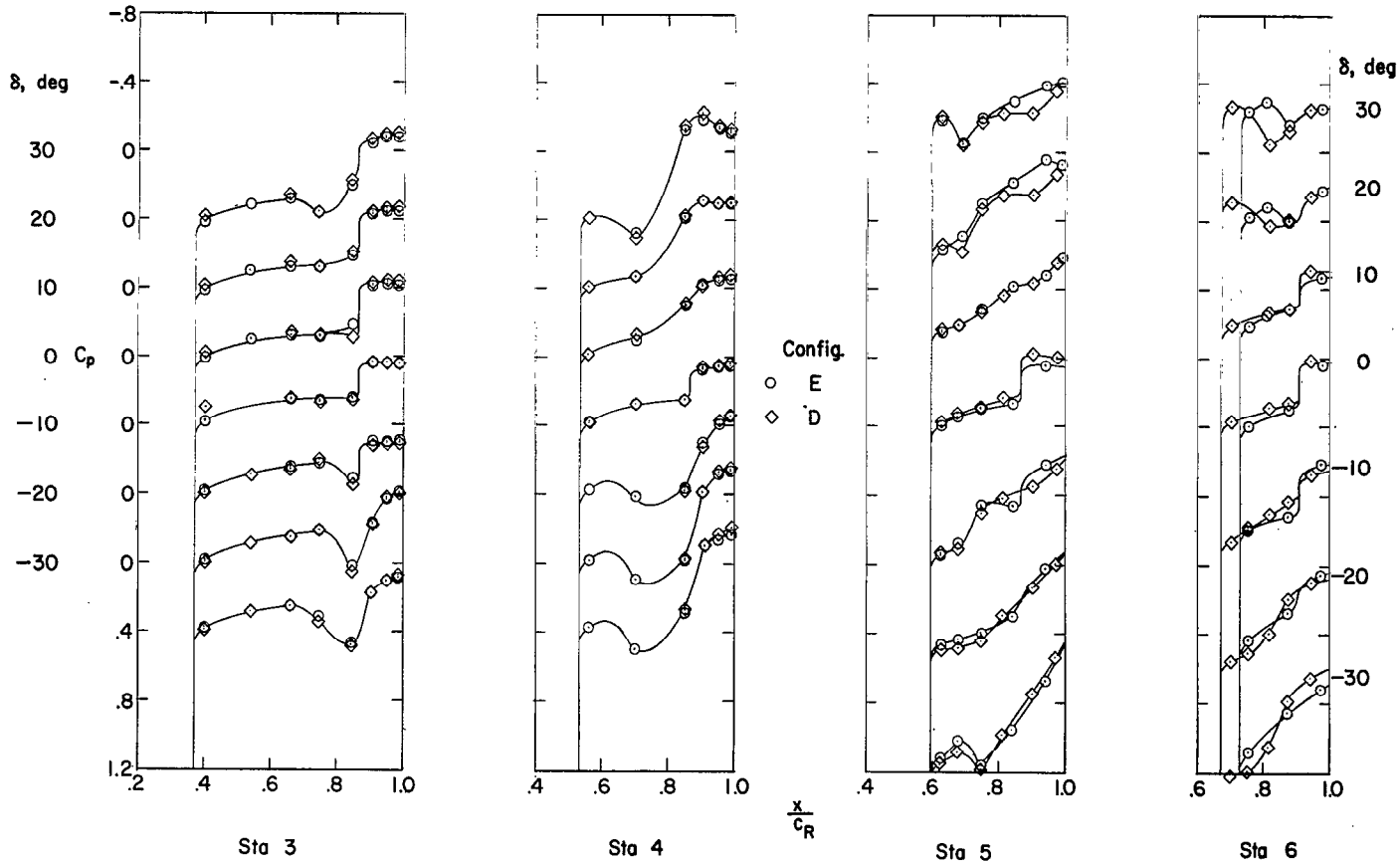

(c) $\alpha = -12^{\circ}$.

Figure 27.- Concluded.

[redacted]

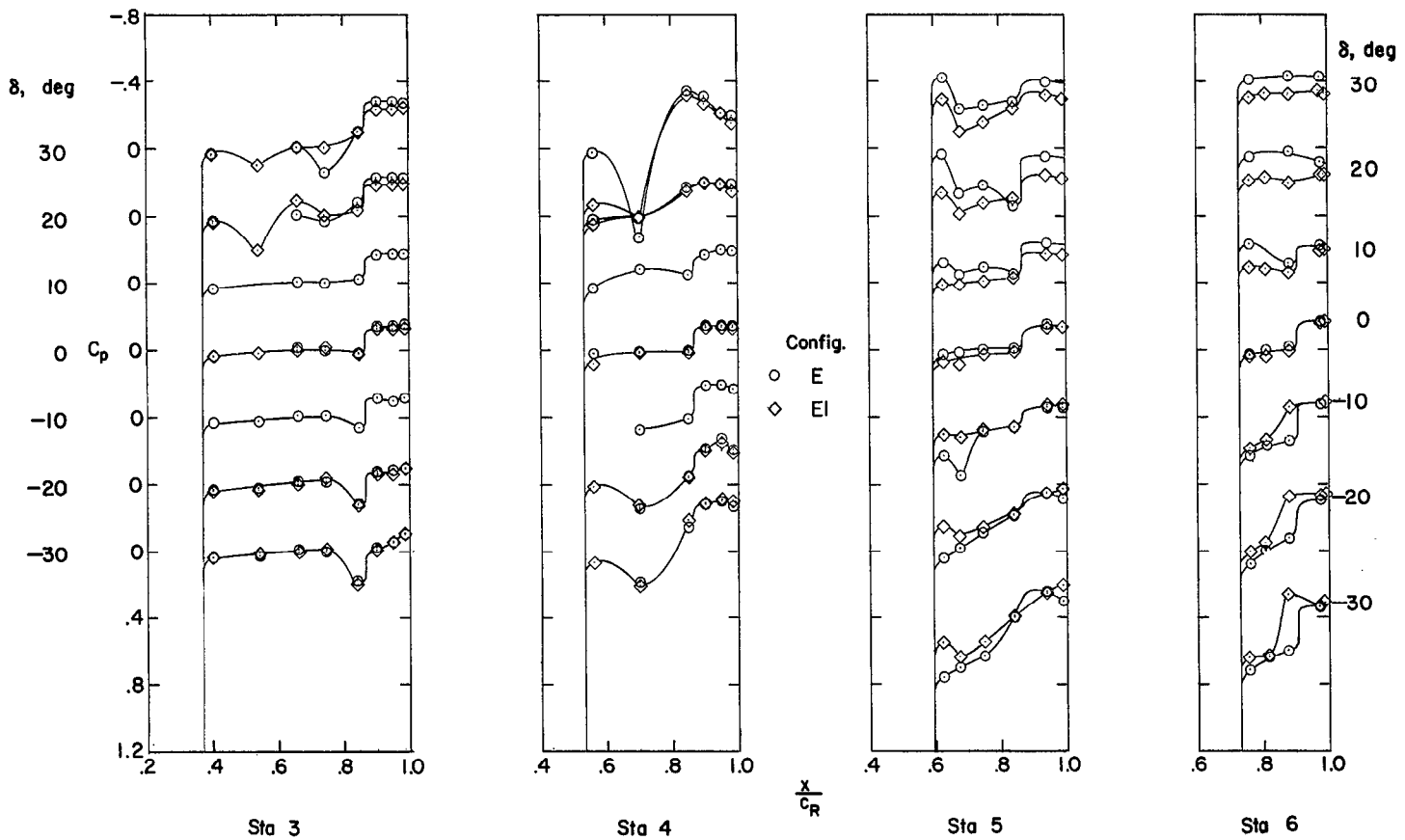

(a) $\alpha = 0^{\circ}$.

Figure 28.- Effect of a fixed tab ahead of a tip control on the wing and control upper-surface pressure distributions. $M = 1.61$; $R = 4.2 \times 10^{6}$.

[redacted]

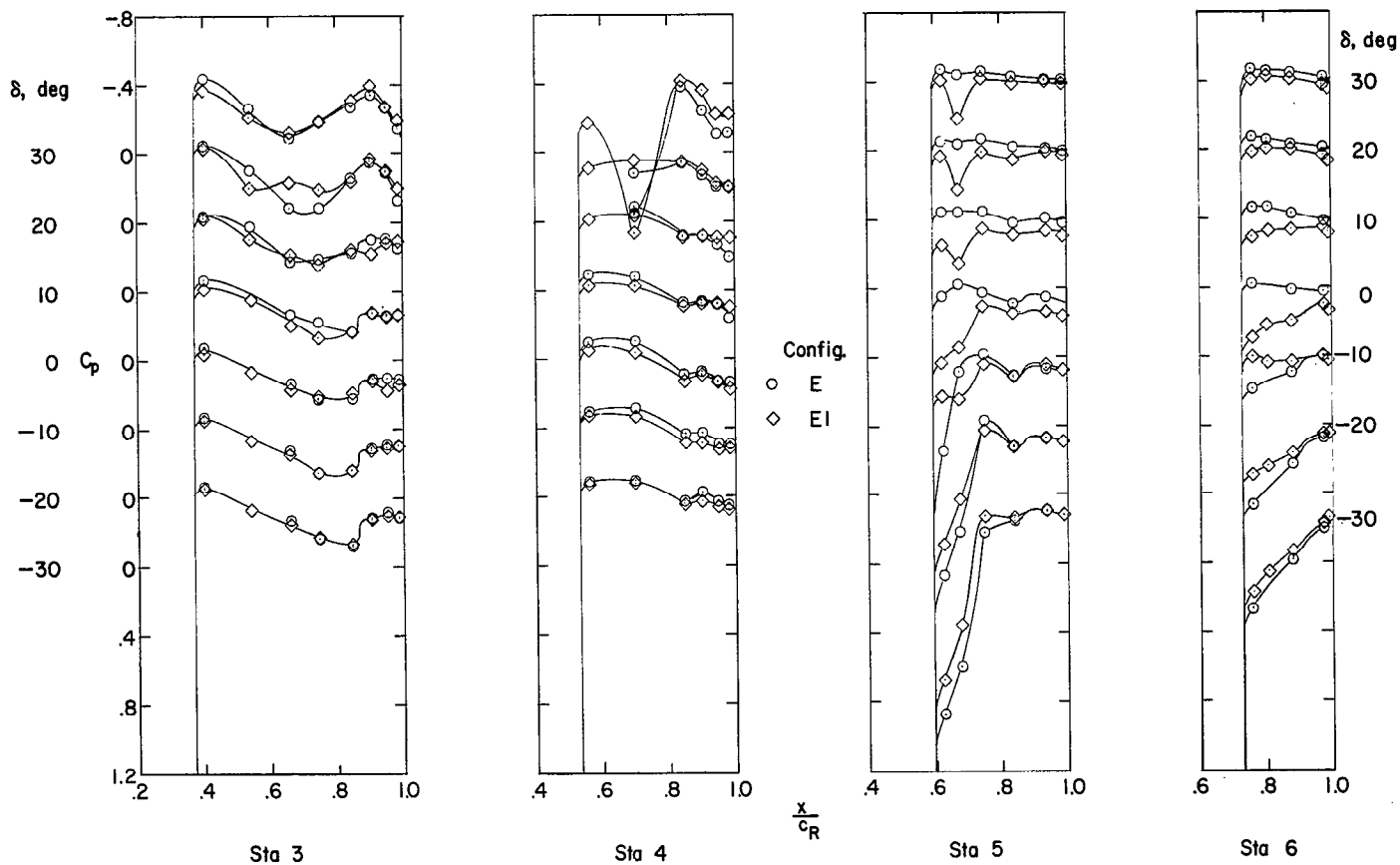

(b) $\alpha = 12^{\circ}$.

Figure 28.- Continued.

[redacted]

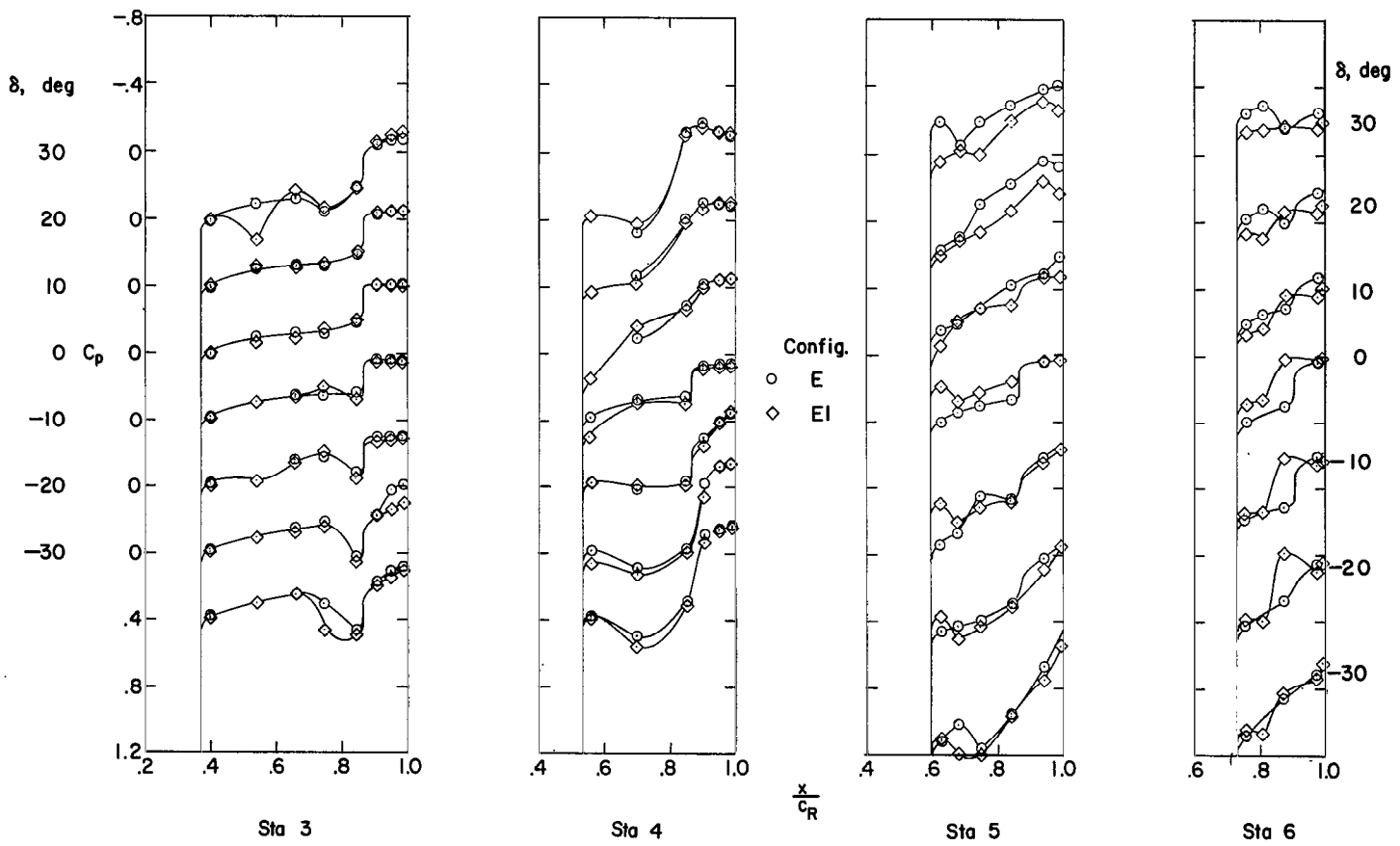

(c) $\alpha = -12^{\circ}$.

Figure 28.- Concluded.

[redacted]

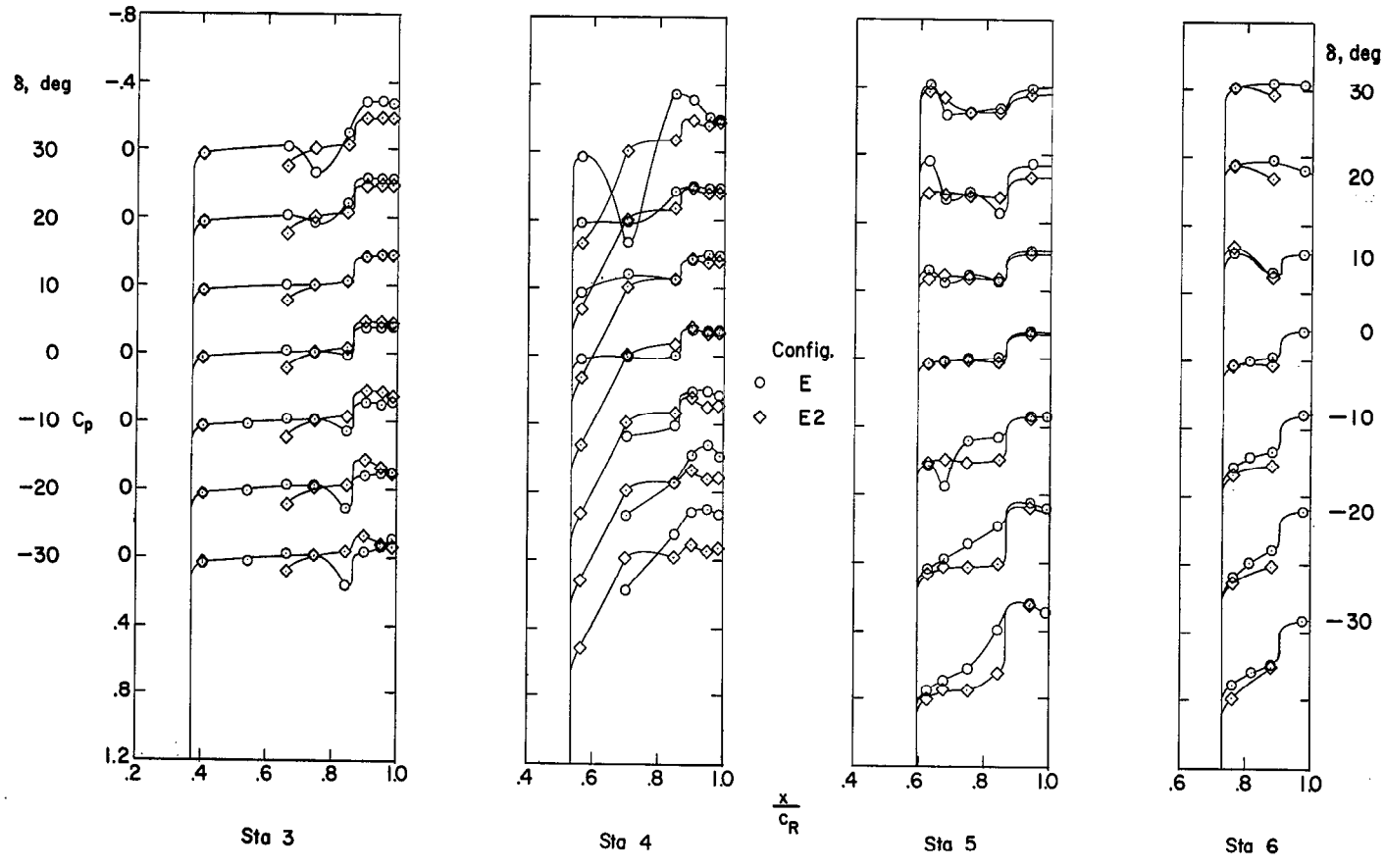

(a) $\alpha = 0^{\circ}$.

Figure 29.- Effect of a full-chord fence on the upper-surface pressure distributions on configuration E. $M = 1.61$; $R = 4.2 \times 10^6$.

[redacted]

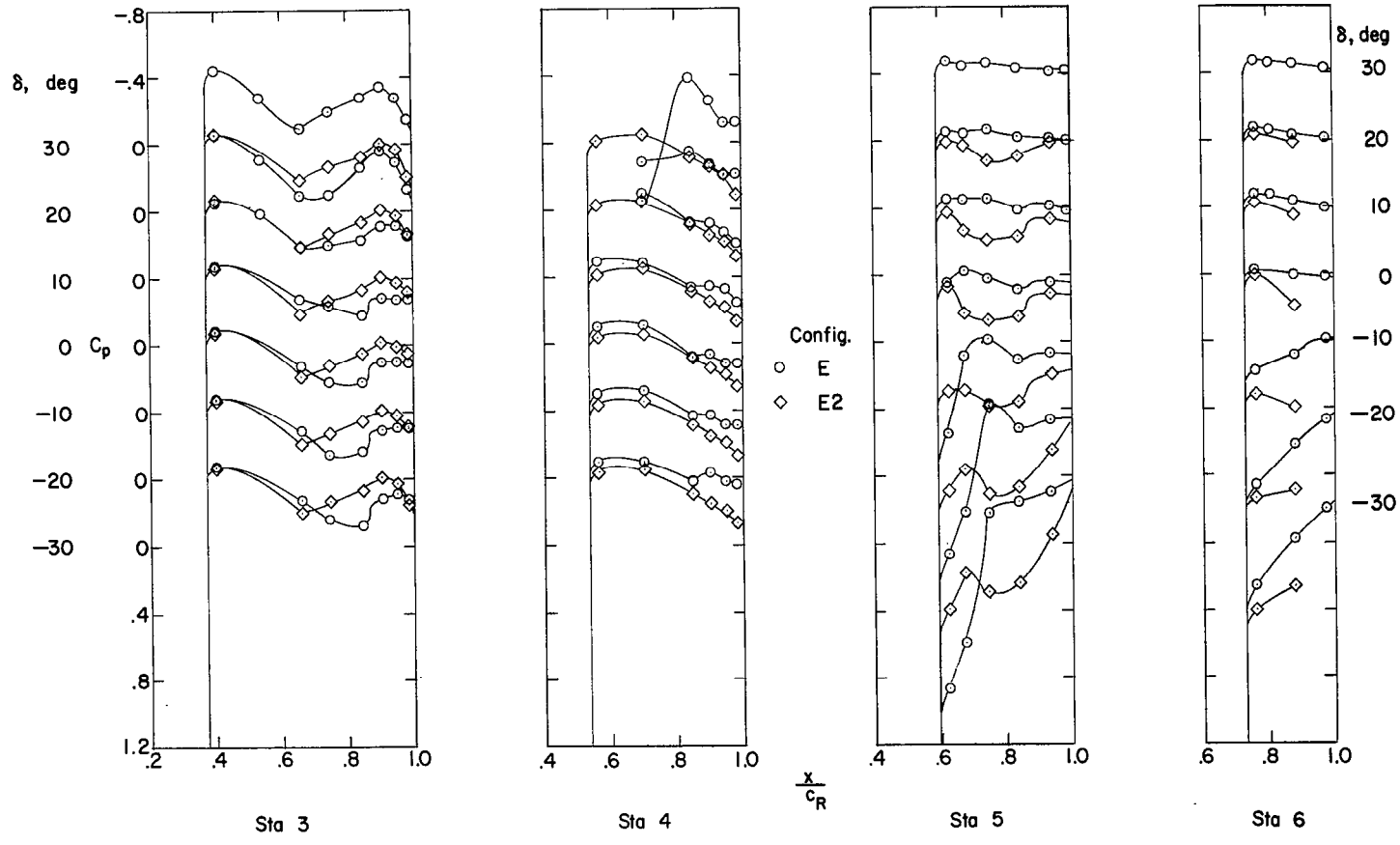

(b) $\alpha = 12^{\circ}$.

Figure 29.- Continued.

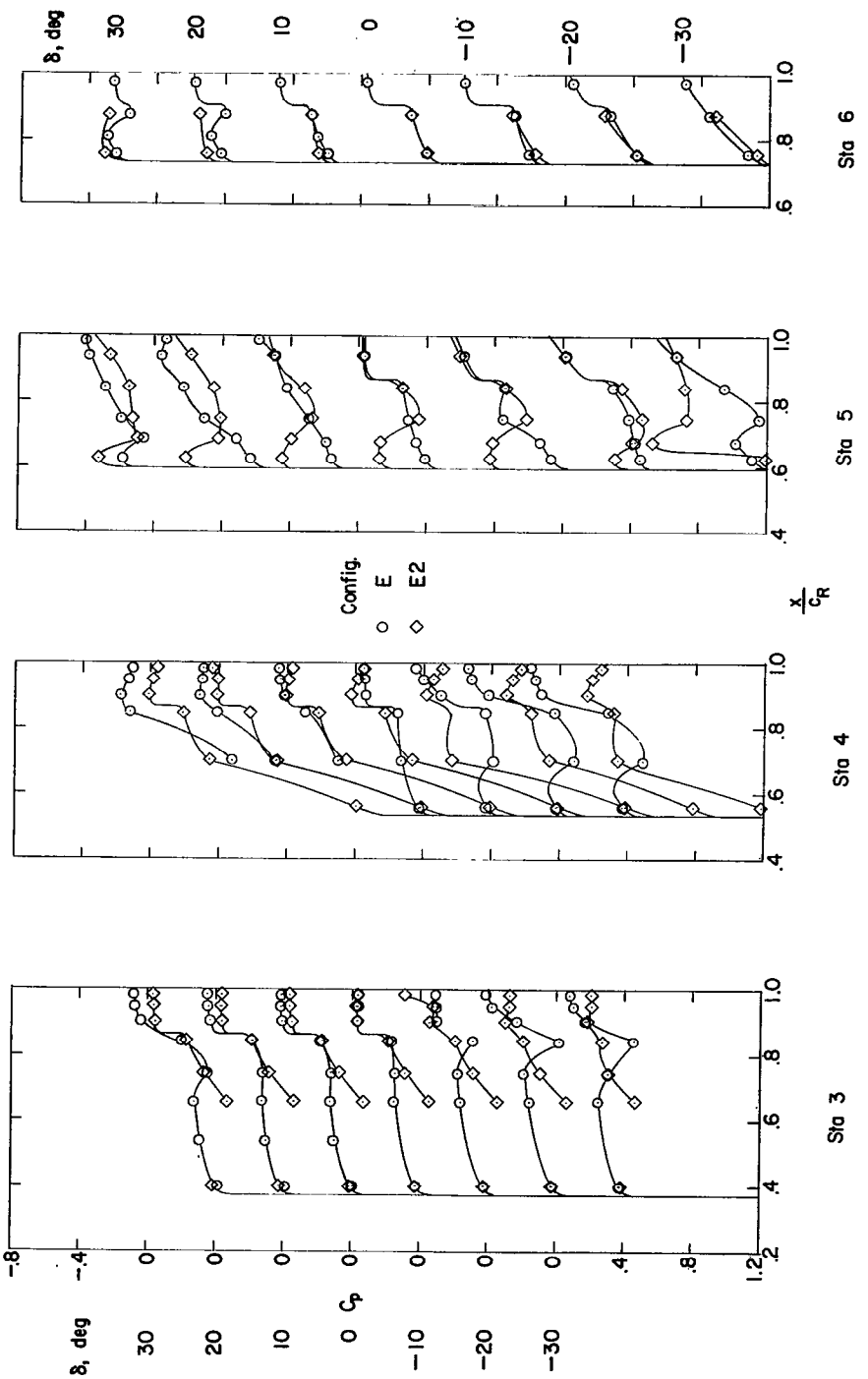

(c) $\alpha = -12^{\circ}$.

Figure 29.- Concluded.

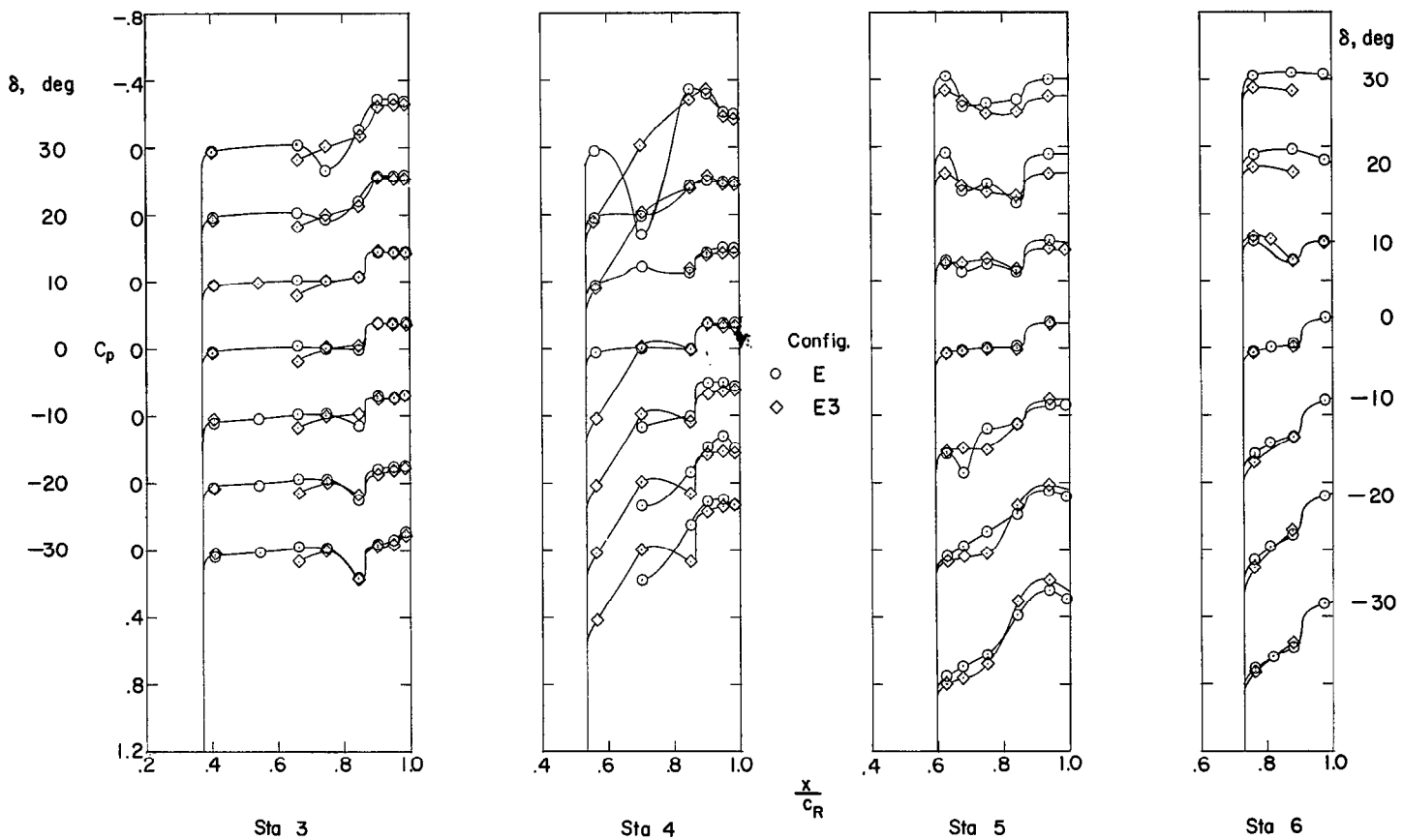

(a) $\alpha = 0^{\circ}$.

Figure 30.- Effect of a partial-chord fence ahead of the hinge-line on the upper-surface pressure distributions on configuration E. $M = 1.61$; $R = 4.2 \times 10^6$.

[redacted]

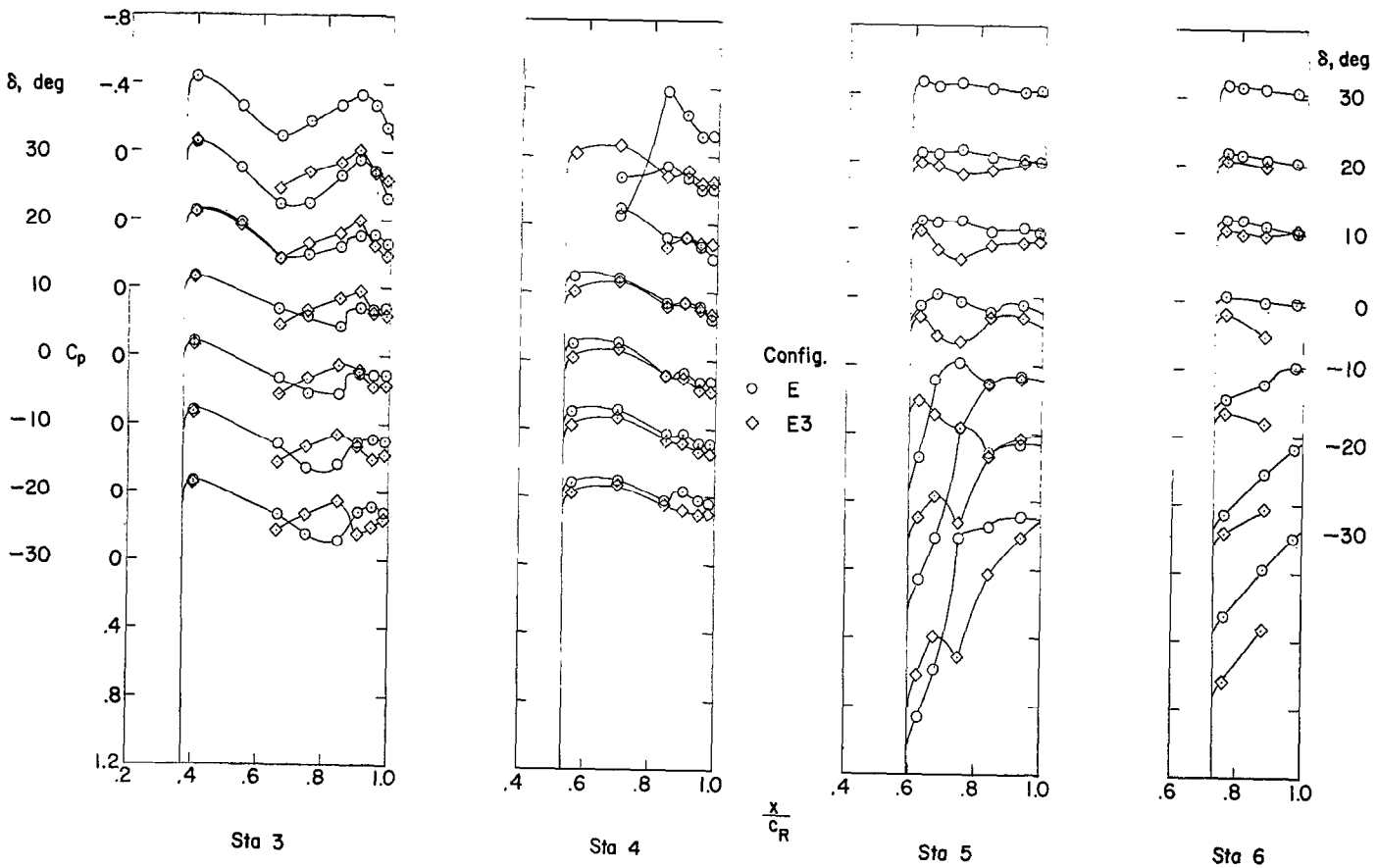

(b) $\alpha = 12^{\circ}$.

Figure 30.- Continued.

[redacted]

[redacted]

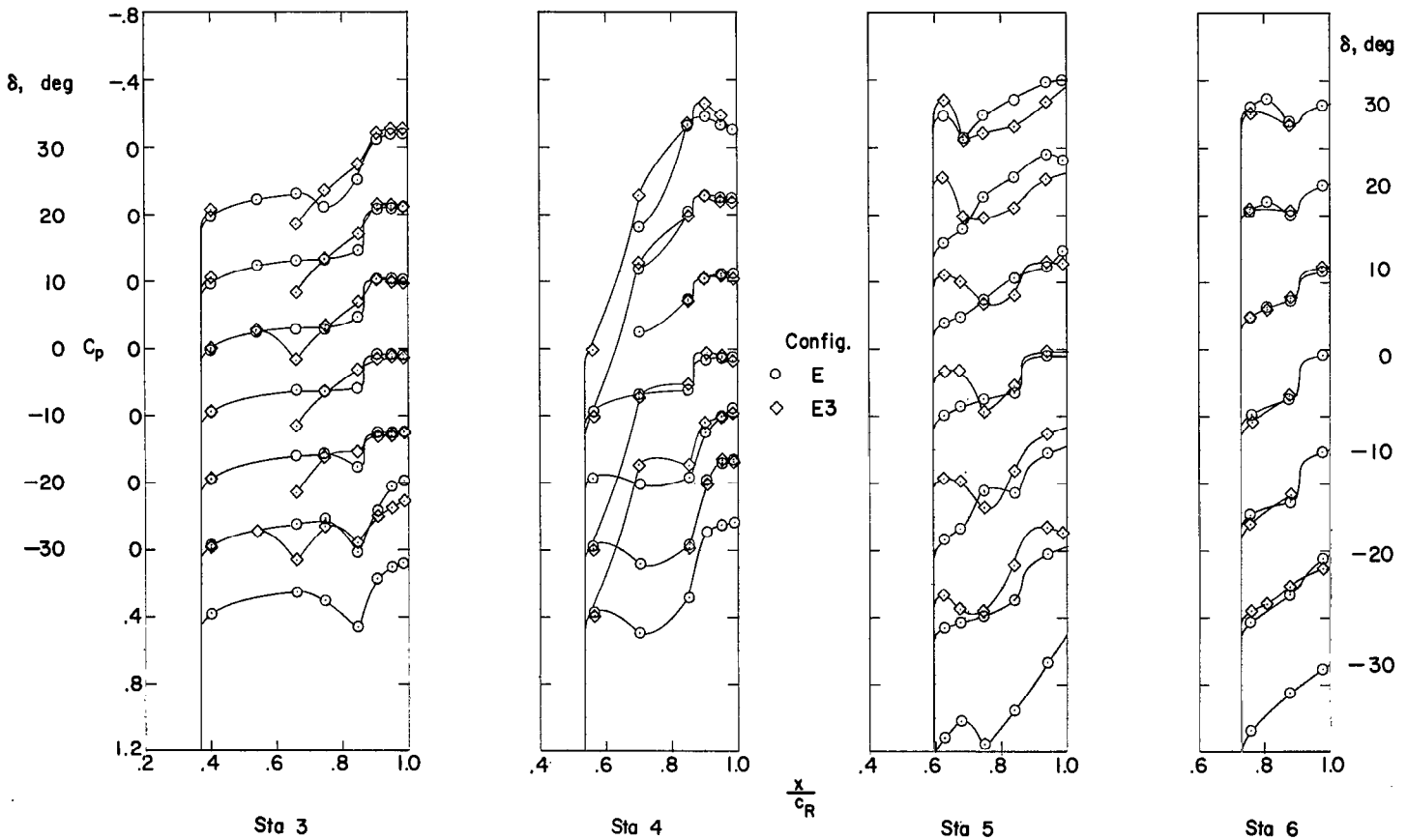

(c) $\alpha = -12^{\circ}$.

Figure 30.- Concluded.

[redacted]

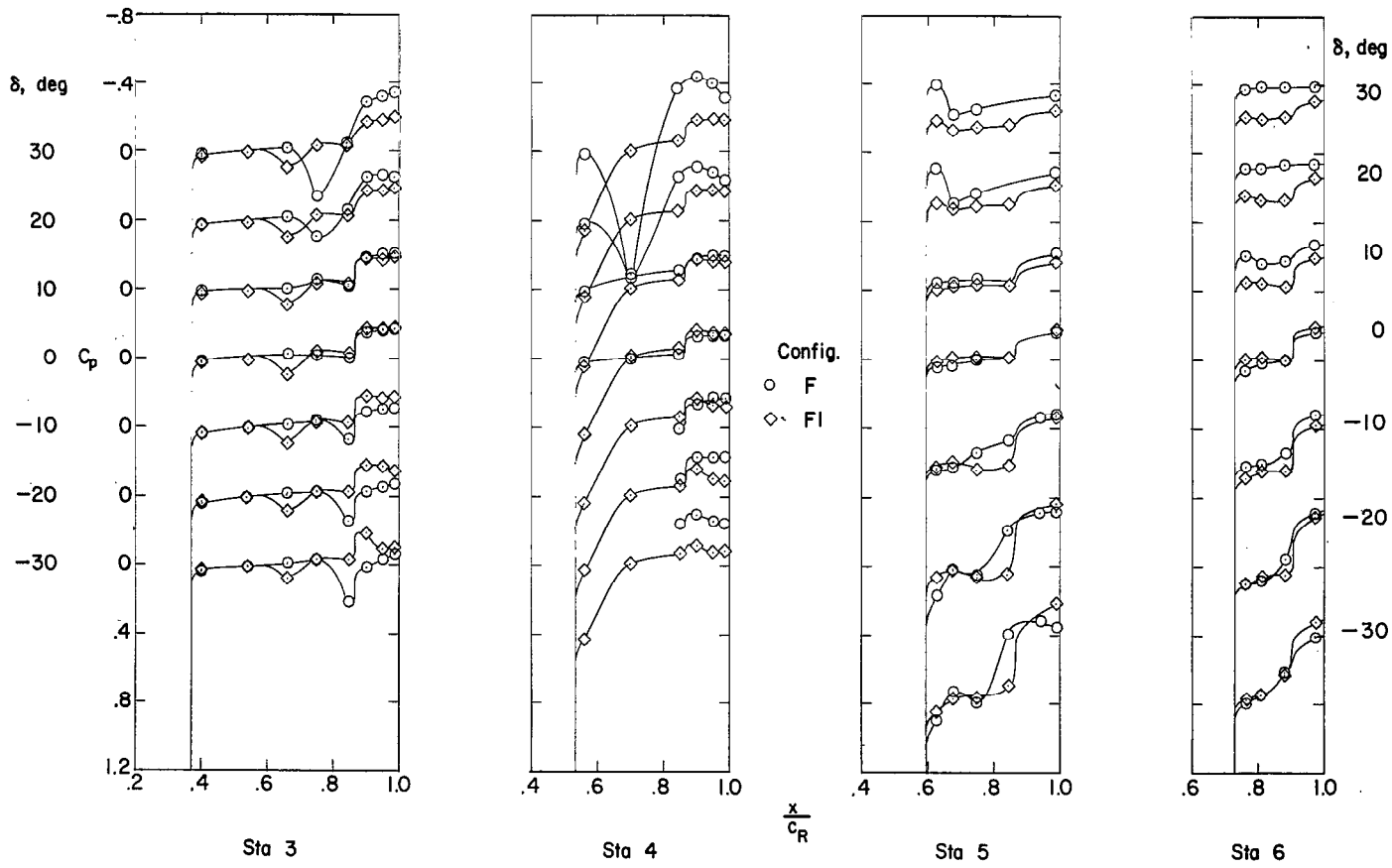

(a) $\alpha = 0^{\circ}$.

Figure 31.- Effect of a full-chord fence on the upper-surface pressure distributions on configuration F. $M = 1.61$; $R = 4.2 \times 10^6$.

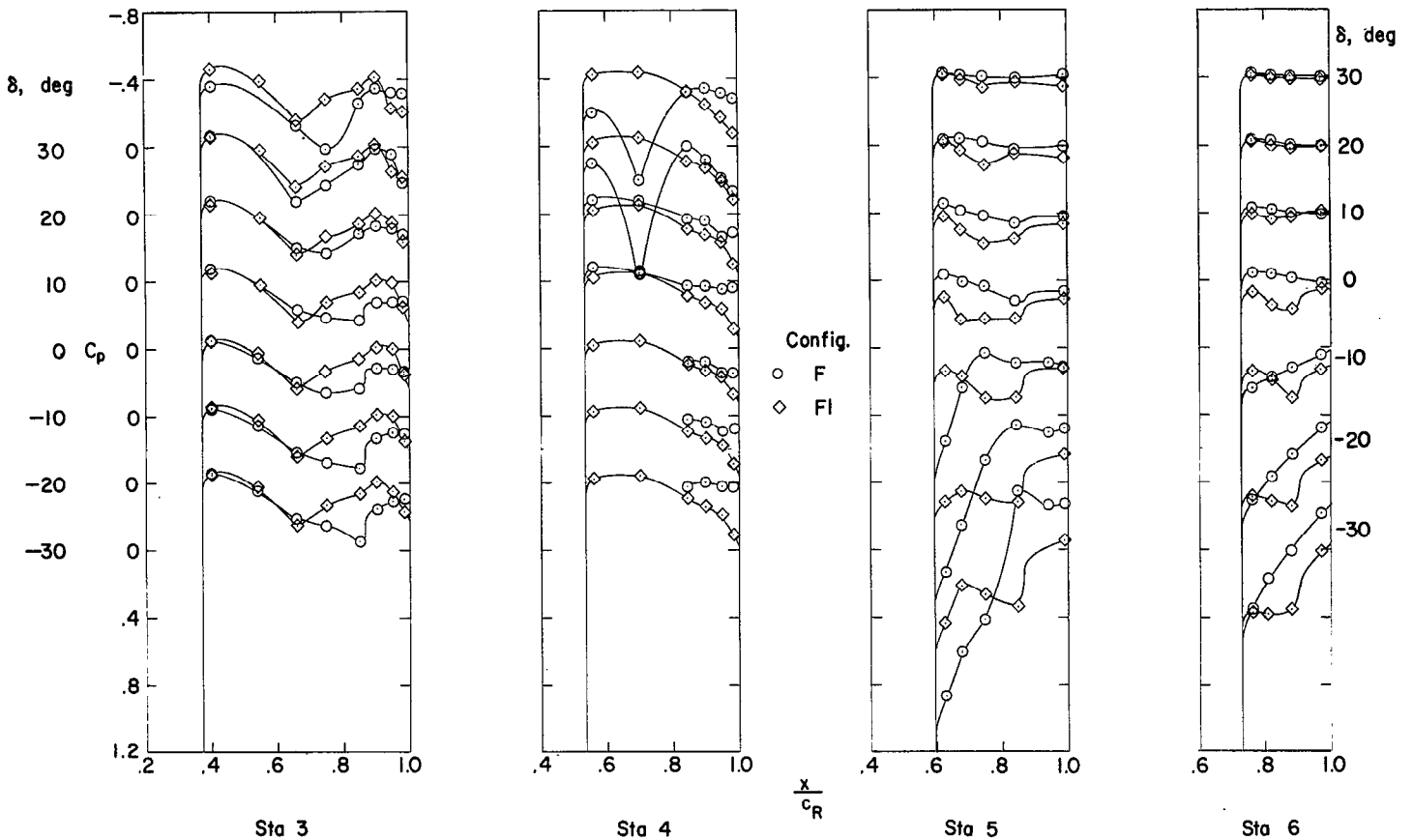

(b) $\alpha = 12^{\circ}$.

Figure 31.- Continued.

[redacted]

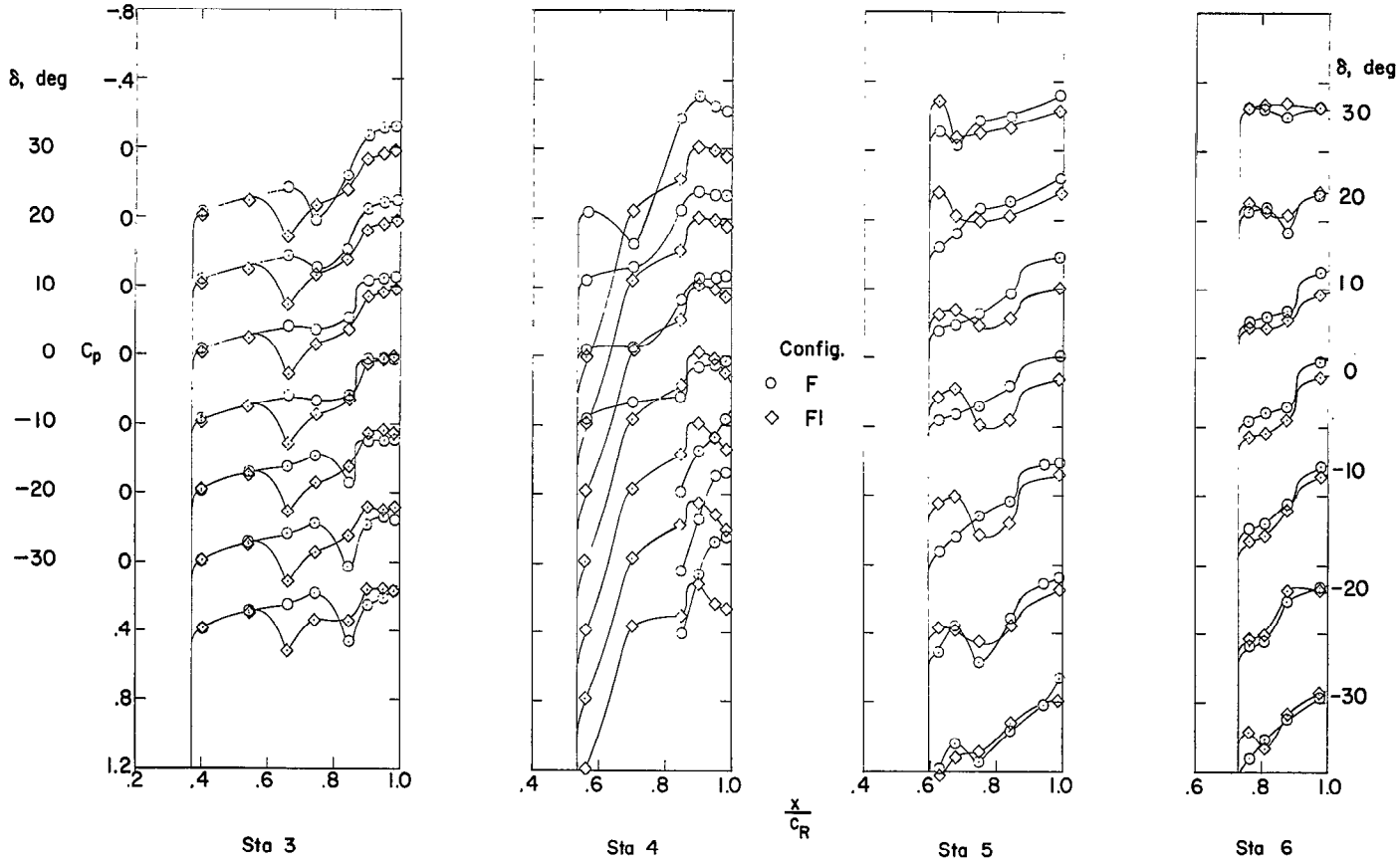

(c) $\alpha = -12^{\circ}$.

Figure 31.- Concluded.

[redacted]

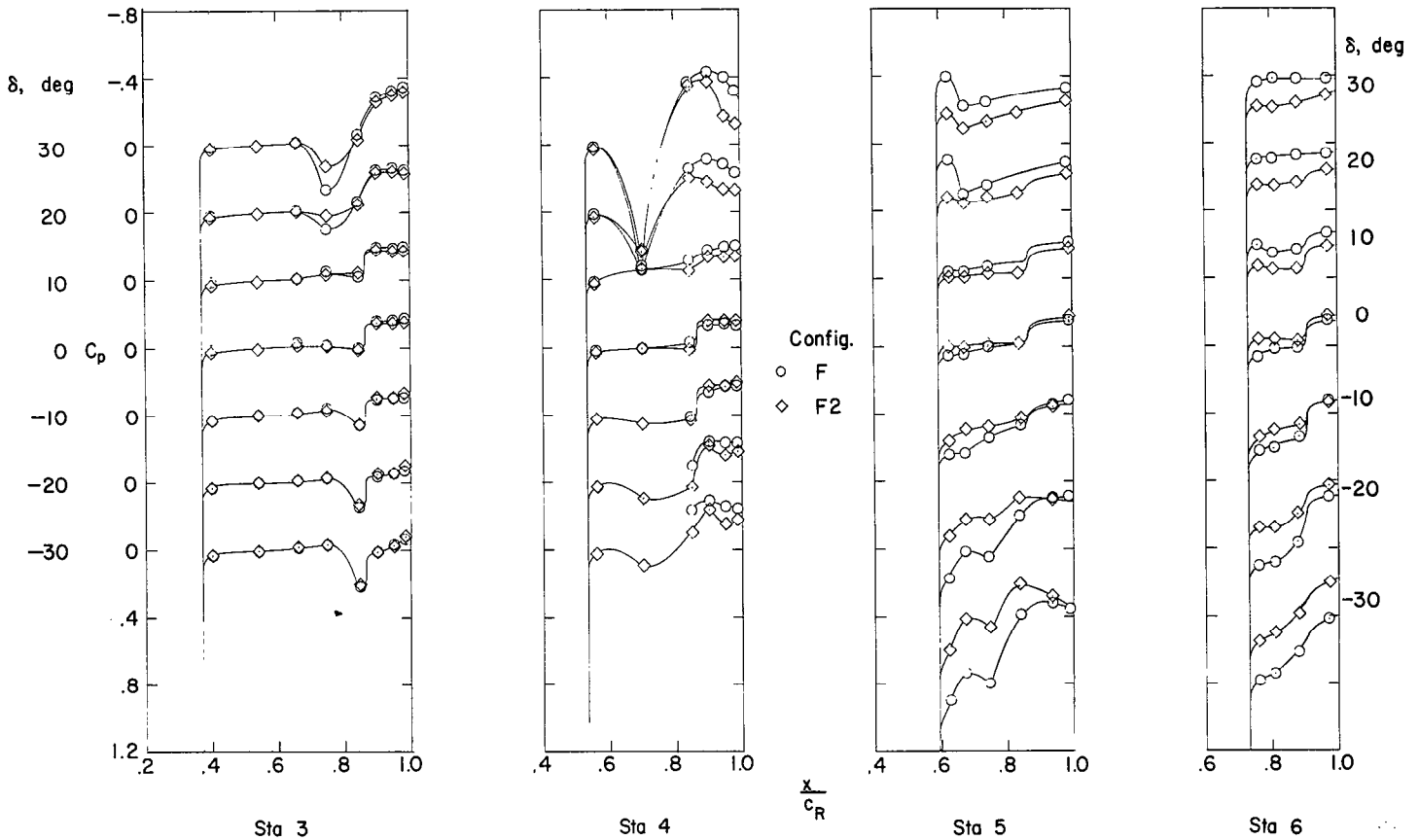

(a) $\alpha = 0^{\circ}$.

Figure 32.- Effect of a partial-chord fence behind the hinge-line on the upper-surface pressure distributions on configuration F. $M = 1.61$; $R = 4.2 \times 10^6$.

[redacted]

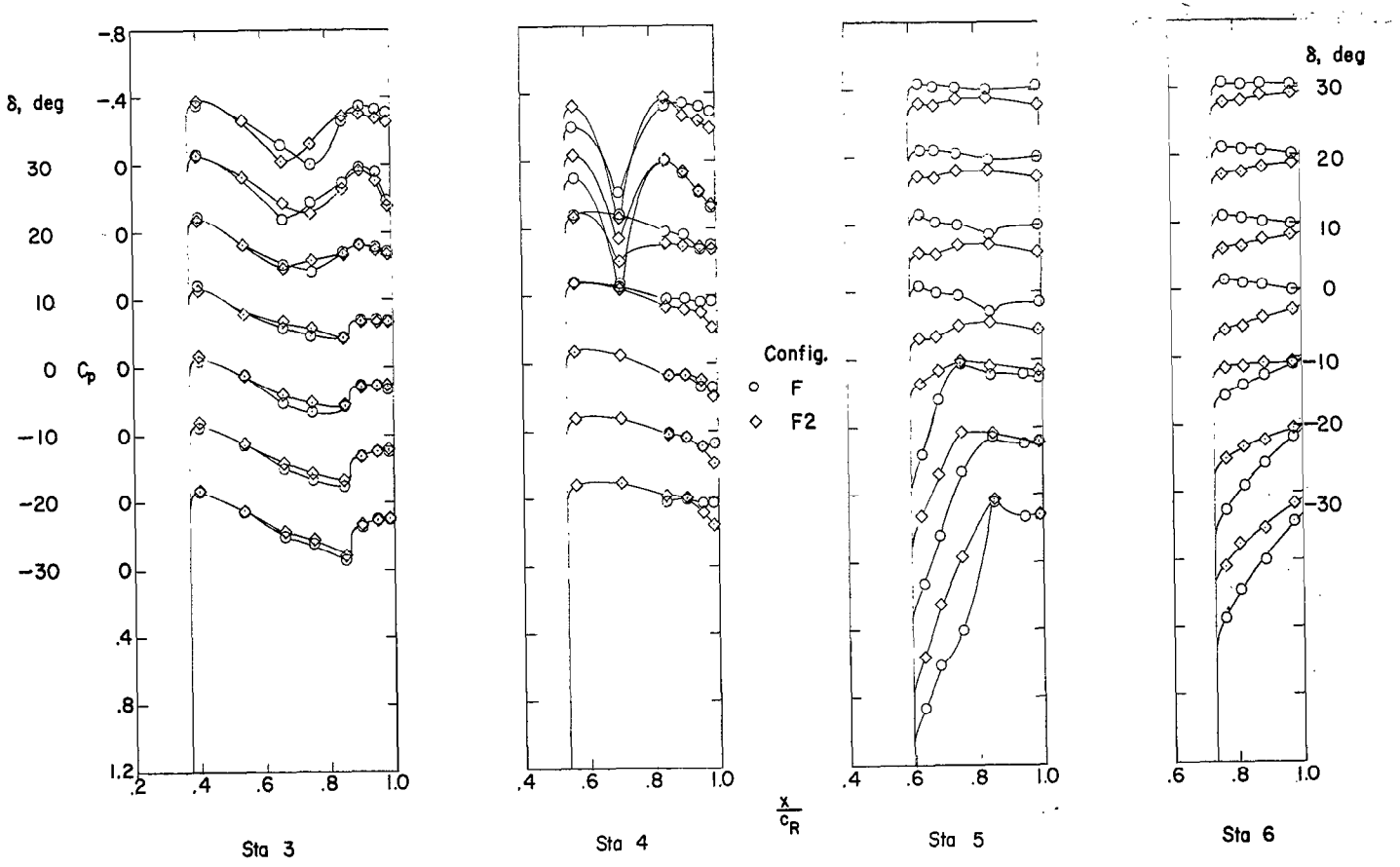

(b) $\alpha = 12^{\circ}$.

Figure 32.- Continued.

[redacted]

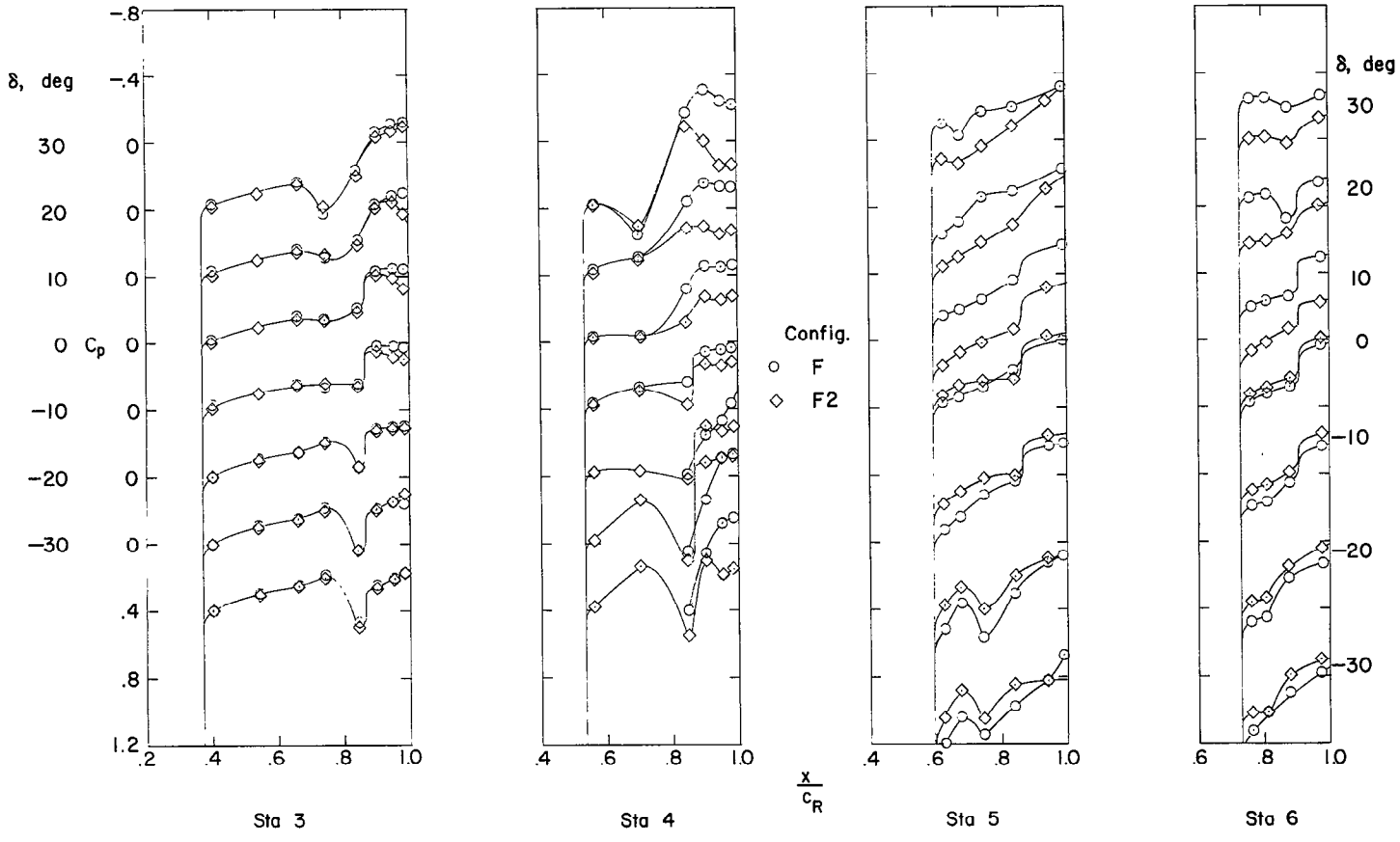

(c) $\alpha = -12^{\circ}$.

Figure 32.- Concluded.

[redacted]

[redacted]

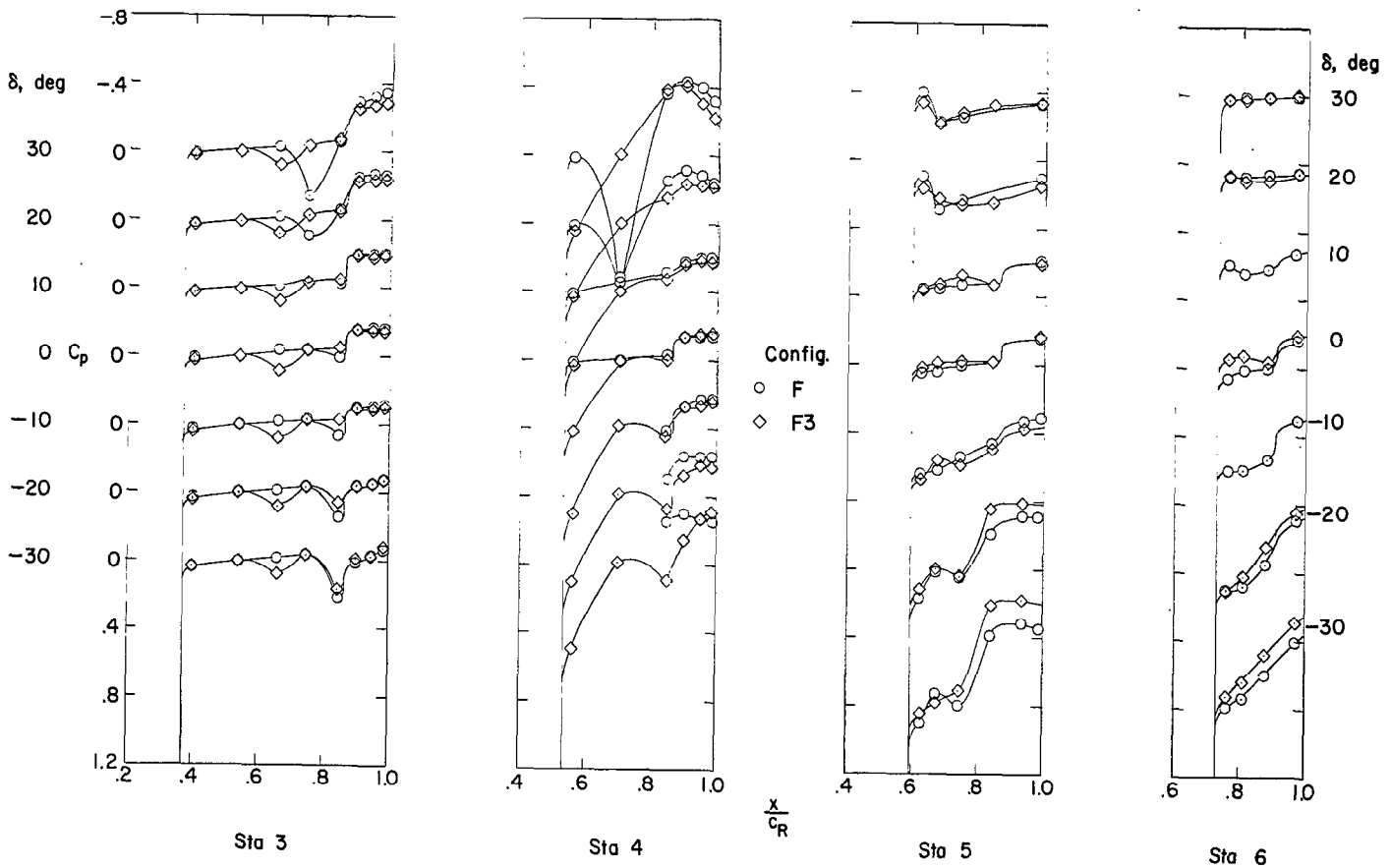

(a) $\alpha = 0^{\circ}$.

Figure 33.- Effect of a partial-chord fence ahead of the hinge-line on the upper-surface pressure distributions on configuration F. $M = 1.61$; $R = 4.2 \times 10^6$.

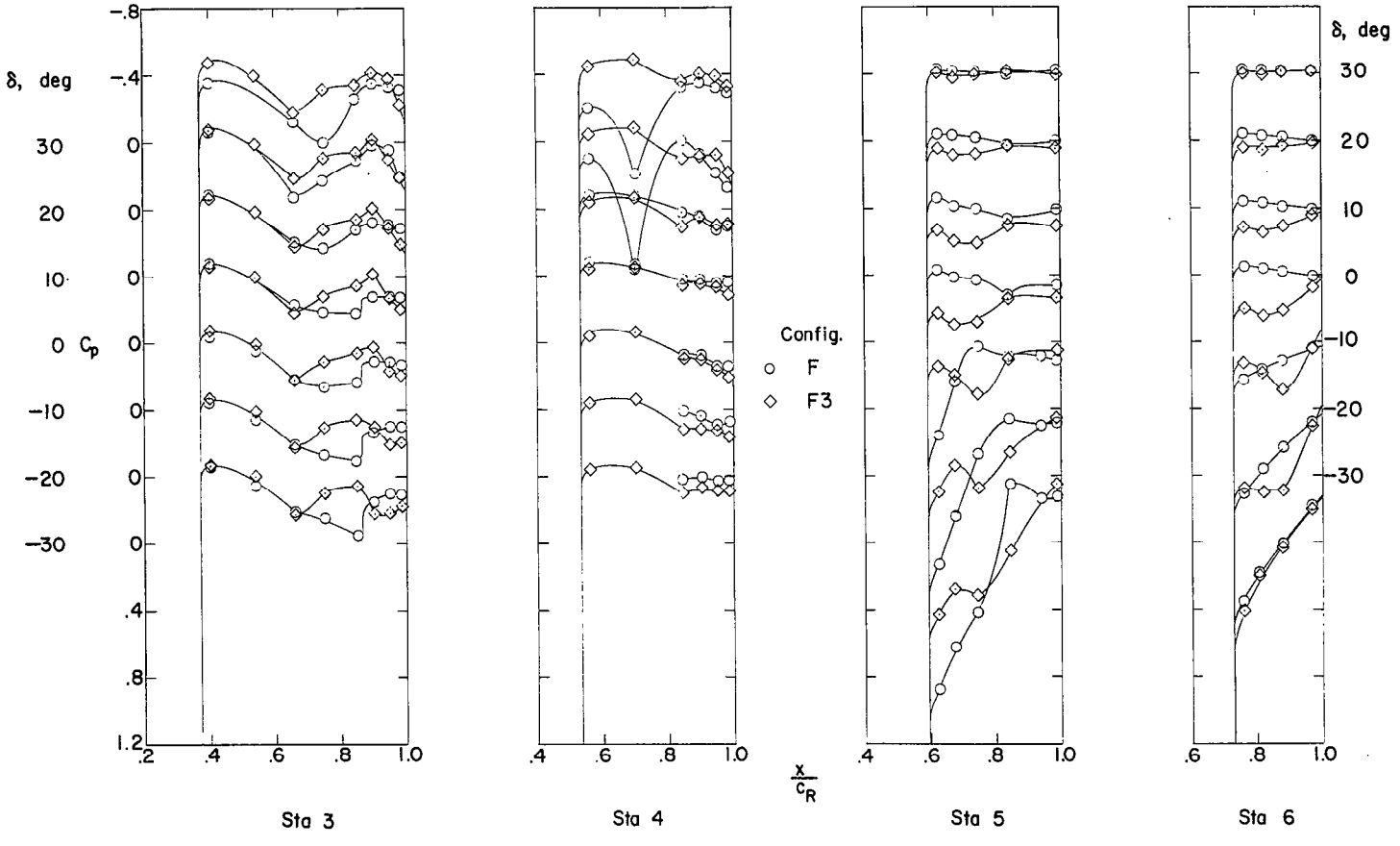

(b) $\alpha = 12^{\circ}$.

Figure 33.- Continued.

[redacted]

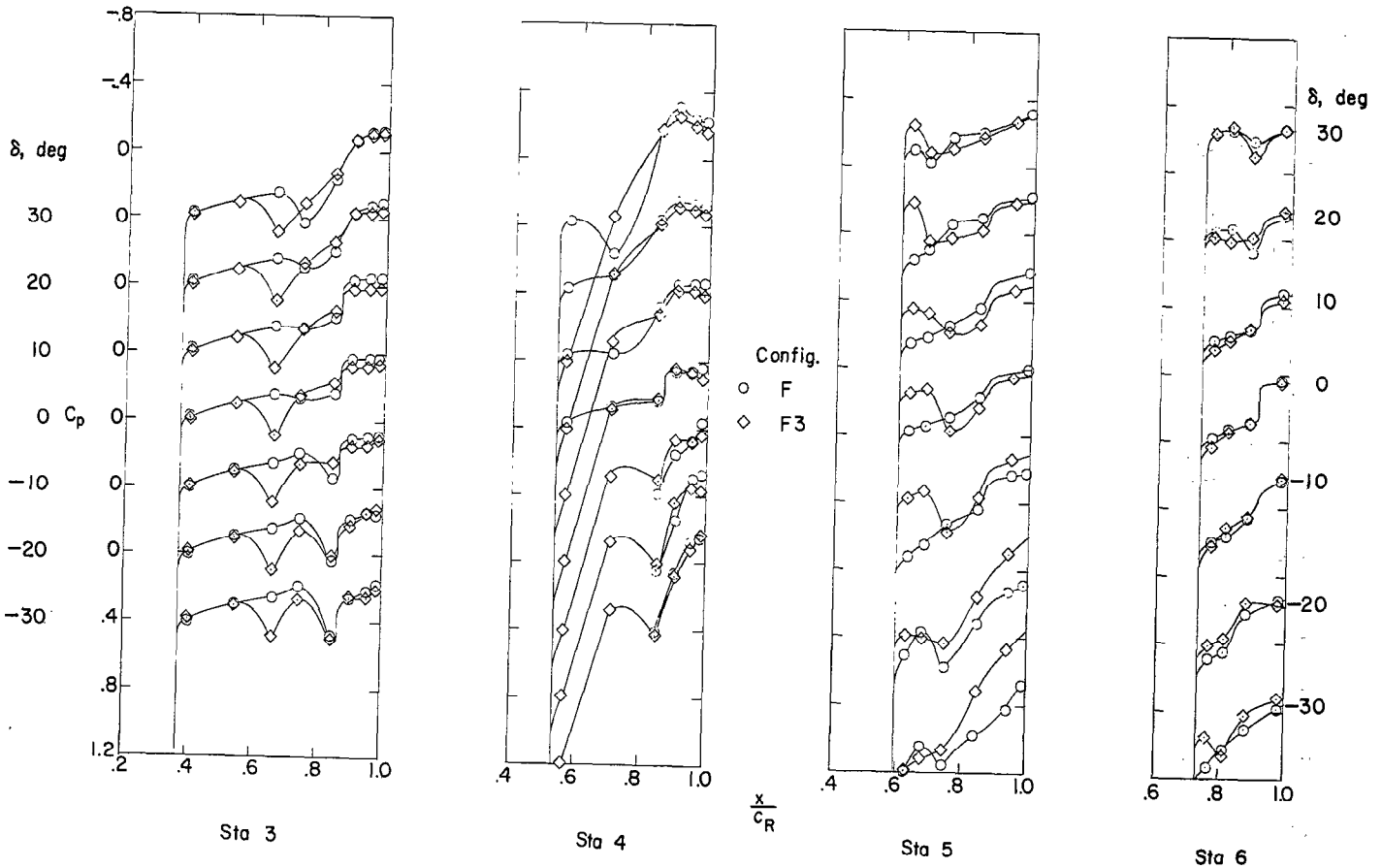

(c) $\alpha = -12^{\circ}$.

Figure 33.- Concluded.

[redacted]

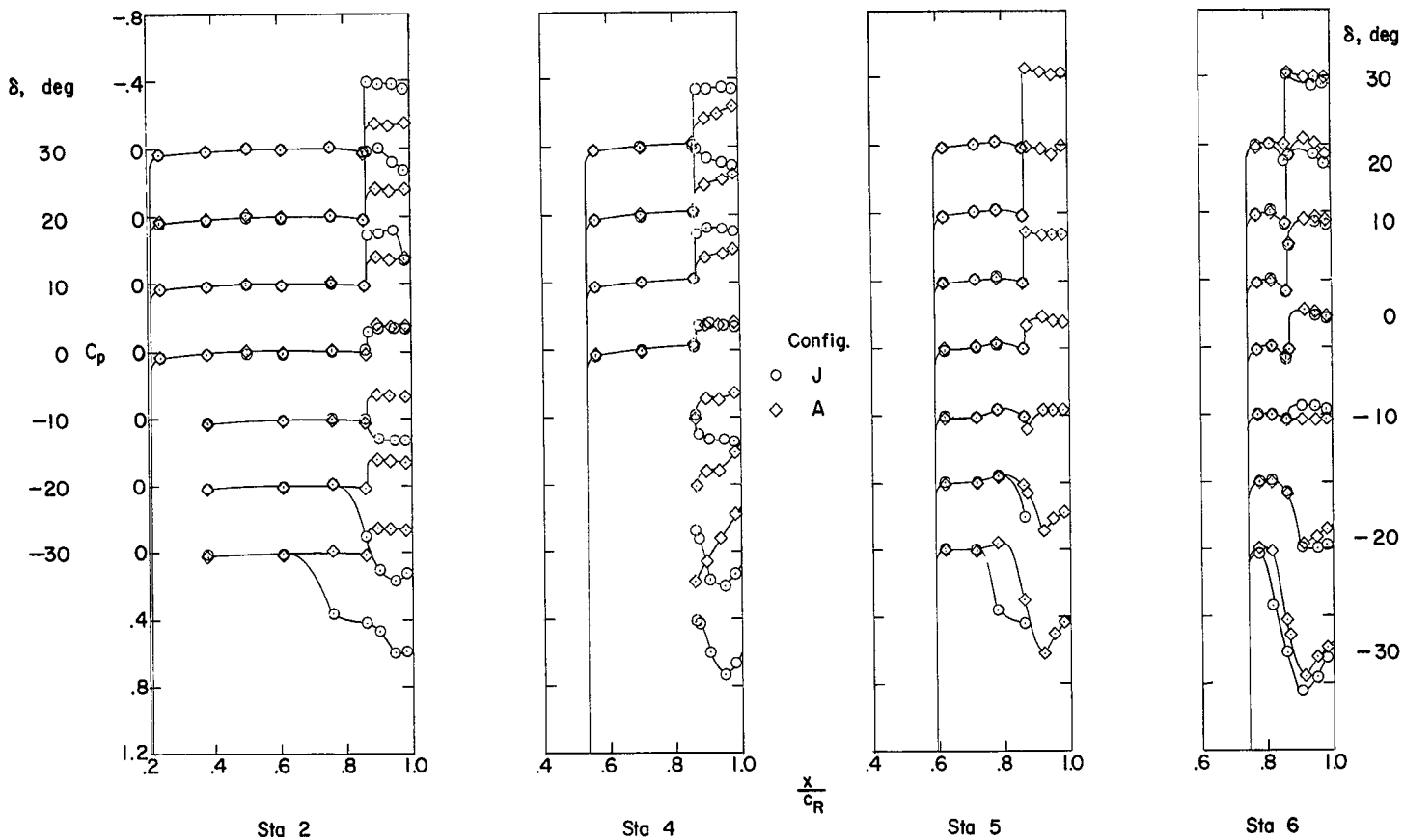

(a) $\alpha = 0^{\circ}$.

Figure 34.- Comparison of the upper-surface pressure distributions on the full-span trailing-edge control with those on the outboard partial-span trailing-edge control. $M = 1.61$; $R = 4.2 \times 10^6$.

[redacted]

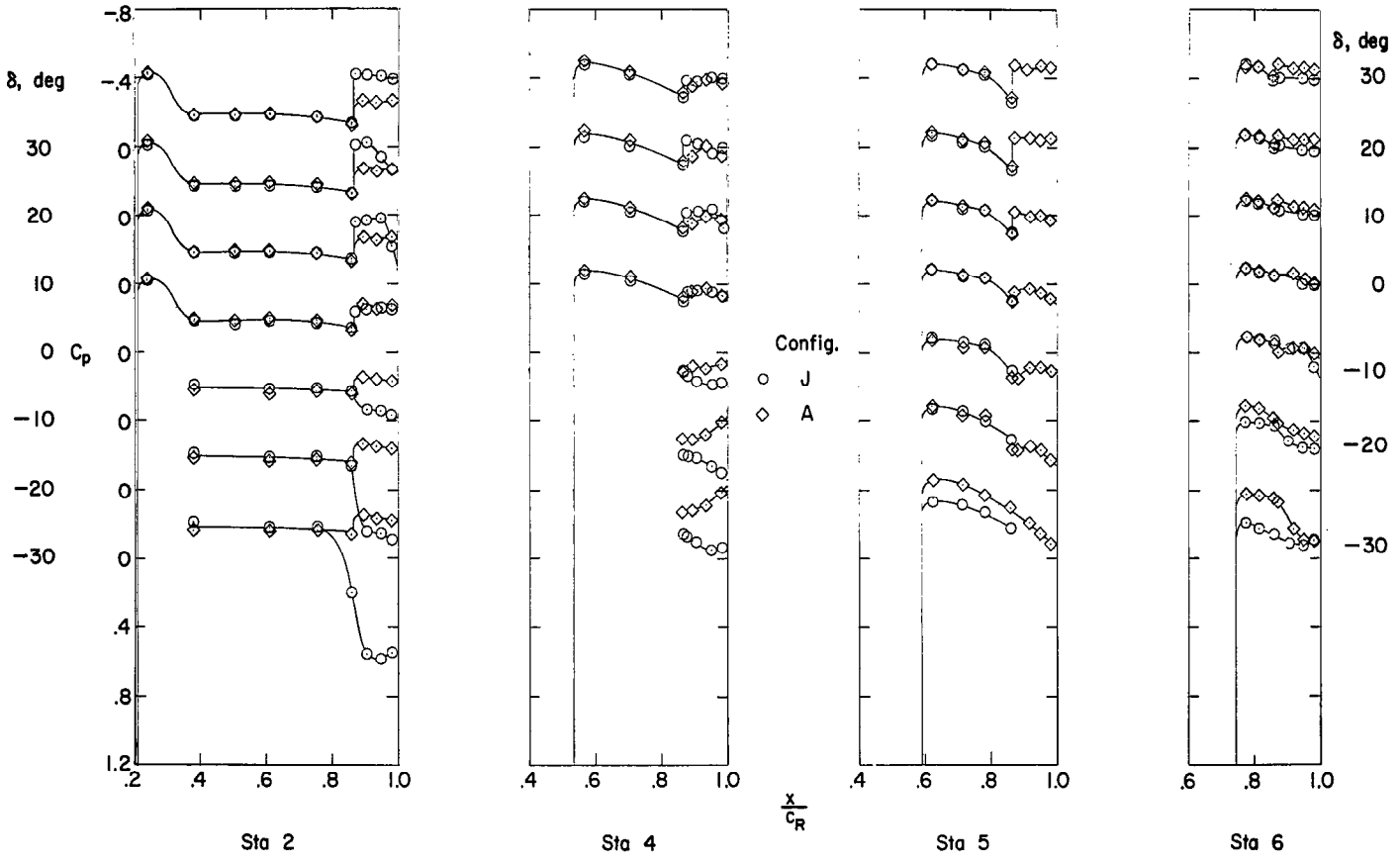

(b) $\alpha = 12^{\circ}$.

Figure 34.- Continued.

[redacted]

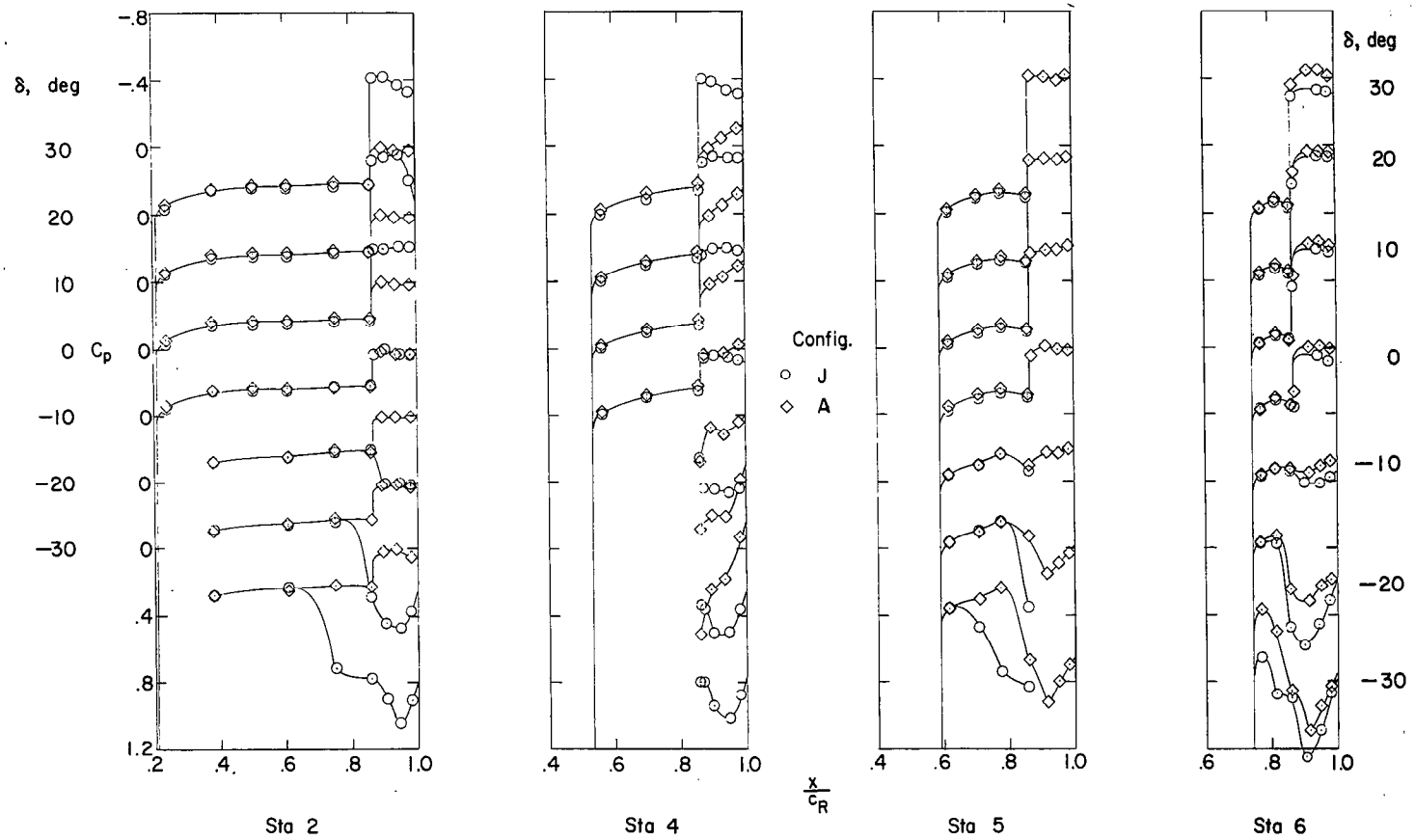

(c) $\alpha = -12^{\circ}$.

Figure 34.- Concluded.

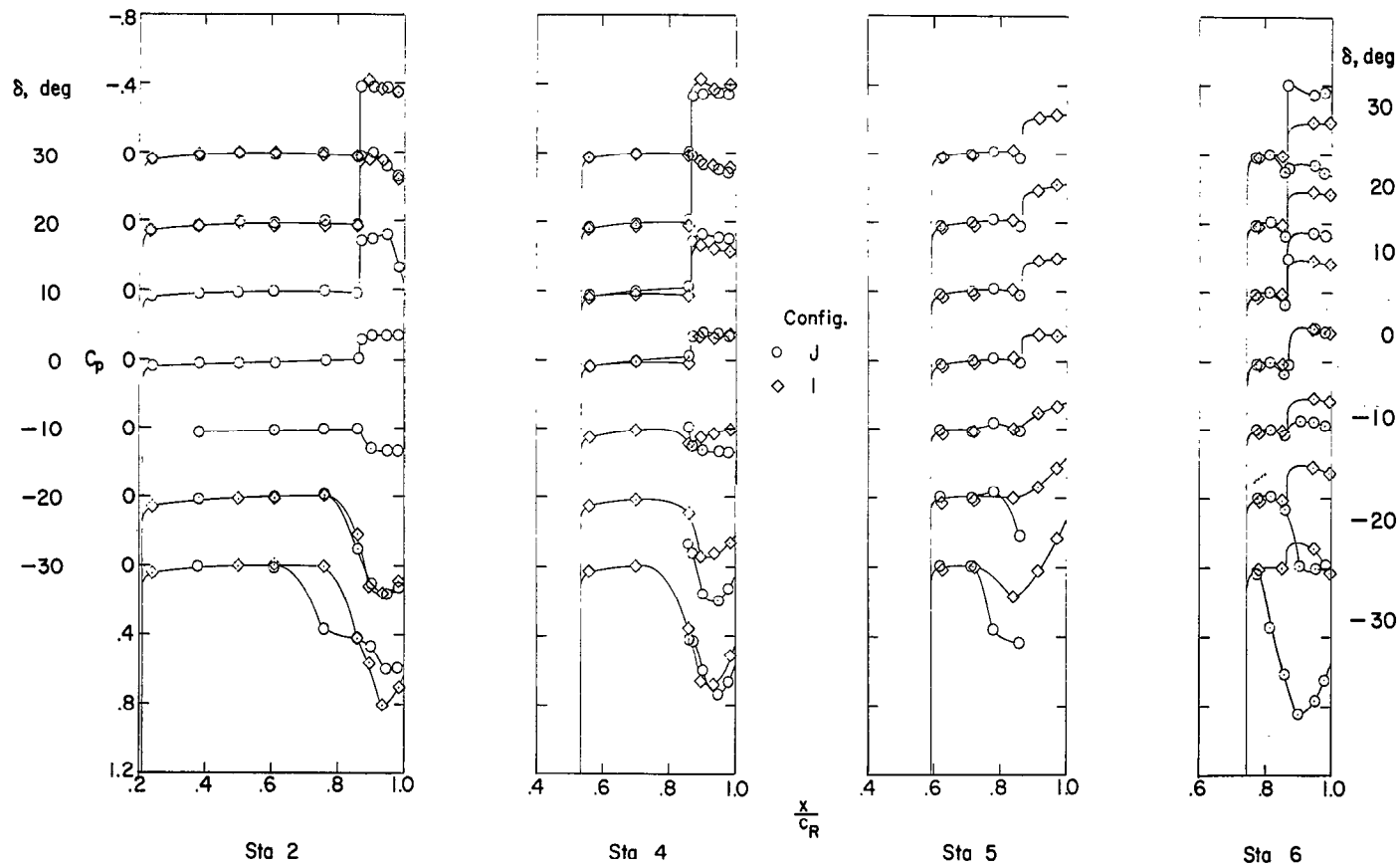

(a) $\alpha = 0^{\circ}$.

Figure 35.- Comparison of the upper-surface pressure distributions on the full-span trailing-edge control with those on the inboard partial-span trailing-edge control. M = 1.61; $R = 4.2 \times 10^6$.

[redacted]

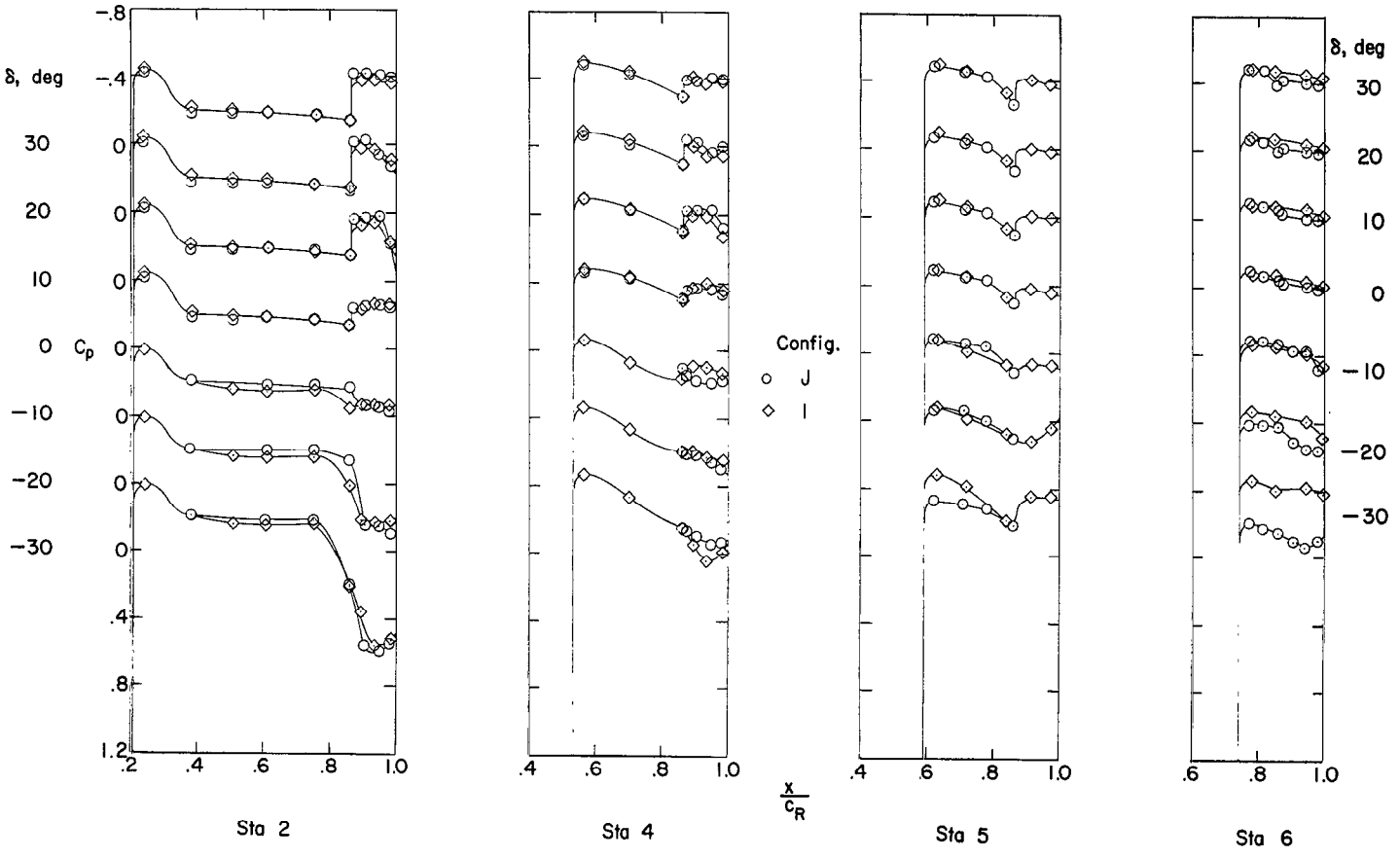

(b) $\alpha = 12^{\circ}$.

Figure 35.- Continued.

[redacted]

[redacted]

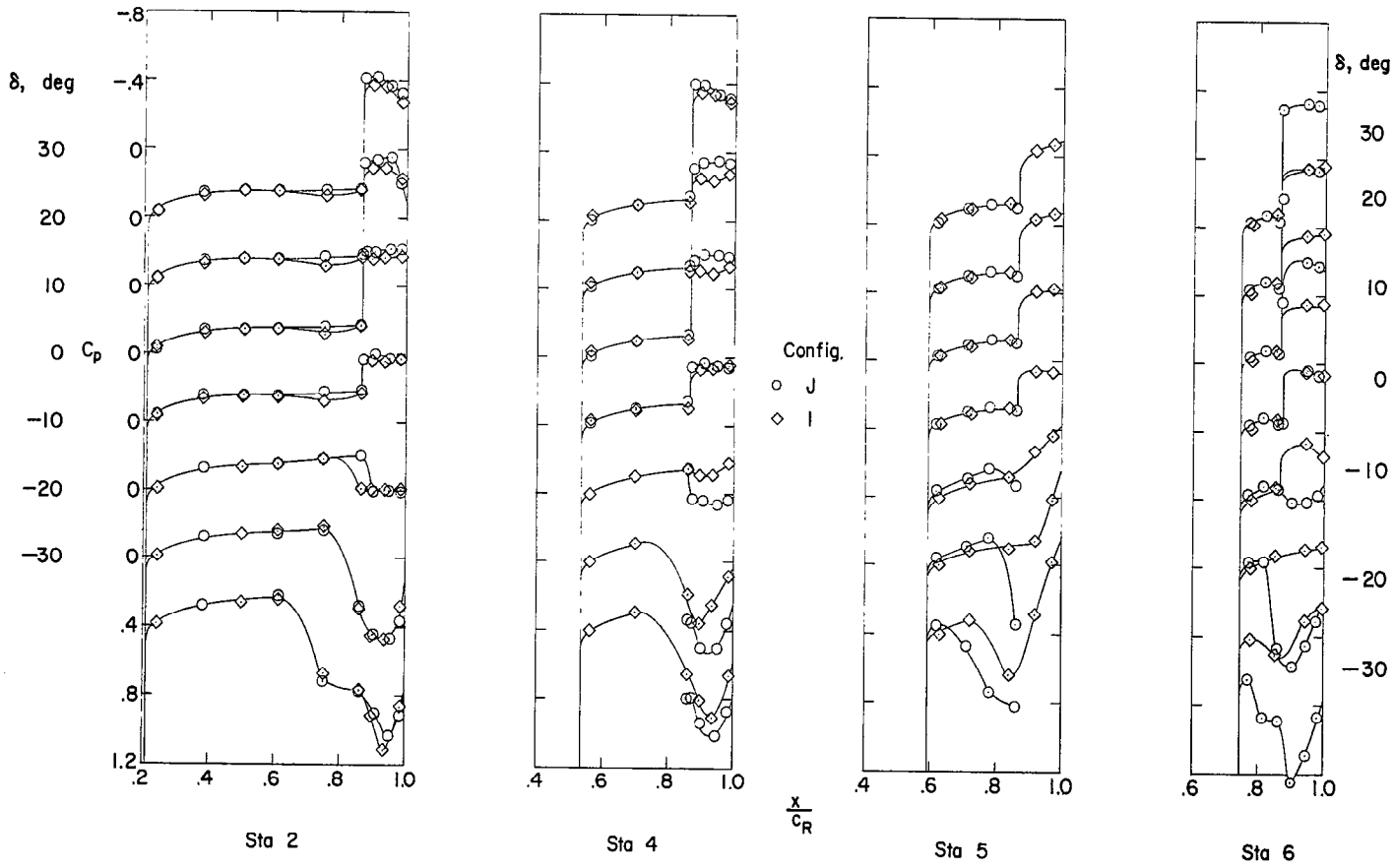

(c) $\alpha = -12^{\circ}$.

Figure 35.- Concluded.

[redacted]

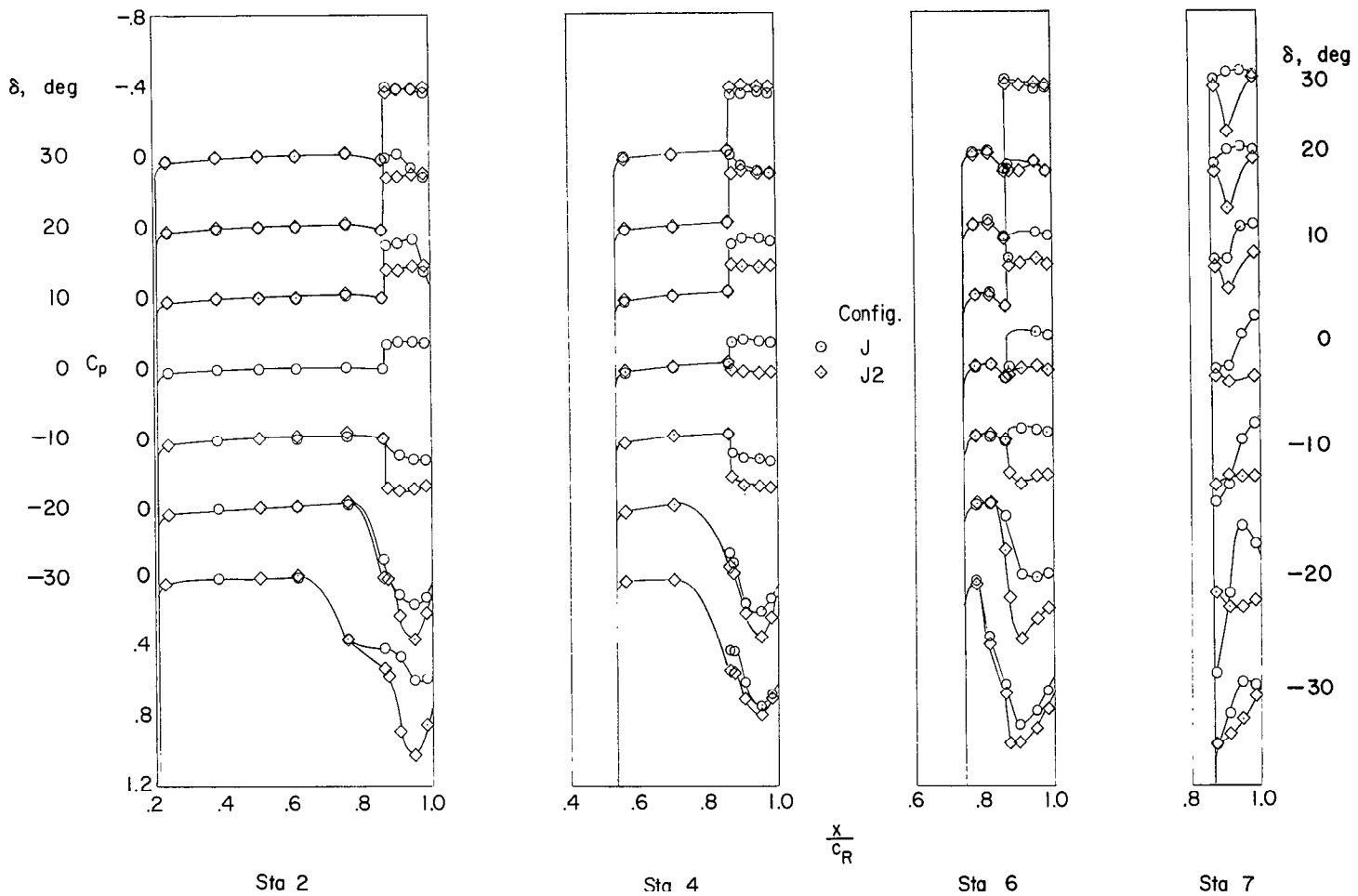

(a) $\alpha = 0^{\circ}$.

Figure 36.- Effect of trailing-edge thickness on the upper-surface pressure distributions of the full-span trailing-edge control. $M = 1.61$; $R = 4.2 \times 10^6$.

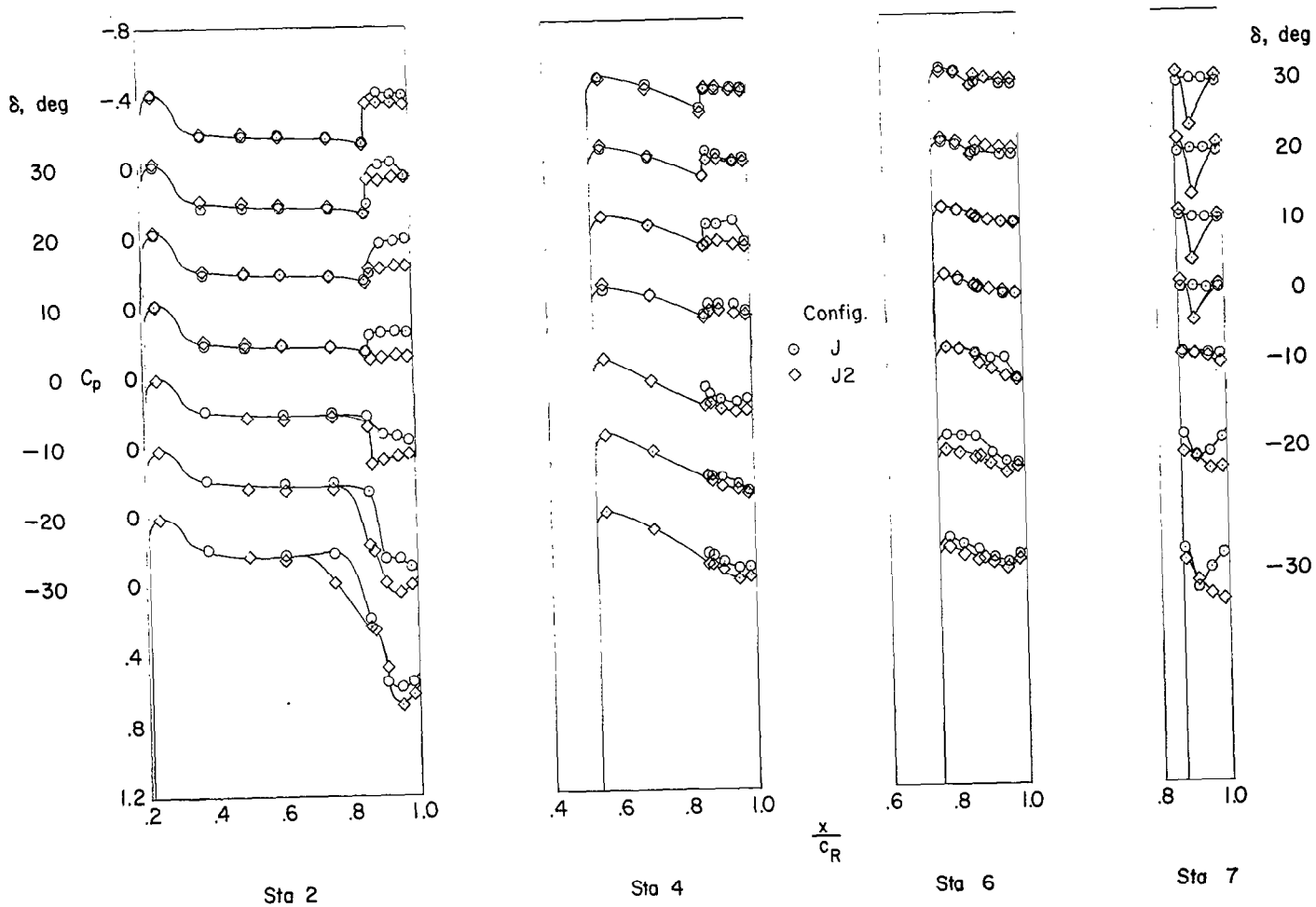

(b) $\alpha = 12^{\circ}$.

Figure 36.- Continued.

[redacted]

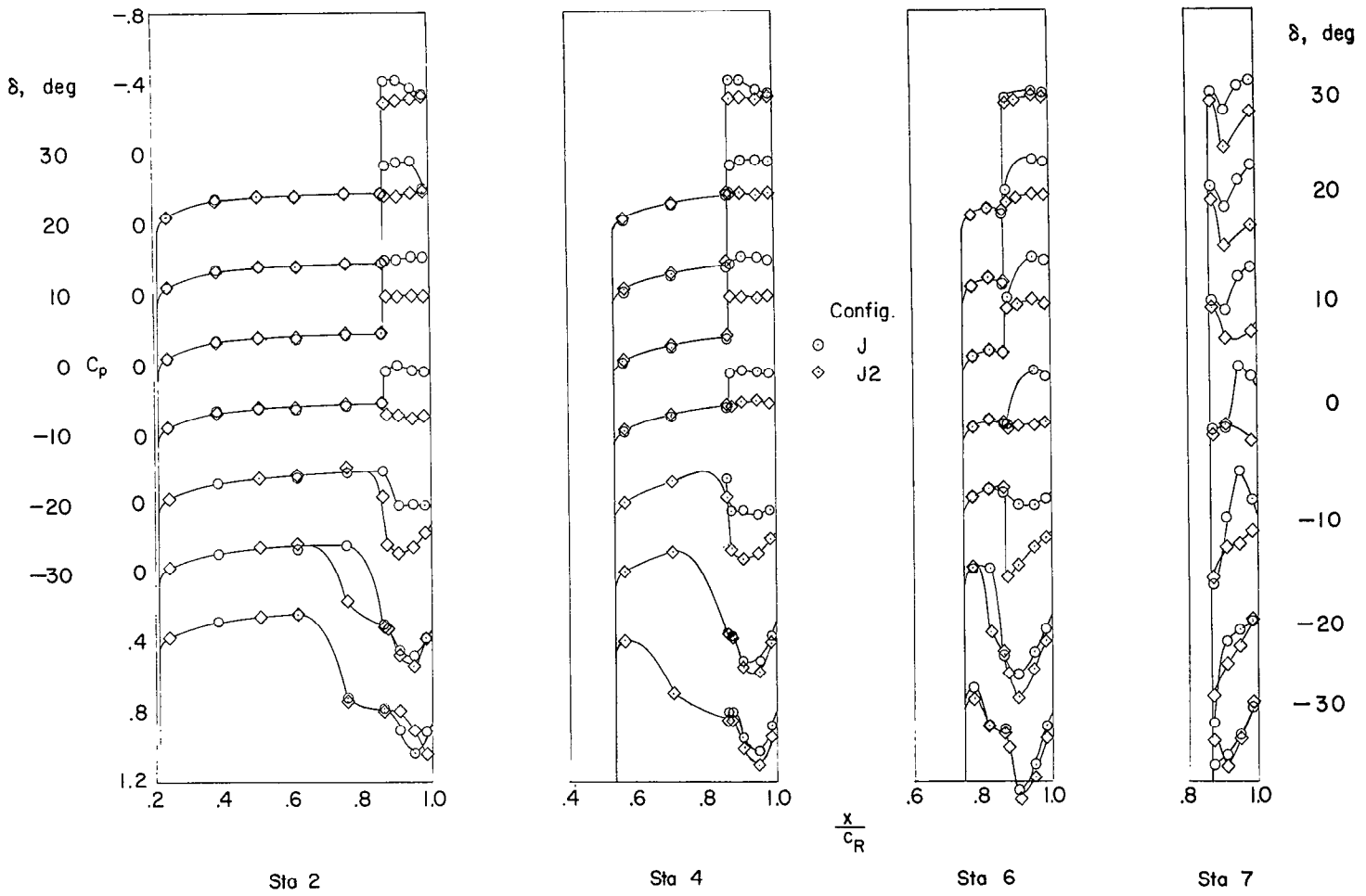

(c) $\alpha = -12^{\circ}$.

Figure 36.- Concluded.

[redacted]

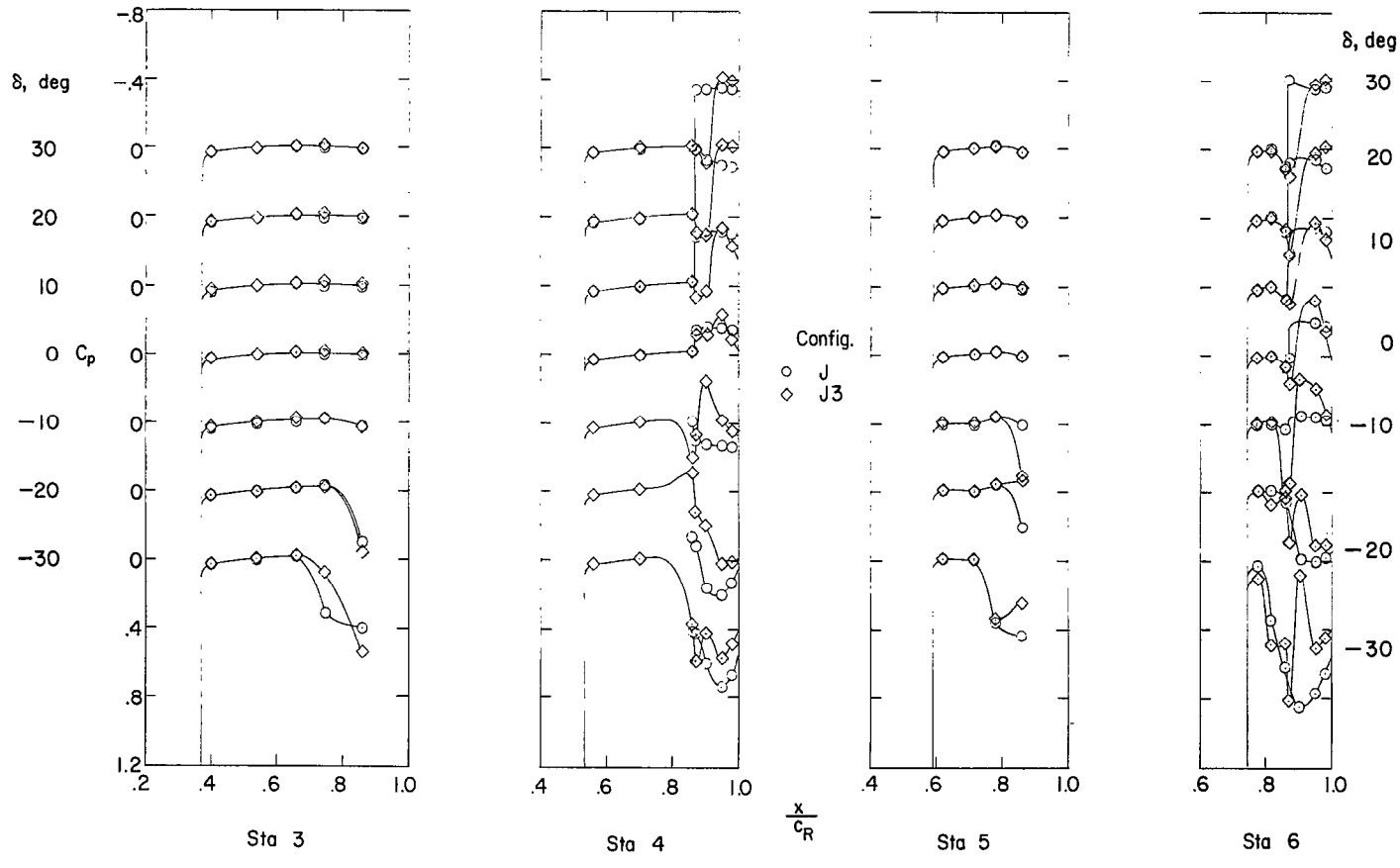

(a) $\alpha = 0^{\circ}$.

Figure 37.- Effect of paddle balances on the upper-surface pressure distributions of the full-span trailing-edge control. $M = 1.61$; $R = 4.2 \times 10^6$.

[redacted]

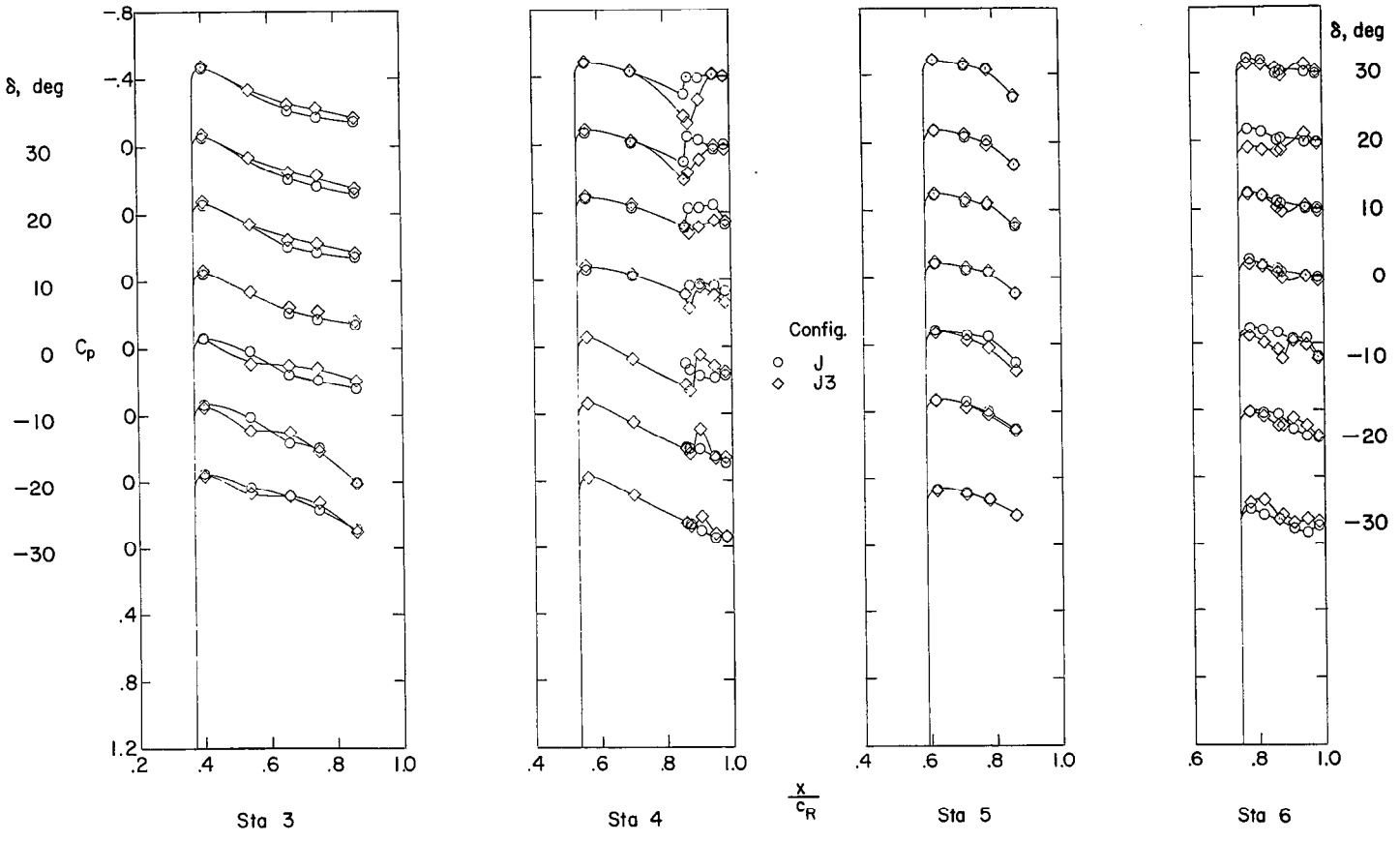

(b) $\alpha = 12^{\circ}$.

Figure 37.- Continued.

[redacted]

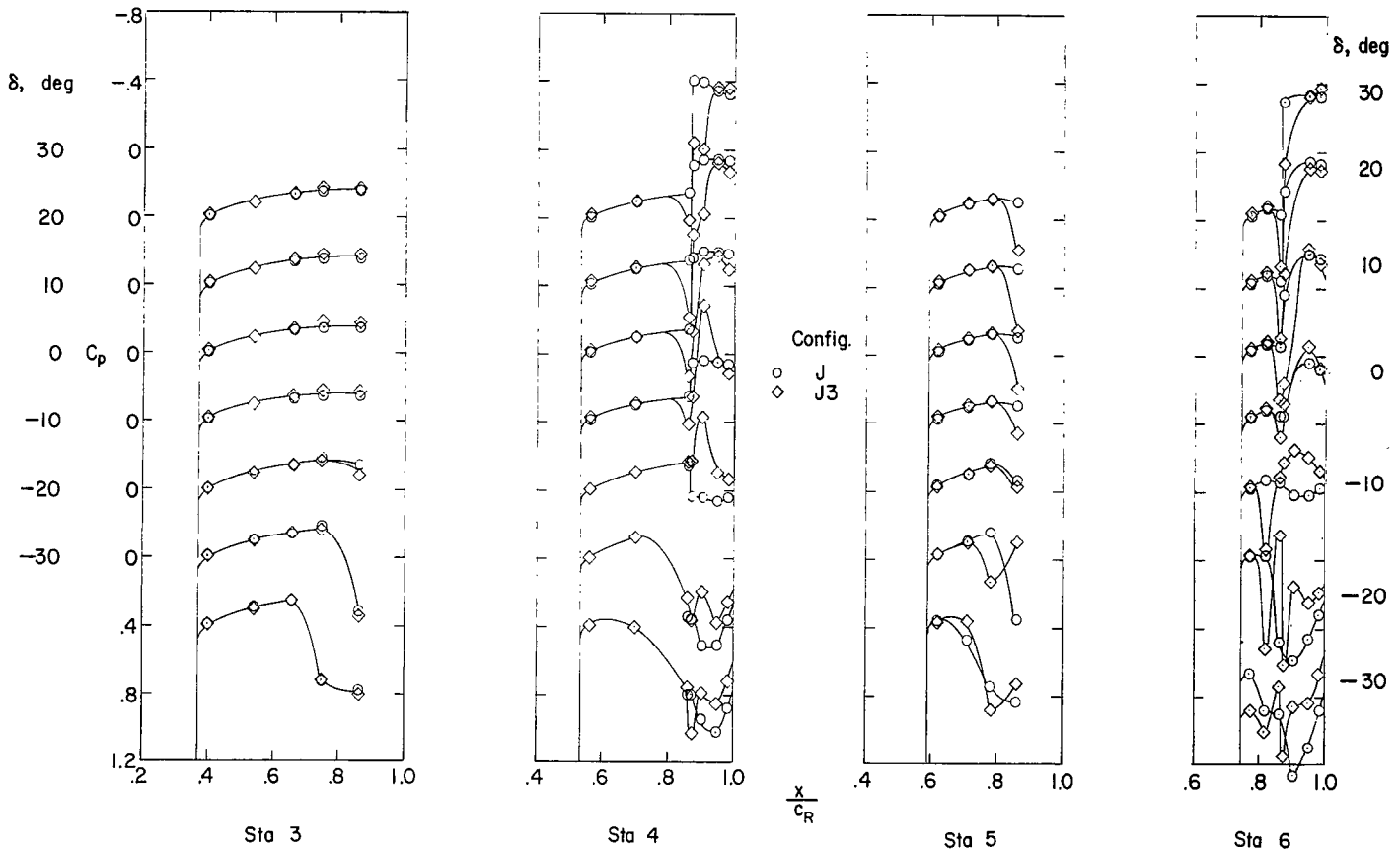

(c) $\alpha = -12^{\circ}$.

Figure 37.- Concluded.

UNCLASSIFIED
[redacted]

NACA - Langley Field, Va.

NASA Technical Library
3 1176 01437 7916